Nature-inspired shape optimization of dental restoration for replacing single missing tooth

A DISSERTATION
SUBMITTED TO THE FACULTY OF
UNIVERSITY OF MINNESOTA
BY

Yung-Chung Chen

IN PARTIAL FULFILLMENT OF THE REQUIREMENTS
FOR THE DEGREE OF
DOCTOR OF PHILOSOPHY

Thesis adviser: Dr. Alex Fok

August 2014

Acknowledgements

I could not have accomplished my dissertation without the guidance of my committee members and support from friends, family and my wife.

My deepest gratitude goes to my advisor, Dr. Alex Fok, for his guidance, care, patience, encouragement and providing me with an excellent atmosphere and financial support for doing research. Many thanks Dr. Ralph DeLong, Dr. William Douglas, Dr. Conrado Aparicio, Dr. Haiyan Li and Dr. Jianying Li for guiding my research for the past several years and helping me to develop my background knowledge in biomaterials, biomechanics, and numerical modelling. Special thanks to Ms. Maria Pintado, who taught me how to use various testing equipment and protocols when I first began my research in the Minnesota Dental Research Center for Biomaterials and Biomechanics (MDRCBB).

Also thank to my good friend, Jin Woo Jung, who was always willing to help and give his best suggestions, especially on programming languages. It would have been a lonely lab without him. Many thanks to Yuping Li, Carola Carrera, YoungCheul Heo, Bonita VanHeel, and other colleagues in the MDRCBB. My research would not have been possible without all their help.

I would also like to thank my parents and many good friends back in Taiwan. They were always supporting me and encouraging me with their best wishes.

Finally, I would like to thank my wife, HsinNing Chang. She was always there cheering me up and stood by me through the good and bad times.

Table of Contents

List of Figures

List of Tables

Chapter 1 Introduction

1.1 Single missing tooth: etiology and prevalence statistics

Most people will experience permanent tooth loss during their lifetimes. Several factors are highly associated with tooth loss, with dental caries and periodontitis being the most critical [1-4]. A small pit-and-fissure lesion can escalate into a pulp-involved or sub-gingival deep caries if one does not receive timely intervention. Some pulp-involved carious teeth could be restored after receiving proper endodontic treatments and its associated dental prostheses such as posts and cores, while most teeth with large subgingival carious lesions are usually recommended to be extracted, although restoration is sometimes carried out.

The other major disease-related factor for tooth loss, periodontitis, can loosen the periodontal attachment, causing high tooth mobility and finally tooth exfoliation. Teeth are subjected to various levels of occlusal load, either vertical or oblique, depending on their positions. Teeth with insufficient periodontal attachments are not able to support the regular occlusal load, causing them to suffer from the so-called secondary occlusal trauma. Secondary occlusal trauma can be further aggravated by parafunctional habits such as bruxism.

Some sociodemographic factors are also highly related to tooth loss, e.g. age, gender, ethnicity or financial status:

- It has been well documented that the mean number of missing teeth increases with age [5, 6]. In 2007, the Center for Disease Control and Prevention (CDC)

reported that the mean number of missing teeth among the adult population (20 ~ 64 years) in the United States ranged from 0.69 (< 34 years old) to 5.30 (> 50 years) [7]. For older individuals, chronic diseases or limited access to dental care can make them more prone to tooth loss [8-10]. Although the most recent (1999-2004) National Health and Nutrition Examination Survey has shown that the prevalence of both partial and total tooth loss in seniors age 65 and over has decreased [11], the average numbers for this elder population (8.32 for age 65 to 74 and 9.41 for age 75 and older) are still high. In comparison with the United States, a higher number of missing teeth can be found in the younger population in some developing countries [12]. In a survey conducted in Brazil in 2001, for example, 70% of females and 65% of male teenagers have lost some of their permanent teeth even before puberty [13].

- Researchers from the CDC have found that women were more vulnerable to oral diseases, especially during pregnancy, as most pregnant women do not visit dentists because of concerns about the safety of dental treatment and medication [14]. However, many physiological changes during pregnancy, such as pregnancy-related gingivitis or tooth erosion from morning sickness, can give women poor oral health, which can be transmitted to their newborns [14].
- It is also known that the mean number of missing teeth is significantly lower in non-Hispanic white population and wealthy household, which is defined as

those with their annual income 200% more than the poverty threshold according to the federal poverty guideline [8].

Although tooth loss is not a life-threatening disease, it does significantly affect one's quality of life; therefore, the World Health Organization (WHO) has set several global goals for oral health every decade since the year 1981 [15]. Reducing the number of missing teeth has always been an important aim for improving oral health and to achieve a better quality of life. The global goal for oral health set by WHO in the year 2000 was that 85% of the world population would not have any missing teeth [15]. For the year 2010, WHO proposed a goal of no missing teeth among the 18-year old individuals [16]. Furthermore, WHO is targeting to increase the number of natural teeth present in the dentition of older population (65~74 years old) to 21 or more by the year 2020 [17].

A 2012 report from the Australian Institute of Health and Welfare in 2012 has shown that the average number of missing teeth ranged from 2.2 teeth for people aged 15–24 to 11.9 teeth for those aged 65 and over [18]. A 2009 survey by the Massachusetts Department of Public Health revealed that approximately 50% of adults over 55 years old are missing six or more teeth [19]. Comparing these facts with the WHO goals, it is obvious that we are still some way away from achieving them. Before the global goals set by WHO are achieved, the only solution for edentulous people to regain a better quality of life is a proper dental prosthesis. This study will focus on treatment options for replacing a single missing tooth; the many different treatments options for replacing multiple missing teeth at the same time will not be considered.

1.2 Treatment options for replacing a single missing tooth

To restore a single missing tooth, several treatment options are available. Amongst these, two major categories, tooth-supported fixed partial dentures (FPD), the so-called dental bridges, and single implant-supported dental crowns (Figure 1.1), are usually considered [20, 21].

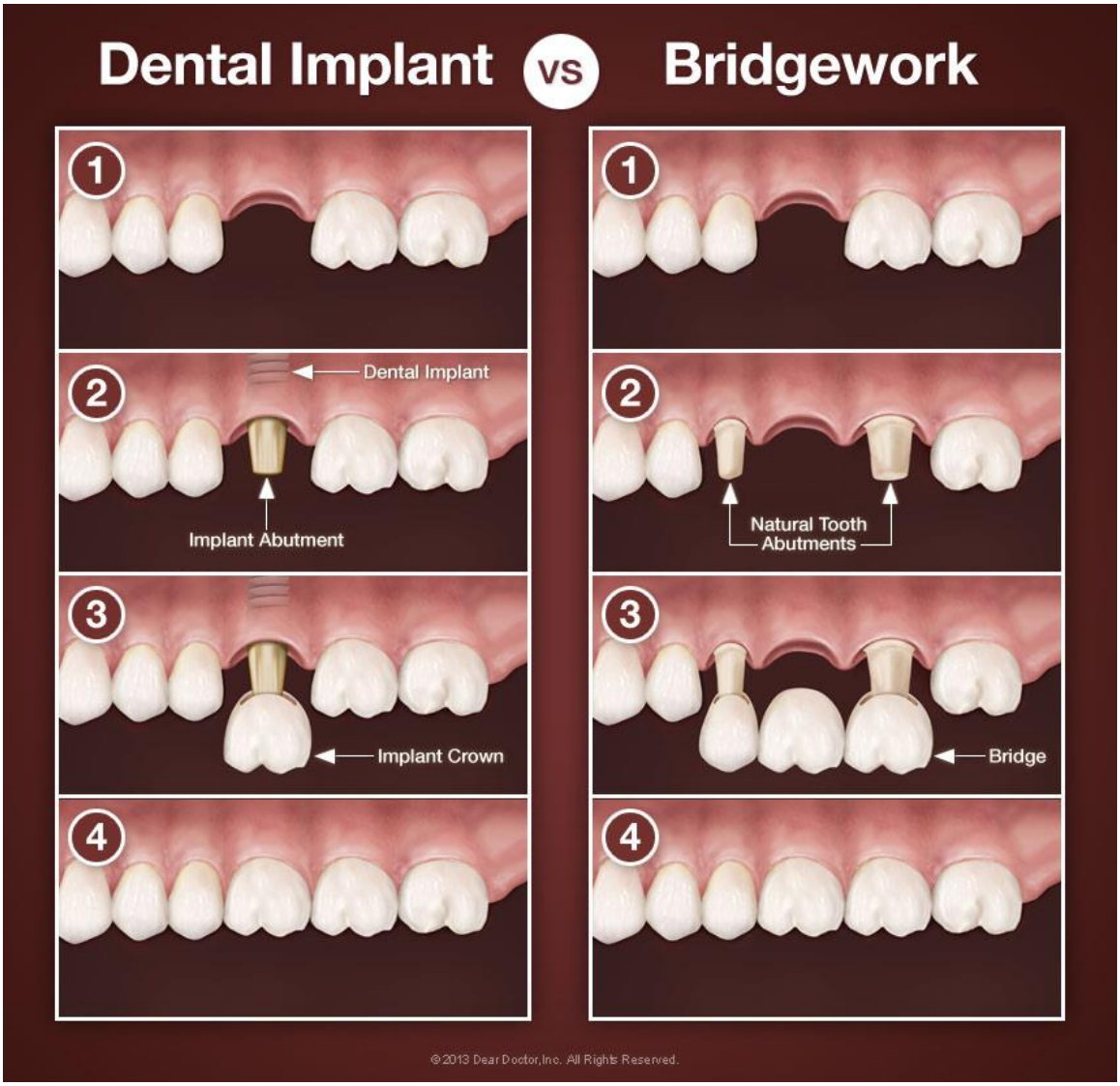

Figure 1.1 The two major treatment options for single tooth replacement: tooth-supported FPDs and implant-supported dental crowns [22].

1.2.1 Tooth-supported fixed partial dentures

The various designs of FPDs can be categorized by the number or type of retainers they use. For instance, the denture can be of a 2-unit cantilever or a 3-unit bridge design, and the retainer can be designed as full or partial abutment coverage. Partial abutment coverage includes wing-shaped retainers placed on the lingual surfaces of anterior teeth and box-shaped inlays, ring-shaped onlays or clasps used for posterior abutments. These FPDs with partially-covered abutments are also known as "adhesive" or "resin-bonded" FPDs. A summary of the prosthetic designs for replacing a single missing tooth is listed in Table 1.1.

Table 1.1 The classification of dental prostheses for replacing a single missing tooth

The type of prosthesis	**The number of abutments**	**The type of retainer**

Tooth-supported Fixed Partial Denture	Two tooth abutments;
	3-unit dental bridge
		• For anterior abutments
		  ○ Lingual wings
		• For posterior abutments
		  ○ Box-shaped inlays
		  ○ Ring-shaped onlays
		  ○ Clasps

	Single tooth abutment; 2-unit cantilevered bridge	
Implant-supported dental crown	Single implant abutment	N/A

In general, implant-supported dental crowns can last longer than tooth-supported FPDs. In a meta-analysis, the 5-year success rate of implant-supported restorations was 95.1%, but that of FPDs was only 84.0% [21]. Among the FPDs, higher failure rates could be found in the adhesive FPDs. Another meta-analysis, which included both 3-unit

and 2-unit cantilevered FPDs and implant-supported restorations, indicated that implant-supported restorations had the highest survival rate of 94.5% after 5 years of observation [23]. However, the 10-year survival rate of implant-supported restorations was only moderately higher than that of bridge-type FPDs. The estimated 10-year survival rate for bridge-type FPDs, cantilevered FPDs and implant-supported restorations were 89.2%, 80.3% and 89.4%, respectively [23].

The failures of FPDs are often caused by secondary caries, periodontitis and intra-pulpal pathologic changes in the supporting teeth [24]. The splinting of dental bridges, especially the 3-unit type, makes the maintenance of oral hygiene difficult. As a result, dental plaque can easily accumulate underneath the pontic and around the margins of the abutments. In addition, some of the dental cements used for fully-covered crowns, such as Zinc Phosphate cement, can be washed out gradually with time. The resulting marginal gaps allow the pathogen (the low pH of dental plaque) to demineralize the tooth structures and then develop secondary caries.

Plaque accumulation causes periodontitis and attachment loss of the abutment tooth. It is also known that periodontal pockets are deeper on the pontic side than the other side due to food debris impaction. Furthermore, because there is no tooth structure in the edentulous space to maintain the alveolar bone, the speed of attachment loss is faster on the pontic side. If the missing tooth was not replaced immediately after tooth extraction, the neighboring abutments could tilt towards each other. A dental bridge constructed on tilted abutments usually induces problematic stresses to the abutements

and their surrounding bones which eventually lead to significant periodontal attachment loss.

Another complication with the dental bridge treatment option is pathologic changes of the pulp in the abutment [25]. Many studies have shown that pulp necrosis could occur after a vital abutment is prepared for a dental bridge [25-29]. In a study involving observations that ranged from 4 to 17 years, 15% of the abutments were found to have necrotic pulps [28]. Another 10-year survey also found radiographically visible lesions in the periapical regions of 10% of the abutments examined [30]. A longer-term longitudinal study indicated that the survival of the pulps of prepared abutments decreased by about 3-5 % every five years, reducing to 83% after 25 years of observation [31]. The heat from dental bur grinding during tooth preparation is considered the most critical factor for pulp necrosis.

1.2.2 Implant-supported dental crowns

In comparison with conventional tooth-supported FPDs, replacing a single missing tooth with a dental implant provides better esthetics, easier hygiene maintenance, and it helps maintain the residual bones and periodontal tissues [32]. Each missing tooth can be replaced with an individual dental implant, so the neighboring teeth are not linked to the prosthesis; therefore, dental floss can still be used for maintaining good oral hygiene. Dental implants, together with a proper reestablishment of biological width (the thickness of attached soft tissue surrounding implants) can promote the regeneration of interdental papillae, which are highly important for restoring the anterior dentitions' esthetics [33-35]. Dark triangles in the interdental space, which are caused by missing dental papillae, can usually be seen in individuals treated with conventional FPDs [36]. This interdental space can be filled using gingiva-colored restorative material in the FPD; however, it will make cleaning around the pontic more difficult.

To achieve a satisfactory outcome, bone or soft tissue augmentation may be carried out prior to the implant surgery [37]. Before the surgery, the bone quality and quantity are usually assessed using a panoramic radiograph or computed tomography (CT). To avoid their perforation during the implant surgery, several important anatomical structures, such as the nasal cavity, maxillary sinus, nasopalatine and inferior alveolar nerve, need to be located. Performing a bone augmentation procedure can help regain the bone volume and also prevent injuring those important structures [38-41]. This procedure is especially important for implant surgery in the anterior maxilla region where the alveolar bony structure is the thinnest and the implants are not axially loaded. Bone

augmentation helps enables the implants to be inserted at a favorable angle, which is important to uniformly distribute the load in the surrounding bone. More details will be discussed in Chapter 4.

Regardless of the implant manufacturers, most implant systems can provide a reliable treatment outcome, and they have an excellent mechanical survival rate. Major failures result from peri-implantitis or non-plague-induced loss of osseointegration [42]. Peri-implantitis can be prevented by a comprehensive periodontal control before implant surgery and elaborate oral hygiene care after implant surgery. Non-plague-induced loss of osseointegration is usually caused by unfavorable or excessive loading conditions from an improper prosthesis [43]. It can be minimized by periodic occlusion check and occlusal adjustment.

Various features of current implant systems have been analyzed extensively, and different designs have been proposed to improve their performance. These include the thread designs [44-46], surface modifications [47-49], abutment connection types [50, 51] and the concept of platform switching [52-54], which uses smaller diameter implants to induce better gingival adaptation. Metal-ceramic or all-ceramic prostheses have been widely used for implant abutments. Despite all these implant differences, the crown design is almost the same as that for the natural tooth abutment. A pre-angulated abutment is sometimes required to correct the crown inclination if the insertion angle of the implant is compromised [55].

1.2.3 Things for consideration during treatment planning

Although the financial status of the patient may limit their treatment options, this section will only focus on the clinical considerations.

Before making a suitable and personalized treatment plan, a comprehensive oral examination needs to be taken, including a complete survey of the periodontal status, pulpal health of the abutment teeth, periapical and panoramic radiographs. Practitioners should also check if their patients have parafunctional habits and any history of trauma or other related systemic diseases. For example, an inlay-retained FPD, which has lower retention, is not recommended for a patient who abruxes. The assessment of each individual abutment includes its periodontal status, the amount of remaining tooth substance, and the need for endodontic therapy.

FPDs can be made of pure metal, metal-ceramic, all-ceramic, fiber-reinforced composite or nanocomposite. Due to patients' demand for esthetics, pure metallic prostheses are no longer suggested except for patients with financial concerns. Tooth-colored materials have become the mainstream in dental prosthesis. Nevertheless, the most important requirement that FPDs have to meet is the rigidity of the structure. To achieve both structural rigidity and esthetics, most tooth-colored prostheses combine two or more materials of different properties. During chewing, a FPD experiences tensile, twisting, compressive and shear mechanical loads. For a dental prosthesis constructed from two or more materials, the material layout plays an important role in its structural stress distribution. To design a FPD with excellent mechanical performance, an optimal material layout for each material system needs to be investigated. An example is provided

by the residual stresses generated in metal-ceramic restorations after the firing process. By changing the shape of the metal substructure, unfavorable residual tensile stresses from the firing process can be transformed into compressive stresses to improve the strength of metal-ceramic restorations.

For the implant-supported prosthesis, the condition of the surrounding bone has to be evaluated. Alveolar bone at the recipient site that has insufficient height or width usually has to be augmented by bone graft through surgery prior to placing the implant. A minimum 6-8 mm clearance between neighboring teeth is usually required mesiodistally for the implant and its prosthesis [37]. If the neighboring teeth are tilted due to long-term edentulism, a partial-arch orthodontic treatment is required to regain enough clearance before the implant surgery [56]. Selecting the proper dimensions for an implant is traditionally guided by a simple principle based on the crown-to-root ratio. A crown-to-root ratio of 0.55 is usually used for a maxillary dentition and 0.6 for the mandibular dentition. However, some short implant (<10 mm) systems, their crown-to-implant ratios being greater than 0.6, still perform very well [57, 58]. In a systematic review, the failure rates of short dental implants and implants of standard length were not found to be significantly different, and over observation periods that ranged from 1 to 10 years, the averaged failure rate of short dental implants was only about 4.5% over six years [58]. Because of its minimal requirement for bone height, short implants can be used without the risk of approaching important anatomical structures and the complications of bone augmentation procedures. Therefore, these short implants are gaining wider acceptance from both clinicians and patients.

The use of implant prosthesis in the maxillary anterior region is the most challenging [59]. This region has the poorest bone condition: only a very thin cortical layer and highly porous cancellous bone underneath. The long-term success rate in this region is, therefore, not as predictable as that in the posterior region. The inherent anatomical shape of the anterior maxilla also increases the risk of perforating the labial plate of the alveolar bone during implant surgery. Modern technology makes it possible for oral surgeons to perform simulated surgery on three-dimensional computed tomography (CT) reconstruction models. Also, a surgical template can be fabricated based on the CT scan using a computer-aided design and computer-aided manufacturing (CAD/CAM) system to guide the implant insertion. Even so, the insertion angle of a dental implant in the anterior maxilla is still limited by its anatomical shape. With poorer bone quality and a compromised insertion angle that cannot distribute the occlusal load evenly, the loss of osseointegration will be more likely; therefore, the optimal placement of a dental implant in the maxillary anterior region needs to be investigated.

1.3 Review of dental material systems for fixed partial dentures

Overall, the dental implant is a better option for restoring a single missing tooth; however, patients often refuse this option because of the very high cost and the risk of surgical procedures involved. As a result, conventional FPDs have continued to be extensively used in prosthetic dentistry. To achieve both adequate mechanical strength and satisfying aesthetics, composite structures such as fiber-reinforced composite resin (FRC), porcelain-fused-to-metal alloy, and two-layered dental ceramic, have been used for the fabrication of FPDs [60]. With these composite forms, the mechanical strength of dental prostheses is mainly provided by the substructural materials, e.g. the metallic framework in porcelain-fused-to-metal restorations, the zirconia coping in all-ceramic applications, and the glass fibers in FRC restorations, while the veneering materials can be tailored to mimic the neighboring natural teeth in appearance. This section gives a brief review of these three material systems.

1.3.1 Porcelain-fused-to-metal system

The use of porcelain-fused-to-metal (PFM) FPDs has been a predictable approach to replacing single missing teeth since the 1950s [60]. This type of dental restoration evolved from the resin-veneered metal restorations. Changing the veneering material from acrylic resin to porcelain preserves the advantage of tooth-mimicking color, while further enhancing the transparency. Because they are wear-resistant and easy-to-polish, dental porcelains are less prone to discoloration. Due to the brittle nature of porcelains, the metal substructure of the PFM restoration has to be designed to minimize the tensile stresses or transform them into compressive stresses in the porcelain layer following the firing process as mentioned above.

The frameworks of PFM restorations are mainly fabricated with a layer of metal alloy that provides the restoration with high fracture strength to increase its clinical survival rate [61]. The currently available metal alloy systems are split into three categories by the American Dental Association: high-noble, noble and base alloy. They are defined by the percentage of noble metals they contain, including Gold (Au), Platinum (Pt) and Palladium (Pd).

As mentioned previously, the substructure of PFM restoration has to be very rigid. The connectors, which link the pontic with the metal copings on the abutments, are highly stressed, and hence, they are usually the most vulnerable regions in the 3-unit FPDs. The dimensions of the connectors can significantly affect the mechanical strength of a FPD.

The traditional design of the metal substructure follows two basic guidelines [62]. First, there must be no sharp edges as they can induce high local stress concentrations that cause cracking in the porcelain layer. Second, the metal-ceramic junction should not be placed near the tooth-contact area, e.g. the lingual surface of the maxillary incisor. The cutting-back technique is often used to obtain a proper geometry for the metal substructure. A wax pattern of the missing tooth is first built up to its original contour on the abutment die. It is then cut back to provide sufficient space for the veneering porcelain. The porcelain should be at least 1 mm thick to mask the metal underneath and it should not exceed 2 mm so as to create unsupported sections that can chip easily. These conventional guidelines do not fully take into account the stress distribution in the structure and the possible distortion of the metal substructure during the porcelain firing process.

Several modifications to the geometry of the traditional metal substructure have been proposed. The Reinforced Porcelain System (RPS) proposed by Shoher and Whiteman [63] reduced the amount of metal used by using a metal coping of uniform thickness in combination with laterally extended shelf on the occluso-axial line angles (Figure 1.2). This shelf design prevents the interproximal porcelain from flaking due to occlusal impact. To ensure that the unsupported interproximal porcelain is less than 2 mm thick, a thick metal collar is used in the traditional cut-back design. In addition, the shelf forms a concave space on the occlusal top that can strengthen the porcelain within the concavity by introducing residual compressive stress within it following firing of the porcelain.

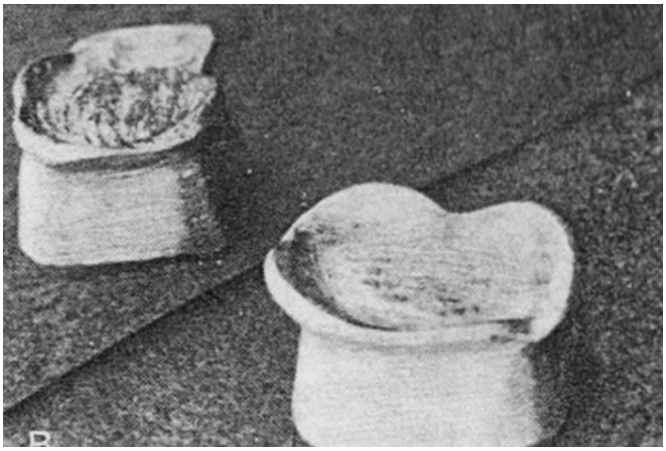

Figure 1.2 The occlusal shelf of the RPS substructure design [63].

For the pontic design of dental bridges, the RPS provides various sizes of pre-fabricated pontic wax-patterns, which consist of an interconnecting bar network. This greatly reduces the amount of metal used in the pontic substructure, while improving its residual stress distribution. Figure 1.3 indicates that several shrinkage cores can be found in the conventional bulky pontic design while only a single shrinkage core was found in the RPS pontic.

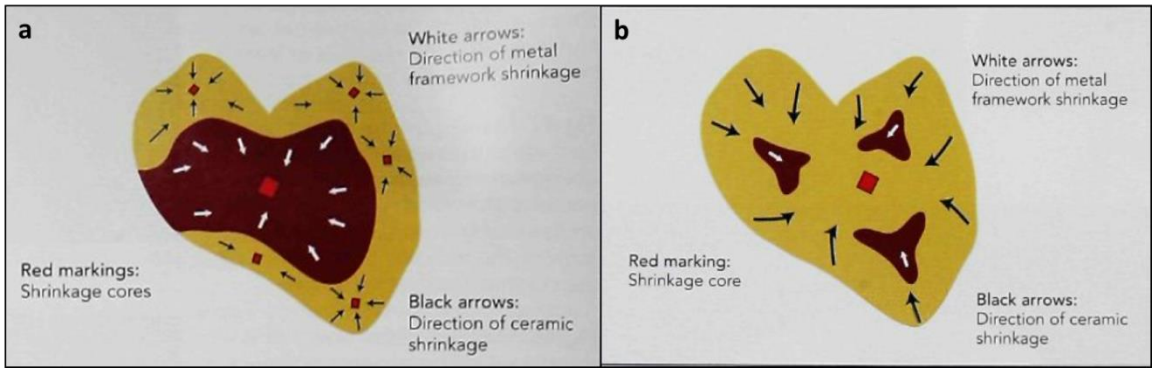

Figure 1.3 (a) Conventional pontic with many shrinkage cores. (b) RPS pontic with a single shrinkage core [64].

The wrinkled substructural design proposed by Sgro [64] uses several metal shoulders both on the buccal and lingual surfaces (Figure 1.4). These shoulders also create the concavity on the axial surface that can strengthen the veneering porcelain by introducing residual compressive stresses to it following firing of the porcelain, if an alloy with a slightly higher coefficient of thermal expansion than that of the porcelain is used.

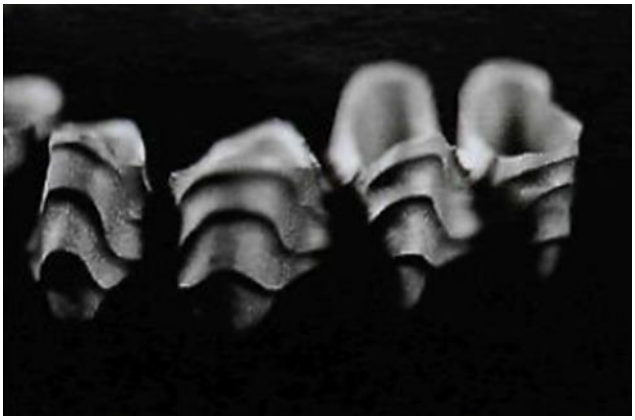

Figure 1.4 The wrinkled substructural design proposed by Sgro [64].

For better esthetics, the metal margins of PFM restorations are usually placed under the gingival margin; however, this sometimes results in the discoloration of gingival tissues [65], if base metal material is used. Although a metal-free margin, which has a stiffer porcelain material around it, has been proposed, the marginal discrepancy due to porcelain shrinkage after firing cannot be easily controlled [66]. Gingival recession with age or marginal porcelain chipping exposes the metal underneath, which compromises patients' esthetics [67].

Because of the great increase in precious metals' price over the last few years, PFM restorations have lost their financial advantage except those using base metal alloys.

The manufacture of PFM restorations also requires the consideration of many variables, including the matching of metal and porcelain thermal expansion coefficients, the porcelain condensation techniques, the selection of bonding agents, the type of furnace, and the temperature or heating curves used for each firing step. Without these complications, all-ceramic restorations made with CAD/CAM systems are rapidly increasing their market share.

1.3.2 All-ceramic systems

Due to the photo-permeability of porcelain, PFM restorations can appear grayish if the porcelain is not applied properly to mask the metal. To better mimic the tooth's appearance, zirconia, which has a tooth-like color and excellent mechanical strength, was introduced in the 1990s as a substructural material. In addition to the excellent esthetics, current all-ceramic systems hold several other advantages, including excellent tissue response, color stability, high wear resistance, similar surface texture to the natural teeth, and low thermal conductivity.

All-ceramic dental restorations have been used for more than a century. The very first all-ceramic dental crown, also known as porcelain jacket crown (PJC), was proposed by Land, and was granted a patent in 1887 [68]. The detailed laboratory procedures for fabricating PJC were later revealed by Spaulding in 1904 [69]; however, the PJC did not receive wide acceptance due to its high fracture rate. Because they were easy to make at the chairside, tooth-colored, resin-veneered metal restorations were leading the market of dental prosthesis until the late 1950s. In the mid-1960s, McLean introduced alumina-reinforced porcelain [70], which used a porcelain containing approximately 50% alumina oxides (Al_2O_3) as the substructure. The flexural strength of the alumina-reinforced porcelain was thus increased to 180 MPa, twice as high as the original ceramic. About two decades later, a leucite-containing porcelain frit for the PFM system was introduced to tailor the coefficient of thermal expansion of the porcelain so that a good match with that of the metal could be achieved [71-73]. Since then, ceramic restorations gained acceptance from dental professionals and patients. During the last two decades, several

substructural materials of high mechanical strength were developed, including high (>95%) alumina-containing ceramic, magnesium aluminate spinel, lithium disilicate, glass-infiltrated zirconia-toughened alumina (ZTA), magnesium partially stabilized zirconia (Mg-PSZ) and 3 mol% yttrium partially stabilized tetragonal zirconia polycrystal (3Y-TZP).

There are three crystallographic phases of zirconia associated with temperature change: the monoclinic phase (from room temperature to 1175°C), the tetragonal phase (from 1175 to 2370°C) and the cubic phase (from 2370 to 2750°C). By adding stabilizing oxides such as calcium oxide (CaO), Ceria (CeO_2), magnesia (MgO) or yttria (Y_2O_3) into zirconia, its tetragonal phase that normally appears at 1170 °C - 2370 °C can be retained in a metastable condition at room temperature. These partially-stabilized tetragonal zirconia transform to the more stable monoclinic phase with approximately 4% volumetric expansion that prevents crack propagation by compressing the crack tip [74, 75]. This so-called transformation toughening process can greatly enhance the mechanical strength and toughness of zirconia. In comparison with the dental ceramic of high alumina content, the flexural strength of zirconia is about twice as high. Because of its simple manufacturing protocol, great mechanical performance, and satisfactory tooth-shade matching, zirconia-based restorations make up the majority of all-ceramic dental restoration fabricated.

According to their manufacturing processes, modern all-ceramic systems can be classified as: (1) pressable/castable and (2) machinable ceramic systems. The pressable/castable ceramic systems require specialized equipment and complicated

fabrication processes. In addition, due to their lower mechanical strength, their indication is limited to veneers, inlays, onlays or single crowns. Studies have shown that posterior restorations fabricated with pressable/castable ceramics have a higher fracture rate [76]. Machinable ceramic systems, in conjunction with modern CAD/CAM technology, used a similar layering technique for veneering as does the conventional PFM; however, with a more predictable outcome. They can be used not only for single unit restorations but also for multiple unit posterior bridges.

The zirconia block can be milled before or after sintering. Milling pre-sintered zirconia block (soft-machining) can significantly save manufacturing time and reduce damage to the milling burs. An additional requirement for milling pre-sintered zirconia block, which can be easily done using CAD/CAM, is that the dimensions of the substructure have to be enlarged by about 20-25% to compensate for the sintering shrinkage [77]. Several studies have shown that all-ceramic restorations fabricated from pre-sintered zirconia blocks have relatively lower marginal discrepancy than those from fully sintered zirconia blocks [78-81]. This is because milling fully-sintered zirconia blocks requires the use of coarse diamond burs which could cause chipping of the margin. Due to the efficiency and accuracy provided by CAD/CAM, soft-machining has become the standard protocol for fabricating zirconia-based all-ceramic restorations.

The amount of tooth reduction for an all-ceramic crown is about 1.5-2 mm to allow enough space for the zirconia and the veneering porcelain. The marginal design for the all-ceramic crown has moved from the 90-degree shoulder to a rounded chamfer to avoid sharp line angles. With sufficient tooth preparation and a proper marginal design,

the rest of the designing process, including determining anatomical contour and the occlusal contact, can be done using CAD/CAM software.

Similar to PFM restorations, zirconia-based FPDs can fracture at the occlusal contact points or connectors [82-86]. Several papers have suggested that the cross-sectional area of the 3-unit ziconia-based restoration's connector should be wider than 9 mm^2 to improve its mechanical performance [83, 86-90]. This requires a larger amount of tooth reduction than does the PFM restoration. From the standpoint of minimal intervention, therefore, a stronger connector design without increasing its cross-sectional dimensions is required for the all-ceramic restoration.

Clinical studies have shown that the most common type of failure among zirconia-based crowns is chipping or cracking within the veneering porcelain layer [89, 91-102]. In addressing this problem, most of the recent research concentrated on improving the veneering porcelain [103-105], veneering technique [100, 103-111], core design [106, 110], or fabrication protocol [109, 111]. An "overpressing technique" which combined the pressable and machinable ceramic systems was introduced to reduce veneer chipping [100, 104]. The restorations made by this technique reduced chipping in laboratory tests and clinically [100], and the final fracture strength remained similar with the other ceramic systems. Another material layout that combines two machinable ceramic materials: lithium disilicate and zirconia, significantly enhances the fracture strength of the restoration [104].

In summary, current CAD/CAM technology can help dental technicians obtain zirconia substructures for all-ceramic systems very efficiently and accurately. However,

restoration fracture and chipping in the porcelain layer remain major problems with this type of restoration. To improve their mechanical performance, alternative design solutions need to be investigated.

1.3.3 Fiber-reinforced composite (FRC) systems

FRC materials have long been used in industry for constructing various types of vehicles such as yachts or recreational vehicles due to their light weight and excellent mechanical properties. FRC was first used in dentistry for the reinforcement of acrylic-based complete dentures in the late 1960s [112, 113]. Today, FRC materials are widely used in endodontic post systems and FPDs. Compared to PFM or all-ceramic restorations, the amount of tooth reduction for FRC restorations is expected to be smaller. Most glass fibers of modern FRC systems are pre-impregnated with resin so that the fiber substructure can chemically bond to the veneering resin matrix. In contrast, conventional resin-veneered metal prostheses usually require mechanical retention of the veneer from their metal substructure. Because resin materials can be directly manipulated by dentists, a FRC restoration for single tooth replacement can be fabricated chairside during an hour-long appointment. In comparison with their PFM counterpart, the cost for the FRC restoration is about 50% lower. In addition to being minimally invasive, and time- and cost-effective, FRC restorations are also tooth-colored, making them an attractive treatment option for replacing the single missing tooth.

The fibers of modern FRC systems are made of glass or polyethylene. Glass fibers possess higher tensile and flexural strengths than those made of polyethylene. Carbon fibers are the stiffest, but because they lack translucency they are mainly used for making endodontic posts. The diameter of the fibers used in dentistry ranges from seven to ten microns. The architectural arrangement of the fibers can be braided, woven or

unidirectional. Studies have shown that unidirectional fibers, i.e. those that are oriented in parallel with each other, demonstrated better mechanical performance.

As a substructural material, fibers behave differently from the metal alloys used in PFM restorations and the zirconia used in all-ceramic restorations. Given that all the ingredients are well mixed during the ingot or block preparation, the material distribution of metal alloys or zirconia should be uniform, homogenous and isotropic, i.e. their mechanical properties are usually non-directional. On the other hand, fiber-reinforced structures usually behave anisotropically; in other words, their mechanical strength varies depending on the direction of load with respect to the direction of the fibers. The elastic modulus in the longitudinal direction is usually several times higher than that in the transverse direction. Because of this anisotropic characteristic, the direction of the occlusal load or the state of the local stress is a very critical factor when deciding where to place the fiber substructure within the restoration. Fiber substructures for FPDs, however, are usually designed as straight beams without taking the local stress distribution into consideration.

In a systematic review of FRC FPDs, their mean survival rate was found to be 73.4% at 4.5 years [114]. The main failure mode was documented as delamination at the interface between the fibers and the resin matrix [115-119]. Fractures also occurred at the loading point [117, 118, 120], the pontic, and the connectors linking the pontic to the abutments [121-123].

1.4 Clinical challenges and short comings of current treatment options

Although a single missing tooth can be restored with a dental implant without compromising the healthy neighboring teeth, it is not a perfect treatment option that is suitable for everyone. Individuals who are willing to replace their missing teeth with dental implants may not have sufficient bone volume. Long-term edentulism usually results in a certain degree of alveolar bone loss. Before placing the dental implant, therefore, patients with significant bone loss may have to receive bone augmentation to ensure adequate volume of alveolar bone, both horizontally and vertically. Even if sufficient bone tissues have been established, the inherent anatomy of the jaws and the oblique load paths of opposing dentitions can still complicate the placement of dental implants, especially in the maxillary anterior region where bone volume is much smaller. The implant may have to be inserted at an angle that can maximize initial bone attachment and, hence, stability. Several studies have indicated that the insertion angle of a dental implant plays an important role in the long-term prognosis of the treatment, especially for the maxillary anterior region. The overall shape and dimensions of the implant also seem to play a role.

With increasing patient demand for esthetics, all-ceramic or FRC systems are being used more frequently for fabricating FPDs. Similar to conventional metal-ceramic restorations, a significant disadvantage of modern all-ceramic applications is that, due to their brittle nature, larger dimensions of the restoration, and thus more tooth tissue removal is required, which significantly limits their clinical application [121, 124]. In addition, these layered ceramic restorations share a common pitfall in that the veneering

material can fracture or chip easily. To expand the clinical applicability of the all-ceramic system, a material layout that provides better mechanical performance has to be designed.

The more recently developed FRC system for FPDs has the major advantages of being minimally invasive, and time- and cost- effective, while providing metal-free prosthetic reconstruction with excellent esthetics; therefore, FRC FPDs have received increasing attention from dentists and dental technicians. As mentioned previously, current designs of FRC bridges do not provide an adequate lifespan. Despite great advances in the development of stronger FRC materials, failures such as interfacial delamination, localized material chipping and even catastrophic fracture still occur with FRC FPDs.

1.5 Approaches

From the above discussions, we know that the material layouts of dental prostheses have a great impact on the stress distribution within them. Most dental prostheses have a composite structure: a reinforcing component and an esthetic veneer. This type of material layout can be found in many commonly-used restorations such as PFM fixed prostheses, FRC systems and zirconia-based all-ceramic restorations. Due to the mismatch of elastic modulus at the interfaces between the components, a discontinuous or even singular stress distribution usually arises. This often leads to the breakdown of the interface in the form of debonding or delamination. Yet, our teeth, which have to sustain a high mechanical load in performing the daily chewing function and which also have a mismatch in Young's modulus between the dentin and enamel layers, do not fail as frequently. It has been pointed out that the high fracture strength of natural teeth is due to the heterogeneity and anisotropy of the tooth structure that help distribute the stress more uniformly; therefore, the relationship between the structures of a tooth and the stress distribution within it needs to be analyzed in more detail (Chapter 5 and 8). The rationale for these natural designs would provide some useful guiding principles for designing better restorations (Chapter 6 and 9).

More broadly speaking, placing a stiff dental implant of titanium into the softer alveolar bone can also be considered as a special case of constructing a composite structure with components of very different mechanical properties. Altering the insertion angle of the dental implant, and hence, the material distribution within this composite structure, and the angle of loading would lead to different stress distributions in the alveolar bone. Important lessons can be learned, and better implant designs and

placement procedures can be derived, by studying the shape and inclination of natural teeth and their mechanical interaction with the surrounding bone under occlusal loads (Chapter 3). In this project, the finite element (FE) method was used to investigate the effect of material heterogeneity (Chapter 5) and anisotropy (Chapter 8) on the stress distribution within natural teeth. The same method was used to study the effect of implant insertion angle on the alveolar bone stress (Chapter 4).

In addition to the strength of the materials used, the mechanical performance of FRC restorations also depends on the layout of the constituent materials in relation to the load paths through the structure. Several FE analyses of posterior 3-unit FRC bridges indicated the presence of tensile stress concentrations at the bottom of the pontic and in the connector regions [125-128]. According to these results, inadequate fiber reinforcement in these regions will lead to clinical failure. Many studies using mechanical testing have been carried out to search for optimal fiber position and orientation for the specific FRC system under consideration [129-133]. Such a load-to-failure approach without the proper use of engineering design principles has several drawbacks: for example, high material expenses and time-consuming specimen preparation. Instead, advanced structural optimization techniques, based on numerical stress analysis, should be considered for obtaining optimal designs of dental prostheses.

Important lessons can be learned and better restoration designs can be derived by studying the material properties and layouts of natural teeth, which are composed of functionally-graded and directionally-reinforced materials arranged in a highly efficient and effective manner.

The present project also used structural optimization that was run within a FE structural stress analysis to derive alternative designs for some of the dental prosthesis. This was achieved by using an optimization subroutine, Stress-induced Material Transformation (SMT), that could update the material properties interactively according to changes in the local stress distribution. Its iterative process gradually reinforces the regions of high tensile stresses that can cause dental prosthesis failure with a stronger material. This subroutine was used to seek an alternative design for the FRC substructure with a more efficient spatial arrangement of the fibers. The detailed procedures of the SMT technique are described in Chapter 9.

The mechanical performances of the optimized designs were then evaluated by in vitro tests using several examination techniques (Chapter 7 and 10). The load-displacement curves helped understand the mechanical behavior of the specimens before the final catastrophic failure. Acoustic emission (AE) measurement recorded in real time and with high sensitivity micro-cracking events of fracture during the mechanical tests. Briefly, AE is a high-frequency elastic wave produced as a result of a sudden release of strain energy within a material following a structural change such as cracking. The released strain energy causes transient sound waves that propagate through the material or structure. An AE sensor can be used to detect these sound waves so that cracking of the material or structure can be evaluated [134-137]. An AE system comprises three main parts: a signal sensor, a preamplifier and a recording device. AE signals collected by the AE sensors during loading are amplified with a proper gain before their amplitudes, frequencies and durations are recorded and displayed. AE measurement has been performed in investigations of the fracture behavior of dental materials [138-141]. Micro-

CT scanning was used to visualize the cracks in 3D after the mechanical test without destroying the specimens.

1.6 Hypotheses and specific aims of the study

The purpose of this research was to explore various inherent structural features of a natural tooth that enable it to perform its mechanical functions effectively, and then to apply the principles and techniques inspired by these investigations to the design of prostheses for replacing a single missing tooth. The biomechanical analysis of the natural tooth was performed on both a macroscopic (overall shape as determined by its anatomy) and a microscopic (effect of microstructures on bulk material properties and their distribution) scale. The nature-inspired design guidelines were then implemented within a FE framework for optimizing dental prostheses designs. Finally, the mechanical performances of the optimal designs derived from the numerical models were validated with in vitro tests.

Hypothesis 1: The orientation of a natural tooth within the surrounding bone tissues and the material properties and their distribution within the tooth itself are optimized to help distribute the stresses created by the occlusal load more uniformly.

Specific Aims for Hypothesis 1:

- Specific Aim 1: To evaluate the stress distributions of a maxillary central incisor and its surrounding bone with different tooth inclinations (Chapter 3).
- Specific Aim 2: To investigate the influence of a graded material distribution on the stress distribution in a natural tooth (Chapter 5).
- Specific Aim 3: To study the effect of anisotropy of human enamel due to directional enamel rod orientations on the stress distribution (Chapter 8).

Hypothesis 2: Nature-inspired, computer-aided structural optimization methods can help design esthetic dental prostheses with better mechanical performance.

Specific Aims for Hypothesis 2:

- Specific Aim 4: To determine the proper angulation for the installation of dental implants in the maxillary anterior edentulous region (Chapter 4).
- Specific Aim 5: To obtain an optimal material layout for the all-ceramic dental crown inspired by the graded material distribution in natural teeth (Chapter 6).
- Specific Aim 6: To implement a user-defined subroutine for unidirectional FRC within the ABAQUS FE suite and to apply it to obtain optimal material layouts for FRC restorations (Chapter 9).

Hypothesis 3: Dental restorations derived from the optimization exercise perform better than the conventional designs.

Specific Aims for Hypothesis 3:

- Specific Aim 7: To perform in vitro validation of the optimized design of fiber-reinforced composite bridges (Chapter 7).
- Specific Aim 8: To perform in vitro validation of the optimized design of an all-ceramic crown (Chapter 10).

Chapter 2 Shape Optimization

2.1 Multi-scale designs in natural teeth

Through evolution, several inherent structural arrangements of animal teeth and their surrounding tissues have been optimized for functional purposes. The structures and functions of vertebral dentition and jaws gradually became adapted for their dietary needs. For example, herbivores have cuspless teeth with a horizontal jaw movement for grinding grasses. On the other hand, carnivores usually have very sharp cusp tips for tearing flesh, and their vertical jaw movements are specialized for cutting foods efficiently. Humans are omnivores, so in order to process food with a wide range of physical properties, such as texture, hardness and toughness, several ingenious and sophisticated designs exist in our oral cavity, and they occur at many different scales. This chapter will first discuss several examples of the optimized structures of natural teeth at various scales, and then review the approaches inspired by some of these natural arrangements that have been applied for the optimization of manmade structures.

The biggest scale on which the masticatory system works is related to occlusion. The main function of the masticatory system is to process a big chunk of food into small pieces for the digestive system. Occlusion defines the relationship between the maxillary and mandibular dentition when they are in motion and in contact, and is controlled by the spatial arrangement of the teeth within the dental arches. It is still not well understood how the cusps are moved into appropriate positions after tooth eruption. Nevertheless, it is clear that posterior teeth, including premolars and molars, guide the motions of the dentition when they come into contact and provide stability in jaw closure. If individuals

lose posterior support, the so-called posterior bite collapse [142], a series of pathological tooth migrations, would occur. The remaining dentition would not be able to withstand the occlusal force at the normal level, and flare-out of anterior teeth and the loss of vertical dimension may occur subsequently. Another important anatomical feature, the inclination of anterior teeth, plays an important role in guiding the protrusive and lateral jaw movements, and defines the parameter of overbite and overjet. Developmental factors such as excessive growth of jaw bone, developmental discrepancy, and insufficient space in the dental arch will result in different levels of malocclusion. Therefore, to reestablish a functional occlusal scheme for patients during surgical or restorative procedures, the inherent design of occlusion, specifically the relationship between the form and function of the dental arch, needs to be considered.

As mentioned previously, the shapes of the teeth are specialized for the functional demands. For example, the incisal edge of the maxillary incisor acts as a sharp knife for chopping food. Canines possess the sharpest cusp tip for tearing, and their root, the longest in the oral cavity, also provides the stability and resistance against the lateral load. Molars and their opposing cusps, which work as the mortar and pestle, are responsible for comminuting food into swallowable particles.

The material distribution of the tooth is also optimized for the functional demands. Enamel, the outermost layer of the tooth, is the hardest material in the human body. It can provide excellent wear resistance to the tooth, and help it sustain high occlusal loads, up to 700 N. Its highly mineralized structure also protects the dentin and pulpal tissues from chemical or thermal challenges. Underneath the enamel, the dentin, with a lower elastic

modulus and higher water content, can act as a buffer against mechanical impact. Additionally, it has been reported that the elastic modulus and mechanical strength of dentin increase significantly from the cervical to the apical region, where the stress is highly concentrated [143]. A parallel example can be found in the surrounding osseous tissues. Cortical bone is about ten times stiffer and stronger than cancellous bone [144]. In this manner, bone can achieve the required mechanical property while minimizing the total weight of the human skeletal system by having the stiffer cortical bone on the outside, and the more porous cancellous bone on the inside.

Furthermore, many researchers have suggested that the material distribution in the tooth structure follows a spatial gradient on a microscopic scale. A study using fluoroscopic X-ray microscopic image analysis and micro-indentation test revealed a correspondence between the gradients of the hardness/elastic modulus and the degree of mineralization [143]. Recently, a more detailed mapping of the material properties, done by nano-indentation, confirmed the graded material distribution in the tooth structure [145]. A functionally graded material distribution can help reduce stress concentration so as to achieve a uniform stress distribution throughout the structure. Thus, a graded distribution in elastic modulus can prevent the formation of hertzian cracks under concentrated loads in brittle materials such as enamel [146]. According to the results from numerical simulations [147-149], high stress concentration was found in the enamel, especially associated with fissures, groves or fossae between the cusps. These highly-stressed areas are usually present in dental restorations; therefore, to enhance the endurance of dental restorations, the potential benefits of using a graded material distribution in their design should be explored.

The orientations of the enamel rods within the tooth and the arrangement of the hydroxyapatite crystals within these rods also seem to be optimized for the functional demands. The orientations of the enamel rods, which are perpendicular to the outer surface, gradually change from vertical at the occlusal third to horizontal at the cervical third [150] (Figure 2.1a). Such an arrangement makes enamel behave anisotropically. As such, the occlusal load can be transferred more effectively into the underlying dentin, which has higher fracture toughness than enamel. Studies using the nanoindentation test at different spots with different enamel rod orientations indicated that the mechanical properties are fundamentally altered by the rod orientation and their topological distribution [145]. The friction and wear of human teeth, for example, vary significantly, depending on the orientation of the enamel rods, which in turn depends on the topological area of the tooth. In a previous study, wear tests of 5000 cycles with a vertical force of 20N and frequency of 2Hz were conducted on different portions of a tooth (Figure 2.2A). A lower coefficient of friction (Figure 2.2B) and higher wear resistance (Figure 2.2C) was found in the enamel of the occlusal region [151]. This phenomenon can also be observed in dentin, where the friction and wear behavior are also determined by the orientation of the dentinal tubule [152]. At an even lower scale, the orientation of the hydroxyapatite crystals has been found to vary within each enamel rod. In the central region of the rod, they are oriented parallel to the longitudinal axis of the rod, while those near the edge of the rods are oriented at 45^0 [153] (Figure 2.1b). The oblique crystal orientation in the peripheral region of the rod results in lower across-prism elastic modulus [154]. It has been shown that the lower across-prism elastic modulus, which is

close to the elastic modulus of dentin, helps reduce the interfacial shear stress across the dentin-enamel junction [155].

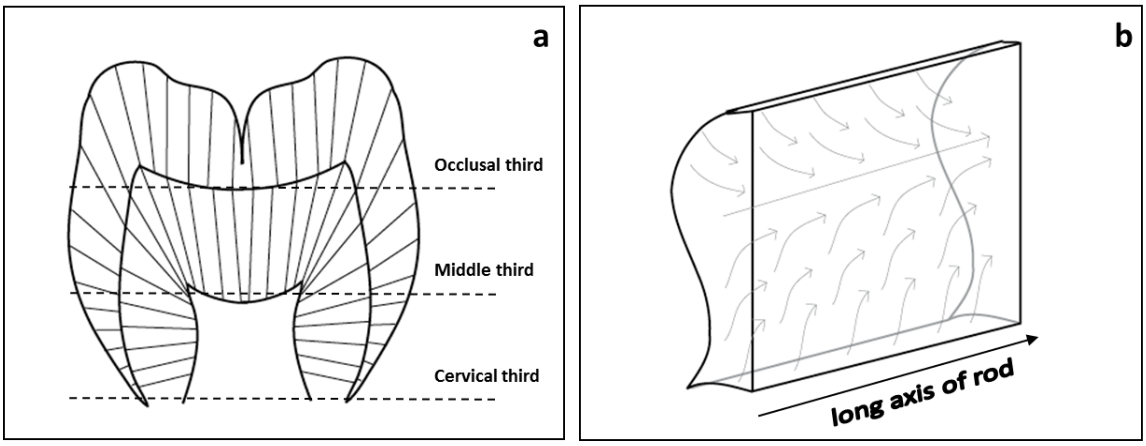

Figure 2.1 (a) Orientations of the enamel rods and dentinal tubules in the tooth structure. (b) Schematic diagram of hydroxyapatite crystal orientations, as indicated by the arrows, in different regions within the enamel rod.

The most important requirement for a dental prosthesis is to properly rehabilitate damaged teeth and/or replace missing teeth. In addition to restoring the chewing function, a successful dental prosthesis often has to satisfy other requirements. First, it has to possess the correct anatomical contour, which is essential not only for reestablishing a stable occlusion but also for speech purposes. Second, the restorative materials used must be compatible with the surrounding biological tissues, and their physical and mechanical properties must also ensure their own durability and longevity. Third, its color must match the neighboring teeth to meet the patient's esthetic demand. To satisfy the last requirement, tooth-colored ceramics and fiber-reinforced composites with anisotropic properties are increasingly being used for the manufacture of dental restorations. However, their mechanical behaviors are very different from those of natural tooth

tissues. To better mimic the natural tooth's ability to cope with the above oral challenges, it is important to better understand its inherent multi-scale structural designs and their relationships with its functions so that the same principles may be aptly applied to dental prostheses design.

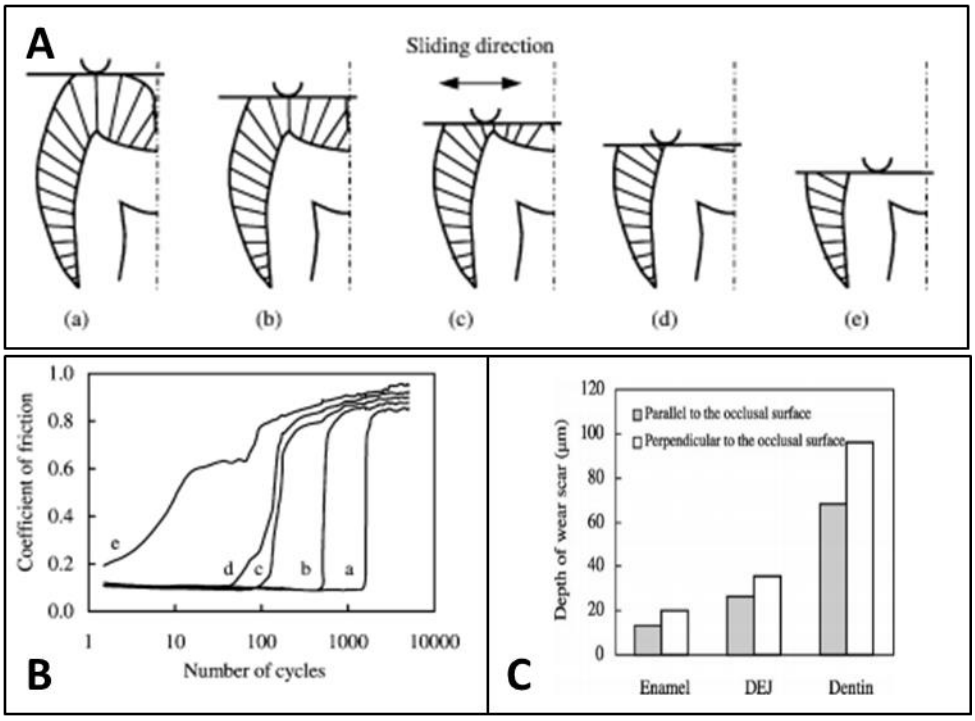

Figure 2.2 (A) (a) to (e) indicates different contact position for friction tests (B) Results of friction coefficient at different contact positions (C) the wear depth at different portion of the tooth [151].

2.2 Review of approaches for shape optimization

To optimize the mechanical performance of dental restoration, the layout of the constituent materials must be designed such that stresses resulting from the occlusal load can be favorably distributed throughout the structure. To date, there are no simple rules to guide the design process. Numerical simulation such as finite element (FE) analysis has been utilized to help improve the design of dental restoration by providing a better insight into the overall stress distribution [125-128, 156-159]. Although FE analysis can help researchers compare structural stress distributions among different designs, one often needs to modify the design and analyze the results repeatedly before arriving at a satisfactory solution. This "trial-and-error" process is very time-consuming, and it is often not possible to confirm if the final design is really optimal. To speed up the design process and to make it more effective, modern structural optimization techniques, which are widely used in designing engineering components and structures, can be used to design dental restorations.

There are many different types of structural optimization techniques. Examples include the Variable Thickness Sheet model developed by Rossow and Taylor [160], the SHAPE method by Atrek [161, 162], the Evolutionary Structural Optimization (ESO) method developed by Xie and Steven [163] and Computer Aided Optimization (CAO) and the Soft Killed Option (SKO) developed at the Karlsruhe Research Center [164]. Amongst these optimization approaches, techniques that are inspired by the adaptive growth of biological structures have proved to be very effective in producing structures that are optimal in terms of the stress distribution. The principles behind some of these

methods are also very similar to the bone remodeling process that takes place in the human body everyday

The Variable Thickness Sheet method [160] minimizes the structural compliance of a planar sheet for a given volume and in-plane load by changing the local thickness and shape of the sheet (Figure 2.3). The final shape of the sheet implied an optimal topology. Another similar approach, the SHAPE method [161, 162], is also based on dividing the optimization problem into several smaller sub-domains in terms of thickness or element volume, but it includes a technique of removing unnecessary elements from the structure. During the optimization process, the volumes of the elements are assigned either the original value or zero. In other words, this algorithm optimizes the structure by either keeping an element in the structure or removing it from the structure. The goal of the optimization is to minimize the volume of the structure and the resultant structure is able to satisfy the structural response (stresses or displacements) considered. The optimization result is evaluated by the following equations.

$$V_v = \frac{V}{Fmin} \quad \text{.....(2.1)}$$

$$Fmin = \min\left(\frac{Rj}{rj}\right) \text{ j=1,…,n} \quad \text{.....(2.2)}$$

where V_v is the virtual volume, V is the current volume, F_{min} is the most critical factor, R_j is the boundary limit of the structural response, r_j is the *j*th structural response and n is the number of the considered structural responses. The virtual volume has to be smaller than the actual volume and a lower virtual volume always implies a better optimization. After each optimization step, a sensitivity analysis is also performed to determine if additional

elements need to be added back to the structure to avoid overt volume reduction. Unlike the Variable Thickness Sheet method, which can only consider planar sheets subjected to in-plane loads, the SHAPE method can deal with 3D structures, loadings and different constraints.

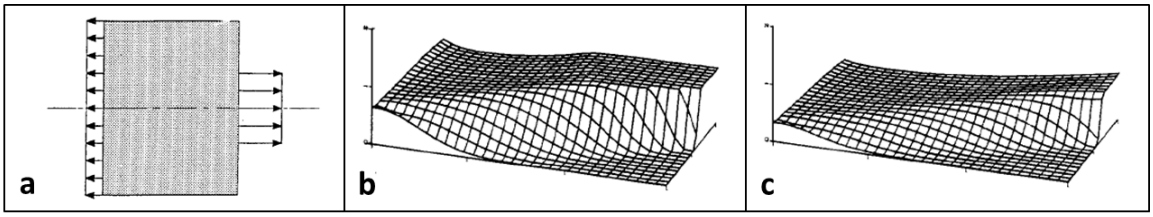

Figure 2.3 (a) A planar sheet with loadings (b) an optimal design of 64% volume (c) an optimal design of 36% volume [165].

The Evolutionary Structural Optimization (ESO) method also attempts to reach an optimal design by removing unnecessary or inefficient materials/elements from a structure. Unlike the previous methods, the removal of the elements in the ESO method is determined by the their stress state. In general, the ESO method removes materials/elements with the lowest stress from the structure. Depending on the designing criterion, the type of stress used for structural optimization can be von Mises, tensile or compressive stresses. For example, for a structure designed mainly to sustain tension, the elements with the highest compressive stresses are deleted from it. The elements with lower tensile stresses can also be removed, if necessary. On the other hand, for a structure designed mainly to sustain compression, the elements with the highest tensile stresses are first deleted from the structure. The ESO method is run iteratively until all elements in the final structures are subjected to a similar level of stresses.

The ESO method needs to start with an “over engineered” structure from which the optimal design is deduced, and it only allows very small modification of the structure during each iteration. The high computational cost is, therefore, its critical weakness. As a result, the Bi-directional Evolutionary Structural Optimization (BESO) method was developed by adding the capability of growing material back to the structure where stress is highly concentrated. Unlike the very conservative initial sketch for the ESO method, the BESO method can start with a model with fewer elements that can support the load cases. By growing and deleting material simultaneously, the BESO method could generate a design with optimal stress distribution in reduced time. A recent study has shown that evolutionary methods such as the ESO method may result in a highly inefficient design due to its rejection criteria [166]. Figure 2.4 shows a simple topology optimization for maximizing the total compliance of a structure by altering its volume subject to a constraint that volume fraction cannot be lower than 40%. Because the ESO method will first delete the element of the least stress, the element closest to the roller at the top will be removed. It results in a structure (Figure 2.4b) of very high compliance but much heavier than another design (Figure 2.4c) that provides a compliance three times as high as the original design.

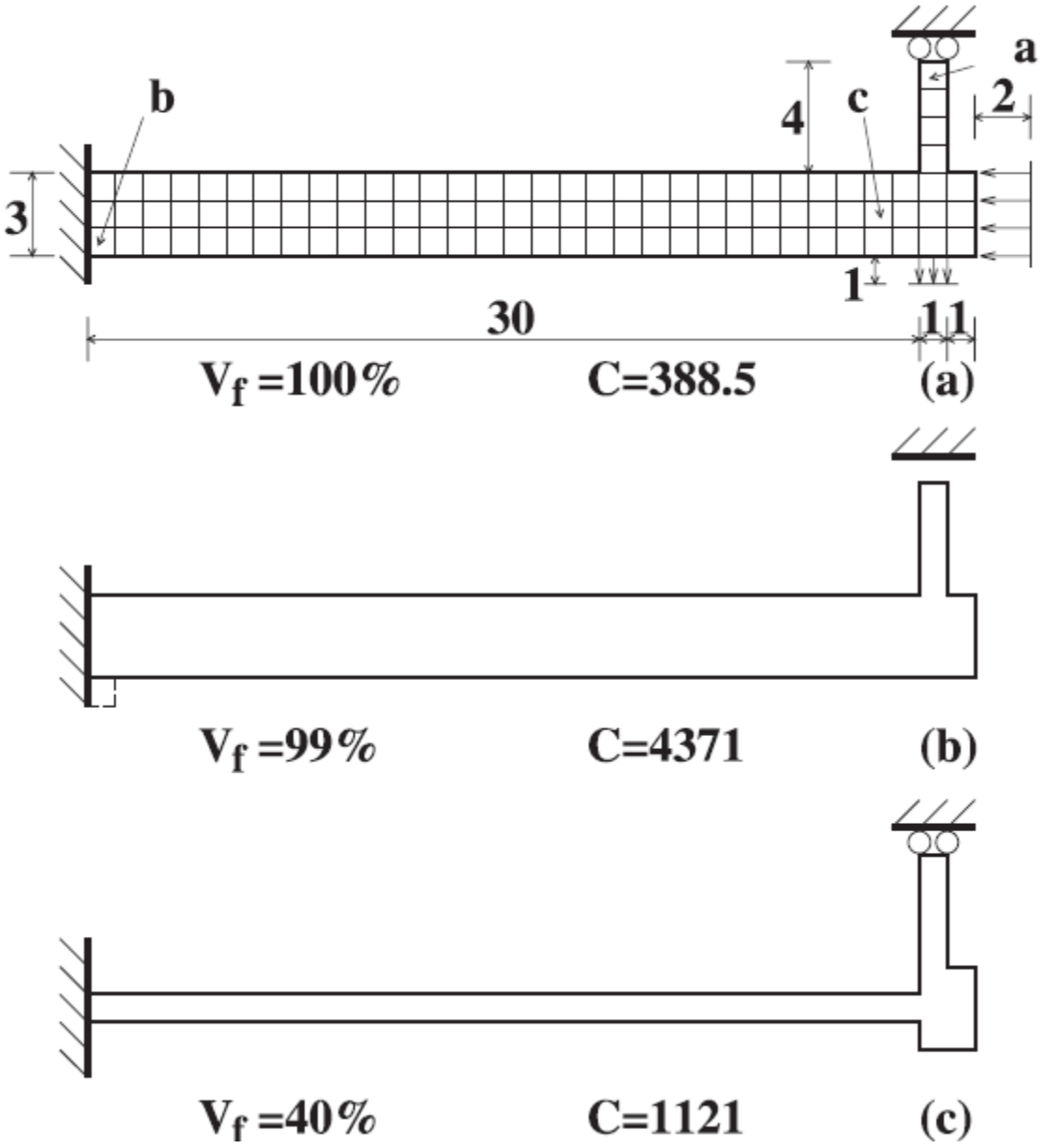

Figure 2.4 An example of topology optimization using the ESO method [166]: (a) the initial sketch; (b) topology obtained using the ESO method; and (c) an optimal solution of 60% volume reduction, V_f represents volume fraction and C represents structural compliance.

Another two evolutionary approaches, the CAO and SKO methods optimize a structure by simulating the biological growth of trees. The optimization process starts from a rough design draft with required boundary conditions. The SKO method is first used to obtain a draft of the structure with proper topology by removing the volume that does not bear any significant load to achieve a light-weight construction. The procedures of the SKO method are described as follows:

1. Create a FE model with the geometry and perform a stress analysis with the same loading and boundary conditions as the practical scenario.
2. The elastic moduli of the highly stressed elements are increased while those of the lowly stressed elements are reduced based on the following equation:

   $\Delta E = k(\sigma_{local} - \sigma_{ref})$ ..... (2.3)

   where ΔE is the change in elastic modulus, k is a constant, σ_{local} is the stress of each element and σ_{ref} is a reference stress, again related to the material's strength.
3. Step 2 will be run iteratively until no significant change is found in the structure.

After obtaining a proper topology of the structure, The CAO method is then applied to perform fine shape adjustment of the structure. The first step of the CAO method is to perform a stress analysis on the initial design under the required loading condition. In the second step, the mechanical stress field obtained from the first step is transformed proportionally to a distribution of temperature and the mechanical loading is

removed from the model. The elements with high stresses, i.e. those with high temperatures, will then be expanded according to the following equation:

$$\Delta l = l_0 \cdot \alpha \cdot (\mathrm{T} - \mathrm{T}_{ref}) \quad \text{..... (2.4)}$$

where l_0 stands for the original size of the element, Δl is the change in element size, α is the coefficient of thermal expansion, T is the local temperature, $\mathrm{T}_{\mathrm{ref}}$ is a reference temperature usually related to the material's strength. Just as trees grow by depositing new material on the surface of their bodies in response to increased loading, the coefficient of thermal expansion is only assigned to the elements on the outer layer of the structure. The stress and thermal analysis are repeated until convergence has been achieved.

The combination of the CAO and SKO methods help engineers design more economical structures by removing inefficient material. Industrial applications of the CAO and SKO methods can be found in references 167 and 168.

Based on the CAO and SKO methods, Shi [167] developed two user-defined subroutines, Stress-induced Volume Transformation (SVT) and Stress-induced Material Transformation (SMT), to integrate with the finite element software ABAQUS. The operating procedures of the SVT subroutine are very similar to the CAO method. A FE model of the draft geometry is first constructed and a layer of elements on the surface is allowed to grow or contract. Then, it uses an UTEMP subroutine to convert the mechanical stress field to a temperature field [168]. The FE mesh is modified according to the resulting thermal growth. This modification iterates until no significant change is

found in the geometry, indicating uniform stresses have been achieved in the growth layer. The SMT subroutine basically follows Eq. 2.3. Thus, instead of removing the materials/elements completely from the structure, it changes the material properties in response to the local stress. This implementation simulates the bone remodeling process whereby bone tissues change their densities to adapt to mechanical loads. By changing the orientation and magnitude of the elastic modulus along the major axis, it can also deal with materials with anisotropy. The SVT and SMT subroutines have been applied to the design of direct composite restoration, dental implants, and the 3-unit fiber reinforced composite bridge [169-171]. In this project, the SMT technique will be used to design the cavity preparation on the abutment tooth and to seek an optimal layout for the fiber substructure for the more challenging 2-unit cantilevered bridge.

Chapter 3 A study on the effect of a central incisor's inclination angle on the stresses in the surrounding bone

3.1 Background

It was pointed out in Chapter 2 that the shape of human teeth is optimized for their positions and functions. For example, for a molar that works as a grinder, and hence, has to sustain very heavy occlusal loads (up to 800 N), its upright position helps to distribute the load to the surrounding bone uniformly. It has been found that molars with either innate or acquired tilts are highly likely to develop periodontal complications such as reduced alveolar bone height or deep periodontal pockets [172-174]. The tilt, therefore, needs to be corrected before any prosthetic treatment in order to ensure a successful outcome [175]. Another example is provided by the maxillary canines. These teeth are located at the corners of the dental arch, and they are supported by the zygomatic bone, which is the strongest bone of the human body. This excellent periodontal support allows the canine to sustain the more challenging lateral loads when tearing through tough foodstuffs.

The incisors, with their blade-like shape, are located in the most anterior part of the dentition, and they are responsible for the first step of breaking down food: cutting. From a bio-mechanical viewpoint, an improper incisor inclination can be traumatic to the tooth structure and the surrounding tissues. Histological studies have shown that the biological responses of the periodontal ligaments and the surrounding bone are influenced by the stresses from the occlusal loads [176-179]. Bone resorption often occurs in zones under high compression, while bone regeneration takes place in the tensile zones; therefore, an improper incisor inclination can jeopardize the periodontal

tissues, including the gingival and alveolar bone attachment, by creating unfavorable stresses in them.

In prosthetic dentistry, the incisor inclination is also a critical factor when designing a dental prosthesis to restore oral functions. To reestablish a proper anterior guidance that controls eccentric movement of the mandible [180], the problems of overbite and overjet need to be considered. Excessive overbite or overjet may result in abnormal eccentric mandibular movement that may induce severe temporomandibular joint disorder. If the inherent incisor inclination is not favorable, any adjustments to correct for overbite or overjet may result in an angulated dental crown. This will produce unfavorable stresses within the restoration and/or the tooth structure that may lead to early prosthesis failure.

In addition to satisfying the biological and functional requirements, the inclination of the incisors is also of importance to the facial appearance. Smiling is a very useful tool for socializing in our daily life. People who smile with beautiful teeth have always been considered as more attractive and intelligent [181]. Thus, getting the right incisor inclination plays an important role in orthodontic treatment to establish an esthetic facial profile [182-184]. Not only do they determine the profile of a smile, the incisors also affect the soft tissues that form our facial characteristics. For example, protrusive incisors may lead to excessively prominent lips, which are considered unattractive [185]. Therefore, for esthetic consideration, it has been suggested that the incisal third of the buccal surface of the maxillary incisors should be parallel to the frontal plane of the face [186]. A problem with this recommendation is that the curvature of the maxillary incisor varies from person to person. Correcting the alignment of the incisors without carefully

looking into the actual inclinations of their roots may lead to unfavorable stress within them and the surrounding tissues, which can induce bone destruction or periodontal disease.

To quantitatively assess the facial profile, cephalometrical analysis is widely used in orthodontic dentistry. This analysis is done by tracing important landmarks of the bone structures and soft tissues on a lateral cephalometrical radiographic image. The angular and linear measurements performed on these landmarks provide a quantitative assessment of the facial profile for orthodontic treatment planning. In particular, they establish the relationship between the Frankfort plane, the occlusal plane, and the incisor inclination [187, 188]. Values of these measurements for a normal person are slightly different among populations from different gender, age or ethnic groups.

To determine the inclination of the maxillary incisor relative to the maxilla, three landmarks are used (Figure 3.1):

- The long axis of the maxillary incisor (UI)
- The nasion (N): the junction of the nasal and frontal bones at the most posterior point on the curvature of the bridge of the nose
- The A-point: the most anterior point of the maxillary apical base

The angle between the long axis of the maxillary incisor and a line connecting the nasion and the A-point, the N-A line, is used as a measure of the former's inclination, and it indicates the level of protrusion. For a normal person, the average value of this angle is $22^{o} \pm 6^{o}$.

It can be seen from the above discussion that the incisor inclination has been of interest to various dental specialties. The current trend of interdisciplinary dental treatment planning follows the sequence described below. Orthodontic treatment is first carried out to correct any tooth misalignment; then a dental prosthesis is used to reestablish the proper occlusion; and finally the periodontal health of the surrounding tissues is restored and maintained by the periodontist [189]. This demonstrates the importance and emphasis placed on tooth alignment in modern dental treatment. Investigation of the effect of tooth inclination on the biomechanical behavior of the tooth and its surrounding tissues under occlusal load is limited. Thus, the aim of this chapter is to evaluate the stress distribution of a maxillary central incisor with different inclination angles under occlusal load. The hypothesis is that the average value of incisor inclination is optimal for distributing the occlusal load within the tooth and surrounding tissues.

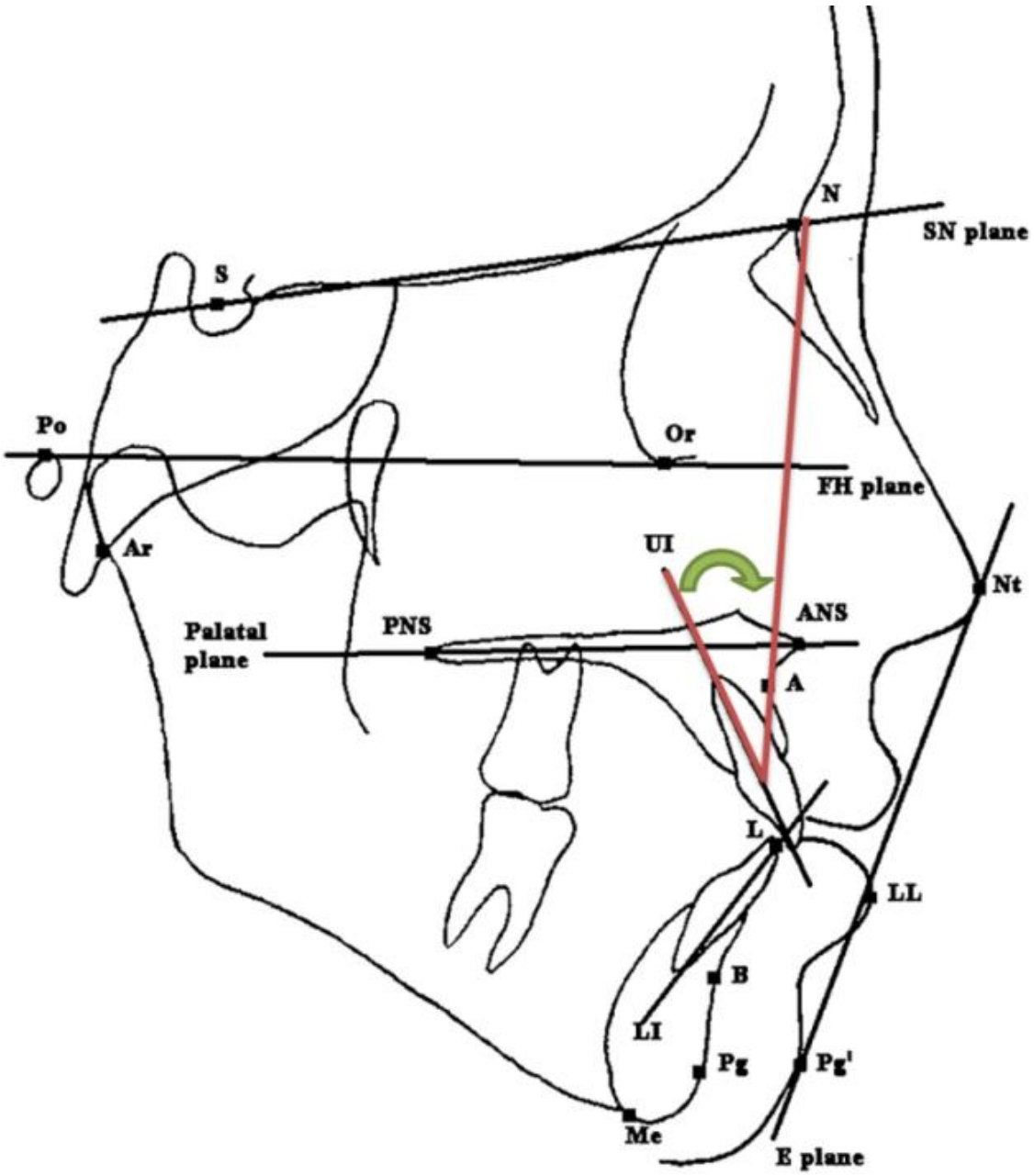

Figure 3.1 Diagram of anatomical landmarks for cephalometrical analysis. The angle (green arrow) between the long axis of the maxillary incisor (UI) and a line connecting the nasion and the A-point, the N-A line (red), is used as a measure of the former's inclination.

3.2 Methods

A two-dimensional finite element (FE) model of a human maxillary central incisor with a 10-mm out-of-plane thickness was constructed (Figure 3.2). The top of the bone region of the model was fully fixed, and a load of 200 N, the average bite force, was applied at the lingual surface of the crown. To investigate the effect of the incisor inclination on its stress distribution, the angle of the force with respect to the long axis of the incisor was altered incrementally. Thus, nineteen models with load angles (between the line of force and the incisor's long axis) ranging from 0^0 to 90^0 were generated using the software Hyperworks (Version 9.0 HyperWorks, Altair Engineering, Troy, MI, USA) and exported to ABAQUS (Version 6.9, Dassault Syetemes Simulia, Waltham, MA, USA) for stress analysis. It is assumed that the long axis of the mandibular incisor is in line with the N-A line, the load angle is equivalent to the incisor inclination described above (Figure 3.3). The mechanical properties used are listed in Table 3.1, with all materials being considered as linearly elastic, isotropic, and homogeneous. The model was meshed with quadrilateral and triangular plane-strain elements (CPE4I and CPE3 [190]). Both the von Mises and the maximum principal stresses along a path that starts from the cervical line on the labial side and goes around the entire tooth surface were retrieved and plotted for each load angle for comparison. The stresses at the root portion of the tooth would be indicative of the stresses in the surrounding bone.

Table 3.1 The material properties used in the model of the maxillary central incisor

Material	Elastic modulus (GPa)	Poisson's ratio	Ref.
Enamel	84.1	0.3	[191]
Dentin	18.6	0.31	[192]
Cortical bone	13.7	0.3	[193]
Cancellous bone	1.37	0.3	[193]
Pulp	2.07×10^{-3}	0.45	[194]
Periodontal ligaments	6.89×10^{-3}	0.45	[195]

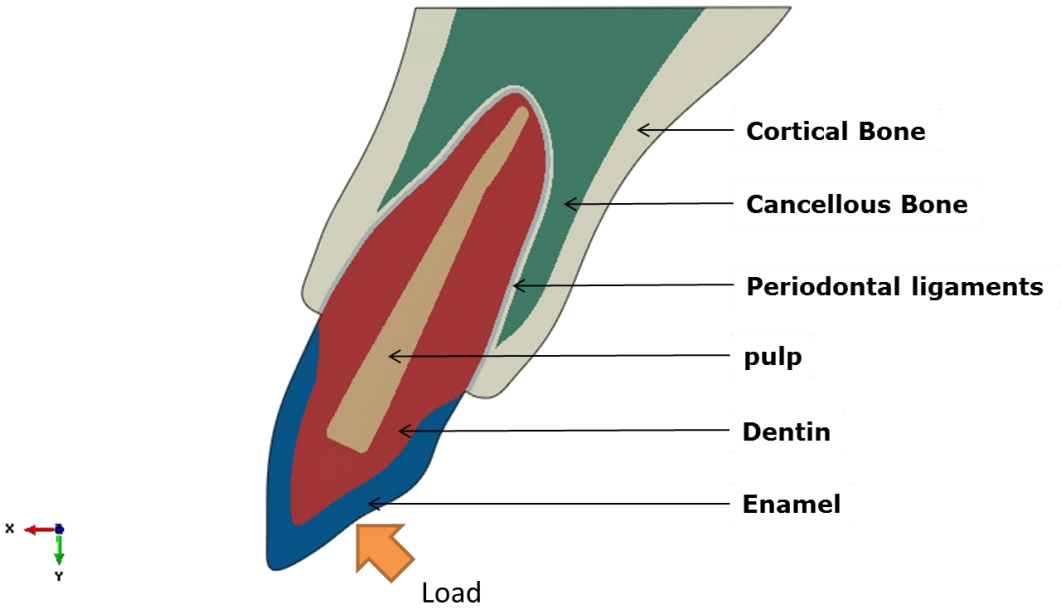

Figure 3.2 The geometry of the FE model for the maxillary central incisor.

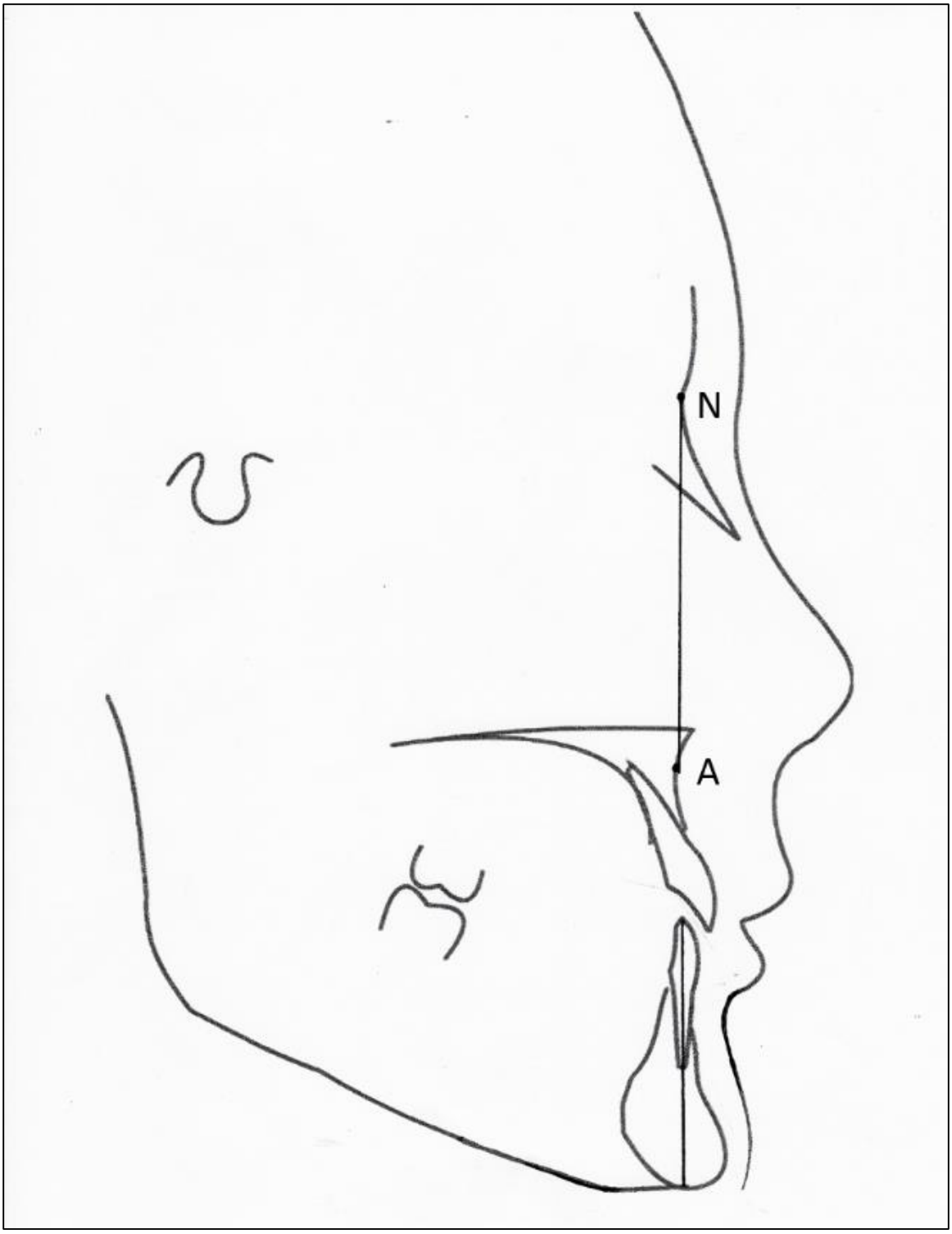

Figure 3.3 The long axis of the mandibular incisor was assumed to be in line with the N-A line so that the load angle is equivalent to the incisor inclination.

3.3 Results

The von Mises stress distribution showed stress concentrations at the apex, labial root surface, labial coronal surface and in the cervical area (Figure 3.4). When the load angle was less than 50°, stresses around the apex and the labial root surface were low. With a larger load angle, the von Mises stress was also higher within the periodontal ligament. Figure 3.5 shows the stress distributions along the tooth surface with different load angles. The upper plots show the results in 3D with the stresses plotted against the two variables, while the lower plots have the stresses at all positions superimposed on each other to show the peak value for each load angle. When the load angle was less than 50º, a sharp drop in stresses (both the von Mises and maximum principal stress) at the labial root surface could be seen (Figure 3.5). Considering the values at all positions, the peak von Mises stress was lowest when the load angle was about 30º; while the peak maximum principal stress was lowest when the load angle was about 20º.

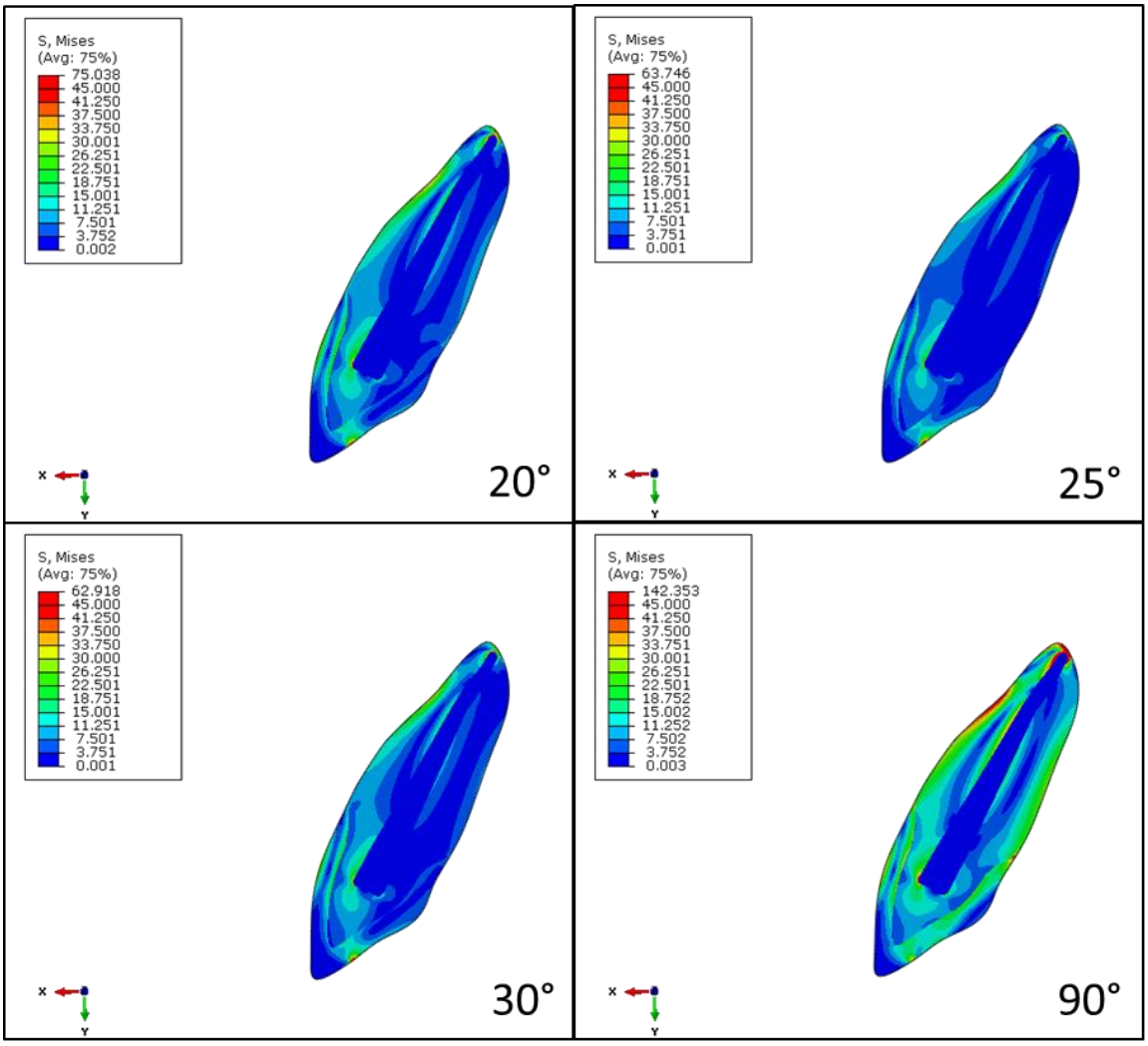

Figure 3.4 Von Mises stress distribution within the tooth under loads at different load angles.

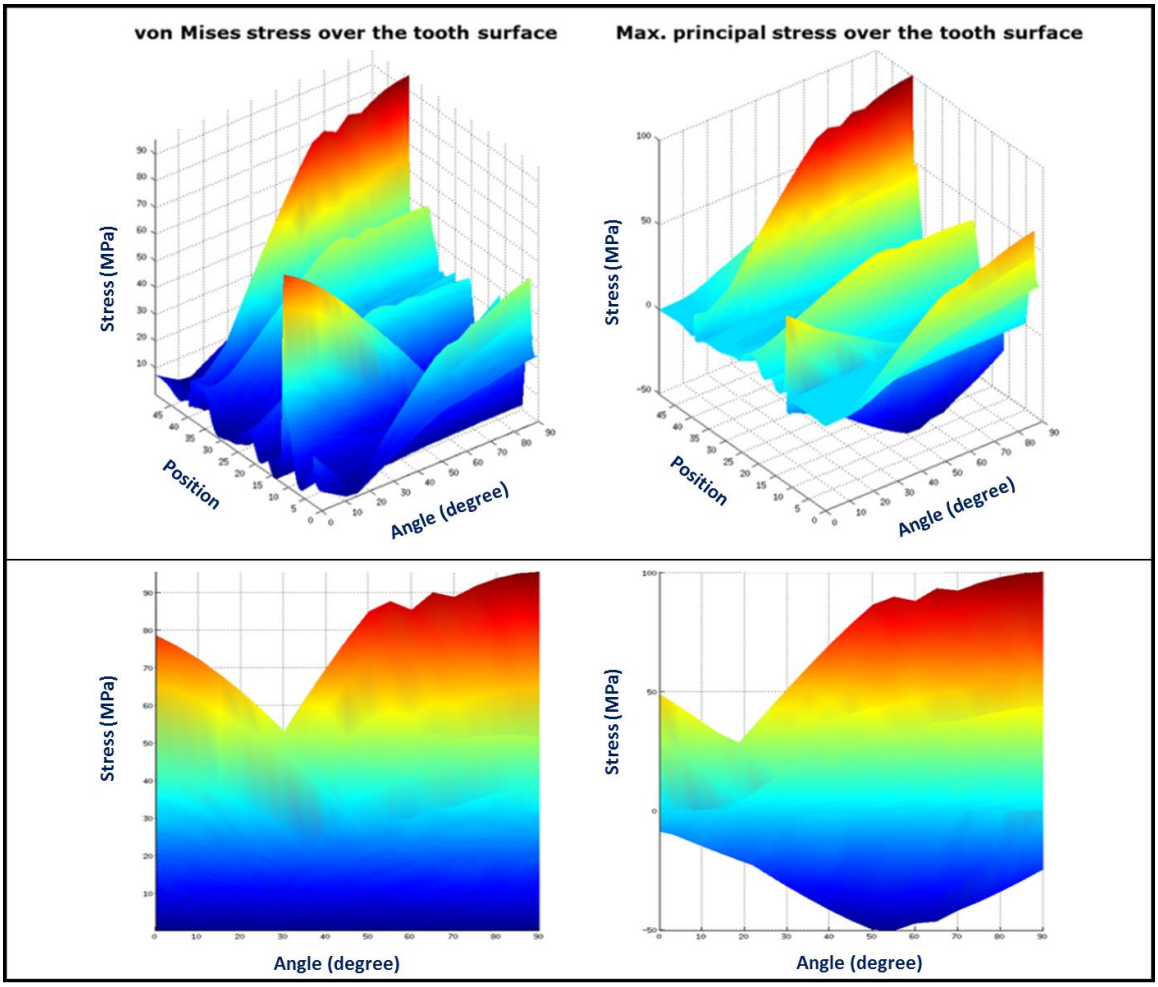

Figure 3.5 Stresses at the tooth surface under different load angles. Top: 3D plots of stresses as functions of position (mm) and load angle. Bottom: The same data sets but with the stresses at all positions superimposed on each other to show the peak value for each load angle.

3.4 Discussion and Conclusion

This study provided a simple but excellent example of structural optimization in nature. The results indicated that the stress distributions around the tooth surface would be most biomechanically favorable when the inclination angle lied between 20º and 30º. This coincided with the clinically observed inclination of the maxillary central incisor for normal patients. With this inclination, the interference by the maxilla on the protrusive movement of the mandible can be minimized. Serendipitously, orthodontists have also suggested that an incisor inclination of around 30º will create the best smile profile.

As mentioned previously, the incisor inclination is highly related to the periodontal health. In an early study [196], it was found that patients who had a severe overjet, i.e. more than 6 mm, experienced more periodontal destruction. Interestingly, among these patients with a severe overjet, if the inclination of their maxillary incisors was less than 100º to the SN plane, which is equivalent to an inclination angle of 20°, their periodontal conditions are healthier. This agrees with the FE results presented in Figure 3.5, which shows that the stresses around the root decrease with a decreasing load angle. A similar outcome was also found with the mandibular incisors: when their final inclination relative to the mandibular plane [197], a line connecting gonion to menton (gonion: most posterior inferior point on angle of mandible; menton: lower most point on the mandibular symphysis) was larger than 95º, which would produce a larger load angle, greater gingival recession resulted after orthodontic treatment [198]. A systematic review [199] evaluated the relationship between the traumatic dental injuries and the size of the overjet. It was concluded that the risk of anterior tooth trauma increased as the overjet

became larger, and children with an overjet larger than 3mm doubled their risk of anterior tooth trauma.

The alveolar bones surrounding the incisors are very thin; they can resorb easily due to unfavorable stresses generated by the biting force. Unlike those of the premolars and molars, the occlusal loads of the incisors are oblique in direction, which results in high stress concentration around the alveolar crest, the thinnest part of the surrounding bone, next to the cervical region of the incisors. The present study shows that altering the inclination of the incisors from the normal angle could significantly raise the stress level within the bone. This also implies that the insertion angle of dental implants in the anterior maxilla needs to be carefully planned, especially in cases where bone resorption following tooth extraction requires the implant to be inserted in a non-ideal angle. Also, given that the material properties and shapes of dental implants are very different from those of human teeth, the ideal inclination of the latter may not necessarily apply to the former. In the next chapter, we will look at the effect of the inclination angle on the stress distribution along the surface of a tilted implant placed in a compromised anterior maxilla.

Chapter 4 The influence of the insertion angle of anterior dental implants with an angulated abutment on the stress distribution within the surrounding bone

4.1 Background

Traumatic injury and congenitally missing teeth are two main reasons for missing incisors. Treatment options for tooth replacement include conventional or resin-bonded fixed partial dentures, removable partial dentures, orthodontic treatment, which displaces the neighboring canines to close the edentulous space, and single-tooth implants [200]. Removable or fixed partial dentures usually bring inconveniences to a patient's daily life in the form of additional oral hygiene upkeep. Orthodontic treatment could be a good option as it eliminates the need to install prosthesis; however, the shape of the canine may compromise anterior occlusion and esthetics. Thus, single-tooth implants are increasingly being used to replace missing incisors.

For implant surgery in the anterior maxilla region, the limited quantity and quality of alveolar bone can significantly affect the clinical outcome. The buccal bone plates of the anterior maxilla are the thinnest among all alveolar bony structures, and they can resorb quite easily after tooth extraction. Resorption of the anterior maxilla results in a concavity on the labial side and a very narrow edentulous ridge (Figure 4.1), which makes conventional upright implant placement impossible. Bone augmentation is required to regain enough bone volume for upright implant insertion. For the cases where bone augmentation cannot be carried out, the implant may have to be inserted at a less than ideal angle, and an angulated abutment has to be used to achieve the right occlusion.

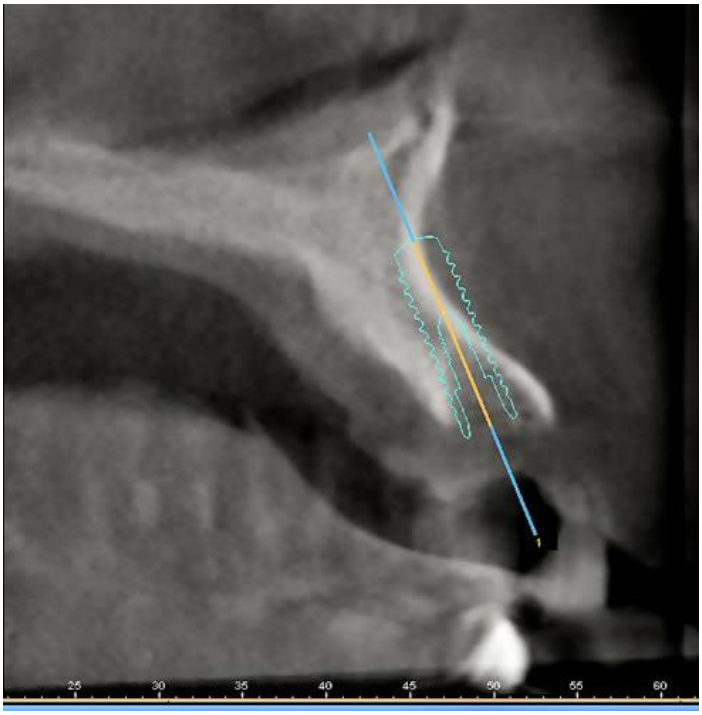

Figure 4.1 A large concavity on the labial side of the anterior maxilla [201], making it impossible to insert an implant at the optimal angle.

The influence of angulated abutments on the clinical prognosis of dental implant treatment remains unclear. A meta-analysis [202] has shown that the clinical success rate between tilted and upright implants was not significantly different in either the prospective or retrospective studies examined. The level of marginal bone loss around the tilted and upright implants seemed to be very similar, about 0.9 mm on average over a 5-year observation period. A more recent study, which examined fifty-eight subjects who had received tilted implants with delayed loading, also found no correlation between implant angulation and marginal bone loss [203]. Marginal bone loss was only related to the length of the follow-up period, regardless of the type of abutment. The rate of bone resorption associated with tilted implants increased by 0.035 mm for every additional

month of follow-up time. Nevertheless, they did not find any signs of significant marginal bone loss during 36 months of observation.

Several studies using the finite element (FE) method have investigated the influence of angulated abutments on the stress distribution within the implant-surrounding bone [204-213]. Implants in both the maxilla [205-208, 210, 212, 213] and the mandible [204, 209, 211] have been considered. These FE studies indicate that the use of angulated abutments may not always be harmful, which may explain the inconclusive clinical findings. For example, while higher strain within the cortical bone was found when angulated abutments were used in the posterior maxilla [213], the opposite was true when they were used in the anterior maxilla [207]. In another study [204], the use of an angulated abutment was able to reduce the stress within the mandibular bone surrounding a tilted implant. These studies indicate that the ideal tooth inclination, as found in the previous chapter, may not apply to dental implants. Therefore, both the anatomy of the surrounding bone and the insertion angle of the implant have to be taken into account when angulated abutments are planned. If the combination of a tilted implant and an angulated abutment give rise to damaging stresses, bone augmentation will need to be considered.

In most of the biomechanical studies involving the maxilla mentioned above [205-207], the numerical model used was not fully representative of the clinical scenario. In those studies, the dental implant was inserted at an optimal angle within a healthy bone structure and the influence of an angulated abutment on the bone stresses was studied by altering the angle of the abutment relative to the implant. The clinical scenario is actually

very different. The abutment has to be placed at a specific position and at a certain angle so as not to interfere with the existing occlusion and to provide satisfying esthetics. But due to compromised bone volume and geometry, the implant insertion angle could be far from ideal. In this case, the effect of the angulated abutment on the bone stresses could be more significant.

In this chapter, a dental implant with various insertion angles for restoring the maxillary incisor in compromised bone was modelled using the FE method. An angulated abutment was used such that the inclination of the prosthetic crown remained constant to the maxilla. In addition, the thickness of the cortical bone of the maxilla was varied to study the influence of different bone quality on the stress distribution. The thickness of the cortical bone simulated in the present study was comparable to that found in the human cadaver [214]. According to Misch's classification of bone type [37], the anterior maxilla usually consists of the D3- and D4-type bones, which are primarily composed of porous cancellous bone and a thin cortical layer. The difference between D3- and D4-type bones is in the thickness of the cortical layer. The cortical layer of D3-type bone is ~1-mm thick, while that of D4-type bone is very thin or even absent.

It has to be emphasized again that the success of a dental restoration depends on how the constituent materials are arranged spatially. More broadly speaking, the optimal insertion angle of a dental implant is equivalent to arranging the titanium material and osseous tissues within the jaw bone in an optimal way. This study hypothesized that the implant inserted at the same angle as the long axis of natural incisor with non-angulated abutments can have better stress distribution with the implant and surrounding bone.

4.2 Methods

The two-dimensional FE model for the dental implant used in this study was based on the geometry of the NobelReplace® Tapered, and its corresponding abutment (Nobel Biocare®, Yorba Linda, CA, USA). For simplicity, the threads on the implant were not modelled. The geometry of the maxilla was extracted from the sagittal view of a set of clinical cone beam computed tomography images from a patient who had a resorbed alveolar ridge. The top of the maxilla in the model was fully fixed, and an oblique load, 30º with respect to the vertical, of 200 N was applied at the lingual surface of the crown (Figure 4.2). To investigate the effect of the implant insertion angle on the stress distributions, three different insertion angles of the dental implant were modelled (Figure 4.3). These included the regular angle, i.e., in line with the main axis of the alveolar ridge, 15º clockwise from the regular angle and 15º counter-clockwise from the regular angle. The crown remained in line with the maxilla for all the cases. In addition, two different thicknesses of the cortical bone, 0.5 mm and 1.0 mm, were modelled. Thus, six models were generated using the software Hyperworks (Version 9.0 HyperWorks, Altair Engineering, Troy, MI, USA) and exported to ABAQUS (Version 6.9, Dassault Syetemes Simulia, Waltham, MA, USA) for stress analysis.

The mechanical properties used are listed in Table 4.1, with all materials being considered as linearly elastic, isotropic, and homogeneous. The model was meshed with triangular and quadrilateral plane-strain elements (CPE3 and CPE4 [190]). An out-of-plane thickness of 10 mm was assumed. The maximum principal and von Mises stresses were retrieved along the entire implant surface, starting from the neck of the labial side

and ending at the neck of the lingual side, and plotted for each insertion angle for comparison.

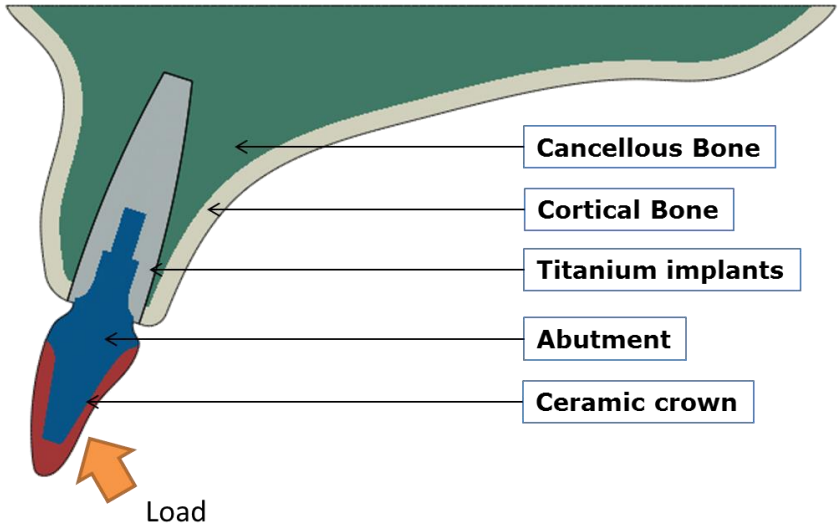

Figure 4.2 Diagram of the FE model showing the implant components and the surrounding bone

Table 4.1 The material properties used in the FE models

Material	Elastic modulus (GPa)	Poisson's ratio	Ref.
Titanium (Ti–6Al–4V)	110	0.3	[215]
IPS e.max®	95	0.3	[216]
Cortical bone	13.7	0.3	[193]
Cancellous bone	1.37	0.3	[193]
Stainless Steel	210	0.3	[217]

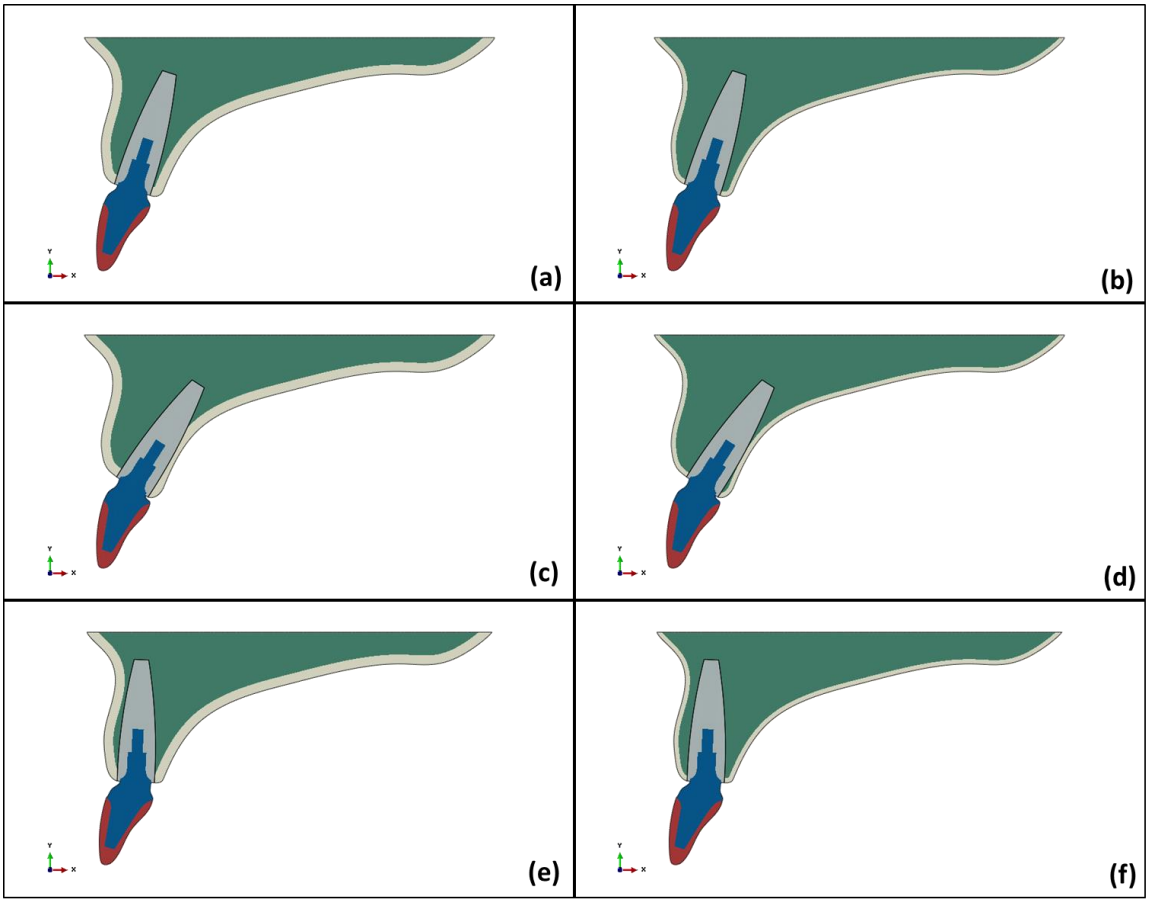

Figure 4.3 The geometries of the FE models for an incisor-replacing implant with different insertion angles and in bones with different cortical thicknesses: (a) Regular insertion angle with cortical bone of 1-mm thick; (b) Regular insertion angle with cortical bone of 0.5-mm thick; (c) 15º clockwise from the regular insertion angle with cortical bone of 1-mm thick; (d) 15º clockwise from the regular insertion angle with a cortical bone of 0.5-mm thick; (e) 15º counter-clockwise to the regular insertion angle with a cortical bone of 1-mm thick; (f) 15º counter-clockwise to the regular insertion angle with a cortical bone of 0.5-mm thick.

4.3 Results

The peak stresses in each essential part of the models are listed in Table 4.2. In terms of the locations of stress concentration, the von Mises stress concentrated at the neck region of the dental implant and the buccal concavity of the maxilla (Figures 4.4 and 4.5). The maximum principal stress concentrated at the neck region and lingual side of the dental implant, but it concentrated at the palatal rather than the buccal surface of the maxilla (Figure 4.6). The von Mises stress distributions within the abutment and implant for the different cases are shown in Figure 4.4. When the implant insertion angle was not regular and an angulated abutment was used, approximately 25% higher von Mises stresses at the neck region could be found within the dental implant and abutment. Within the cortical bone, approximately 15% higher von Mises stresses could be found in the models with thinner cortical bone (Figure 4.5). This higher cortical bone stress also applied to the maximum principal stress, except for the model inserted at 15º clockwise from the regular angle. Although the peak bone stresses of the 15º counter-clockwise models were comparable to those of the regular models, they, and the 15º clockwise models, showed higher von Mises stress concentrations at the implant's lingual neck region than the regular models. The thickness of the cortical bone did not significantly influence the peak stress value within the dental implant and abutment. The von Mises and maximum principal stresses within the crown were not significantly different between the models, except the regular model with 1-mm thick cortical bone, which showed higher von Mises stress in the crown.

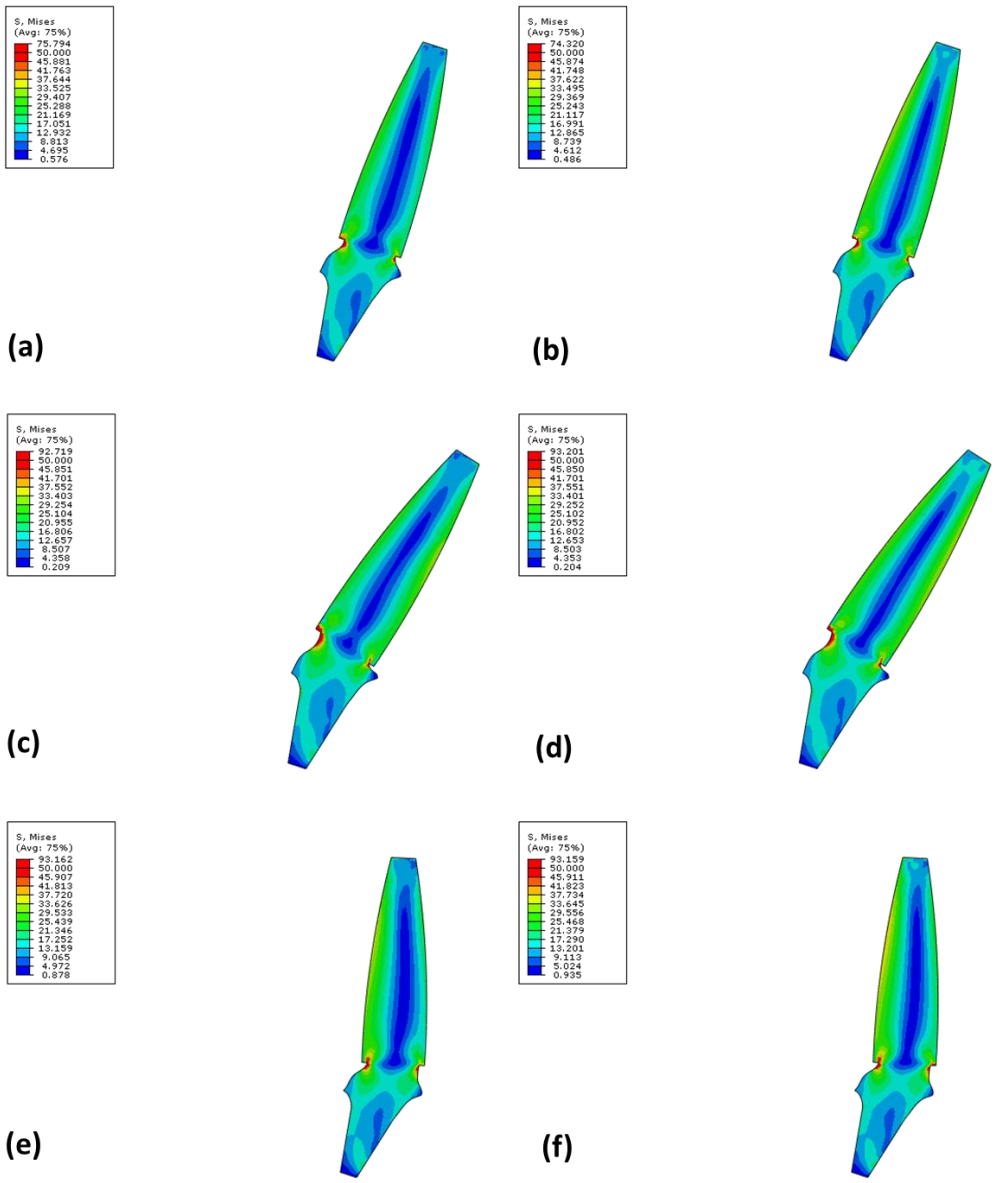

Figure 4.4 Von Mises stress distribution within the implant and abutment with different insertion angles and cortical bone thickness: (a) Regular insertion angle with cortical bone of 1-mm thick (b) Regular insertion angle with cortical bone of 0.5-mm thick (c) 15º clockwise from the regular insertion angle with cortical bone of 1-mm thick (d) 15º clockwise from the regular insertion angle with a cortical bone of 0.5-mm thick (e) 15º counter-clockwise to the regular insertion angle with a cortical bone of 1-mm thick (f) 15º counter-clockwise to the regular insertion angle with a cortical bone of 0.5-mm thick.

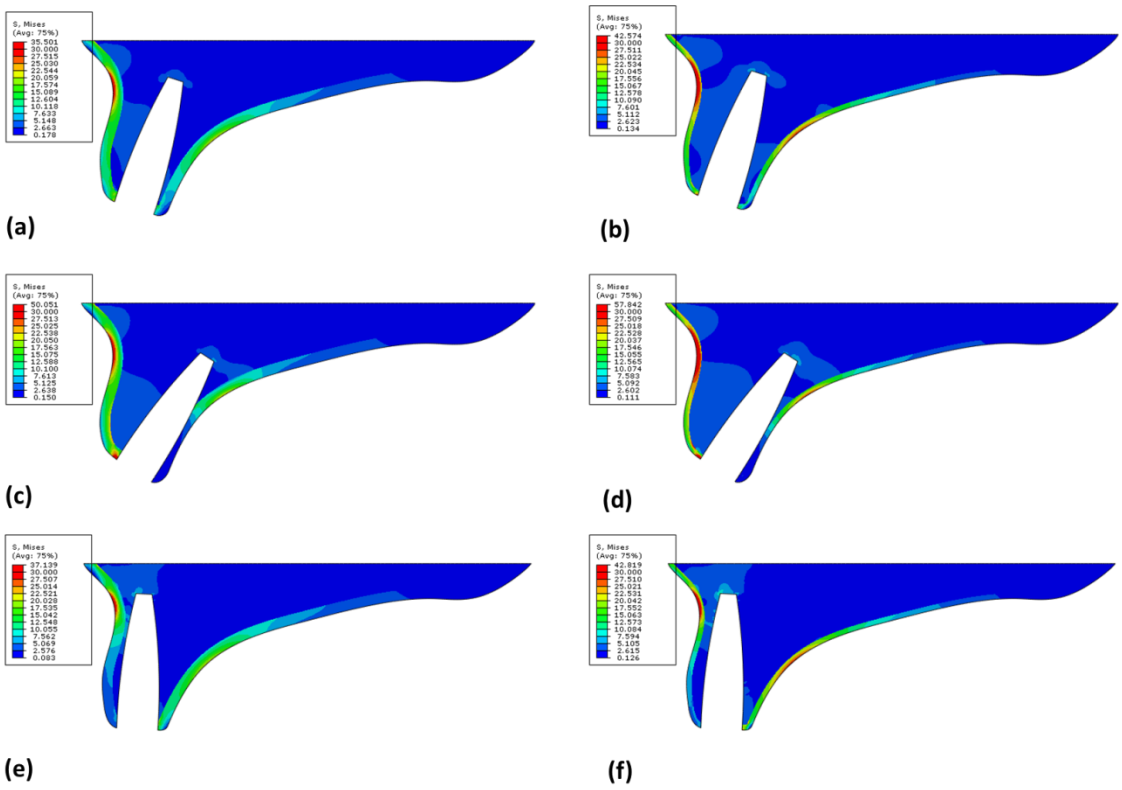

Figure 4.5 Von Mises stress distribution within the bone with different implant insertion angles and cortical bone thickness: (a) Regular insertion angle with cortical bone of 1-mm thick (b) Regular insertion angle with cortical bone of 0.5-mm thick (c) 15º clockwise from the regular insertion angle with cortical bone of 1-mm thick (d) 15º clockwise from the regular insertion angle with a cortical bone of 0.5-mm thick (e) 15º counter-clockwise to the regular insertion angle with a cortical bone of 1-mm thick (f) 15º counter-clockwise to the regular insertion angle with a cortical bone of 0.5-mm thick.

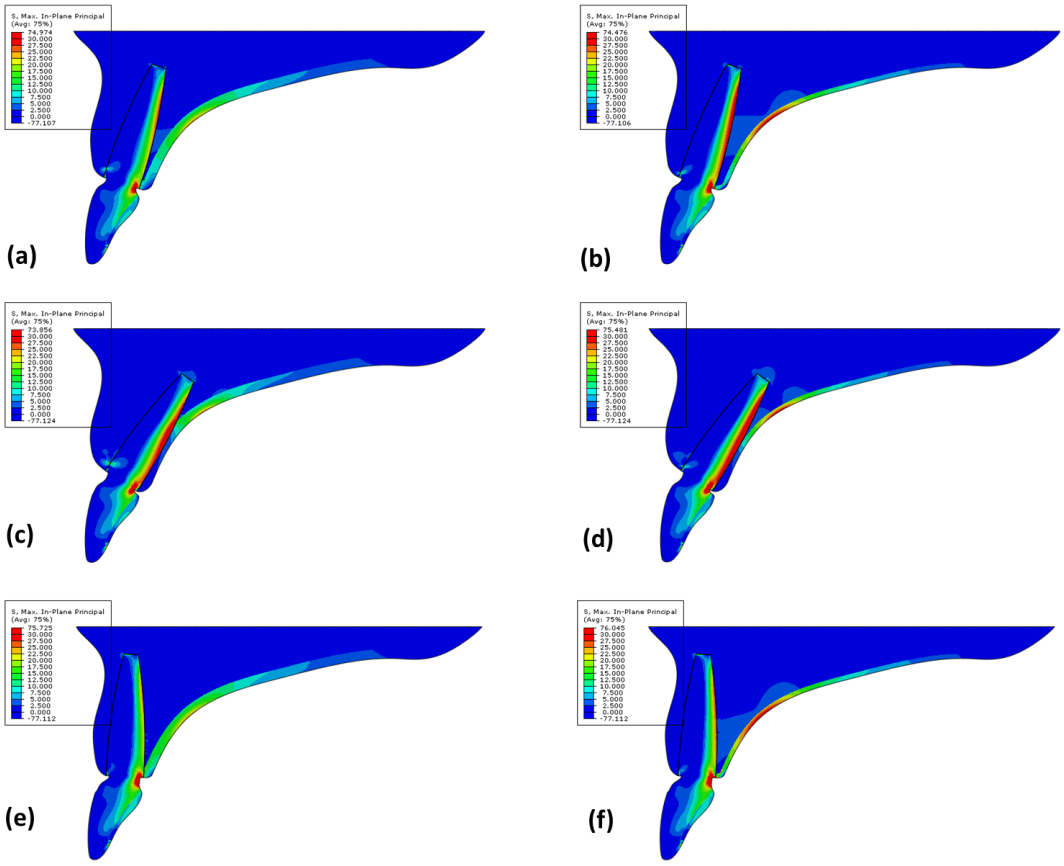

Figure 4.6 Maximum principal stress distribution with different implant insertion angles and cortical bone thickness: (a) Regular insertion angle with cortical bone of 1-mm thick (b) Regular insertion angle with cortical bone of 0.5-mm thick (c) 15º clockwise from the regular insertion angle with cortical bone of 1-mm thick (d) 15º clockwise from the regular insertion angle with a cortical bone of 0.5-mm thick (e) 15º counter-clockwise to the regular insertion angle with a cortical bone of 1-mm thick (f) 15º counter-clockwise to the regular insertion angle with a cortical bone of 0.5-mm thick.

Table 4.2 The peak stress (MPa) in each material section of the six FE models

Material section	Cortical Bone		Implant & Abutment		Crown	
The peak stress in models with 1-mm think cortical bone						
Insertion angle	**Mises**	**Max. Principal**	**Mises**	**Max. Principal**	**Mises**	**Max. Principal**
Regular	35.501	24.944	75.794	74.974	13.254	9.869
15º counter-clockwise	37.139	24.582	93.162	75.725	9.283	10.228
15º clockwise	50.051	37.312	92.719	73.856	9.578	9.597
The peak stress in models with 0.5-mm thick cortical bone						
Insertion angle	**Mises**	**Max. Principal**	**Mises**	**Max. Principal**	**Mises**	**Max. Principal**
Regular	42.574	32.759	74.320	74.476	9.401	9.846
15º counter-clockwise	42.819	37.549	93.159	76.045	9.282	10.229
15º clockwise	57.847	32.014	93.201	75.481	9.613	10.103

Figures 4.7 and 4.8 show, respectively, the von Mises and maximum principal stresses along the bone-implant interface. The distance has been normalized, with 0 being the point at the labial neck region and 1 being that at the lingual neck region. Similar trends could be found in the models with the two different cortical bone thicknesses. Figure 4.7 shows that with the implants inserted at 15° clockwise from the regular angle, the level of von Mises stress at the labial bone-implant interface was the highest while those with the other two insertion angles were about the same. On the lingual side of the implant, the von Mises stress in the 15° counter-clockwise model was higher than the other two models from the middle third to the cervical third of the implant.

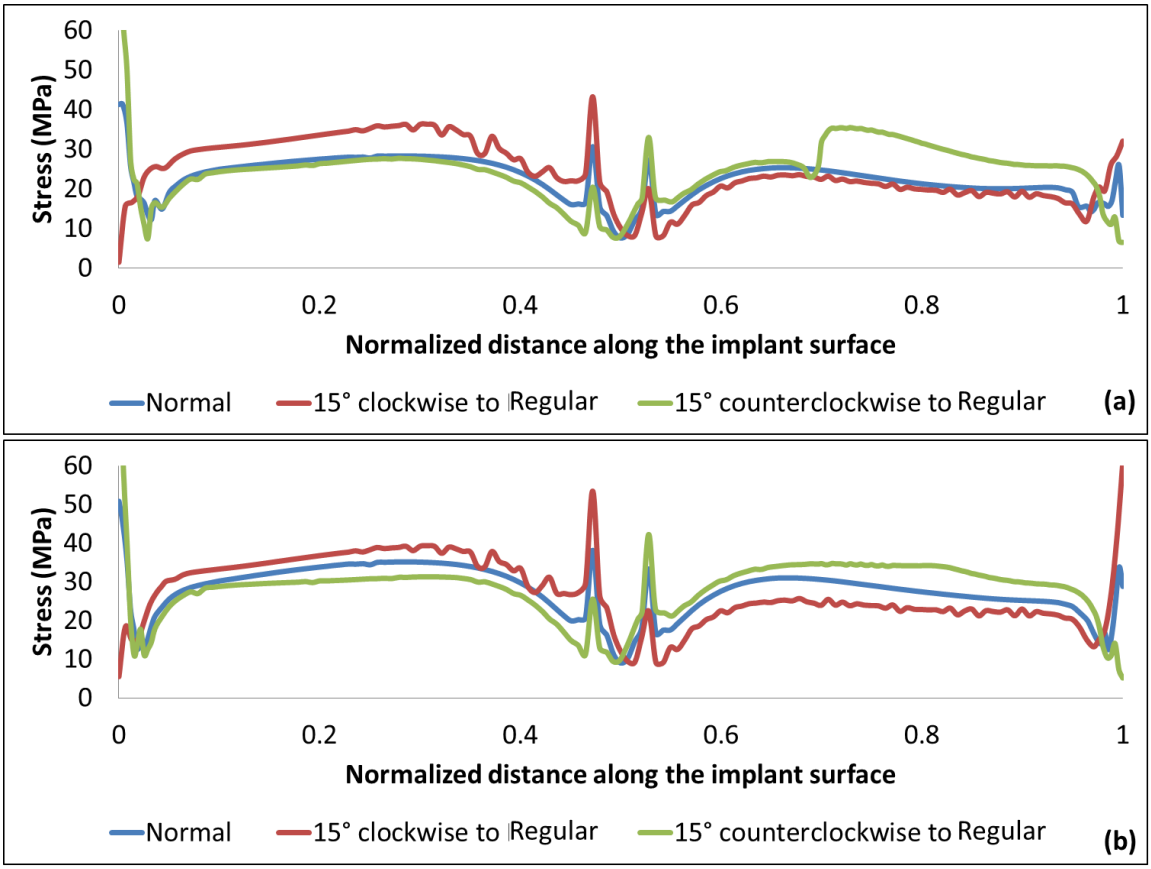

Figure 4.7 Von Mises stresses at the bone-implant interface: (a) Results from the models with 1.0-mm thick cortical bone. (b) Results from the models with 0.5-mm thick cortical bone.

Figure 4.8 shows that the highest maximum principal stress was found at the lingual bone-implant interface, with the models having the implants inserted at 15° counter-clockwise from the regular angle giving the highest value, followed by the one with the regular insertion angle, and then the one at 15° clockwise to the regular. The same trend was found for both cortical bone thicknesses.

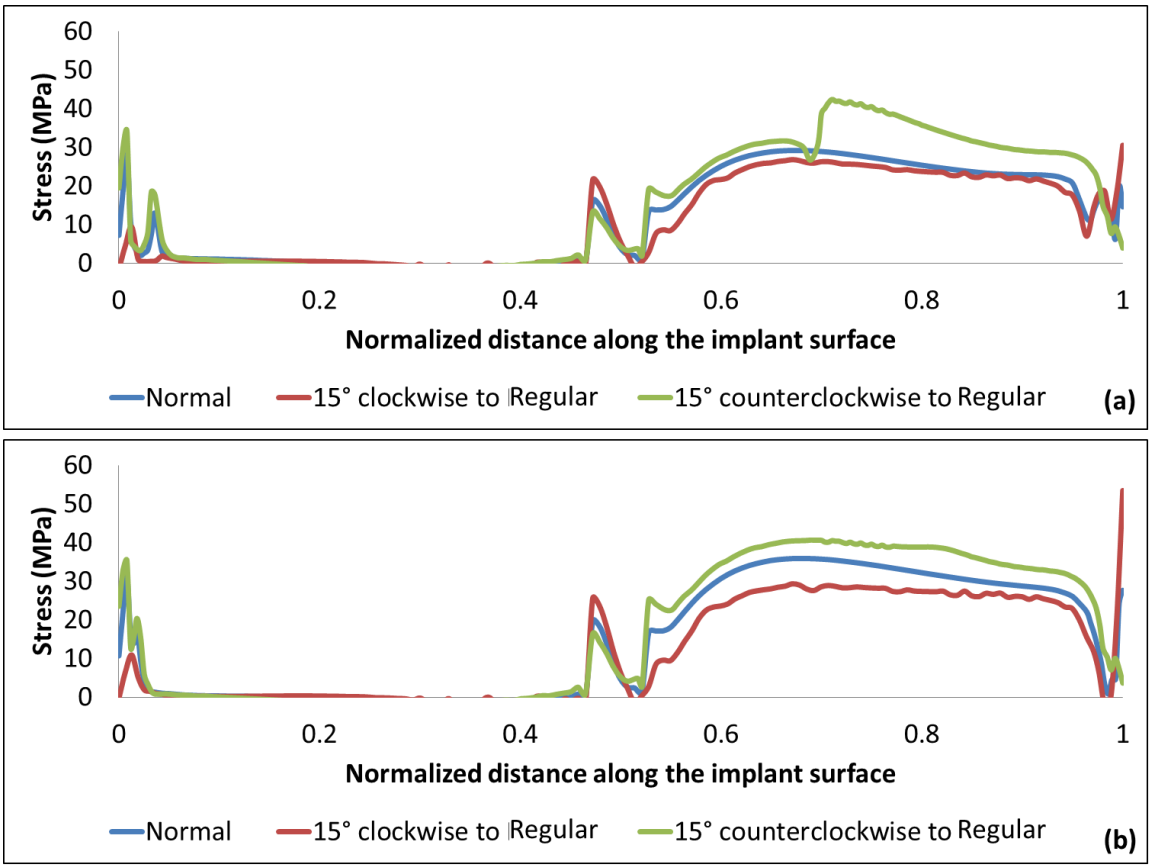

Figure 4.8 Maximum principal stresses at the bone-implant interface: (a) Results from the models with 1.0-mm thick cortical bone. (b) Results from the models with 0.5-mm thick cortical bone.

4.4 Discussion and Conclusion

The FE results have shown that higher von Mises stresses at the neck region could be found within the dental implant and abutment, when the implant insertion angle was not regular and an angulated abutment was used. They also confirm the stress concentration around the neck reported by others [204-213]. The results from the present study show that a thinner cortical layer can further increase the stress level around the neck region, which can lead to saucerization of the crestal bone around the implant. As shown in Figures 4.7 and 4.8, higher stress levels were also found at the bone-implant interface in the models with a thinner cortical layer.

High values of the maximum principal stress were found at the lingual bone-implant surface. The model with the implant inserted at 15° counter-clockwise from the regular angle had the highest stress level; however, based on the averaged chewing force, the calculated stress level- did not exceed the tensile strength of the bone tissues, i.e. 70~130 MPa [218-220]. The calculated stress level (40-50 MPa) was close to that required for osteoblast differentiation and bone apposition [221-226]. Also, inserting the implants at 15º counter-clockwise from the regular angle can actually reduce the maximum bone stress on the palatal side of the maxilla. These numerical results may explain the clinical findings that show no significant difference in peri-implant bone loss between upright and tilted implants.

From the patient's point of view, esthetics is the most important factor for an anterior prosthesis. To achieve esthetics the implant may have to be placed at a non-optimal angle. Three-dimensional computed tomography has been used to determine the

optimal insertion angle for esthetic consideration. In combination with CAD/CAM technique, a surgical template can be fabricated to ensure that an implant is inserted at the angle as planned during surgery. The current study shows that certain implant insertion angles can produce unfavorable stresses to the implant system and surrounding bone. To provide a better prognosis, stress analysis is required to evaluate whether the stress level would jeopardize the peri-implant tissues when tilted implants and angulated abutments are used for the treatment. Therefore, more frequent post-operative follow-up is required when angulated abutments are used.

Current dental implants are shaped very differently from natural teeth, especially the premolars and molars. To simplify the surgical procedure and to make it easy to maintain oral hygiene, most dental implants use a single, rather than multiple, root straight screw design. From the biomechanical point of view, this design may not be appropriate for all regions, especially the molar region, which sees the heaviest occlusal load. Further numerical analysis should be performed for tilted implants replacing these posterior teeth.

Chapter 5 A study on the graded material distribution of natural teeth

5.1 Background

Through evolution, animals have developed various types of mineralized biological tissues with optimal mechanical properties for their survival. For example, the skeletal system of vertebrates was developed to support their body weight, facilitate muscle movement, and protect the many important organs in the body. Invertebrates, on the other hand, have developed different types of exoskeleton to protect themselves. Examples include the shells in mollusks and cuticles in arthropods. Another mineralized biological structure, teeth, with their stiff and wear-resistant nature, play an important role in the daily lives of animals – food intake and breakdown. The shape and layout of the constituent materials of a tooth have evolved to meet the dietary needs of an animal. For example, carnivores usually own very sharp and strong teeth for hunting, killing and ripping the meat off their prey, while herbivores usually have cuspless teeth for grinding vegetation. Irrespective of the diet, teeth are often subjected to large mechanical forces.

With their constituents organized in highly specific manners, mineralized biological tissues such as nacre [227] usually exhibit far better mechanical properties than their synthetic counterparts made of the same constituent materials. In recent years, there has been increased attention paid to how these unique material layouts in nature are able to maximize and optimize the mechanical performance of natural structures. These specific material layouts, including porous, fibrous and laminate structures, result in tissues with different strengths or anisotropies that meet their functional demands [228]. For example, osseous or bone tissues are mainly composed of hydroxyapatite (HA)

crystals. Depending on the density of these minerals, the elastic modulus of bone can vary by a factor of up to ten [193]. High mineral density in the outer cortical bone provides the required strength and bending stiffness for sustaining the body weight. On the other hand, the large porosity in the inner cancellous bone helps reduce the weight of the whole structure and gives it the capacity for shock absorption. Such a structured organization of osseous tissues with different properties in bone makes it an optimized design for accommodating the functional loads.

A similar material layout can be found in teeth or related structures. Although their shapes vary according to their functions, the fundamental structures of fangs, tusks and human teeth share the same material layout [228]. Specifically, they all have a hard outer layer of enamel that provides a strong and wear-resistant surface that gives them the strength for fighting, killing, biting and/or chewing. Underneath, a softer inner layer of dentin contributes to their toughness and resilience to buffer the impact force from these actions. Not only is there a difference in the overall mechanical properties between the inner and outer tissues, there is also a graded spatial distribution of these properties within each of them.

Marshall Jr. et al. [229] conducted nanoindentation tests using a modified atomic force microscope (AFM) to obtain profiles of the hardness and elastic modulus of human teeth across the dentinoenamel junction (DEJ). Their results showed that both of these mechanical parameters decreased gradually from enamel to dentin. Fong et al. [230] also reported that the nanohardness across the DEJ gradually decreased from 4.8 GPa to 0.8 GPa, with the elastic modulus following a similar profile. Kishen et al. [143] found a

significant correlation among the mineral density, hardness and elastic modulus in human dentine using fluoroscopic X-ray imaging and microindentation. Their results showed that the hardness and elastic modulus of root dentin increased gradually from the central region to the outer surface of the root. Another AFM study further indicated that the nanomechanical properties of dentin varied among its microstructures, including the intertubular dentin, peritubular dentin and peritubular-intertubular dentin junction [231].

In addition to dentin and the DEJ, a graded distribution of mechanical properties has also been found in enamel using indentation [145, 150, 229, 230, 232-240]. The reported values from these studies varied with the indenter's size and shape, and the site where the indentation was performed. Nevertheless, the spatial distribution of the mechanical properties followed a similar pattern to that found in dentin, in which the elastic modulus was highest in the outer layer and gradually decreased as one moved towards the DEJ. Moreover, Cuy et al. [233] found that the lingual cusp (the one that is chiefly responsible for breaking down food) of a maxillary molar had a thicker, stiffer layer of enamel. Therefore, researchers have hypothesized that the graded distribution of mechanical property within human teeth was developed to adapt to their particular functional needs [143, 233]. A digital photoelastic analysis showed high concentration of bending stresses in the cervical region of a mandibular incisor [143]. It was found that this region of high stress concentration also had higher mineral density, hardness and elastic modulus. This example further demonstrates that tooth structures are optimized for the mechanical loads that they sustain.

Despite the above findings, in most stress analysis of tooth structures using the

finite element (FE) approach, the tissues and materials are usually defined as homogeneous and isotropic. Stress analysis using a graded material distribution for tooth structures has been very limited. Without modeling the material properties properly, the stress distribution obtained from the FE analysis may not be accurate. This study, therefore, aims to better understand how the graded distribution of the elastic modulus affects the structural stress distribution within a tooth. It is hypothesized that such a material layout would produce a more uniform stress distribution with lower stress concentrations.

5.2 Materials and Methods

5.2.1 Preparation of hydroxyapatite (HA) tablets

As mentioned, it has been found that the degree of mineralization is a major contributor to the mechanical properties of mineralized tissues [241, 242]. The present study used a micro-CT scanner to provide the spatial distribution of mineral density within teeth to construct the FE models required for the stress analysis. To do so, a relationship between the mineral density of enamel and the corresponding attenuation coefficient in the CT images needed to be established. This was achieved by using tablets, or phantoms, made of HA, the major constituent in teeth, with different densities.

Approximately 25 mg of HA powder was manually filled each time into a tableting die and compressed with a predetermined compaction force (0.5–3 kN) using a universal material testing machine (Model 1485, Zwick, Germany). The compression speed and holding time at the maximum compaction force were set at 1 mm/min and 120 s, respectively. The density of the resulting round tablets (flat-faced, 4 mm diameter) were determined by their weights, diameters and thickness. Twelve tablets were successfully constructed in this way, and their density ranged from 0.99 to 1.54 $g \cdot cm^{-3}$. The dimensions and properties of these tablets are listed in Table 5.1. Attempts were made to fabricate tablets with higher densities; however, cracks were found inside these high-density HA tablets during the initial CT inspection. The cracks were probably caused by the high pressure used in their fabrication. Also, these tablets chipped very easily. The mean attenuation coefficients calculated from these fractured tablets were thus lower than they should be. As a result, they were excluded from this study.

Table 5.1 The dimensions and properties of the HA tablets used to relate the attenuation coefficient to the mineral density

ID	Weight (mg)	Diameter (mm)	Thickness (mm)	Volume (mm^3)	Density ($g \cdot cm^{-3}$)	Attenuation coefficient (cm^{-1})
1	25	4.01	2.01	25.372	0.985	109.775
2	26.2	4.03	1.95	24.861	1.054	119.319
3	25.4	4	1.84	23.110	1.099	122.910
4	25.3	4.01	1.51	19.061	1.327	145.506
5	25.3	4.02	1.5	19.029	1.330	149.139
6	26.4	4.03	1.67	21.291	1.240	140.305
7	25.7	4.03	1.61	20.526	1.252	141.128
8	27.7	4.03	1.57	20.016	1.384	155.606
9	26.5	4.02	1.48	18.775	1.411	156.645
10	25.6	4.02	1.39	17.633	1.452	167.356
11	27	4.02	1.44	18.268	1.478	168.537
12	26.3	4.02	1.35	17.126	1.536	175.005

5.2.2 Establishing a relationship between the mineral density and attenuation coefficient

The twelve intact HA tablets were vertically stacked using an acrylic holder (Figure 5.1a) and scanned with a micro-CT system (HMX-XT 255, X-tek system, United Kingdom). Scanning was performed using X-rays produced with a tube voltage of 90 kV and tube current of 90 μA. A total of 720 projections, with 4 frames per projection, were acquired. The volumetric reconstruction with the microradiographs was performed using the software CT Pro 3D (Nikon Metrology, Brighton, MI, USA). The reconstructed volume was then post-processed using the software VG Studio Max (Version 2.1.3, 64bit, Volume Graphics, Charlotte, NC, USA) and exported as a DICOM image stack for further image analysis. The beam-hardening effect could produce artificially very high attenuation coefficients in the HA tablets' outer layers. To avoid this artifact, measurement of the attenuation coefficient was confined to a central area of 50×50 pixels on the center slice of each HA tablet (Figure 5.1b). A total of 2500 measurements of the attenuation coefficient were extracted from each HA tablet and averaged using the software ImageJ (Version 1.47d, National Institutes of Health (NIH), Bethesda, MD, USA). The averaged attenuation coefficients were then plotted (Figure 5.3a) against the densities of the HA tablets using Microsoft Excel 2010 (Microsoft, Redmond, WA, USA) to establish their relationship.

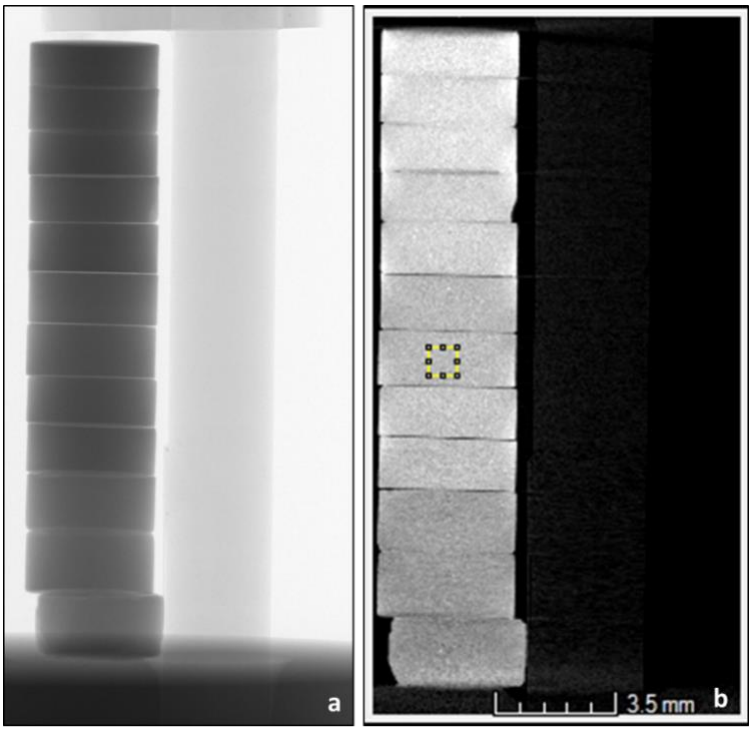

Figure 5.1 a: A microradiograph of the HA tablets. b: The yellow square box of 50×50 pixels was used to measure each tablet's attenuation coefficient.

5.2.3 Construction of the finite element models

A human maxillary first premolar and a second premolar were scanned using the same micro-CT system to obtain their geometry and spatial distribution of the attenuation coefficients. These teeth were extracted from young patients (approximatly 18 years old) who were receiving orthodontic treatment. The teeth were stored in distilled water with 0.1% Thymol before scanning. To allow direct conversion of the attenuation coefficient to the elastic modulus via the mineral density, the same scanning parameters as those for the HA tablets were used, including the number of projections, number of frames per projection, tube voltage and tube current,. The reconstructed volumes of the premolars were post-processed using VG Studio Max. A central slice from the sagittal plane of each tooth (Figure 5.2a) was exported as a DICOM image for the construction of two-dimensional FE models (Figure 5.2b).

The coordinates of the points along the boundaries of each of the materials, including enamel, dentin and pulp, were extracted at 0.2 mm intervals using ImageJ. The coordinates were then imported into the software HyperMesh (Version 11.0, HyperWorks, Altair Engineering, Troy, MI, USA) as nodes for constructing the FE models. To avoid undue singular stresses on the surface nodes from the use of a concentrated point-load, as is often done in most stress analysis, a semicircle of 2-mm radius was used to load the teeth (Figure 5.2b). Each constructed model contained six materials: enamel, dentin, pulp, zirconia for the semicircle, cortical and cancellous bone. Zirconia, which is frequently used to make dental prostheses, was chosen for the loading semi-circle because its high Young's modulus would maximize the contact stresses in the

tooth. The mechanical properties for each material, assumed to behave linear elastically, are listed in Table 5.2. Each material section was meshed with a mixture of quadrilateral and triangular plane-strain elements (CPE4 and CPE3). Four FE models were constructed in total, two for the first premolar (M1U and M1G) and two for the second premolar (M2U and M2G). M1U and M2U were assigned with uniform elastic moduli for the dental tissues, including the enamel and dentin, while M1G and M2G were given a distribution of elastic modulus values for the same tissues based on the spatial distribution of the attenuation coefficient. To allow direct comparison of the results, the elastic moduli of the enamel and dentin used in the models with a uniform distribution was derived from the average values of those in the models with a graded distribution. The other materials were given uniform properties, as listed in Table 5.2. During the first step of stress analysis, the models M1G and M2G were run in parallel with a user-defined material subroutine (UMAT [243]) that assigned elastic modulus values to each element in the enamel and dentin layer according to the distribution of the attenuation coefficient. The formula for converting the attenuation coefficient to the elastic modulus will be described in the Results section.

A uniformly distributed load of 800 N was exerted at the top surface of the semicircle. A rectangular block 14.5 mm high with a 1.5 mm thick top layer were used to represent the surrounding cancellous bone and cortical bone, respectively. All the nodes at the bottom surface of the bone block were fully fixed to serve as the boundary condition. The models, with a uniform out-of-plane thickness of 10 mm, were exported to the FE software ABAQUS (Version 6.10 EF-1, Dassault Syetemes Simulia, Waltham, MA, USA) for stress analysis. Comparisons were then made of the mechanical

performances between those with uniform properties and those with a graded material distribution.

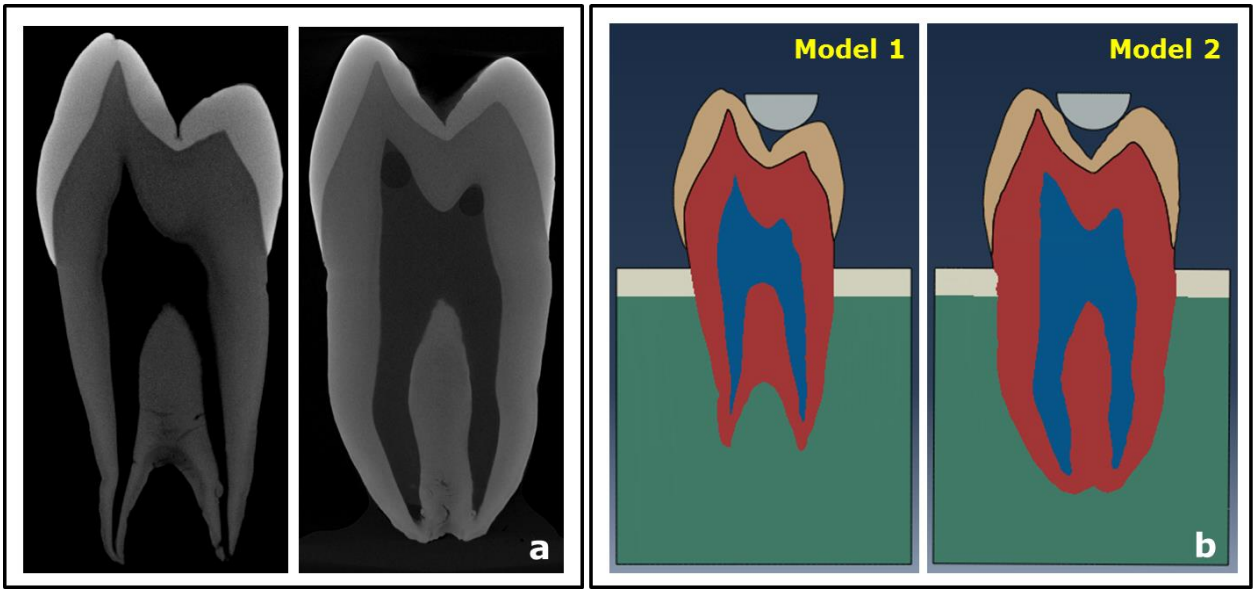

Figure 5.2 a: The DICOM images from the CT scans for FE model construction. b: The FE models constructed from the DICOM images added with a semicircle for loading and a simulated bone block for support. Model 1 is the first premolar and Model 2 is the second premolar.

Table 5.2 Material properties used in the FE models

Material	Elastic modulus (GPa)	Poisson's ratio	Ref.
Cortical bone	13.7	0.3	[193]
Cancellous bone	1.37	0.3	[193]
Pulp	2.07×10^{-3}	0.45	[194]
Zirconia	210	0.3	[244]

5.3 Results

5.3.1 Relationship between HA mineral density and attenuation coefficient

As shown in Table 1, the densities of the twelve intact HA tablets ranged from 0.99 to 1.54 g·cm^{-3}, and the corresponding attenuation coefficients ranged from 109.77 to 175.01 cm^{-1}. Figure 5.3a shows that, within these ranges of values, the attenuation coefficient is linearly related to the HA mineral density (R^2=0.99) with the following relationship:

$$\mu = 115.73\rho - 4.1275 \quad (1)$$

where μ is the attenuation coefficient (cm^{-1}) and ρ is the density (g·cm^{-3}). There is evidence that this linear relationship still holds for higher density values [245].

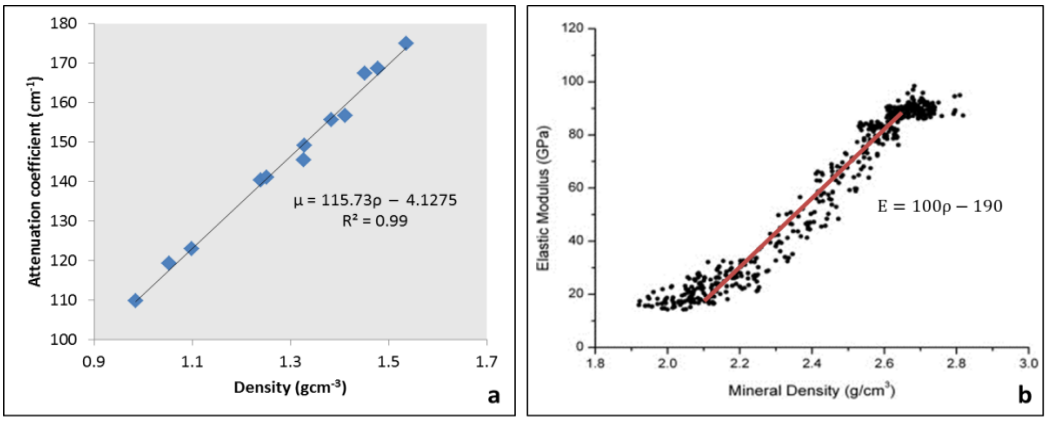

Figure 5.3 a: The relationship between the attenuation coefficient and the density of the HA tablets. b: The relationship between Young's modulus and mineral density [246].

To convert the attenuation coefficients of enamel to the corresponding elastic modulus values, the results from [242] was adopted (Figure 5.3b). The relationship between the elastic modulus and the mineral density of enamel was reported to follow an

S-shaped curve; see Figure 5.3b; however, the mineral densities of enamel measured in the present study lied mainly within the central linear portion. Therefore, a simplified linear relationship, Eq. (2), was used in the present study, where E stands for the elastic modulus (GPa).

$$E = 100\rho - 190 \quad (2)$$

Combining Eqs. (1) and (2) gives the equation used in the user-defined material subroutine for converting the attenuation coefficient into the elastic modulus, i.e.

$$E = 0.86\mu - 186.43 \quad (3)$$

5.3.2 Graded distributions of elastic modulus in the FE models

The histograms and spatial profiles of elastic modulus in the enamel layer for the graded-material models, M1G and M2G, are shown in Figure 5.4a. The same trend, with which the modulus increased from the inner region to the outer region of the enamel layer, was found in both models. For the elements close to the dentin layer, especially those beneath the central fossa, their elastic modulus was generally below 20 GPa. In the outer region, the elastic modulus could be greater than 110 GPa. Compared to Model M2G, Model M1G had a thicker, stiffer shell in its enamel region.

As can be seen from the histograms in Fig. 5.4a, a left-skewed distribution was found for the enamel's elastic modulus values in model M1G, while those for model M2G showed a bell-shaped distribution. Roughly 28% of the elements in M1G had an elastic modulus greater than 90 GPa, while most of the elements (67%) in M2G had a lower elastic modulus, ranging from 40~80 GPa. In the dentin layer, a lower elastic modulus could be found in the region surrounding the pulp chamber as well as the bifurcation area (Figure 5.4b). In general, the first premolar (Model 1) showed a higher mean elastic modulus than the second premolar (Model 2) in both the enamel layer (71.3 GPa vs. 65.9 GPa) and the dentin layer (17.2 GPa vs. 11.5 GPa).

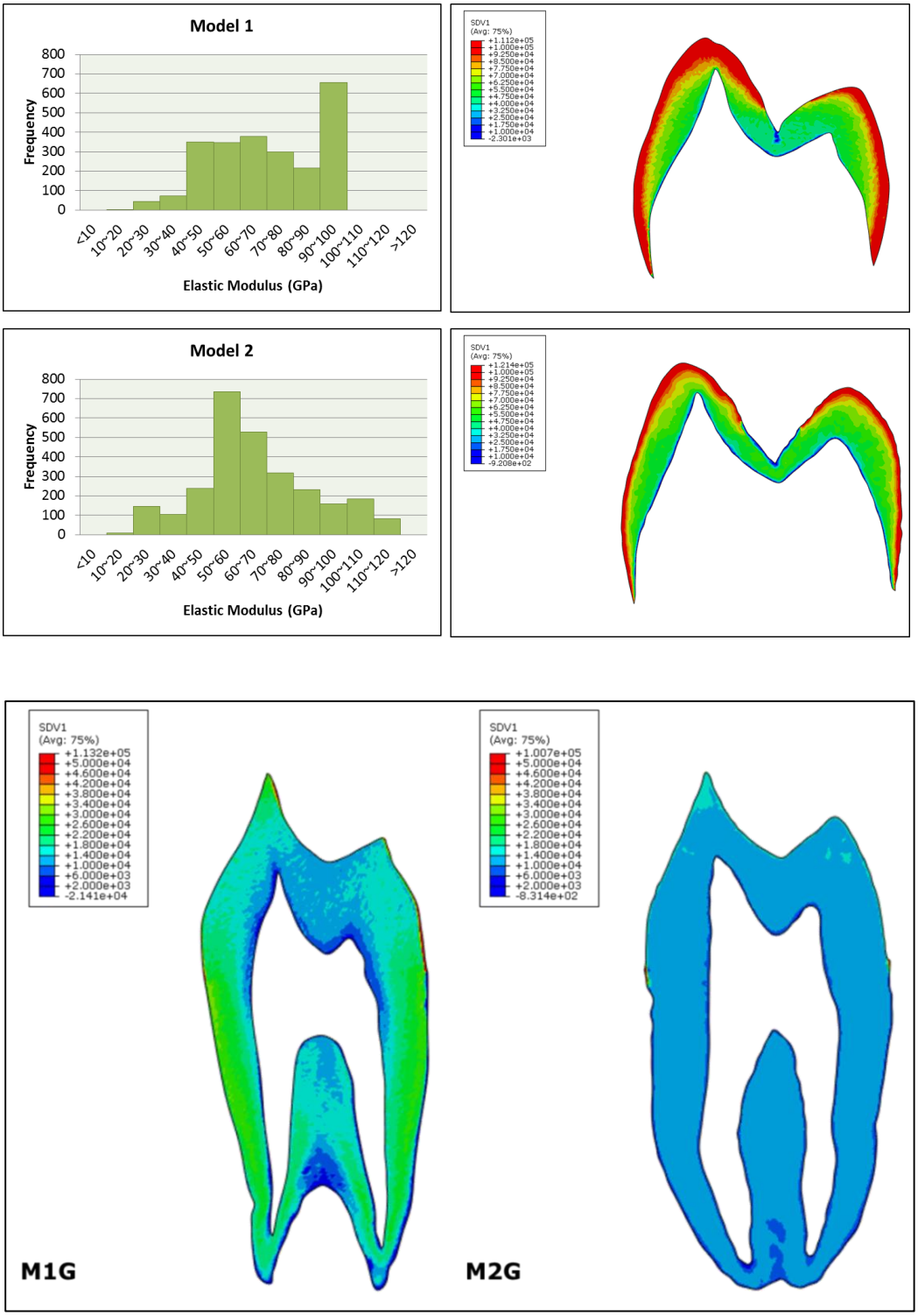

Figure 5.4 a: The histograms and profiles of elastic modulus in the enamel layer for the graded-material FE models M1G and M2G. b: The profiles of elastic modulus in the dentin layer for both graded-material FE models.

5.3.3 Stress analysis

Due to the way the load was applied in the stress analysis, the central fossa was expected to be the region of the highest stress concentration. Thus, the stress value at the deepest point of the central fossa was used for comparison between the models. The maximum principal stress decreased from 131.8 MPa in model M1U to 84.2 MPa in model M1G, and from 491.1 MPa in model M2U to 213.5 MPa in model M2G (Figure 5.5). Thus, with a graded distribution of elastic modulus, the highest maximum principal stress was reduced by 36% and 57% in the first and second premolar, respectively. In the first premolar, the total elastic strain energy within the enamel was 331.2 and 349.9 mJ in the model M1U and model M1G, respectively. In the second premolar, the total strain energy within the enamel was 1189.9 mJ in the model M2U and 1212.9 mJ in the model M2G. The models had a similar level of elastic strain energy stored in their enamel layers, irrespective of the material layout.

The values of the maximum principal stress in both the enamel and dentin along the DEJ from the buccal side to the lingual side were plotted in Figure 5.6. In general, the stress values were lower in the first premolar. On the enamel side, the results showed that the models with a constant elastic modulus for the dental tissues, i.e. M1U and M2U, had higher stresses, with two prominent stress peaks around the dentin horns. In contrast, the models with a graded material distribution had a more uniform stress distribution along the DEJ and lower stress values in the regions near the dentine horns. Relatively high stresses could still be found around the buccal dentine horn in the M1G model. On the dentin side, no significant difference in the stress values was found between the models

with a uniform enamel layer and those with a graded one. The same was found for the normal and shear stresses along the DEJ, which are plotted in Figure 5.7 from the buccal side to the lingual side.

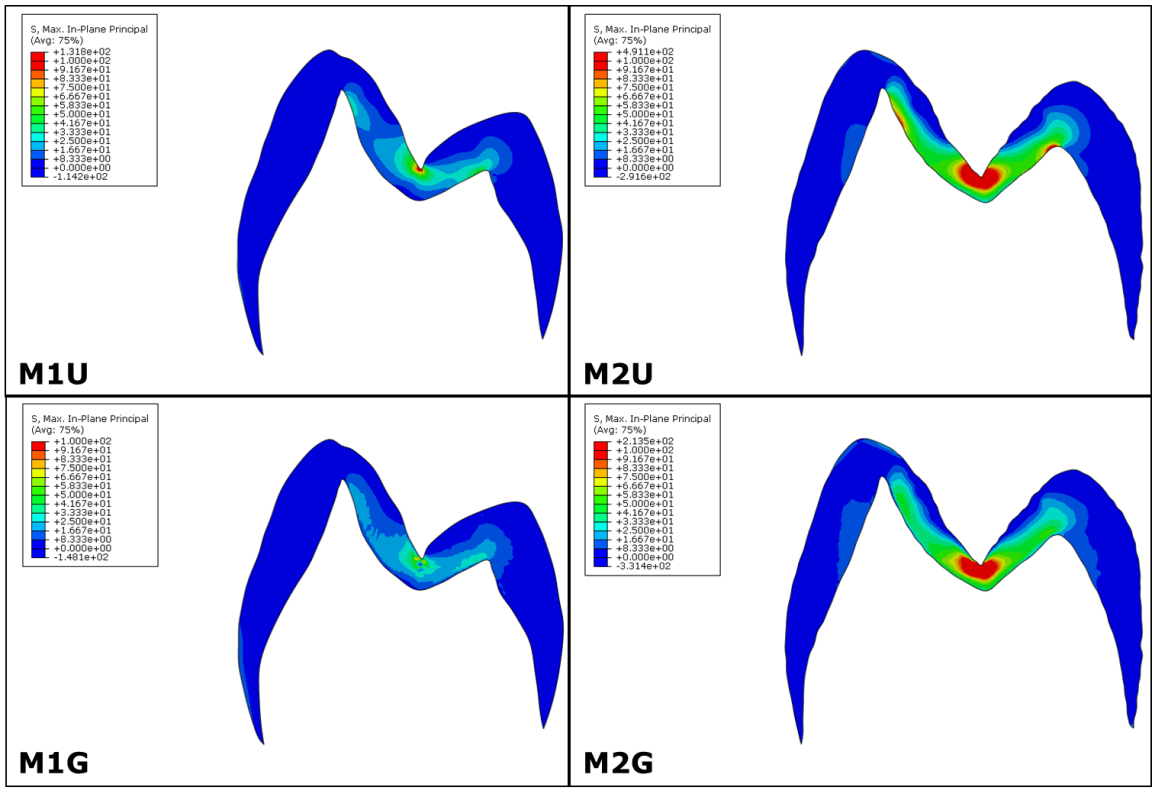

Figure 5.5 Contour plots of the maximum principal stress in the enamel layer for the four models.

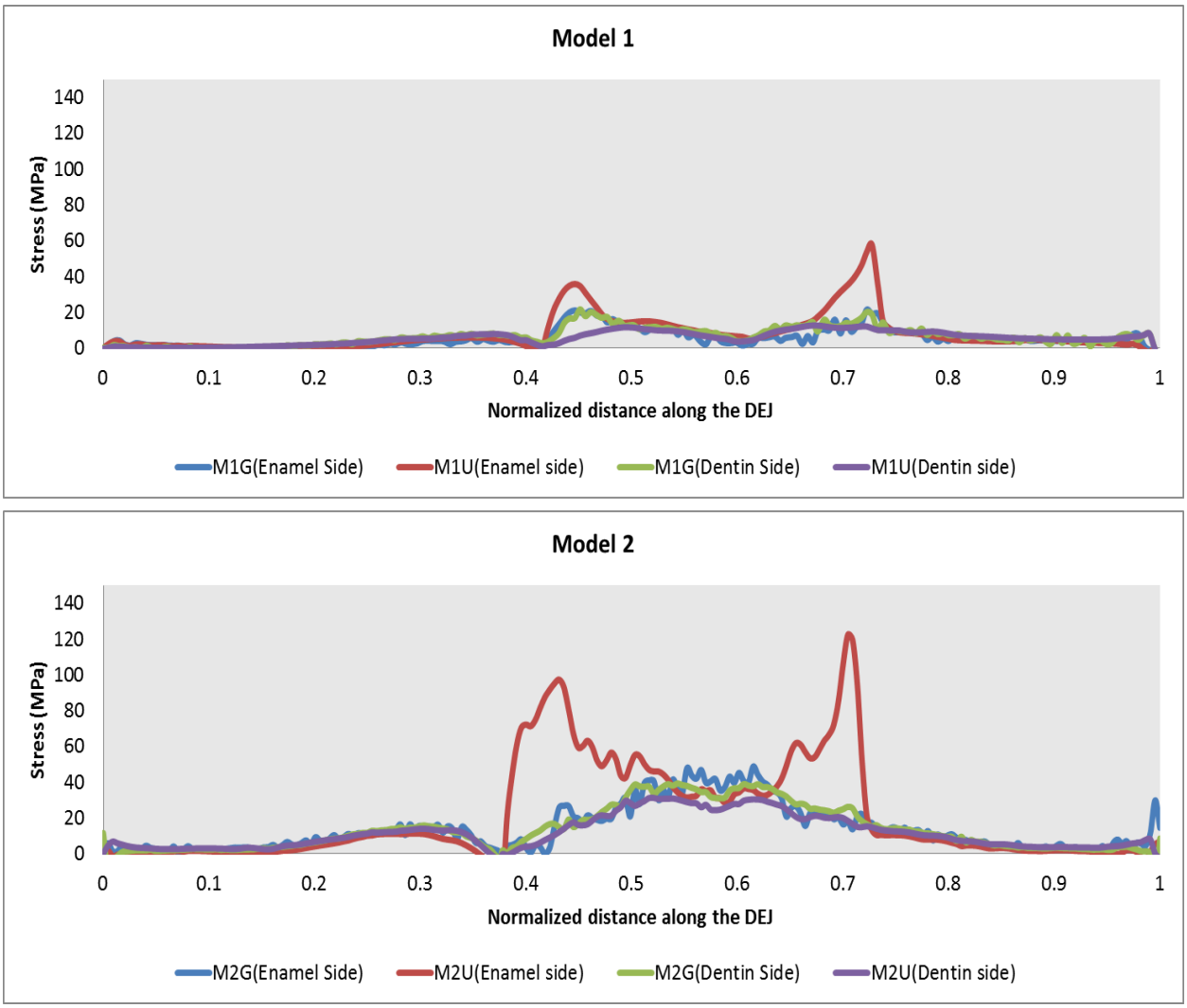

Figure 5.6 Profiles of the maximum principal stress in the enamel and dentin along the DEJ. Model 1 is the first premolar and Model 2 is the second premolar.

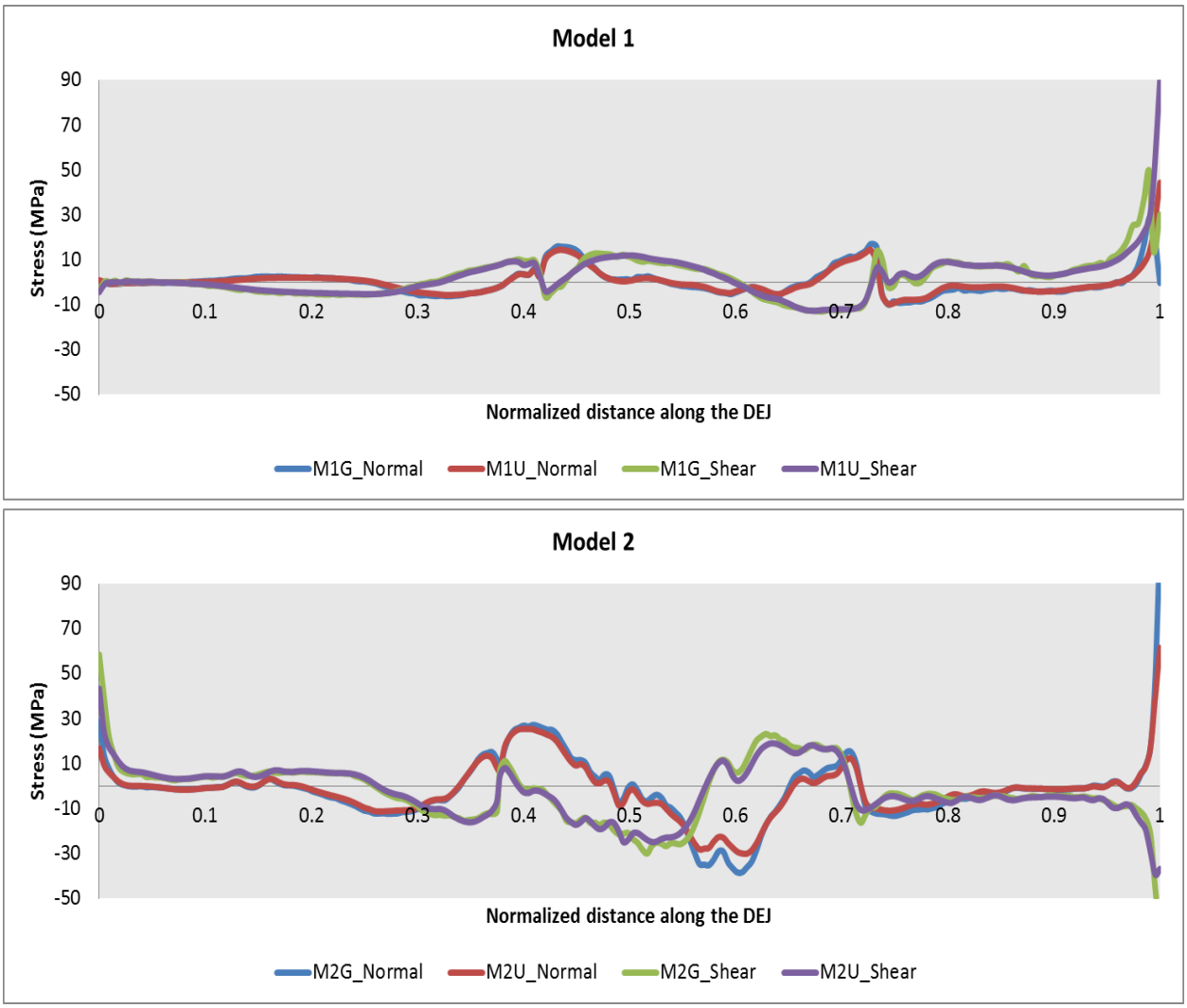

Figure 5.7 The normal and shear stresses at the dentin-enamel interface. Model 1 is the first premolar and Model 2 is the second premolar.

5.3.4 The relationship between the elastic modulus and the maximum principal stress

The elastic modulus and the value of the maximum principal stress at the centroid of each element were extracted and plotted against each other as a scatter plot (Figure 5.8). The results confirmed that the models with a graded material distribution in the enamel provided a more uniform and lower stress distribution. However, the elements located near the central fossa had higher stresses, despite their lower modulus; see also Figure 5.5.

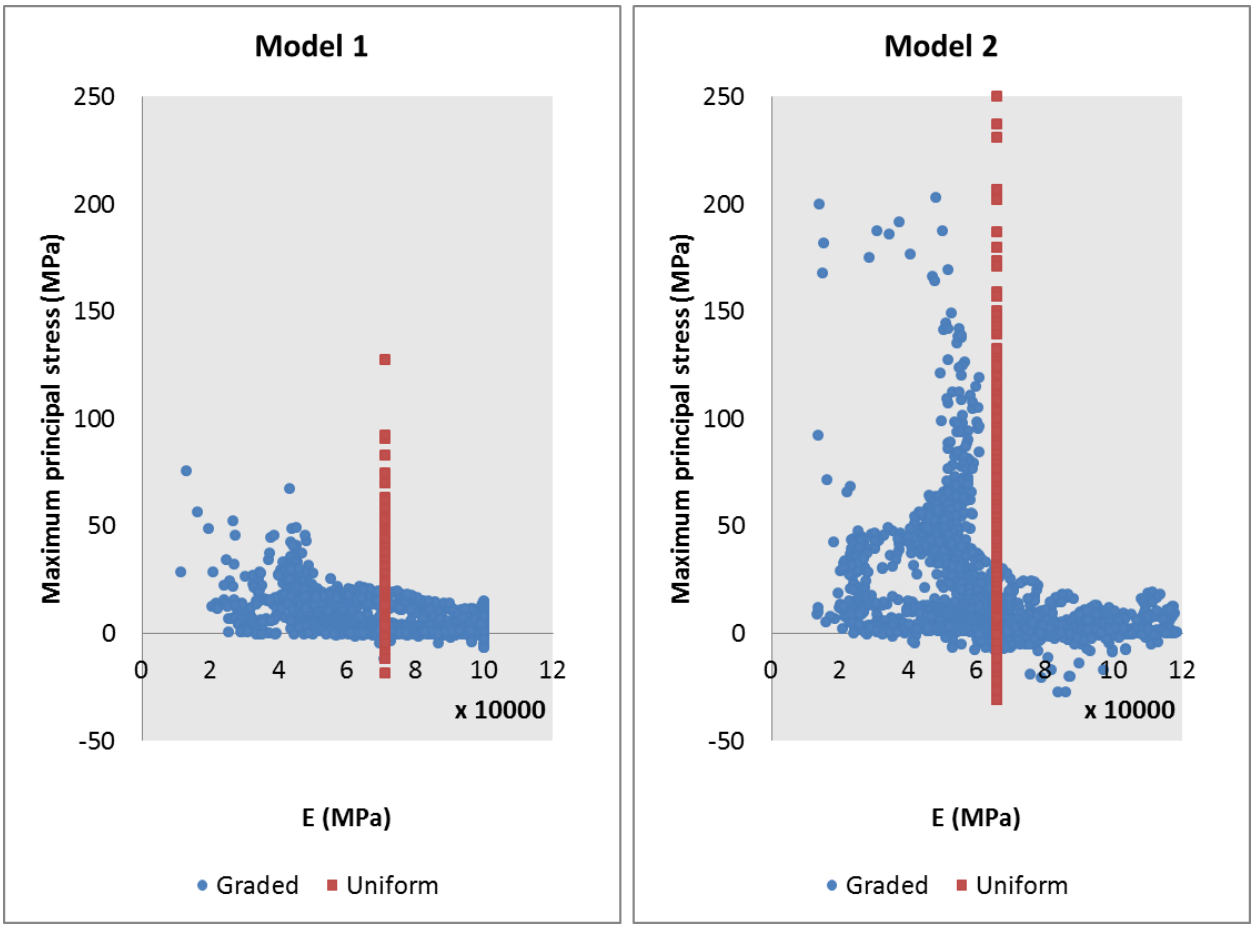

Figure 5.8 Scatter plot of the elastic modulus against the maximum principal stress at the centroid of each element.

5.4 Discussion

In most of the dental literature on the biomechanical analysis of tooth structures, the graded material distribution in the biological tissues was not considered. The present study represented the first attempt at analyzing the effect of modeling the dental tissues with a distributed material layout, as found by nanoindentation [232-238, 240], on the stress distribution in human teeth. To accurately incorporate the graded material distribution in nature into the numerical models constructed from micro-CT images, a relationship between the attenuation coefficient and elastic modulus was established. The relationship between the attenuation coefficient and the mineral density was first derived based on the CT scans of the HA tablets. The attenuation coefficient was then linked directly to the elastic modulus using a relationship between the elastic modulus and the mineral density of enamel established by others through indentation [242].

The highest density of the HA tablets used in the present study was 1.5 $g \cdot cm^{-3}$, which is much lower than the average value of 2.49 $g \cdot cm^{-3}$ for enamel . Several tablets with a higher density were fabricated; however, because of existing internal cracks they were excluded from the study. The density of enamel was obtained by extrapolation from the measurements of the remaining HA tablets. The estimated densities for these enamel specimens were comparable to those reported in other studies (2.6 - 3.0 $g \cdot cm^{-3}$) using either radiographic analysis [247-250] or direct measurement [251, 252] .

Micro-CT was used in the present study to determine the attenuation coefficient of enamel and to capture the geometry of teeth for FE modeling. Compared with Micro-CT, traditional dental radiography can only generate 2-D radiographic images that are

projections of all the structural features within the object being scanned; therefore, they cannot provide an accurate spatial distribution of the attenuation coefficient. There are two major advantages for using Micro-CT to obtain the images required for FE modeling: it provides precise measurement of the attenuation coefficient for deriving the material property, and it resolves details as small as a few microns in size. With a voxel size of 14.6 μm, the spatial resolution of the CT images used in the present study accurately captured the geometry and the distribution of the elastic modulus of the teeth analyzed.

Results from the stress analysis strongly support our hypothesis that the graded material distribution often found in nature was developed to minimize the stresses in natural structures, such as teeth, by distributing the load more evenly. Notably, the two stress peaks near the buccal and lingual dentin horns were significantly lowered in magnitude by the introduction of a graded material layout to the enamel layer. And, this was achieved by storing approximately the same amount of elastic strain energy with the same amount of mineral content in the enamel – the models had the same average elastic modulus, and therefore, the same average mineral density. The reduction of the stress peak at the central fossa, where cracks usually initiate, helps explain why vertical tooth fracture does not happen more often, as would be the case if the stresses predicted by the models with a uniform elastic modulus for enamel were true. Evidence exits that show that a graded material layout can promote crack arrest [253, 254].

The interfacial normal and shear stresses at the DEJ were not significantly affected by the presence of a graded material distribution. This may be because, despite the graded distribution, the average elastic modulus of the enamel was still much higher

than that of the dentin. Therefore, as far as the DEJ was concerned, the enamel layer behaved as a very stiff layer, irrespective of its degree of heterogeneity.

While the current results (Figures 5.5, 5.6 and 5.8) showed that, overall, the graded material distribution promoted a more uniform stress distribution within human teeth, high stresses still existed in the elements surrounding the central fossa, despite their lower elastic modulus. This was attributed to the fact that the FE models used in this study did not fully capture the detailed anatomy of the pits and fissures in the fossa. A closer view of a fossa captured by Micro-CT (Figure 5.9a) showed that the fissure had the shape of a long rounded notch, a geometry well known in mechanics that can help reduce stress concentration. To further investigate this effect, we constructed two FE models of a central fossa with and without a deep fissure. Under the same loading and boundary conditions, the results showed that with a deep fissure in the central fossa, the maximum principal stress was reduced by 30% (Figure 5.9b). This feature of the human teeth can be considered as another example of shape optimization that has taken place in nature.

Although only 2-D FE models were used in the present study, they were considered to be adequate for answering the question posed; that is whether a graded material distribution would produce a more uniform stress distribution with lower stress concentrations in a human tooth. While 3-D models are more representative anatomically, they are more expensive computationally to construct and analyzed, and yet they often do not provide more useful or fundamentally different information than the simpler, 2-D models [255].

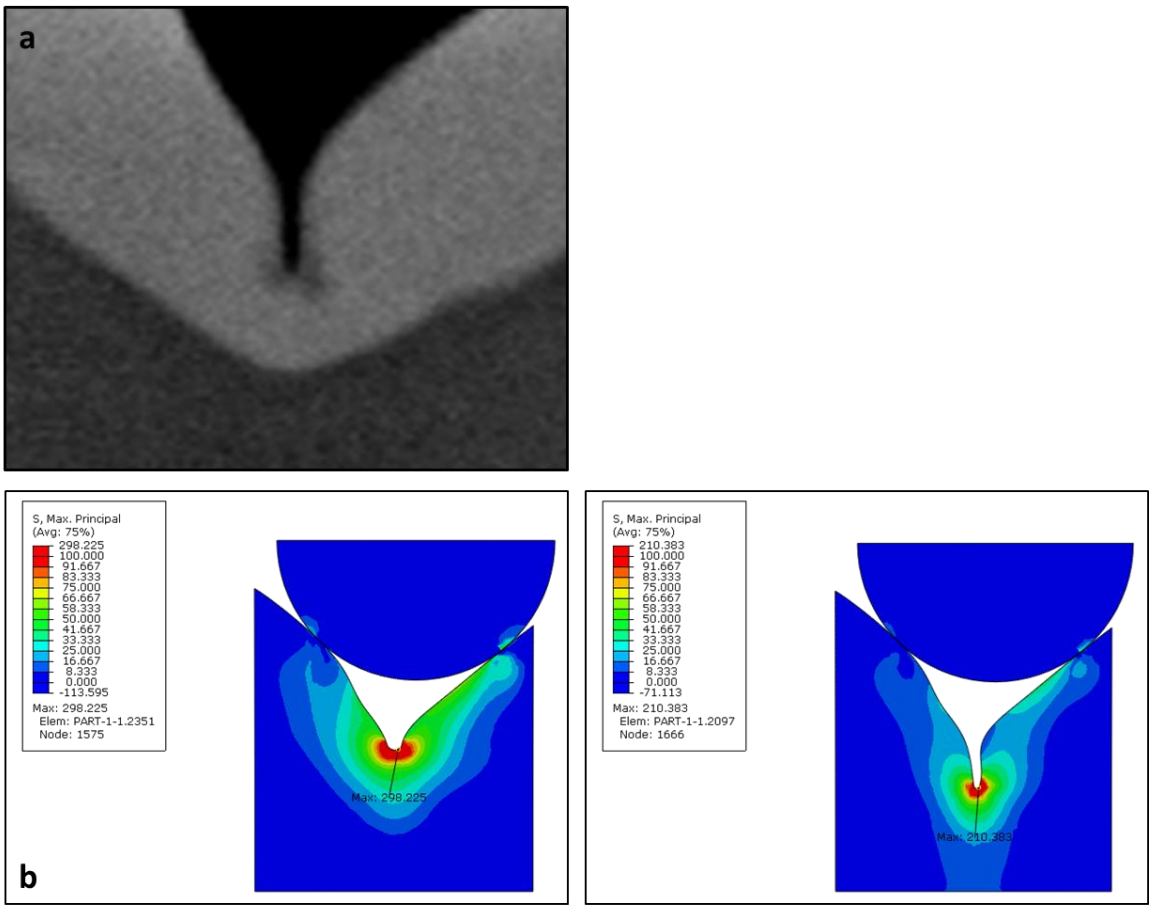

Figure 5.9 a: A closer view of the central fossa b: The FE results showed that a deep fissure in the central fossa can effectively reduce the maximum principal stress concentration.

A graded material distribution was also applied to the dentin layer in the present study using Eq. 3, despite the fact that the linear relationship between the attenuation coefficient and mineral density was derived from pure HA tablets with no organic contents. Unlike enamel, which consists of 96% mineral, dentin is composed of 20% organic matrix, 10% water and only 70% mineral [256]. The atomic weights of Calcium and Phosphate in the HA crystals are much greater than that of Carbon, Hydrogen and Oxygen in the organic tissues and water. It is the mineral content, the heaviest and most

abundant component that determines dentin's attenuation coefficient. As a result, it was decided that Eq. (3), which was derived from pure HA tablets, can be applied without corrections for the organic matrix and water content for converting the attenuation coefficient of dentin into the corresponding elastic modulus. The results showed that the distribution of elastic modulus in the dentin followed a similar trend to that in enamel, where the outer dentin was harder than the inner dentin, as found in previous studies [143, 247, 250].

While the present study has shown the importance of mineral distribution on the mechanical performances of a tooth, the significance of the organic components and the microstructures should not be neglected. As mentioned previously, the mechanical performances of mineralized biological tissues are usually better than their synthetic counterparts made of the same constituent materials. This is because the organic component, usually collagen protein, greatly improves the tissue's toughness [257]. In addition, the spatial arrangement of the enamel rods makes enamel behave anisotropically. Studies using nanoindentation tests at different spots with different enamel rod alignments indicated that the mechanical properties are fundamentally altered by the rod orientation and their topological distribution [145, 233, 258, 259]. The friction and wear of human teeth also vary significantly depending on the orientation of the enamel rods, which in turns depend on the topological area of the tooth [151]. A lower coefficient of friction and higher wear resistance was found in the occlusal region [151]. This phenomenon can also be observed in dentin, where the friction and wear behavior are also determined by the orientation of the dentinal tubule [260]. Several studies have attempted to numerically simulate the hierarchical structure of the enamel [154, 261-265].

The results from these studies have indicated that the crystal orientation within each rod and the rod arrangement within the enamel have been optimized for greater load capacity, wear resistance, and fracture strength.

5.5 Conclusion

The results from this study support the hypothesis that the material layout in human enamel is optimized for distributing the external load evenly. To predict more accurately the stresses in tooth structures, their natural, graded material layout must be taken into account in any future FE study. Otherwise, the maximum stress will probably be over-predicted, and the stress distribution will be less uniform than the actual one.

Chapter 6 Deriving a new material layout for all-ceramic dental crowns based on the graded material distribution of natural teeth

6.1 Background

Based on the statistical data from the most recent National Health and Nutrition Examination Survey (NHANES), 1999-2004, the mean number of missing permanent teeth among adults 20 to 64 years of age is 2.52 [11]. This means that there are more than 475 million missing teeth in the adult population that need to be replaced to raise the overall oral health status in the United States. The fabrication and placement of dental crowns and other prostheses form a major part of the rehabilitation process. In the United States, more than 15 million dental crowns are fabricated every year [266]. In addition to the restoration of damaged natural teeth, dental implants that replace missing teeth also require crown restorations. According to an estimate by the dental implant manufacturer STRAUMANN [267], approximately 1-2 million dental implants are placed in the United States every year. The demand for dental implants is still growing steadily, and it is believed that the number of dental implants inserted annually will double by 2020 [267]. The demand for dental crowns and other related prostheses is, therefore, expected to increase steadily.

The first materials used for fabricating dental prostheseswere metal alloys. Their castability makes it possible to reproduce the complicated tooth contour and to obtain marginal fit with high precision. Due to increasing esthetic demands, dental prostheses have evolved into layered structures such as resin-bonded-to-metal (RBM) or porcelain-fused-to-metal (PFM) constructions since the 1950s. Various metal alloy systems are

used in the RBM or PFM crowns or bridges as the core to ensure structural rigidity. To better mimic the tooth appearance, zirconia, which has a color close to teeth and also holds excellent mechanical strength, has been considered as a core material since the 1990s.

Current designs of layered dental crowns have the exact opposite layout of that of natural enamel. They use a harder material, e.g. metal or zirconia, for the substructure and a softer esthetic material, e.g. feldspar ceramic, for the veneer. It is believed that the entire structure's rigidity and strength should come from a stiff and strong core, similar to the steel reinforcement in concrete for construction. In practice, however, all these layered dental restorations, including RBM, PFM or zirconia-ceramic, share a common pitfall in that the softer outer layers of conventional dental crowns are usually weak and vulnerable to chipping, flaking or delamination. Like ceramics, hydroxylapatite is vulnerable to fracture by tensile stresses. In addressing the problem of veneer chipping, most recent researchers have concentrated only on improving the veneering porcelain [268-270], veneering technique [268-275], core material [268, 276], core design [271, 275] or fabrication protocol [111, 271].

In the past two decades, evidence of regular spatial variations of material properties, such as the elastic modulus or hardness, within the tooth tissues has been established by using various indentation techniques [145, 233, 277, 278]. The mechanical properties of human enamel show a gradient such that the outer enamel is the hardest and its stiffness gradually reduces towards the dentin (Figure 6.1). Moreover, the elastic modulus and hardness of the outer enamel are higher at the cusps than at the axial

surfaces [277]. It has also been found that the functional cusp has a stiffer and thicker outer enamel layer than the non-functional cusp [233]. Such a graded material distribution is also found in many other biological structures, e.g., shells, anthropod exoskeletons, antlers, and bird beaks [279]. This functionally graded material distribution within the enamel is attributed to gradual changes in the mineral density and the enamel rods' orientation. Kodaka and his colleagues [280] have found that the hardness of the human enamel is highly correlated to its mineral content. It is also known that each percentage change in the volumetric concentration of hydroxyapatite can account for a 3-GPa increase of the elastic modulus [281]. Studies using nanoindentation performed at different positions with different enamel rod orientations indicated that the mechanical properties are fundamentally altered by the rod orientation [145, 233, 258, 259].

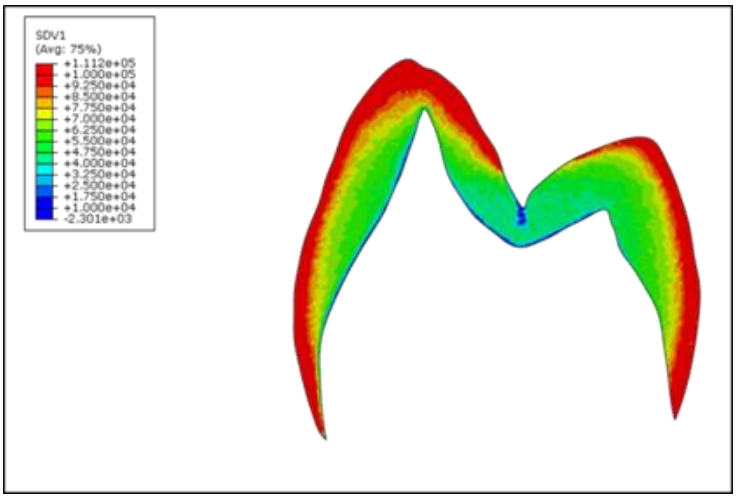

Figure 6.1 Distribution of elastic modulus in human enamel. For more details, refer to Chapter 5.

In Chapter 5, it was demonstrated using the FE method that the structural stress distribution in human teeth was altered by the presence of a graded material distribution.

The results showed that, with a graded material layout, the peak maximum principal stress in the enamel was reduced by about 50%, and the overall stress distribution was more uniform. Along the dentino-enamel junction, two stress peaks were found near the dentine horns; however, they were much lower in magnitude in the models with a graded material distribution. The results from this study support the hypothesis that the material layout in human enamel is optimized for distributing the external load evenly.

The material layout of natural teeth has never been suggested as a blueprint for designing and fabricating the dental crown. Although the fracture strength of hydroxylapatite is lower than some of the ceramics used for making dental crowns, natural teeth do not chip or fracture easily. In view of this and the results from Chapter 5, the graded material distribution of enamel should be applied for the design of crowns made of ceramics.

This project was a first attempt at seeking a suitable material layout for layered all-ceramic restoration based on the functionally graded material distribution found in natural enamel. Although a graded distribution has previously been proposed for fabricating ceramic-based dental crowns, it is still based on the conventional design of a hard substructure covered with a softer veneer [282]. Several multilayer crown designs based on the enamel layout with different material properties assigned to the different layers were considered by subjecting them to simulated occlusal loads. To avoid the need for creating new materials, three ceramic materials available in the market were selected and used in this study. The FE method was again used for performing the stress analysis and computing the safety factor for each candidate design.

6.2 Methods

A two-dimensional FE model was constructed from the computed tomography images of a human mandibular molar restored with a dental crown using the software HyperMesh (Version 11.0, HyperWorks, Altair Engineering, Troy, MI, USA). Previous studies and the work presented in Chapter 5 have shown that enamel has a distributed material layout, which is optimized for distributing the occlusal load. To mimic this natural material layout, the crown was divided into nine layers in the model (Figure 6.2). Different material properties were assigned to the different layers to achieve a graded distribution. Three clinically available ceramic materials of different elastic moduli were used for the present study: IPS e.max® (Ivoclar vivadent, Amherst, NY, USA), VITAVM® 9 (VITA Zahnfabrik, Germany) and VITABLOCS® Mark II (VITA Zahnfabrik, Germany). IPS e.max® is made of lithium disilicate, and it has the highest elastic modulus of 95 GPa among the three materials. VITAVM® 9 and VITABLOCS® Mark II are both feldspar ceramics, and their elastic moduli are 65 GPa and 40 GPa, respectively. The aim was to obtain proper thickness ratios between the different material layers that can best distribute the occlusal load.

The materials were assigned to the layers using the following principle inspired by nature: the exterior materials must be stiffer than the interior materials. i.e., IPS e.max® always formed the outermost layer and VITABLOCS® Mark II the innermost layer if any of these materials participated in the structure. In this manner, fifty-five models of different thickness ratios were generated and the composition of each material layout is listed in Table 6.1 and illustrated in Figure 6.3. The elastic moduli of the

ceramic materials used in the model were adopted from the manufacturers' data sheets, and a Poisson's ratio of 0.3 was assumed for all of them. The mechanical properties for the materials, all assumed to behave linear elastically, are listed in Table 6.2.

To simulate the loading on the cusps during chewing, a semicircle of 2-mm radius was used to load the tooth and its material properties were set the same as those of human enamel. A uniformly distributed load of 800 N was exerted at the top surface of the semicircle. Each section of the model was meshed with a mixture of triangular and quadrilateral plane-strain elements (CPE3 and CPE4 [190]). The mesh within the crown was much finer than those in the other regions. A rectangular block 13.5 mm high with a 1.5 mm thick top layerwas used to represent the surrounding cancellous bone and cortical bone, respectively. All the nodes at the bottom surface of the bone block were fully fixed to serve as the boundary condition. The models, with a uniform out-of-plane thickness of 10 mm, were exported to the FE software ABAQUS (Version 6.10 EF-1, Dassault Syetemes Simulia, Waltham, MA, USA) for stress analysis.

The mechanical performance of the crown with each material layout was evaluated by considering the safety factor within each ceramic layer. The safety factor is a ratio of the material strength to the peak maximum principal stress within each ceramic layer. The material strengths used in the present study were the biaxial flexural strengths (ISO 6872:2008) provided by the manufacturers. The flexural strengths for IPS e.max®, VITAVM® 9 and VITABLOCS® Mark II are 375, 100 and 150 MPa, respectively [216, 283, 284].

For comparison, stress analysis was also performed for a crown with the conventional design, which uses a zirconia substructure and a porcelain veneer.

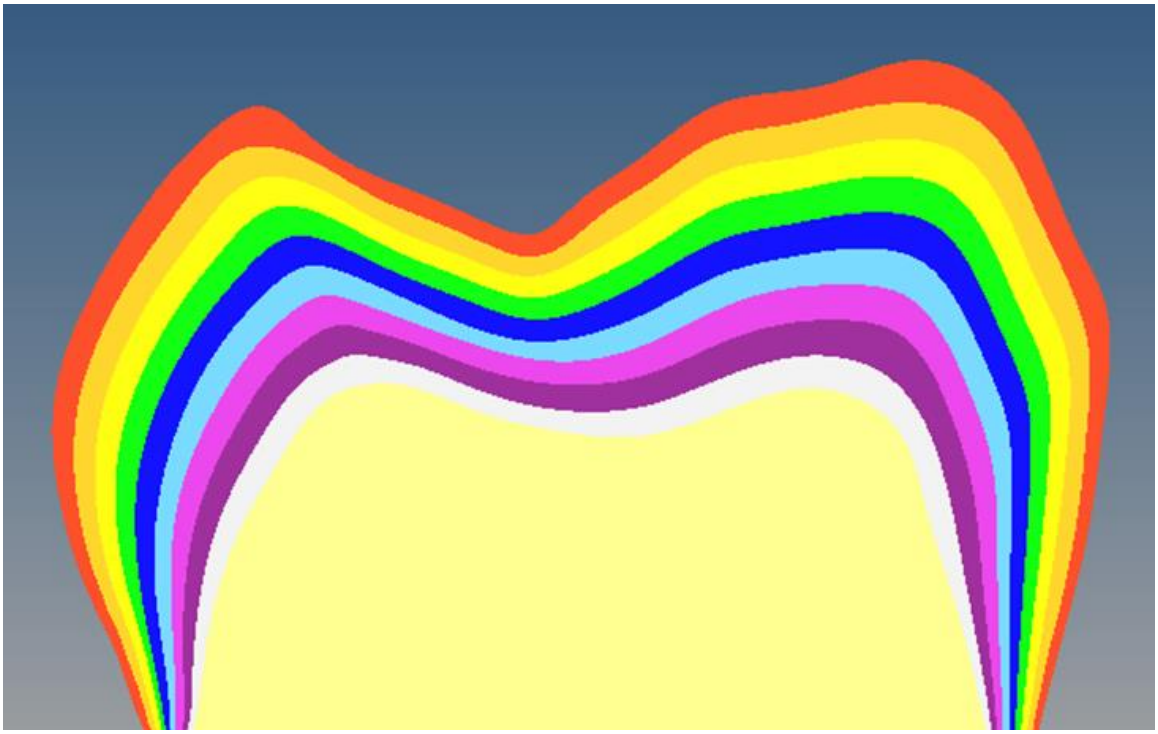

Figure 6.2 The nine-layered ceramic crown model.

Table 6.1 The composition of each material layout. The entries indicate the number of layers occupied by each material.

NO.	IPS e.max®	VITAVM® 9	VITABLOCS® Mark II	NO.	IPS e.max®	VITAVM® 9	VITABLOCS® Mark II
1	9	0	0	**29**	2	7	0
2	8	1	0	**30**	2	6	1
3	8	0	1	**31**	2	5	2
4	7	2	0	**32**	2	4	3
5	7	1	1	**33**	2	3	4
6	7	0	2	**34**	2	2	5
7	6	3	0	**35**	2	1	6
8	6	2	1	**36**	2	0	7
9	6	1	2	**37**	1	8	0
10	6	0	3	**38**	1	7	1
11	5	4	0	**39**	1	6	2
12	5	3	1	**40**	1	5	3
13	5	2	2	**41**	1	4	4
14	5	1	3	**42**	1	3	5
15	5	0	4	**43**	1	2	6
16	4	5	0	**44**	1	1	7
17	4	4	1	**45**	1	0	8
18	4	3	2	**46**	0	9	0
19	4	2	3	**47**	0	8	1
20	4	1	4	**48**	0	7	2
21	4	0	5	**49**	0	6	3
22	3	6	0	**50**	0	5	4
23	3	5	1	**51**	0	4	5
24	3	4	2	**52**	0	3	6
25	3	3	3	**53**	0	2	7
26	3	2	4	**54**	0	1	8
27	3	1	5	**55**	0	0	9
28	3	0	6				

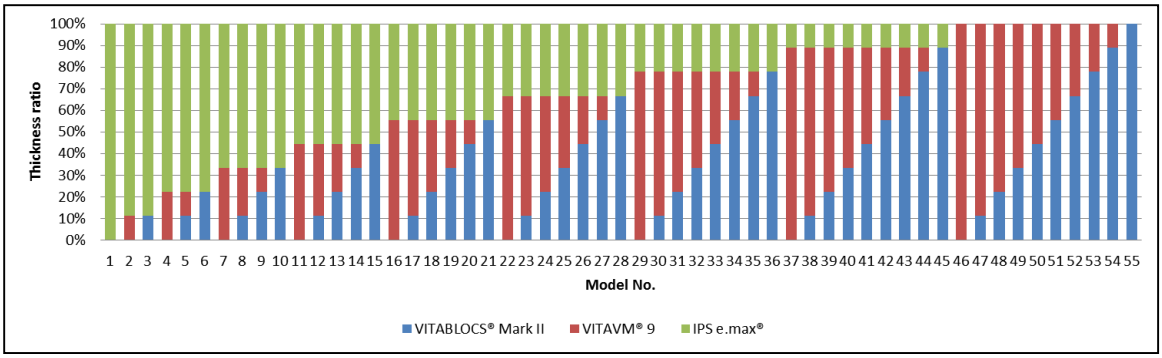

Figure 6.3 The percentage thickness of the three ceramic materials in each model.

Table 6.2 The material properties used in the models

Material	Elastic modulus (GPa)	Poisson's ratio	Ref.
IPS e.max®	95	0.3*	[216]
VITAVM® 9	65	0.3*	[283]
VITABLOCS® Mark II	40	0.3*	[284]
Enamel	84.1	0.3	[191]
Dentin	18.6	0.31	[192]
Cortical bone	13.7	0.3	[193]
Cancellous bone	1.37	0.3	[193]
Pulp	2.07×10^{-3}	0.45	[194]

6.3 Results

6.3.1 Stress analysis

The peak maximum principal stress in each material was lowest when all three materials were present in the crown (Figure 6.4). This is most obvious with the peak stress in IPS e.max®, which always exhibited a jump in value when VITAVM® 9 was absent. The stresses in all three materials were lowest with Model no. 32, which had thickness ratios of 2/9, 4/9, and 3/9 for IPS e.max®, VITAVM® 9 and VITABLOCS® Mark II, respectively. The corresponding peak maximum principal stresses in these materials were 22.06 MPa, 18.00 MPa and 16.66 MPa.

If only IPS e.max® (Model no. 1) or VITAVM® 9 (Model no. 46) was used in the crown, high stress concentration was found at the bottom of the crown, and the peak maximum principal stress were 41.51 MPa and 29.57 MPa, respectively. With only VITABLOCS® Mark II used, the highest maximum principal stress of 18.15 MPa was found at the central fossa (Model no. 55), See Figure 6.5.

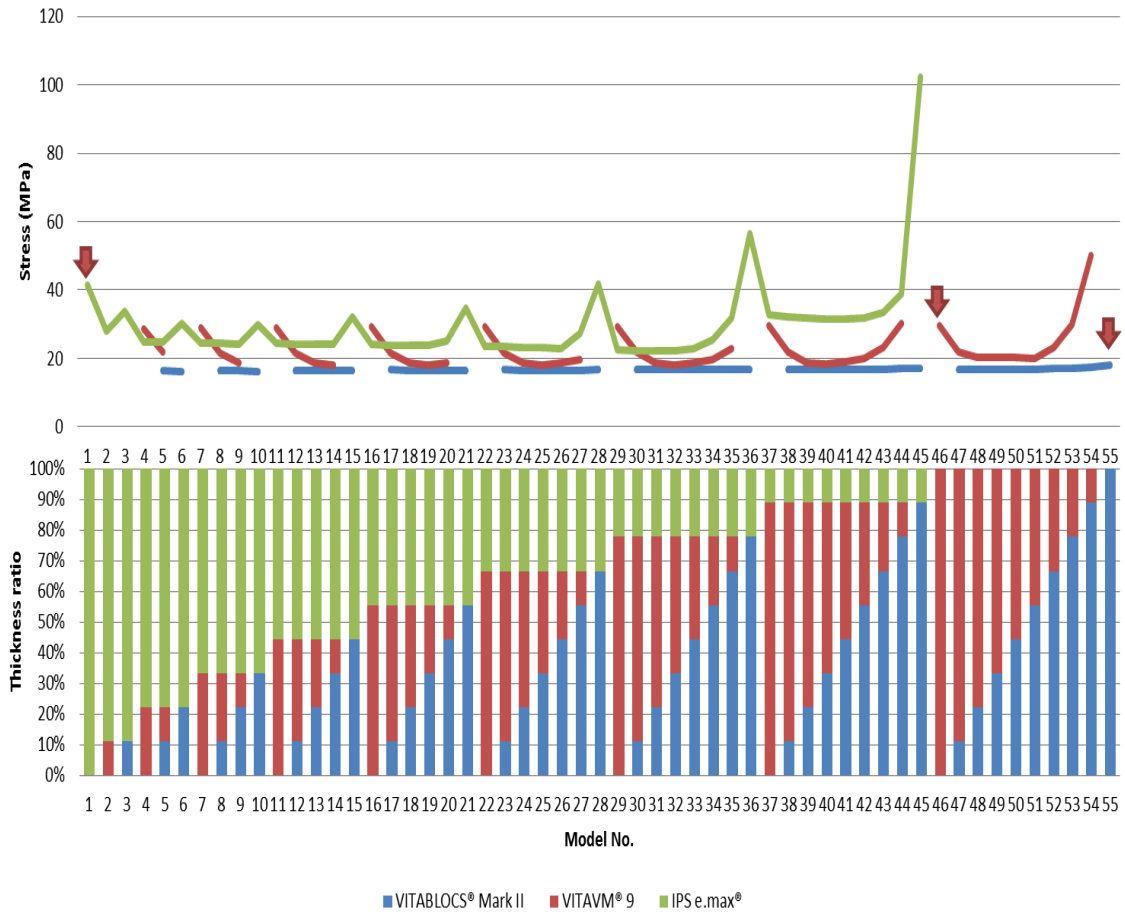

Figure 6.4 The peak maximum principal stress in each material for the 55 layouts. Red arrows indicate the values of the peak maximum principal stress in models which only contain one material.

With a combination of IPS e.max® and VITABLOCS® Mark II only, the highest maximum principal stress was found at the bottom of the outer layer of IPS e.max®. The peak maximum principal stress within IPS e.max® first reduced slightly with reducing thickness then increased sharply with further reduction in its thickness (Figure 6.5). The model with the thinnest (1/9 of the total thickness) IPS e.max® outer layer, no. 45, had the highest maximum principal stress of 102.13 MPa, while that with a 6/9 of the total thickness (model no. 10) had the lowest stress value of 29.90 MPa. The peak maximum

principal stress within VITABLOCS® Mark II remained roughly constant at about 16 MPa.

With a combination of IPS e.max® and VITAVM ® 9 only, the peak maximum principal stress remained approximately constant at about 30 MPa (Figure 6.6). The highest stress was always found at the bottom of the inner layer of VITAVM® 9, except Model no. 37, which had the thinnest (1/9 of the total thickness) IPS e.max® outer layer. In this case, the highest maximum principal stress of 32.69 MPa was found within the IPS e.max® layer.

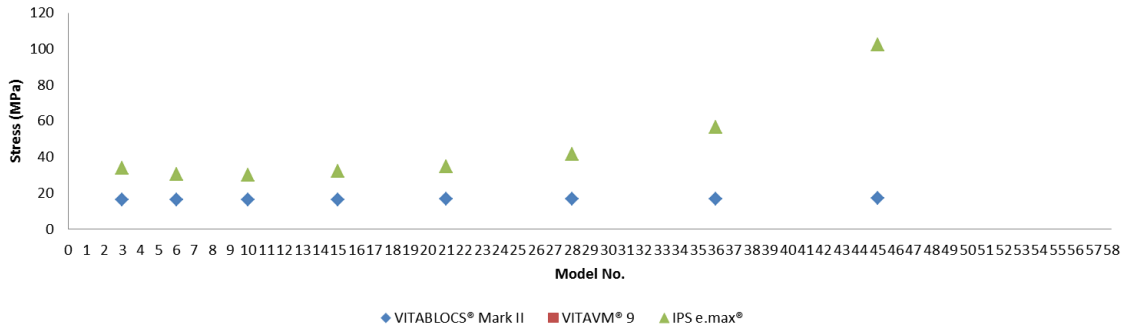

Figure 6.5 The peak maximum principal stress within each layer of the models made of IPS e.max® and VITABLOCS® Mark II only.

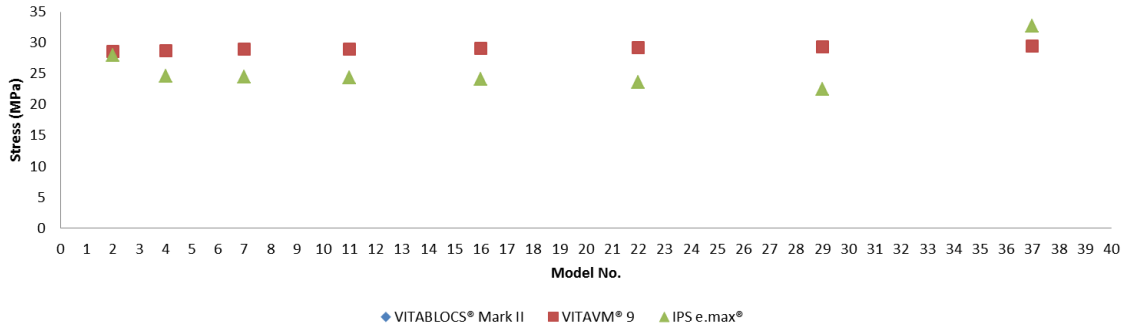

Figure 6.6 The peak maximum principal stress within each layer of the models made of IPS e.max® and VITAVM® 9 only.

With a combination of VITAVM® 9 and VITABLOCS® Mark II only, the peak maximum principal stress within the layer of VITABLOCS® Mark II again remained approximately constant at 16 MPa, irrespective of its thickness. The peak maximum principal stress within the layer of VITAVM® 9 increased as its thickness decreased (Figure 6.7). The model with the thinnest (1/9 of the total thickness) VITAVM® 9 outer layer, no. 54, had the highest maximum principal stress of 50.09 MPa. For the crowns with a thicker VITAVM® 9 layer of 7/9, 6/9 and 5/9 of the total thickness (models no. 48, 49 and 50), the peak stress was found around the contact area. For the other models, it was found at the bottom of the innermost layer of VITABLOCS® Mark II.

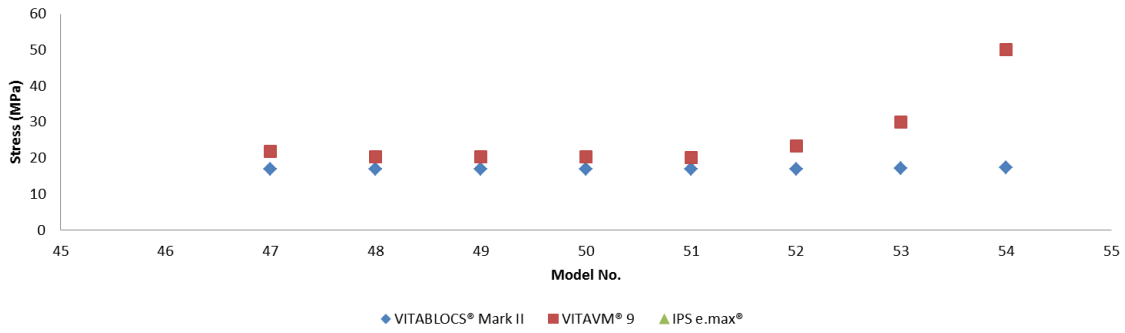

Figure 6.7 The peak maximum principal stress within each layer of the models made of VITAVM® 9 and VITABLOCS® Mark II only.

With all three materials present in the crown, the highest maximum principal stress was always found within the outer IPS e.max® layer, irrespective of the thickness of each material. The values of the highest maximum principal stress for these models are illustrated in Figure 6.8. The peak maximum principal stress within the layer of VITABLOCS® Mark II remained roughly constant at 16 MPa.

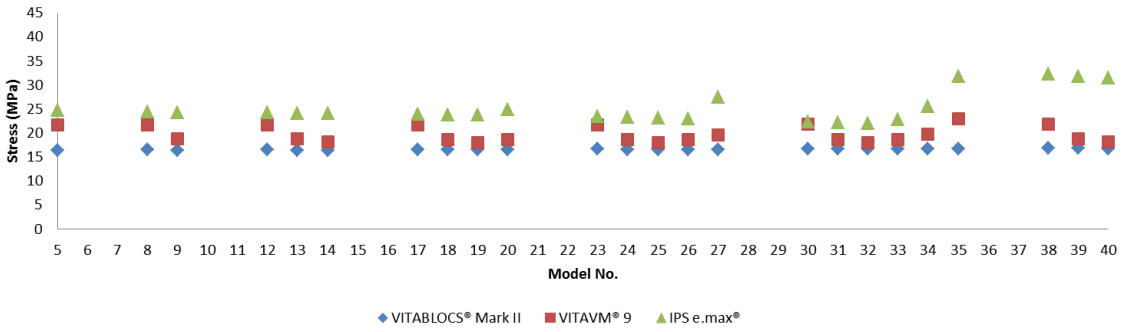

Figure 6.8 The peak maximum principal stress within each layer of the models made of all three materials.

6.3.2 Safety factors

Except for models no. 36 and 45, which had the thinnest IPS e.max® layer, the crowns using a combination of IPS e.max® and VITABLOCS® Mark II had relatively higher safety factors, ranging from 7.20 to 9.28 (Figure 6.9). Model no. 6 showed the highest safety factor (9.28). For other combinations, the safety factor dropped below 5.6 and it ranged from 1.99 to 5.58. For the conventional zirconia-porcelain crown, which uses zirconia as the substructural material and feldpathic porcelain as the veneering layer, the safety factor is only 4.82.

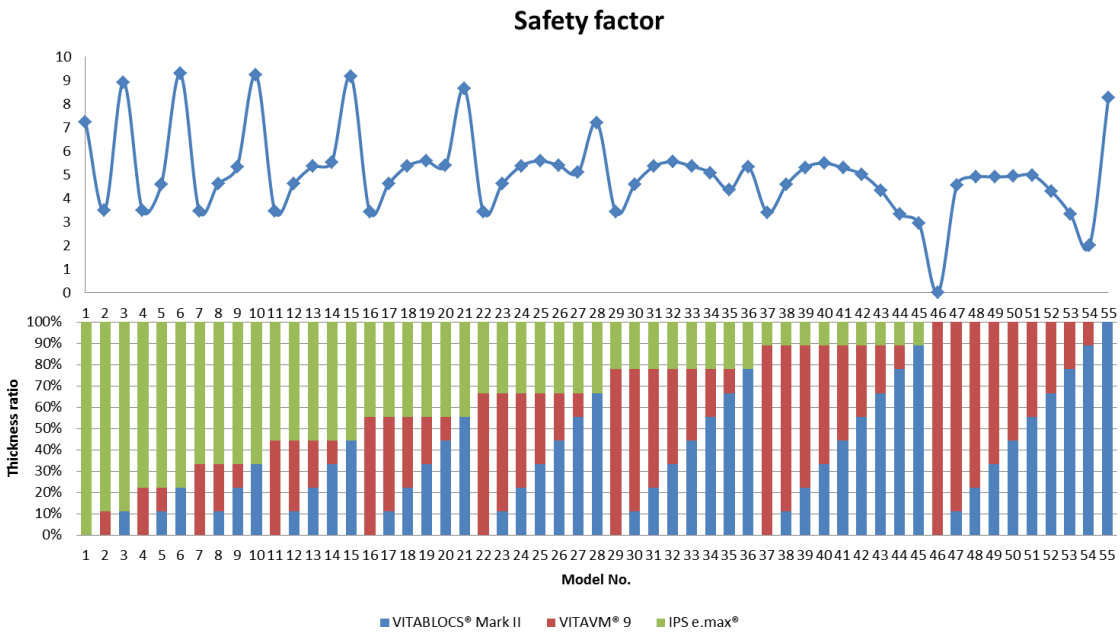

Figure 6.9 The safety factor of each crown design.

6.4 Discussion

The present study has shown that using an outermost layer that is stiffer than the innermost layer leads to an improved safety factor, stress distribution, and mechanical performance for the all-ceramic crown. When compared with the conventional zirconia-porcelain design, the best design from this study, Model no. 6 increased the safety factor of the crown by 92% (4.82 versus 9.28). Even though the zirconia core has a very high flexural strength, zirconia-porcelain dental crowns do not perform better than the optimized design because the flexural strength of the veneering porcelain (100 MPa) is the lowest amongst all the ceramic materials. Under a load of 800 N, the peak maximum principal stress within the veneering porcelain is 20 MPa in the conventional zirconia-porcelain design.

There is some discrepancy between the peak stress results and those of the safety factor. Models having the lowest stress did not necessarily have the highest safety factors. This is because the strengths of the materials do not follow the same trend as the Young's moduli. Although VITAVM® 9 lies second in terms of material stiffness, its strength is the lowest amongst the three materials. As a result, despite the low stress in this material, the safety factors for some of the designs are relatively low. If a stronger material with a similar stiffness is used in place of VITAVM® 9, higher safety factors would be obtained.

Nevertheless, given its higher safety factor, the optimized design should provide a higher load capacity and a longer life-span for the dental crown. In particular, the micro-cracking and surface chipping that form the major failure modes in the conventional design are expected to occur later in service. The optimized material layout was the result

of applying an inverse material distribution to the design of all-ceramic layered dental restoration. This inverse material layout can be applied to other dental restorations that are used to replace hard tooth tissues, including all those that are made of highly filled composites, ceramics, metals, porcelains and a combination of them.

The use of a ceramic core has been facilitated by the great advances in CAD/CAM technology that allows ceramic or composite blocks to be reduced to the required shape with high precision. In fact, all-ceramic crowns made using CAD/CAM technology are expected to grow rapidly, and its market will reach $540 million by 2016 [285]. Due to the non-tooth-like color of metal and zirconia, to achieve satisfying esthetics, conventional metal-ceramic or all-ceramic crowns require extensive effort by the dental technician to build up a porcelain veneering layer. Manufacturing dental crowns of the proposed material layout can be performed using modern CAD/CAM systems and at lower costs. Therefore, not only is the crown with the optimized material layout expected to have better mechanical performance, it is also expected to be more economic.

Although the optimized material layout (Model no. 6) derived in this chapter only makes use of two discrete layers of different materials, with further advances in 3-D printing technology, it will be possible to build up an all-ceramic crown that more closely replicates the graded material distribution in natural enamel. The in-vitro validation of the optimized design derived from the present study has been performed, the details of which are given in the next Chapter.

Chapter 7 In vitro validation of layered all-ceramic crowns with an optimized material layout

7.1 Background

The advantage of the graded distribution of material properties within natural teeth has been demonstrated in Chapter 5, and a practical layout for fabricating an all-ceramic crown using existing materials has been developed in Chapter 6. The finite element results show that using an outermost layer of material that is stiffer than the innermost layer can lead to improved stress distribution, safety factor, and mechanical performance. This chapter presents results of in-vitro testing of all-ceramic crowns with the optimized layout developed in Chapter 6, and it compares their mechanical performance with that of the conventional zirconia-porcelain design.

The first challenge encountered was to develop a proper laboratory protocol for fabricating the crowns with the optimized material layout. Most all-ceramic systems provide a complete assortment of substructural and veneering ceramic materials with matching coefficients of thermal expansions, which is important in preventing premature cracking during fabrication, and excellent tooth shade reproduction. It was not the aim of this study to mimic natural tooth color perfectly with the optimized design. The development of a laboratory protocol for fabricating the optimized design focused on the selection of ceramic materials with appropriate mechanical and thermal properties and identifying the proper heating and cooling protocols for the sintering processes to minimize residual stresses. It is widely known that the mismatch in the coefficients of thermal expansion (CTE) between the substructure and veneering materials could

generate residual stresses that lead to premature cracking or chipping of the veneering porcelain [286-288]. The materials' CTE were taken into account during the selection of ceramic materials with suitable elastic moduli for the optimization study in Chapter 6. The three ceramic materials chosen were IPS e.max® (Ivoclar vivadent, Amherst, NY, USA), VITAVM® 9 (VITA Zahnfabrik, Germany) and VITABLOCS® Mark II (VITA Zahnfabrik, Germany)., Their CTEs are 10.2×10^{-6} [216], 9.2×10^{-1} [283] and 9.4×10^{-6} K^{-1} [284], respectively. The CTEs of the chosen ceramic materials are quite close to each other; therefore, premature cracking due to post-sintering residual stresses could be minimized when these materials are fused together to fabricate dental crowns.

To replace the conventional manual layering technique for fabricating layered all-ceramic crowns, techniques that use CAD/CAM systems have been proposed. These include Rapid Layer Technology by VITA, IPS e.max® CAD-on technology by Ivoclar Vivadent, and LAVA Digital Veneering System by 3M ESPE. These techniques use a similar approach whereby each layer within the structure is machined from a ceramic block using a CAD/CAM system, and all the layers are then assembled together for a final sintering process. They can significantly reduce the time for manufacturing layered crowns and greatly increase productivity.

The chipping of crowns fabricated with conventional layering and the CAD-on technique was evaluated by Schmitter et al [289]. To simulate aging, the crowns were treated with thermocycling and artificial loads before being subjected to fast fracture test. Almost all (87.5%) of the crowns made with the conventional layering technique failed during the chewing simulation; only one survived and underwent the fracture test. The

IPS e.max® CAD-on crowns displayed ultimate loads to failure of about 1600 N, which were significantly greater than the 934 N of the conventional one. Further, the artificial ageing did not have any significant effect on their failure loads. An internal study by Ivoclar Vivadent also showed that the average fracture load of IPS e.max® CAD-on bridges was significantly higher than that of conventional layered zirconia-porcelain bridges (2188 vs. 1388 N) [290], and it was comparable to that of monolithic IPS e.max® bridges (2576 N) [291]. The IPS e.max® CAD-on bridges fractured at the connector region or through the pontic without any visible chipping of the veneering layer, while the conventional layered zirconia-porcelain bridges chipped at very low loads.

Although the all-ceramic restorations produced by the above CAD/CAM techniques have comparable mechanical strengths as their monolithic counterparts, they still use the conventional material layout, i.e. an inner stiffer coping (zirconia) veneered with a softer material (lithium disilicate or feldspathic ceramic). According to the stress analysis presented in Chapter 6, the mechanical performance of these all-ceramic crowns can be improved further by reversing the spatial arrangement of the constituent materials. The present study represents the first attempt at applying such a material layout, as inspired by that of natural teeth, to fabricating all-ceramic crowns. As a proof of concept, the crowns were made with two layers of ceramic materials only. The two CAD/CAM ceramic materials selected were IPS e.max® and VITABLOCS® Mark II, and the CAD-on approach would be used to fabricate the crowns.

7.2 Materials and Methods

7.2.1 Sample preparation

The fabrication of the all-ceramic crowns was performed on a model first molar in a prosthetic restoration jaw model (D18FE-500A-QF, Nissin, Japan) prepared using the following guidelines (Figure 7.1):

(1) The marginal design was of the heavy-chamfer type with a rounded inner angle.

(2) The circumferential cutting depth was at least one millimeter.

(3) The taper angle of the proximal wall was about six degrees.

(4) All the line angles between the axial and occlusal walls were rounded.

(5) To provide sufficient space for the veneering material, a minimum of 1.5-mm and a maximum of 2-mm thick tooth substance was removed from the occlusal top.

(6) All prepared tooth surfaces were smoothed using a finishing bur.

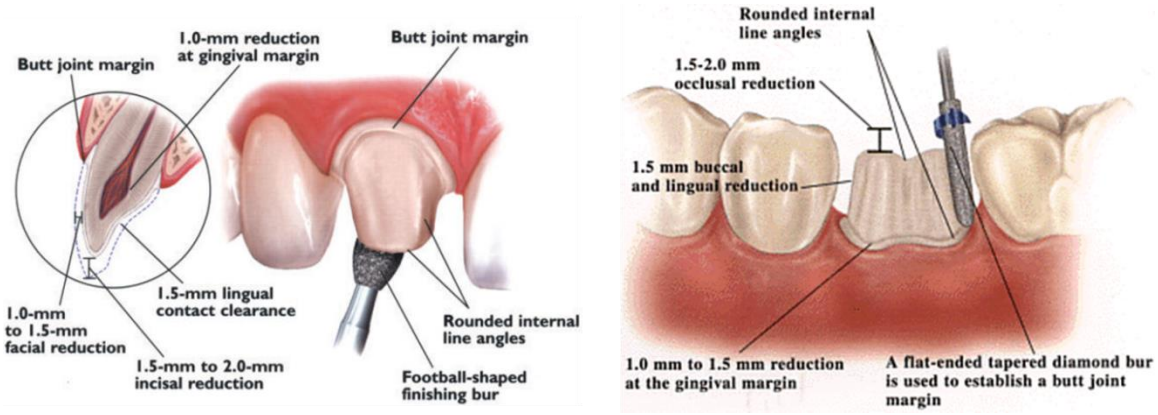

Figure 7.1 The preparation guidelines for all-ceramic crowns [292].

A total of thirty crowns, fifteen for the conventional zirconia-porcelain design and fifteen for the optimized bi-layered design, were prepared. For the zirconia-porcelain group, the crowns were fabricated with the conventional laboratory protocols. A working model was prepared using an impression, made with vinyl polysiloxane impression material (Examixfine™ (injection type), GC, Japan) and silicone putty (Vertex™ Putty 1:1, Vertex-Dental, The Netherlands), of the prepared model tooth. Then, the working model was scanned to obtain the geometry of the prepared abutment using a CAD/CAM system (ARDENTA, Activity 850, Taiwan). The zirconia coping was designed using the software exoCAD dental (build 4903, exocad GmbH, Germany), and replicates were milled from material blocks (VITA In-Ceram YZ, VITA Zahnfabrik, Germany) using the same CAD/CAM system. The milled copings (Figure 7.2a) were cleaned using a steam cleaner (Super steam cleaner, VITA Zahnfabrik, Germany) with a pressure of 70 psi and then dried thoroughly. To achieve adequate bonding between the zirconia copings and the veneering material (VITA VM9®, VITA Zahnfabrik, Germany), the copings were subsequently wetted with a mixture of modeling liquid (VITA Modelling fluid, VITA Zahnfabrik, Germany) and a porcelain powder (BASE DENTINE, VITA VM9®, VITA Zahnfabrik, Germany) to create a washbake layer (Figure 7.2b). The copings were then fired in a furnace (VACUMAT 6000M, VITA Zahnfabrik, Germany) using the following temperature control: pre-heating the furnace to 500°C for two minutes, raising the temperature to 950 °C at a rate of 55°C per minute and holding at 950 °C for another 60 seconds (Table 7.1). After they cooled to room temperature, veneering porcelain was applied onto the zirconia copings. To compensate for firing shrinkage, the crown was built approximately 20% larger than the actual dimensions (Figure 7.2c). The second

firing was performed using the temperature control listed in Table 7.1. The sintered crowns were retrieved from the furnace and their contours were checked using a silicone mold to ensure uniformity.

Figure 7.2 Fabrication of a conventional zirconia-porcelain crown: (a) CAD/CAM prepared zirconia coping; (b) A washbake layer was added onto the zirconia coping and (c) The crown with an oversized porcelain layer before firing.

For the optimized group, two CAD/CAM ceramic materials, IPS e.max® and VITABLOCS® Mark II, were selected for fabricating the bi-layered all-ceramic crowns. The stiffer IPS e.max® formed the outer layer (1.3-mm thick) and the softer VITABLOCS® Mark II formed the inner layer (0.7-mm thick); see Figure 7.3a. The two layers were designed without any undercuts so that they could fit together in a telescopic manner (Figure 7.3b). The assembled ceramic crowns were sintered using the temperature control listed in Table 7.1. After sintering, the door of the furnace was kept 70% open so that the temperature decreased gradually to 500°C. The furnace temperature was then kept at 500°C for 12 minutes before coming down to room temperature at a rate of -30°C per minute. The final product is shown in Figure 7.3c.

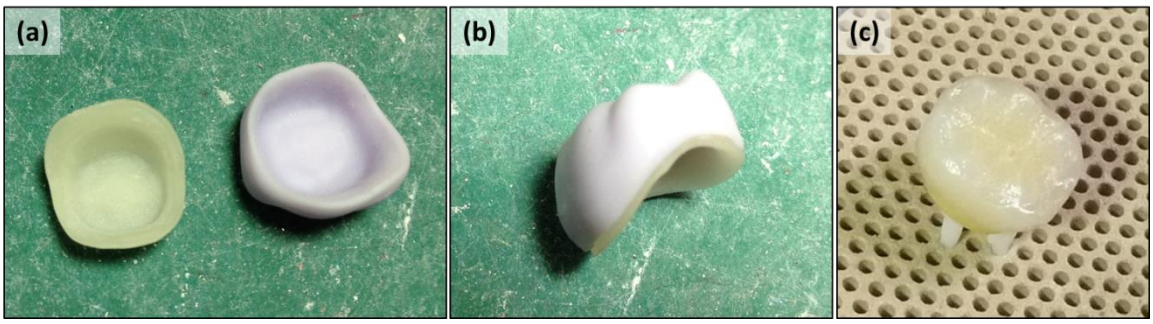

Figure 7.3 Construction of a bi-layered all-ceramic crown using IPS e.max® and VITABLOCS® Mark II with optimized layer thicknesses.

Diamond grinders and finishers (Easy polishing system, Vident, Brea, CA, USA) were used to polish all the fabricated crowns. A Micro-CT scanner (HMX XT H 255, Nikon Metrology, Brighton, MI, USA) was used to ascertain whether premature cracking due to inadequate laboratory protocols had occurred in the specimens before testing. The following CT scan parameters, which had been found to be optimal for scanning human teeth and dental materials, were used: a tube voltage and current of 90 kV and 90 μA, respectively; an exposure time of 708 milliseconds; a total of 720 projections; and 4 frames per projection.

Table 7.1 Firing protocols used for manufacturing the all-ceramic crowns

Firing	Preheating temp. [°C]	Hold time [min]	Temp. rise [°C/min]	End-temp. [°C]	Hold. time [min]
Conventional group					
washbake	500	2	55	950	1
porcelain	500	6	55	900	1
Optimized group					
Assembled bi-layer	500	6	45	900	1

7.2.2 In vitro mechanical test

The prepared model tooth used for fabricating the ceramic crowns was replicated with polymethyl methacrylate resin that had a similar elastic modulus to human dentin. Thirty replicates were formed using the same CAD/CAM system for fabricating ceramic crowns. Each of them was mounted in a Delrin ring with an orthodontic resin (L.D. Caulk, Milford, DE, USA) to simulate the surrounding bone. The fabricated crowns were then cemented onto the tooth replicates using resin cement (RelyX™ Ultimate, 3M ESPE, St. Paul, MN, USA) and stored in deionized water at 37^0C in an incubator for 24 hours before testing.

A servo-hydraulic testing machine (MTS 810, MTS, Minneapolis, MN, USA) was used to test the load capacity of the individual specimen, which was placed at the lower, stationary part of the testing machine. A compressive force was applied on the occlusal surface via a stainless steel ball of 6-mm diameter using a loading speed of 0.2 mm per minute until final fracture. Loading was stopped immediately when a significant drop in load occurred was detected, which indicated major cracking or catastrophic fracture. During loading, both the force and displacement of the steel ball was recorded using the software LJstream (LabJack Corp., Lakewood, CO, USA) for subsequent analysis. A two-channel Acoustic Emission (AE) system was used to monitor subcritical cracking in the specimens during loading. An AE sensor was glued onto the lingual surface of the crown (Figure 7.4) and signals detected by the sensor were passed through a preamplifier with a 40-dB gain. Recording of the signals was performed with the AEwin software (Physical Acoustic Coorporation (PAC), Princeton Jct, NJ, USA) using a sampling

frequency of 1 MHz. The load-displacement data and the AE results obtained from the compression test were processed using the computing software Matlab (MathWorks, Natick, MA, USA). AE signals with amplitudes lower than 35 dB were ignored as background noise.

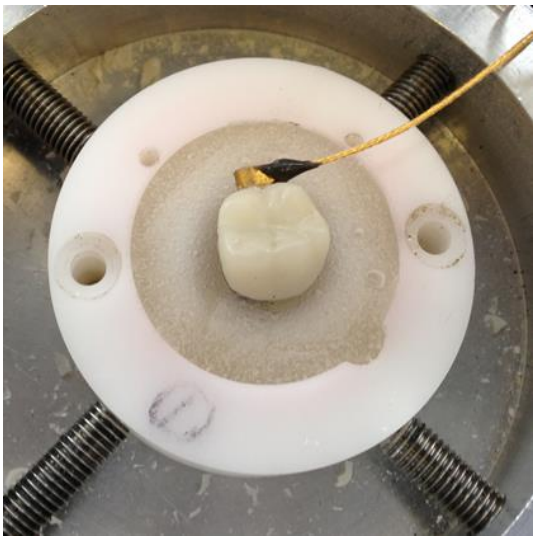

Figure 7.4 An AE sensor was glued onto the lingual surface of a specimen to capture the cracking events during the in-vitro test.

7.2.3 Data analysis

The peak load, the accumulated number of AE events, and the amplitude of individual AE event for each specimen were extracted for comparison. The mean and standard deviation of all the measured values were computed. The two-tailed T-test was used to evaluate the statistical significance of the differences in the measured parameters between the two groups of crowns.

7.3 Results

Before mechanical testing, no visible surface cracks were found on the specimen surfaces using the optical microscope, and CT inspections also confirmed that no premature cracking occurred within any of the fabricated crowns.

The AE measurement demonstrated that much less cracking and chipping occurred in the group of optimized crowns prior to final fracture, with the mean number of AE events per specimen being significantly different between the two groups (Conventional group: 3228 ± 2745; Optimized group: 627 ± 346; P-value < 0.001). When comparing the times to the first detected cracking event between the two groups of specimens, it was found that cracking occurred earlier in the conventional crowns than in the optimized ones (Conventional group: 115.75 ± 72.35 seconds; Optimized group: 156.56 ± 61.24 seconds; P-value = 0.04). From the curves of the accumulated number of AE events versus Force (Figure 7.5), it can be seen that the rapid occurrence of AE events occurred at a load >1000 N in the crowns from the optimized group and at a much lower level of load (~400 N) in the conventional zirconia-porcelain crowns, indicating that the conventional zirconia-porcelain crowns chipped or cracked more easily during initial loading. There was a relatively quiet period that followed before the number of AE events increased sharply again with increasing load up to the point of final fracture. No chipping or delamination was found in the crowns with the optimized layout prior to final fracture. The mean amplitude of an AE event from the conventional group was slightly lower than that from the optimized group (Conventional group: 54.4 ± 0.87 dB; Optimized group: 55.7 ± 2.04 dB; P-value = 0.03).

The load-displacement curves also demonstrated different failure behaviors between the two groups (Figure 7.6). Following the establishment of contact between the loading ball and the specimen, the load in the conventional group remained low for a long period of time before it increased sharply to reach the value for final failure. This initial period with a sustained low load was largely absent in the optimized group.

Six specimens from the conventional group were found to have their substructures fractured totally; the remaining zirconia copings remained intact. No significant difference in the final fracture load (Conventional: 1998.9 ± 653.3 N vs. Optimized: 1810.4 ± 342.1 N; P-value = 0.33) was found between the two groups. The results from the mechanical test of the all-ceramic crowns are summarized in Table 7.2.

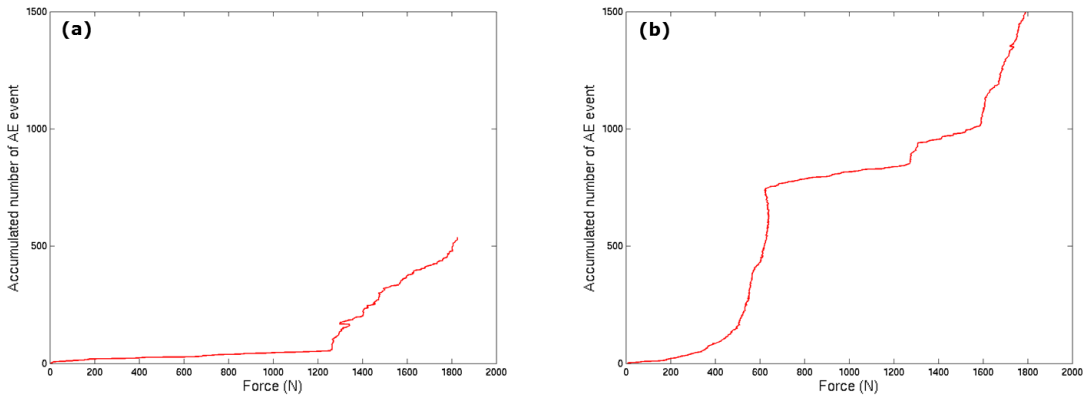

Figure 7.5 Curves of accumulated number of AE events versus Force from: (a) an optimized crown and (b) a conventional crown.

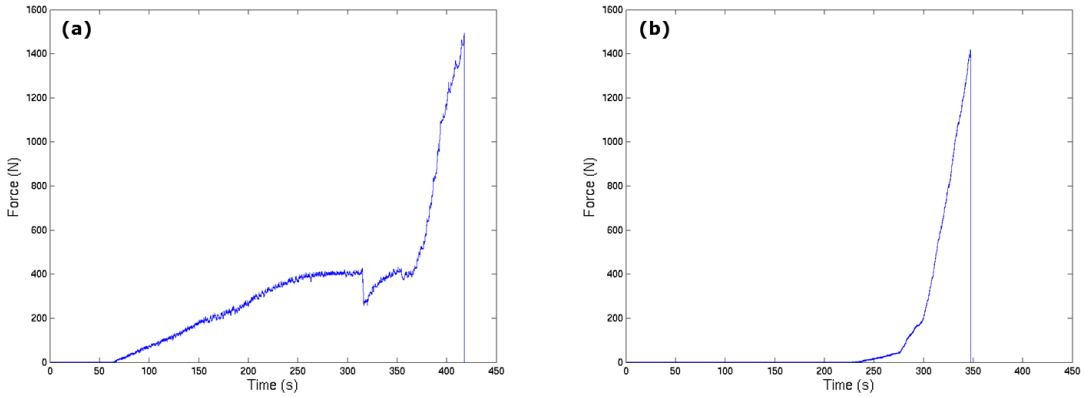

Figure 7.6 Load-displacement curves from the compression fracture tests: (a) zirconia-porcelain group and (b) optimized group.

Table 7.2 Results from the in-vitro tests of the two groups of all-ceramic crowns

	Zirconia				Optimized			
Sample #	**Max. Load (N)**	**No. of event**	**Mean amplitude of AE signal (dB)**	**Time to failure (second)**	**Max. Load (N)**	**No. of event**	**Mean Amplitude of AE signal (dB)**	**Time to failure (second)**
1	1517.3	3410.0	55.6	452.4	1614.0	1185.0	56.3	330.4
2	1498.5	1927.0	54.4	452.4	1423.3	642.0	54.2	347.7
3	1904.1	828.0	55.6	417.9	1584.5	299.0	54.8	249.5
4	1587.2	1705.0	54.2	334.9	1898.7	538.0	55.9	284.5
5	1001.7	4093.0	53.8	523.7	1686.5	711.0	55.5	378.5
6	2261.2	4937.0	53.8	574.6	1479.7	1017.0	53.7	323.9
7	880.9	1514.0	53.6	574.7	2465.3	297.0	59.5	365.9
8	1845.0	1511.0	55.0	422.3	2175.3	263.0	58.6	213.7
9	2658.7	11839	55.8	572.8	1458.3	1124	52.7	379.8
10	2857.4	2323.0	54.3	411.2	1648.9	676.0	56.0	284.2
11	1587.2	4461.0	54.4	520.6	1890.6	953.0	53.8	289.4
12	2462.6	1764.0	52.9	416.7	2132.3	196.0	58.4	226.1
13	2290.8	4791.0	55.1	414.6	1992.7	187.0	54.5	485.9
14	2844.0	1424.0	53.5	580.7	1401.9	896.0	54.0	190.0
15	2787.6	1888.0	53.8	572.8	2304.2	426.0	57.7	349.9
Mean	1998.9	3227.7	54.4	534.2	1810.4	627.3	55.7	312.1
±S.D.	653.3	2744.9	0.9	81.4	342.1	345.9	2.0	79.8
P-value	0.33	0.00	0.03	0.00				

7.4 Discussion

A large amount of micro-cracking occurred within the veneering porcelain of the conventional crowns during the early stage of loading. This was why the load remained low initially with increasing displacement in this group (Figure 7.6). Only when the loading sphere had gone through the porcelain layer and made direct contact with the zirconia coping, did the load begin to increase rapidly with displacement. In contrast, the load in the optimized group increased more quickly with increasing displacement following the establishment of contact with the loading sphere. No chipping or delamination occurred prior to final fracture. The average final fracture load of the optimized group was comparable to that of the conventional design (1998.9 ± 653.3 N vs. 1810.4 ± 342.1 N; P-value = 0.33). However, under a load that is equal to the averaged maximum bite force, 500 N for men and 400 N for women [293], the conventional crowns would produce more cracking than the optimized crowns, as shown by the AE measurements in Figure 7.5. Clinically, even a small chip in the crown will be considered as restoration failure. If the first cracking event as detected by AE was used to evaluate the mechanical performance of the crowns, the optimized layout can be seen to significantly postpone failure of the crown. These results confirm the numerical simulation in Chapter 6 that shows that the optimized design can better distribute the stresses to delay the onset of cracking.

The crowns made with the traditional layering technique usually need a silicone mold for checking the final morphology. This is because the build-up of the porcelain veneering layer is a manual process and the material shrinks following sintering. That is

why the porcelain veneer needs to be made 20-25% larger initially. The two ceramic materials used in the optimized crown, IPS e.max® and VITABLOCS® Mark II, do not have the problem of firing shrinkage. Therefore, when preparing each ceramic layer, it is not necessary to oversize them to compensate for shrinkage. The CAD/CAM process can reproduce the required morphology with high precision. Although morphological inconsistency is not a main clinical concern, the time spent on occlusal adjustments can be significantly reduced if a dental crown or bridge can be fabricated precisely.

It has been documented that the conventional layering technique resulted in a high rate of chipping in the porcelain veneer, about 20% after 3 years [294], and 15% [295] and 30% [92] after 5 years. This is because the manual layering process often introduces fracture-causing voids and flaws in the veneering porcelain [296]. For the bi-layered crowns with the optimized material layout, a simpler but more advanced laboratory protocol can be applied for their fabrication. By sintering two layers of different CAD/CAM ceramics together, the fracture-causing flaws can be minimized. Materials with matching coefficients of thermal expansion and a suitable temperature control in the sintering process need to be used to prevent premature failure of the crowns through residual stresses.

Other laboratory protocols can also be considered in the future for making the layered crowns. For example, the ceramic layers can be sintered separately first and then connected together using a suitable bonding agent. The advantage of this method is that the residual stress can be minimized; however, inadequate strength of the bonding agent may lead to interfacial failures. Another example is provided by the computer-aided

overpress (CAO) technique [297]. A pressable ceramic material is pressed onto the surface of the substructure, also designed by a CAD/CAM system. A clinical study [298] evaluated nineteen individuals with twenty-one all-ceramic restorations made with the CAO technique, and no chipping of the veneering porcelain was found over 3 years. The authors then kept track of these individuals up until 44 months, and only two restorations need to be replaced. One molar restoration fractured due to insufficient thickness of the zirconia coping, which was only 0.3-mm thick at the fractured site, and the other one failed due to loss of retention. A systematic review [299] also found that the CAO technique resulted in better clinical outcomes than the conventional layering technique. When this technique is considered, the CTE of the ceramic materials still needs to be properly matched.

7.5 Conclusion

The present in-vitro study validated the dental crown design based on the optimized material layout derived in Chapter 6. The optimized crown suffered from far less chipping before final fracture than the conventional design. Dental crowns with the optimized material layout are expected to perform better clinically than the current all-ceramic restorations, while its cost can be as low as that of the conventional metal-ceramic restorations. The potential for this new crown design is, therefore, very significant.

Chapter 8 A study on the mechanical anisotropy of human enamel due to directional enamel rod orientations

8.1 Background

The enamel of human teeth is predominately (96%) composed of hydroxyapatite (HA) minerals, with the remaining 4% being mainly water and a very small amount of proteins that hold the HA minerals together [300]. These HA minerals are arranged in a hierarchical manner at three different levels. The complex hierarchical structure starts with the smallest units of needle-like HA crystallites. The dimensions of these HA crystallites are about 68 nm in length and 26 nm in thickness [301]. They are bundled together by a 2-nm thick protein layer to form structures at the next hierarchical level: the enamel rods [301, 302]. At this level, the orientation of the HA crystallites can be seen to vary within an enamel rod. The HA crystallites in the central region of the rod are oriented parallel to the longitudinal axis of the rod, while those near the edge of the rods are oriented at 45^0 [153] (Figure 8.1a). In a finite element (FE) simulation [154], the longitudinal and transversal elastic moduli of a HA crystallite were first computed using a simple composite theory with the following equations:

$$E_{longitudinal} = V_{HA}E_{HA} + (1 - V_{HA})E_{organic\ tissue}$$

$$E_{transversal} = 1/\left\{(V_{HA}/E_{HA}) + \left((1 - V_{HA})/E_{organic\ tissue}\right)\right\}$$

where V_{HA} is the volumetric fraction of the HA, $E_{HA}$is the elastic modulus of the HA (114 GPa) and $E_{organic\ tissue}$is the elastic modulus of the organic tissues surrounding the HA (4.3 GPa). When V_{HA} was increased from 0.81 to 0.99, the elastic modulus of the HA

crystallite increased from 93 to 113 GPa and from 19 to 91 GPa in the longitudinal and transversal direction, respectively. These computed longitudinal and transversal elastic moduli of the HA crystallite were then assigned to a prismatic model for the enamel rod (Figure 8.1). The resulting elastic moduli within the enamel rod were found to be dependent on both the chemical composition and crystal orientation. These location-specific orientations of the HA crystallites make the enamel rods behave anisotropically. The oblique crystal orientation in the peripheral region of the rods results in a lower transverse elastic modulus [154] of the entire rod. It has been shown that the lower transverse elastic modulus, which is close to the elastic modulus of dentin, helps reduce the interfacial shear stress across the dentin-enamel junction [155].

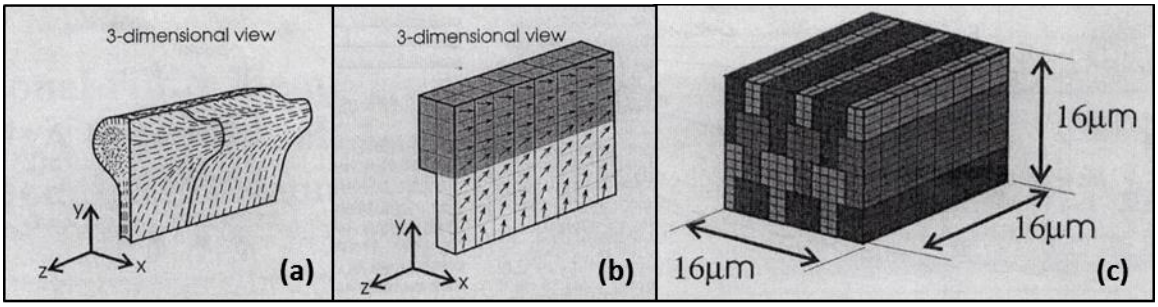

Figure 8.1 (a) The orientations of HA crystallites within an enamel rod. (b) The orientations for assigning the longitudinal elastic modulus of the HA crystallite to each element of a FE enamel rod model. (c) The FE model for enamel used in [154].

The enamel rods have a keyhole-shaped cross-section with a circular head of 5-µm diameter and a tail of 2-µm length. Each enamel rod is encapsulated with a protein sheath of about 800 - 1000 nm thick and is closely packed in parallel with other rods in a centered cubic arrangement. The protein matrix that separates the enamel rods also gives

enamel the lower transverse modulus. The rods extend from the dentin to the outer enamel surface in a direction perpendicular to the dentino-enamel junction.

The orientation of the enamel rods defines the last hierarchical level. They lie perpendicularly to the outer tooth surface so they gradually change from vertically-oriented in the occlusal third to horizontally-oriented in the middle third [150] (Figure 2.1b). In addition, the enamel rods within the cusp tips of molars are twisted together to form the so-called "gnarled enamel" with increased fracture resistance [300]. Material properties such as the elastic modulus and yield strength vary at each hierarchical level, and they have been measured with indentation techniques using different sizes of indenters [303].

Studies using nanoindentation have indicated that the mechanical properties of enamel are fundamentally altered by the rod orientation [145, 233, 258, 259]. The friction and wear of human teeth also vary significantly with the orientation of the enamel rods, which in turn depends on the region of the tooth [151]. A lower coefficient of friction, and thus, higher wear resistance was found in the occlusal region [151]. This phenomenon can also be observed in dentin, the friction and wear behaviors of which are determined by the orientation of the dentinal tubules [260]. As mentioned above, several studies have attempted to numerically simulate the hierarchical structure of enamel [154, 261, 262, 264, 265]. The results from these studies indicated that both the crystal orientation within each rod and the rod arrangement within the enamel are optimized for effective load transfer, high wear resistance, and high fracture strength.

The effects of enamel anisotropy on the stress distribution within a tooth was investigated in the early 90s [155] using a semicircular model (Figure 8.2). The results showed that the occusal load was channeled through the enamel if it was assumed isotropic, while the anisotropic enamel transferred the load directly into the tougher dentin. Similar results were obtained with a two-dimensional model of a premolar [155]. This effect is very important for preventing enamel, which is vulnerable to tensile stress, from fracturing or cracking. Due to the limited computing power at the time, the model was very simple, the FE meshes were coarse, and the aspect ratios of the elements were also poor, which could cause numerical inaccuracy.

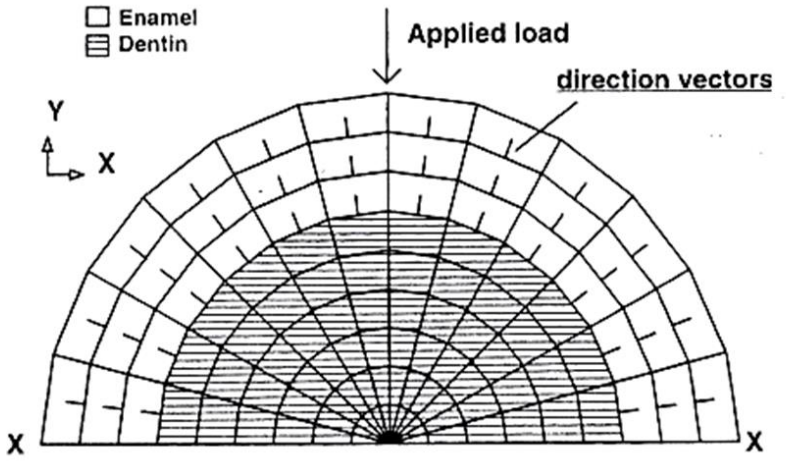

Figure 8.2 A semicircular model for investigating the effects of enamel anisotropy on stress distribution within a tooth [155].

This chapter presents an investigation on how the anisotropic characteristic of the human enamel can influence the stress distribution within a tooth by using more representative models. The simple semicircular model as that described in [155] was first analyzed to verify if the same results could be obtained. Then, a dual semicircular model

was used to simulate a bicuspid tooth. Finally, the anisotropic characteristic of the enamel was analyzed using a model with realistic tooth geometry. It is hypothesized that the enamel anisotropy can better distribute the stress within a tooth.

As described in Chapter 1, one of the dental restorative materials, fiber reinforced composite (FRC), also possesses anisotropic material properties. While the veneering resin is homogenous and isotropic, the unidirectional fibers give the composite a heterogeneous structure with longitudinal and transverse elastic moduli/strength of different magnitudes. Thus, the orientation of the fiber substructure with respect to the directions of the occlusal load plays an important role in the mechanical performance of the FRC restoration. This is similar to the effect of enamel's anisotropy on its mechanical behavior, as demonstrated by the simple example given above. FRC materials are increasingly being used for fabricating dental restorations. Thus, to design stronger dental restorations using this type of material, it would be useful to examine in more detail the effect of mechanical anisotropy on the stress distributions within the human tooth. The results may then be aptly applied to dental prostheses design.

8.2 Materials and Methods

8.2.1 Modelling technique

All the FE models used in this chapter were constructed using the software HyperMesh (Version 11.0, HyperWorks, Altair Engineering, Troy, MI, USA). The models were analyzed using the solver ABAQUS Standard (Version 6.10 EF-1, Dassault Syetemes Simulia, Waltham, MA, USA). The anisotropic characteristic of the enamel was defined by assigning a material orientation to each element within the enamel layer using a method called "Discrete Orientation" (ABAQUS/CAE User's Manual, 12.16: Using discrete orientations for material orientations and composite layup orientations.). It allows the user to assign a spatially varying orientation to a section of the model by assigning the normal axis and the primary axis. The normal axis used in the following models is the out-of-plane axis (z-direction) and the primary axis, perpendicular to the free surface, varies along the surface of the tooth; see Figure 8.3. In this manner, the anisotropic characteristic of the enamel with a higher Young's modulus along the primary axis can be defined easily. The maximum principal stress distribution and the reaction force from the base were compared between the models with isotropic and anisotropic properties.

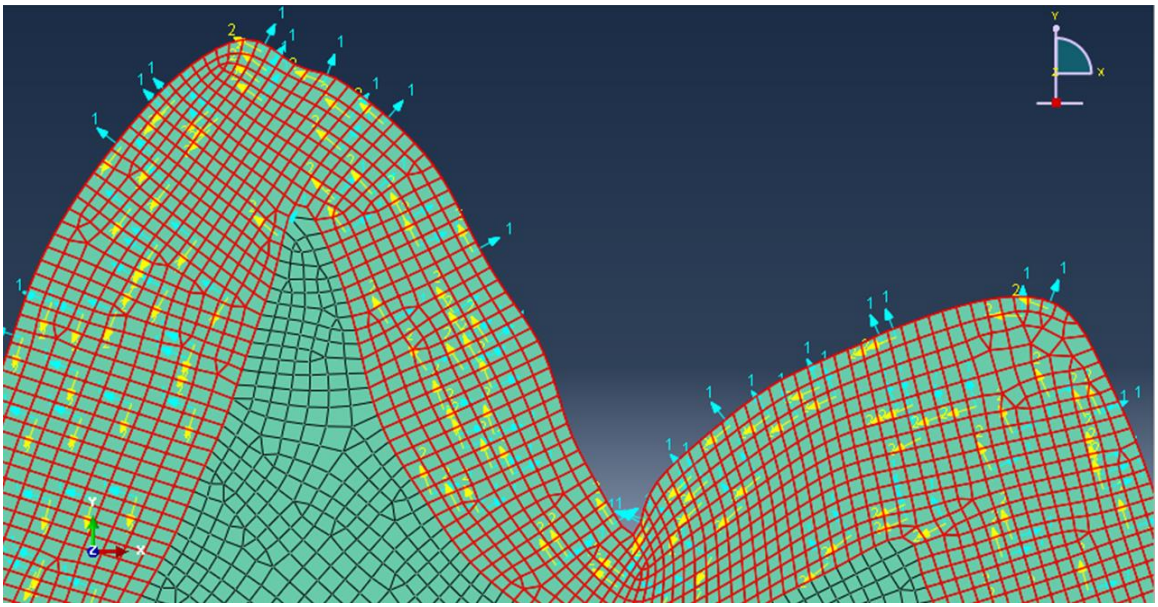

Figure 8.3 The varying material orientations in the enamel that allow anisotropic properties to be defined. To show them more clearly, the material orientations were only shown on some elements. The blue arrows indicate the longitudinal direction of the enamel rods, the orange the transverse direction.

8.2.2 A semicircular model of a tooth crown

A two-dimensional FE model of a semicircle, with a uniform out-of-plane thickness of 10 mm, was constructed to represent a tooth crown. This model was composed of an inner semicircle of 3.5-mm radius and a 1.5-mm thick outer layer to simulate the dentin and enamel, respectively (Figure 8.4). A vertical concentrated load of 200 N was applied to the topmost node of the model. The bottom of the model was fully constrained. The mechanical properties for each material, assumed to behave linear elastically, are listed in Table 8.1. For the anisotropic case, a longitudinal elastic modulus of 84.1 GPa and a transverse elastic modulus of 10 GPa were assumed for the enamel. The other materials' properties remained the same as those in the isotropic model. The types of element used were quadrilateral and triangular plane-strain elements (CPE4I and CPE3 [190]) and their size was approximately 0.1 mm in length. The model consisted of 1190 nodes and 1131 elements in total.

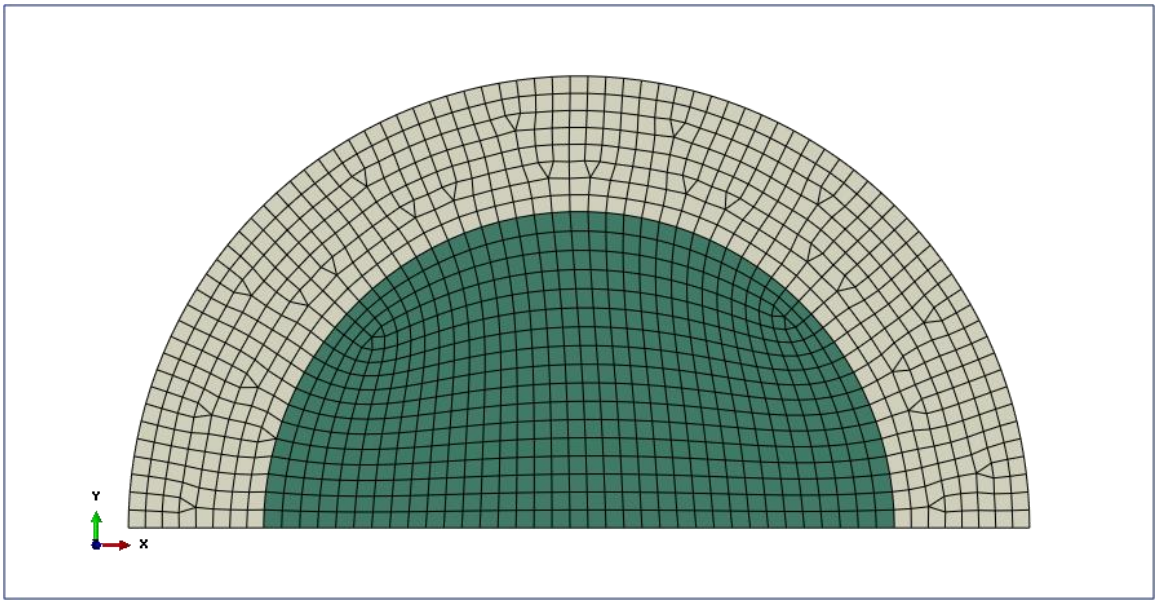

Figure 8.4 The FE mesh of the semicircular model of a crown.

Table 8.1 The material properties used in the FE models

Material	Elastic modulus (GPa)	Poisson's ratio	Ref.
Enamel (Isotropic)	84.1	0.3	[191]
Enamel (Anisotropic)	84.1 (longitudinal); 10 (transverse)	0.3	
Dentin	18.6	0.31	[192]
Cortical bone	13.7	0.3	[193]
Cancellous bone	1.37	0.3	[193]
Pulp	2.07×10^{-3}	0.45	[194]
Zirconia	210	0.3	[244]

8.2.3 A simple model of a bicuspid tooth

This simple two-dimensional model of a bicuspid tooth was composed of two semicircles of 2.5 mm radius and a 2 mm by 10 mm rectangular box. The semicircles were used to simulate the tooth cusps and the rectangular box formed the middle third of the tooth structure (Figure 8.5). A uniform layer of 1 mm thick lining the outer surface represented the enamel. A semicircle of 2 mm diameter was placed between the two cusps to load the model. Its material properties were the same as those of the isotropic enamel. A uniformly distributed load of 400 N was exerted at the top surface of the loading semicircle. Again, the bottom of the model was constrained in all directions. The material properties and the technique for assigning anisotropic properties to the enamel were the same as those described previously. The same out-of-plane thickness, mesh size and element types were used. The resulting model had a total of 4511 nodes and 4401 elements.

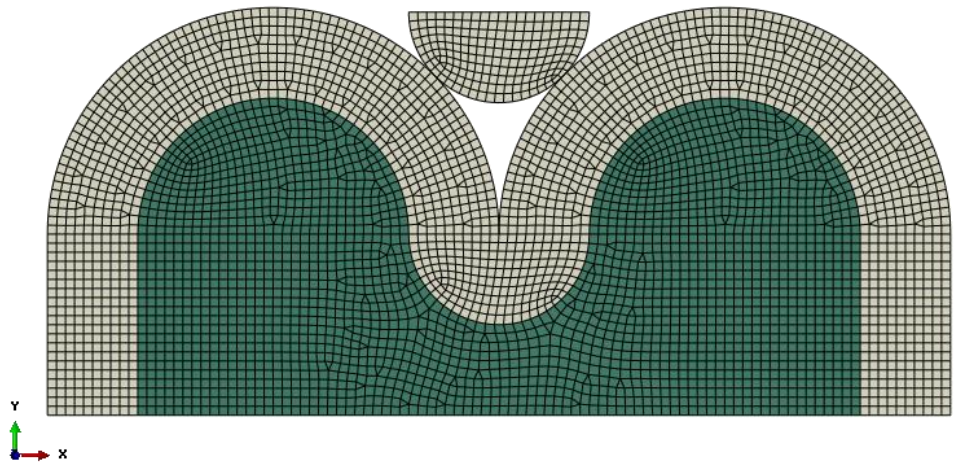

Figure 8.5 The FE mesh of a simple bicuspid tooth model.

8.2.4 A geometrically realistic tooth model

A human maxillary first premolar was scanned using a micro-CT scanner (HMX-XT 255, X-tek system, United Kingdom) to obtain its internal as well as external geometry. A two-dimensional model of the premolar was constructed using the image slice from the central sagittal plane of the reconstructed volume (Figure 8.6). Again, a semicircle of 2-mm radius was used to load the tooth in between the cusps. A uniformly distributed load of 800 N was exerted at the top surface of the semicircle. A rectangular block 14.5 mm high with a 1.5 mm thick top layer was used to represent the surrounding cancellous and cortical bone. All the nodes at the bottom edge of the bone block were fully fixed to serve as the boundary condition. The same material properties, out-of-plane thickness, mesh size, and element types as those for the previous models were used for

the dentine and enamel. The mesh for the bone, however, was coarsened by about a factor of 2 to minimize computational cost.

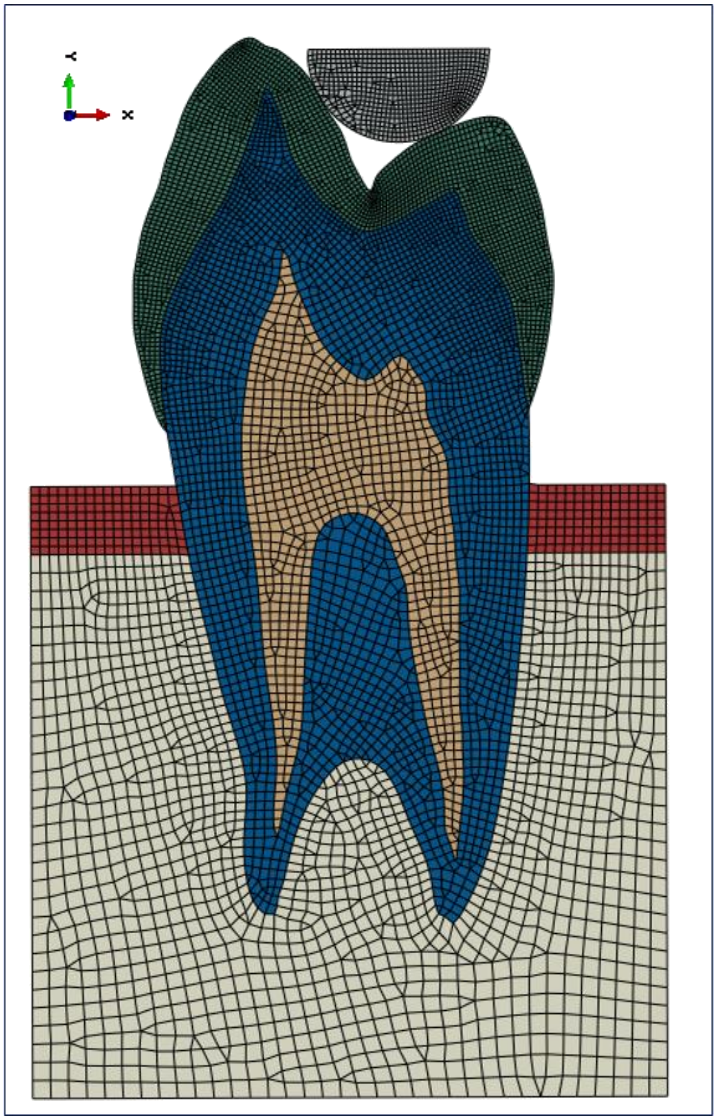

Figure 8.6 The FE mesh of a human premolar model.

8.3 Results

8.3.1 Results from the semicircular model

The plots of the maximum principal stress vectors from the present study show very similar patterns to those from [155]. They also show that, with an isotropic enamel layer, the load path was mainly through the enamel. On the other hand, when the enamel was anisotropic, most of the load was transferred directly into the dentin (Figure 8.7). This was reflected in the higher reaction forces at the bottom of the dentin region when the enamel was anisotropic (Figure 8.8). From the contour plots of the maximum principal stress, much higher tensile stress concentrations can be found at the DEJ near the load and support points in the isotropic model, while stresses were distributed more uniformly in the anisotropic model (Figure 8.9). These can be seen more readily in the line plots of the same stress entity along the DEJ (Figure 8.10).

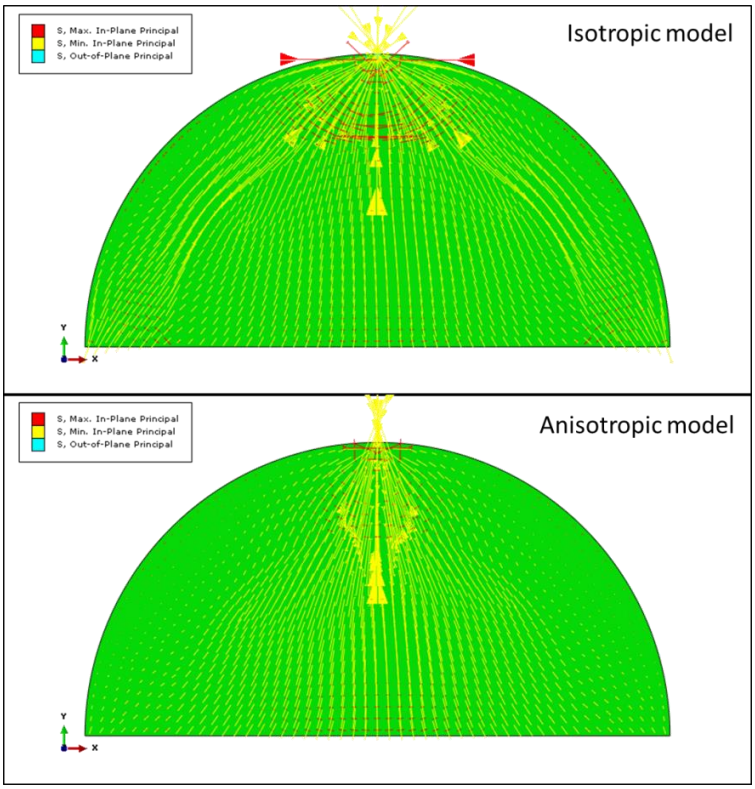

Figure 8.7 Plots of the maximum principal stress vectors in the isotropic model (top) and anisotropic model (bottom).

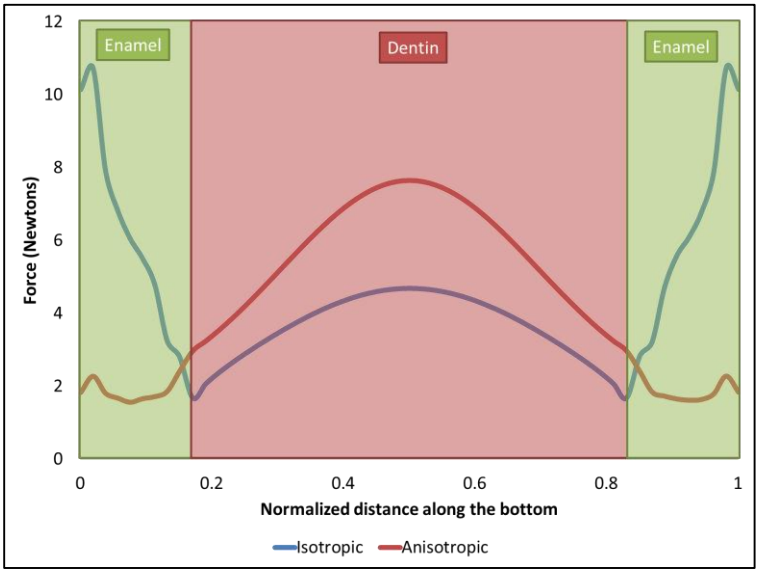

Figure 8.8 Distributions of the vertical reaction force along the base of the two semicircular models.

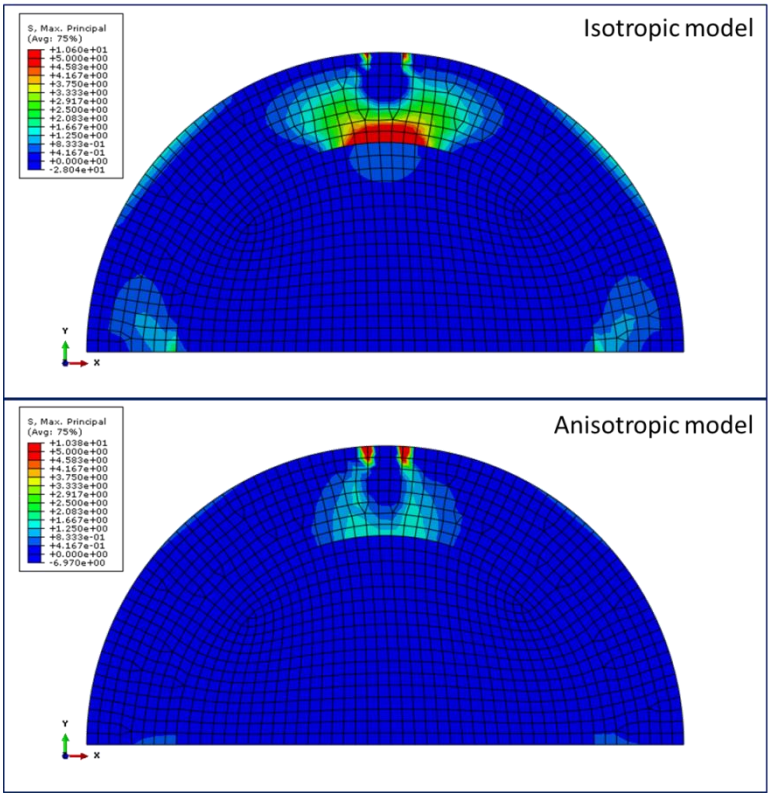

Figure 8.9 The maximum principal stress contour plots of the two semicircular models.

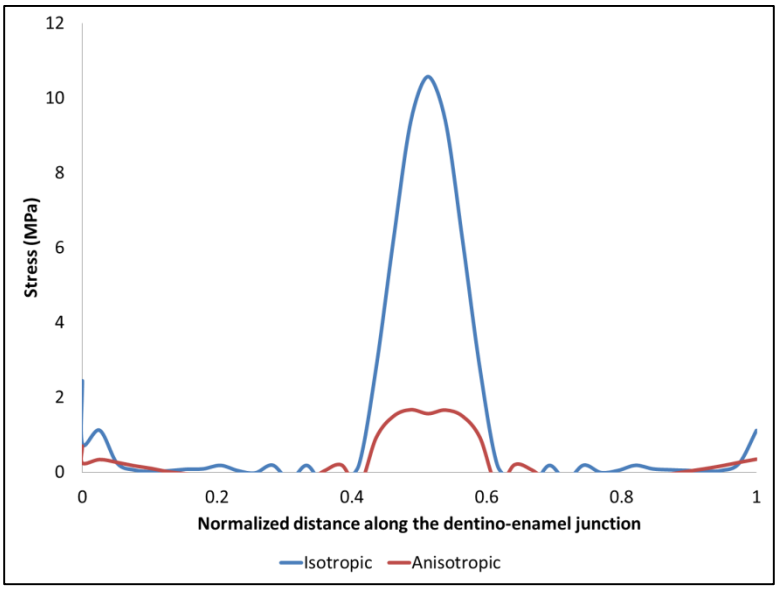

Figure 8.10 Values of the maximum principal stress along the dentino-enamel junction of the two semicircular models.

8.3.2 Results from the simple bicuspid tooth model

The plots of the maximum principal stress vectors (Figure 8.11) indicate that the load path was mostly directed into dentin, and the concentrations of the maximum principal stress were absent with an anisotropic enamel layer. Figure 8.12 shows that the distribution of the reaction force at the bottom was more uniform in the anisotropic model, while the reaction forces in the enamel of the isotropic model remained high.

From the contour plots of the maximum principal stress, higher stress concentrations could be found at the DEJ in the isotropic model, while stresses were distributed more uniformly in the anisotropic model (Figure 8.13). The maximum principal stress along the DEJ is plotted in Figure 8.14. Two peaks of relatively high stresses can be found near the loading point in the isotropic model. For both models, high stresses can be found at their central fossae.

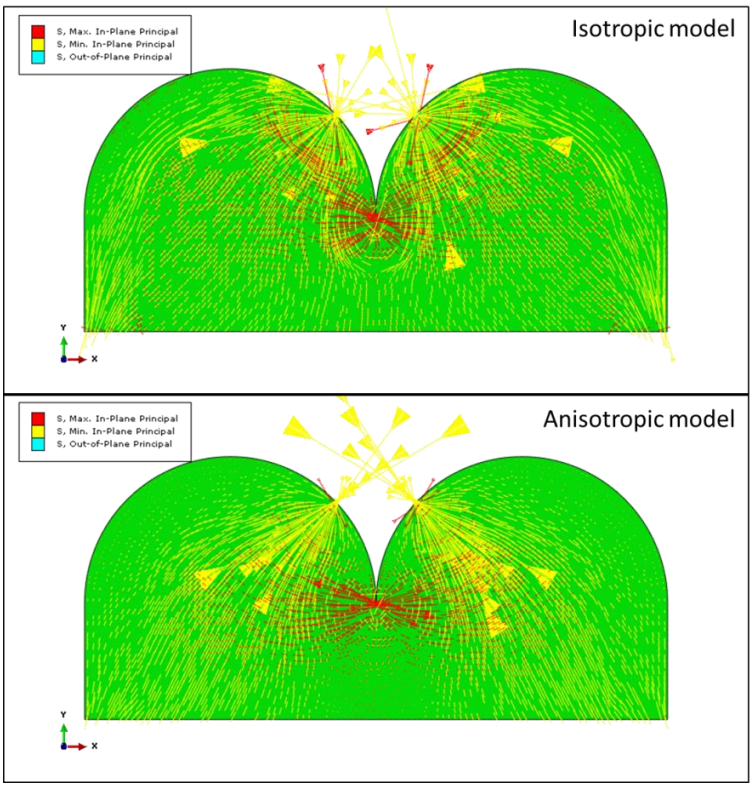

Figure 8.11 Plots of the maximum principal stress vectors in the isotropic model (top) and anisotropic model (bottom).

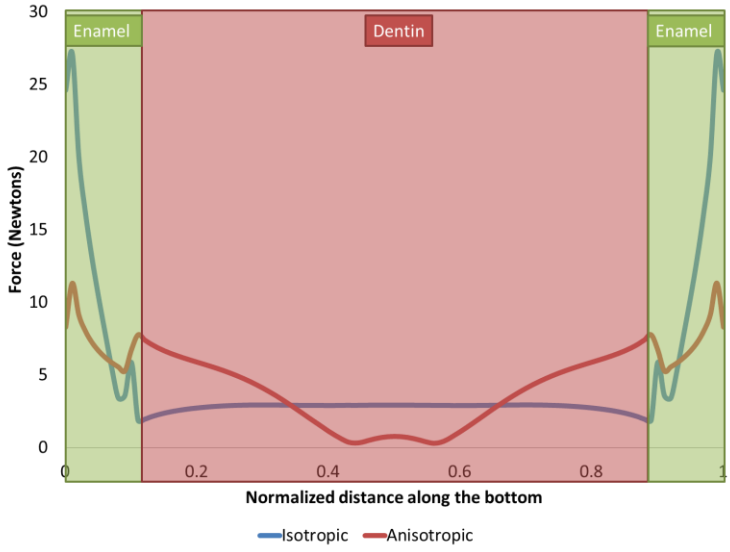

Figure 8.12 The vertical reaction force along the bottom of the simple bicuspid models.

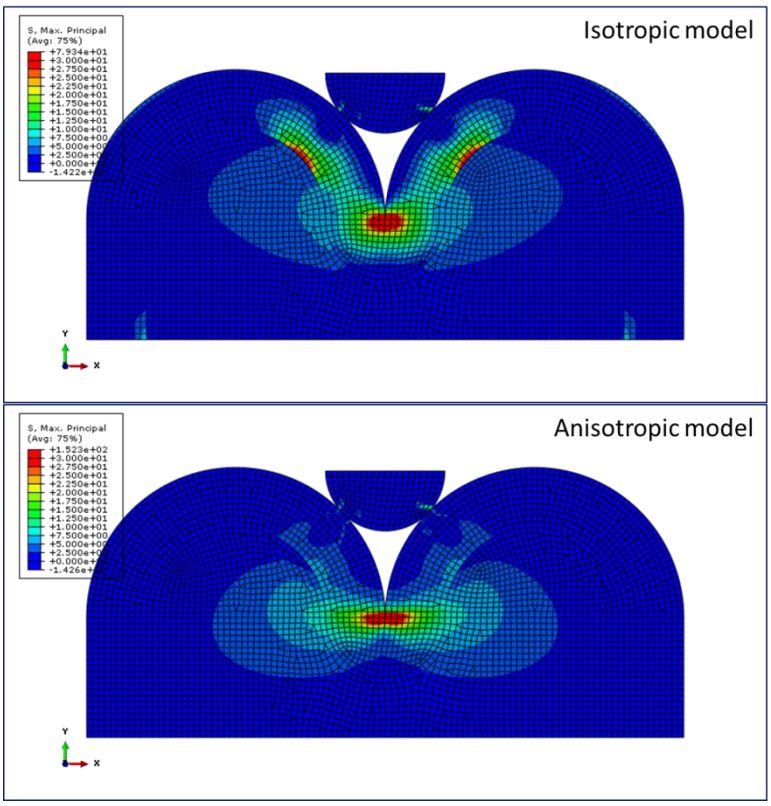

Figure 8.13 The maximum principal stress contour plots of the two simple bicuspid tooth models.

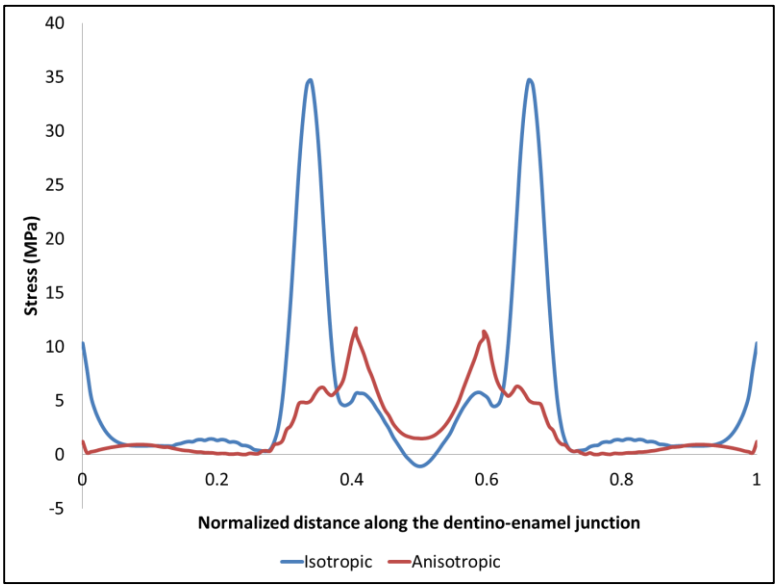

Figure 8.14 Values of the maximum principal stress along the dentino-enamel junction of the bicuspid models.

8.3.3 Results from the realistic tooth model

From the contour plots of the maximum principal stress, higher stress concentrations were found at the DEJ near the buccal and lingual dentin horns in the isotropic model. The maximum principal stress decreased from 127.8 MPa in the isotropic model to 103.8 MPa in the anisotropic model (Figure 8.15). The values of the maximum principal stress along the DEJ from the buccal side to the lingual side are plotted in Figure 8.16. Same as the simple bicuspid tooth model, two peaks of relatively high stresses occurred around the buccal and lingual dentin horns in the isotropic model. In contrast, the stress distribution in the anisotropic model was more uniform and lower stress values could be found along the DEJ.

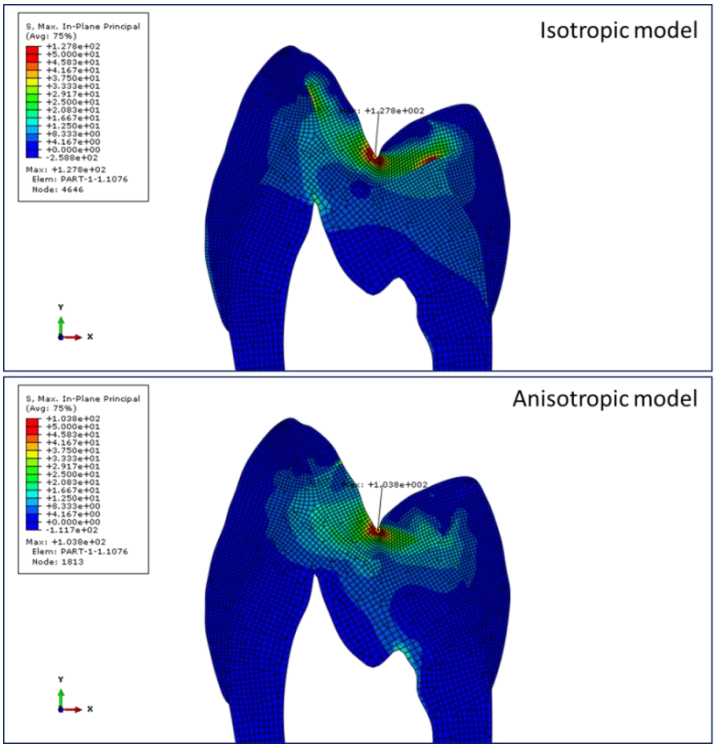

Figure 8.15 The maximum principal stress contour plots of the two human premolar models.

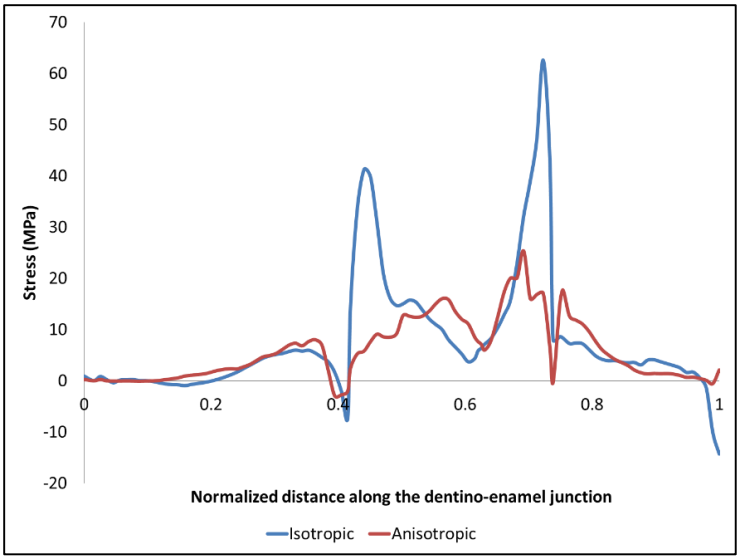

Figure 8.16 The values of the maximum principal stress along the dentino-enamel junction of the two human premolar models.

8.4 Discussion

The discrete orientation method available in ABAQUS allowed varying material orientations to be assigned efficiently to elements in a FE model of complicated geometry. The results generated by the semicircular model were comparable to those reported in [155].

Due to technical limitation in defining material orientation in the past, for simplicity, the mesh used in [155] was concentrically symmetric. This resulted in non-uniform element sizes, with the outer elements being much larger than those close to the center. The inner elements also had less than ideal aspect ratios (Figure 8.2). In fact, a semicircular model using the same mesh as that in [155] was first created for the present work. The calculated stress distributions were discontinuous and stress singularities could be found near the center of both the isotropic and anisotropic models. This was attributed to the triangular elements there having very sharp angles and large aspect ratios. To obtain smoother and more accurate stress distributions, the model was re-meshed with smaller and more regularly shaped quadrilateral elements.

Because the ratio between the elastic moduli of the enamel in the longitudinal and transverse directions was not well known, the present study applied a ratio of about eight similar to what was used in previous studies [155, 304]. Using anisotropic ratios of two, four and eight, it was concluded that changing the ratio of enamel anisotropy had little effect on the stress distribution over the range of values considered [155].

Although the geometry of the bicuspid model was more complicated than the semicircular model, the advantage of having mechanical anisotropy in the enamel for

transferring the load to the underlying dentin was still evident. The peak maximum principal stress near the central fossa, however, was increased when mechanical anisotropy was introduced into the enamel. The opposite was observed in the realistic human premolar model. This discrepancy was attributed to the very simplified geometry of the bicuspid models: the central fossa in these models had the shape of a very sharp fissure, which gave rise to a stress singularity. This problem has been considered in more detail in Chapter 5 with a more geometrically realistic model.

The results presented in this chapter have shown that the mechanical anisotropy of enamel can help transfer the occlusal load more effectively into the underlying dentin, thus limiting the stresses in the more brittle enamel [155]. Furthermore, much higher tensile stress concentrations can be found at the DEJ near the load and support points when isotropic properties are assumed. These are the points where chipping and fracture are often seen in all-ceramic crowns. Therefore, a crown with anisotropic properties is expected to reduce these failures. In effect, the anisotropy decouples the horizontal connections between the enamel rods. In this way, compressive stresses are transferred directly into the dentin without creating transverse stresses or bending moments within the enamel. This is akin to the better supporting action of mattresses that are composed of closely packed but unconnected springs. More importantly, the direction of the maximum principal stress was found to align better with the stronger primary axis of the enamel when anisotropy is present. The same principle could be applied to the design of FRC restorations, even though the stresses of concern are mainly tensile and not compressive.

8.5 Conclusion

It has been found that enamel's anisotropic property plays an important role in reducing unfavorable stresses within the enamel. Without this directional characteristic, bending, and hence, potentially damaging tensile and shear stresses would be generated in the brittle enamel layer. By aligning their long axis along the perpendicular direction to the occlusal surface and decoupling the horizontal connections, the enamel rods would be subjected mainly to compressive stresses, which transfers the occlusal load more effectively into the underlying dentin. In a similar vein, FRC bridges must be effective in using their unidirectional fibers to transfer tensile loads. Any misalignment between the fibers and the tensile stresses would create undue stresses in the resin matrix that can cause delamination or fracture. This problem will be addressed in Chapter 9.

Chapter 9 Shape optimization of a 2-unit inlay-retained fiber-reinforced composite cantilevered bridge

9.1 Background

During the past few decades, new developments and improvements of dental adhesive materials resulting in higher bonding strength have changed the design of dental prostheses. Adhesive fixed partial denture (AFPD) was first introduced by Ibsen [305, 306] and Rochette [307] in 1973. Since then, it has been recognized as a minimally-invasive treatment option for caries-free dentition. In the earlier designs, the retainer of AFPD was mainly fabricated as a thin wing-shaped plate of metal alloy for the anterior region and box-shaped inlay or C-shaped clasp for the posterior dentition (Figure 9.1). These retainer designs for AFPDs follow the treatment philosophy of minimally invasive dentistry, which is to preserve healthy tooth tissue [308].

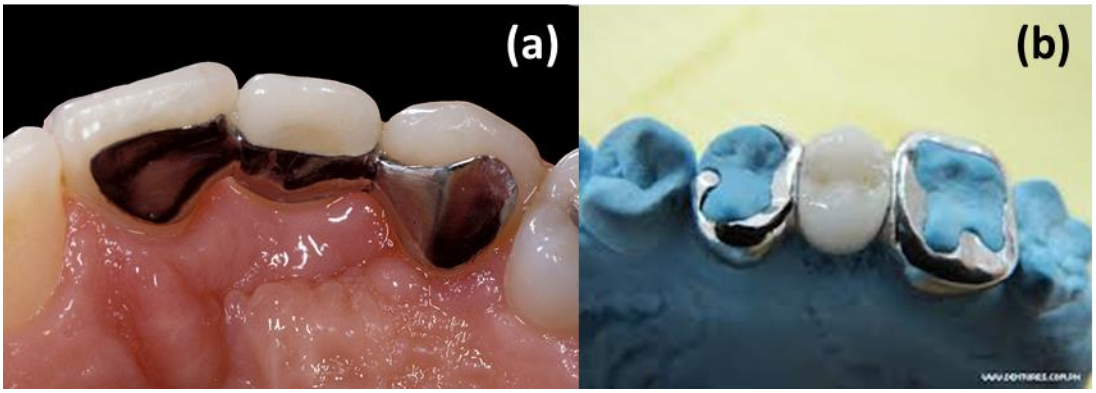

Figure 9.1 Various types of retainer for AFPD: (a) a thin wing-shaped plate of metal alloy for the anterior region. (b) C-shaped clasp for the posterior dentition [309].

To satisfy patients' demand for esthetics, in the mid-1980s, metallic materials used for the substructure of AFPDs were replaced with tooth-colored ceramic materials

[310] or fiber-reinforced composite (FRC) resins [311] . The brittle nature of ceramic materials required larger connector dimensions, and hence, more tooth tissue removal. This went against the principle of minimally invasive dentistry, and significantly limited their clinical application [121, 124]. FRC bridges can retain the major advantage of minimal invasion in AFPDs, while providing metal-free and tooth-colored prosthetic reconstruction with excellent esthetics. Therefore, using FRC systems to fabricate AFPDs has received increasing attention from dentists and dental technicians.

Clinically, the ideal indication of FRC restoration is single tooth replacement. Depending on the periodontal status of the abutment teeth, the position of the missing tooth, individual's occlusal force, or any existing parafunctional habits, the type of restoration can be conventional dental bridges, supported by two abutments at both ends of the edentulous area or cantilevered dental bridges, supported at only one end [311]. The retainer of the FRC restoration does not have to be a full-coverage crown; an inlay-retained design, which can further decrease the amount of unnecessary tooth reduction, is preferred. Current designs of FRC bridges do not have an adequate lifespan. In a systematic review of FRC fixed partial dentures, which evaluated FRC fixed partial dentures with different types of framework design, including inlay-retained, surface-retained, and complete coverage crown-retained, the mean survival rate was 73.4% at 4.5 years [114]. The main failure mode was delamination at the interface between the fibers and the resin matrix [115-119]. Fractures also occurred at the loading point [117, 118, 120], the pontic, and the connectors linking the pontic to the abutments [121-123]. In comparison with the survival rate of metal-ceramic fixed partial dentures, 96.4% over 5 years [312], the durability of FRC fixed partial dentures needs to be improved.

Current FRC systems have excellent flexural strength. For example, the flexural strength of the Fibrekor/Sculpture system (Pentron Clinical, USA) can be up to 1400 MPa. Moreover, a study using standardized bar specimens to evaluate the probability of failure of veneered structures, including unidirectional glass FRC (FibreKor/Sculpture), bidirectional glass FRC (Vectris/Targis), glass-infiltrated alumina (In-Ceram Alumina/Vita alpha) and zirconia-reinforced glass-infiltrated alumina (In-Ceram Zirconia/Vita alpha), found that the failure load of FRC specimens at 10% failure probability were not significantly different from metal-ceramic specimens [313]. In spite of the similar failure load, the clinical survival rate of FRC dental restoration is still not favorable. Several studies have shown that the main contributing factor of clinical failure is inappropriate fiber orientation and position [125-128].

Instead of using stronger materials, the mechanical performance of FRC restorations can be improved by altering the layout of the constituent materials according to the load paths through the structure. Many studies have aimed to determine the optimal fiber position and orientation for the FRC system [129-133] to extend the lifespan of FRC fixed partial dentures. The usual evaluation method was to mechanically test a particular design to failure. This load-to-failure approach has several drawbacks, for example, high material costs, time-consuming specimen preparation, and difficulty in controlling specimen dimensions. Furthermore, it is not straightforward to determine the influence of material layout on the stress distribution within the structure to guide the design process. Numerical simulation, such as finite element analysis, has been used to help improve the design of FRC structures by providing a better insight into the overall stress distribution [125-128, 156-159]. Several finite element analyses of posterior 3-unit FRC bridges

indicated the presence of tensile stress concentrations at the bottom of the pontic and in the connector regions [125-128]. According to these numerical predictions, inadequate fiber reinforcement in these regions will lead to clinical failure.

Although finite element analysis can help researchers compare structural stress distributions among different designs, one often needs to modify the design and analyze the results repeatedly before arriving at a satisfactory solution. This "trial-and-error" process is very time-consuming and it is often not possible to confirm if the final design is really optimal. To accelerate the design process, modern structural optimization techniques, which are widely used in designing engineering components and structures, can be used to design dental implants and bridges. Some of these techniques have been covered in detail in Chapter 2. Amongst these, techniques inspired by the adaptive growth of biological structures have proven to be very effective in producing structures that are optimal in terms of stress distribution.

In a recent study, the so-called stress-induced material transformation (SMT) technique, which is a variant of the Computer Aided Optimization (CAO) method developed at the Karlsruhe Research Center, was used in conjunction with the finite element method to optimize the FRC substructure layout of a 3-unit fixed partial denture [314]. This was achieved by gradually reinforcing the regions with high tensile stresses with FRC material such that the fibers were aligned with the direction of the maximum principal stress. Using the SMT technique, parameters such as the volume, position and orientation of the fibers in a dental restoration can be simultaneously optimized according to the stress distribution. The optimization analysis indicated a U-shape FRC substructure

for the 3-unit inlay-retained dental bridge that followed the bottom profile of the pontic. The results of the finite element stress analysis showed that the proposed optimized design significantly reduced the highest maximum principal stress in the veneering composite at both the connector and pontic positions. In vitro mechanical tests to validate this optimized design have been performed, and the results strongly support the numerical prediction. In comparison with the conventional design, the optimized group showed much less micro-cracking under the same loading condition. Details on the validation of this 3-unit inlay-retained FRC dental bridge will be described in Chapter 10.

This chapter aimed to optimize a more challenging restoration, namely, the posterior 2-unit cantilevered dental bridge. The cantileverd bridge requires an optimal abutment cavity design for its bond strength and an optimal fiber layout for its structural strength. The advantages of a cantilevered dental bridge are: less tooth removal, easier oral hygiene maintenance, and lower cost [315]. For patients who have a missing tooth space less than 7 mm and caries-free neighboring abutments, or with financial concerns, this type of restoration can be a viable treatment alternative [316]. A retrospective study by Botelho et al. [317] on thirty-three 2-unit cantilevered fixed partial dentures reported that the mean lifespan of these prostheses was 65 months, which is satisfactory for interim purpose but needs to be improved for permanent use. They also reported that tooth mobility due to periodontal diseases or inadequate periodontal support would compromise the treatment prognosis. The clinical failures of 2-unit cantilevered fixed partial dentures, especially the inlay-retained ones, are largely through loss of retention. Given that there is only one abutment, the connecting area through which the load is transferred from the pontic to the abutment is smaller than that for the 3-unit fixed partial

denture with two abutments. This makes the design of the cavity preparation that houses the connector very challenging. To optimize the design of the 2-unit fixed partial bridge, the fiber arrangement within the structure and the cavity preparation on the abutment have to be considered.

In this Chapter, the SMT technique will be used to optimize structurally the 2-unit cantilevered FRC fixed partial denture. The mechanical performance of the optimized design has also been validated using in vitro tests, the details of which will be described in Chapter 10 together with those for the 3-unit bridge.

9.2 Materials and Methods

Shape optimization of the 3-unit inlay-retained FRC fixed partial denture was performed by Shi and Fok [318]. A similar method wasused in this work for optimizing the 2-unit cantilevered FRC dental bridge. Because the cantilevered design has a single retainer, one should first consider lowering the interfacial tensile stress at the abutment-pontic connection to reduce the risk of debonding. To achieve this, a two-step approach was adopted for the shape optimization of the 2-unit inlay-retained cantilevered bridge in this study.

9.2.1 Finite element model construction

A human mandibular first molar and a second premolar were embedded in orthodontic resin to form a physical model (Figure 9.2a). Then, a two-step (putty/wash) impression of this physical model was taken using a partial tray (Kwik-Tray, Kerr, USA) with heavy-bodied consistency (Imprint™ 3 Quick Step Heavy Body (injection type), 3M ESPE, USA) followed with light-bodied (Imprint™ 3 Quick Step Regular Body (injection type), 3M ESPE, USA) vinyl polysiloxane impression materials (Figure 9.2b). An initial impression was made using only the heavy-bodied impression material to form a custom tray that could provide a space for the secondary wash impression. After the heavy-bodied impression material had set, the material within a perimeter that was approximately 2mm away from the teeth was removed. The light-bodied material was syringed over this custom tray to make the secondary wash impression. A stone material (Die-Keen, Columbus Dental, St. Louis, MO) was then poured into the impression mold to form a working cast (Figure 9.2c). The premolar portion was removed from the working cast using the cast trimmer, and the remaining molar portion was fitted back into

the original impression mold (Figure 9.2d). A composite resin (Filtek Z250 universal composite, 3M ESPE, USA) was used to fill up the space for the premolar to build up a pontic without a retainer (Figure 9.2e). Finally, a second-premolar pontic was fabricated and attached to the mesial surface of the molar with resin cement (Figure 9.2f).

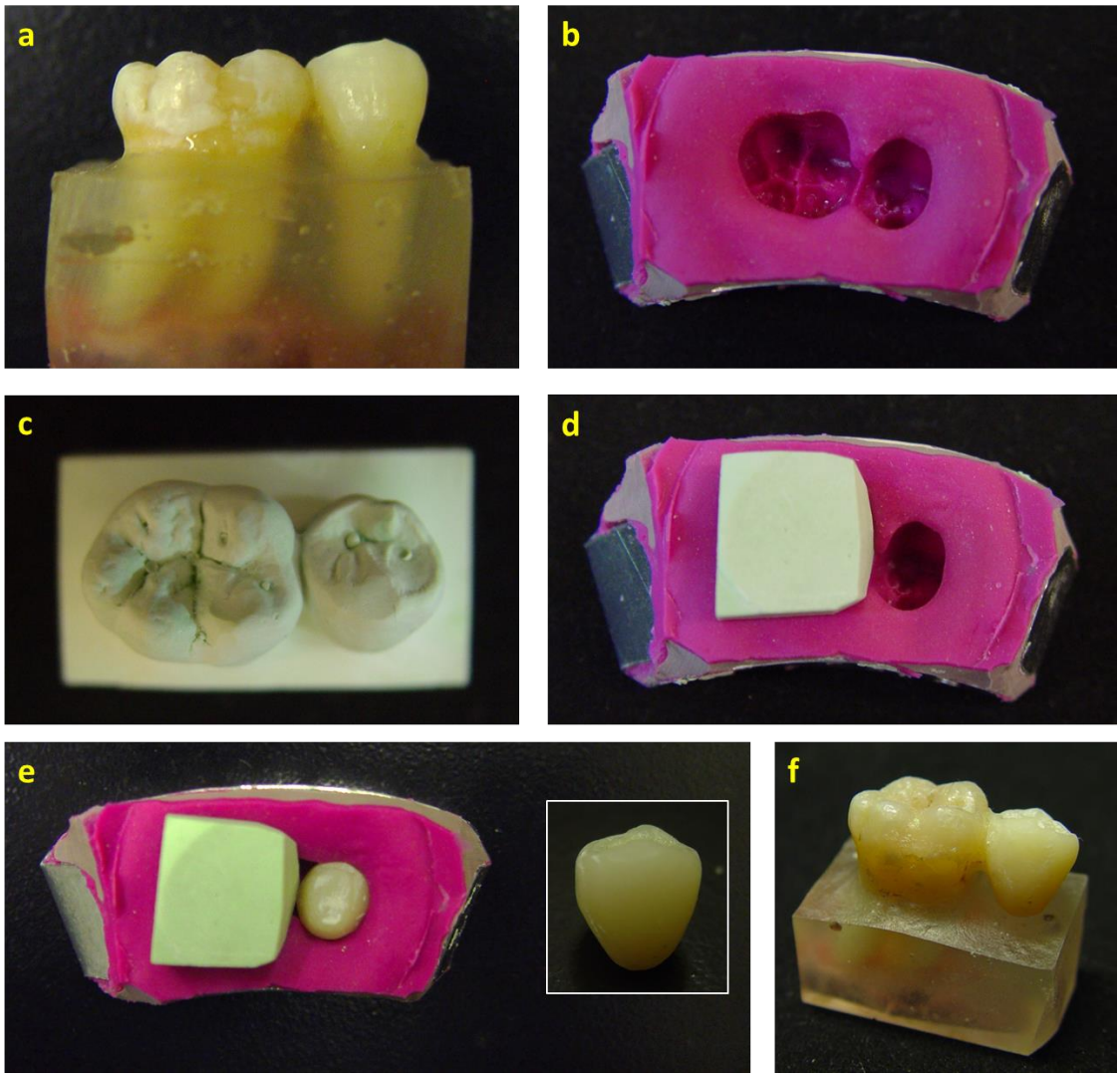

Figure 9.2 Construction of the physical model for the mandibular first molar attached with a second-premolar pontic.

The whole entity was scanned using a micro-CT scanner (HMX-XT 255, X-tek system, United Kingdom) with a tube voltage of 100 kV and a tube current of 170 μA. A total of 720 projections and four frames per projection were taken. The acquired images were reconstructed into a three-dimensional (3D) volume using the software CT Pro 3D (Nikon Metrology, Brighton, MI, USA). A central slice from the frontal plane of the 3D reconstructed image stack was selected for the construction of a two-dimensional (2D) finite element model. The selected image was exported to the software SolidWorks (Version 2011, Dassault Systèmes SolidWorks Corp., Waltham, MA, USA) as a reference sketch for creating the finite element model. Due to its simplicity and the quick turnaround, the 2D model was used extensively in the beginning to test the functionality of the structural optimization subroutine and to perform parametric studies.

For the 3D finite element model, segmentation of the three-dimensional volume was performed using the software Avizo 6.0 (Visualization Sciences Group, Burlington, MA, USA) to divide it into its constituent materials, i.e. enamel, dentin, bone and composite resin. The three-dimensional surface for each component was created and then exported as a stereolithography (STL) file. The STL file was imported into the software Hypermesh 10.0 (HyperWorks, Altair Engineering, Troy, MI, USA) for finite element model construction.

Because the present study mainly focused on the stress distributions within the restoration and the abutment tooth, the morphology of the mandibular jaw bone, which was sufficiently far away from the regions of interest, need not be modeled accurately. Thus, a rectangular block of 11-mm thick with a 2-mm thick top layer , which

represented the cancellous and cortical bone, respectively, was used to simulate the surrounding bone tissues (Figure 9.3). In addition, the mesh density of the bone block was made coarser than those in the restoration and tooth structure to reduce computational cost. The entire finite element model contained 26,636 nodes and 134,863 4-node tetrahedral elements (C3D4 [319]). All the interfaces were assumed to be tied perfectly in the finite element model. The material properties for each component are listed in Table 9.1. A concentrated force of 200 N was applied on the mesial fossa of the premolar pontic to simulate the worst chewing scenario. The boundary condition was defined such that all displacements were fixed at the bottom of the bone structure.

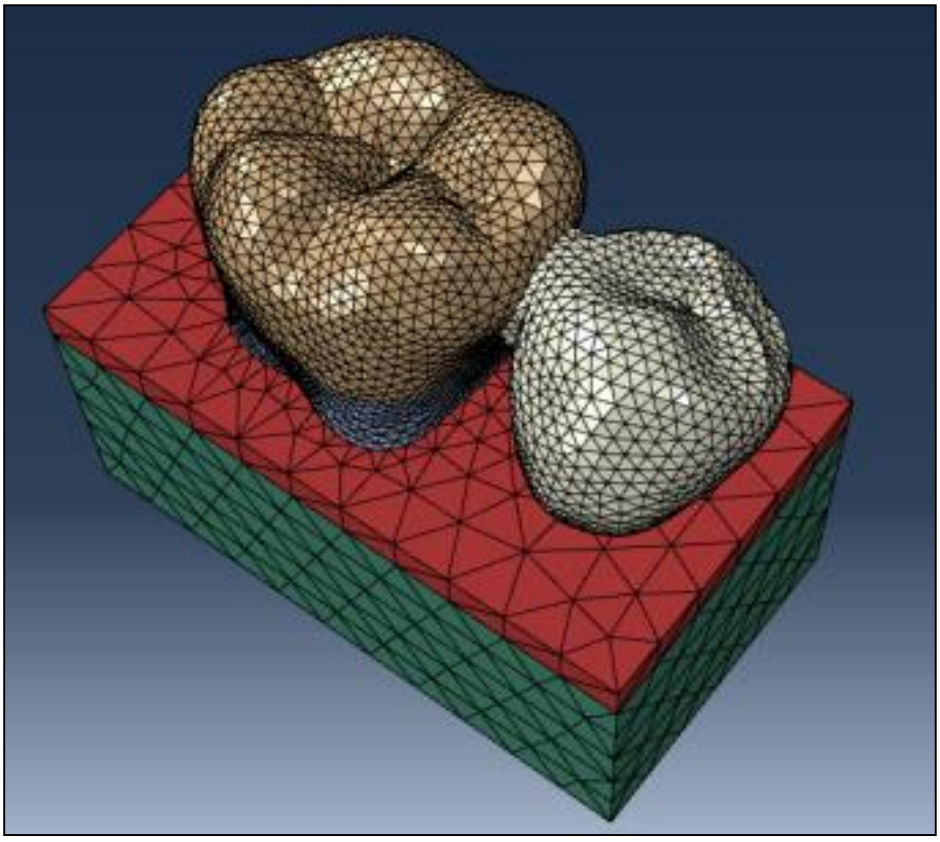

Figure 9.3 The finite element model of the 2-unit cantilevered bridge.

Table 9.1 Material properties used in the finite element model of the 2-unit cantilevered bridge

Material	Elastic Modulus (GPa)	Poisson's ratio	Ref.
Enamel	84.1	0.33	1
Dentin	18.6	0.31	2
Cortical Bone	13.7	0.3	3
Cancellous Bone	1.37	0.3	3
Composite	14	0.31	4
Glass Fiber	Ex 37 Vxy 0.27 Gxy 3.1 Ey 9.5 Vxz 0.34 Gxz 3.5 Ez 9.5 Vyz 0.27 Gyz 3.1		5

9.2.2 Two-step shape optimization

Shape optimization of the 2-unit cantilevered bridge was carried out in two steps using the software ABAQUS 6.10-EF1 (Dassault Systèmes Simulia, Waltham, MA, USA) in conjunction with a user-defined material subroutine that defined the constitutive model of a material according to its stress state. The first step of shape optimization was to obtain the optimal shape for the cavity preparation/retainer on the abutment by applying the subroutine to the tooth tissues only. Then, with the optimized retainer, the subroutine was applied to the restoration to seek an optimal fiber layout.

In the first step, the enamel and dentin of the abutment tooth were assigned with the User-Material in the input file so that they would call the SMT subroutine to update their solution (stress)-dependent material properties during the stress analysis. Initially, the material properties of these tooth tissues were set the same as those listed in Table 9.1. Subsequently, their elastic moduli were modified according to the predicted local stresses using the SMT subroutine to reduce the interfacial stress between the abutment tooth and the retainer. To this end, all elements within the tooth with stresses larger than the assumed failure stress were given the properties of the "softer" composite resin material. All other parameters, including the material properties for the remaining tooth tissues and bones, the applied load, and the boundary conditions, were kept the same during the whole analysis. In this way, a retainer with minimal interfacial stress gradually grew from the pontic into the abutment tooth.

In the second step, an inlay retainer was created within the abutment tooth using the cavity design derived in the previous step. The material properties of the remaining

enamel and dentin were reverted back to those constant values listed in Table 9.1 while the restoration was assigned with those of the User-Material that now assumed the properties of the unidirectional fibers. To obtain a proper fiber-reinforcing layout within the restoration, veneering resin composite material with local stresses higher than the assumed failure stress was gradually replaced with the "stronger" fiber material. Also, one important feature of the SMT subroutine was that it aligned the fiber automatically with the direction of the maximum principal stress.

There is a wide range of values reported for the bond strength between tooth and restoration and the fracture strength of resin composite material. A parametric study was performed to understand the effect of changing the assumed bond strength on the shape of the cavity preparation and that of changing the strength of resin material on the fiber layout. The failure stress was based on the bond strength of the resin material in the first step for the cavity design and on the fracture strength of the resin material in the second step for the FRC bridge design. For both steps, the assumed failure stress ranged from 5 to 30 MPa, in steps of 5 MPa. The material transformation process would continue iteratively until the results converged.

9.2.3 Final comparison between the conventional and optimal designs

A step-box shaped cavity/retainer was used for the conventional 2-unit cantilevered FRC dental bridge [156, 320]. The width of the box started at 2.5 mm in the mesial fossa of the first premolar and increased to 3.5 mm on the marginal ridge. The depth of the occlusal inlay was 2 mm and the occlusal step was 4 mm (Figure 9.4). The glass fiber was horizontally placed and fully embedded with composite resin in the middle third of the connector region and the mesial part of the pontic (Figure 9.4). The designs provided by the optimization exercise may contain features that cannot be realized easily in practice; therefore, when constructing the model for the optimized design, practical issues, such as the cavity shape that can actually be made, need to be taken into account. Thus, the final finite element model for the optimized FRC bridge was a simplified version of the design suggested by the shape optimization.

Finally, stress analyses of the shape-optimized and conventional designs were carried out to compare their mechanical performances. To evaluate their resistance against retainer debonding and restoration fracture, the stresses at the tooth-restoration interface and those within the restoration were compared between the two designs.

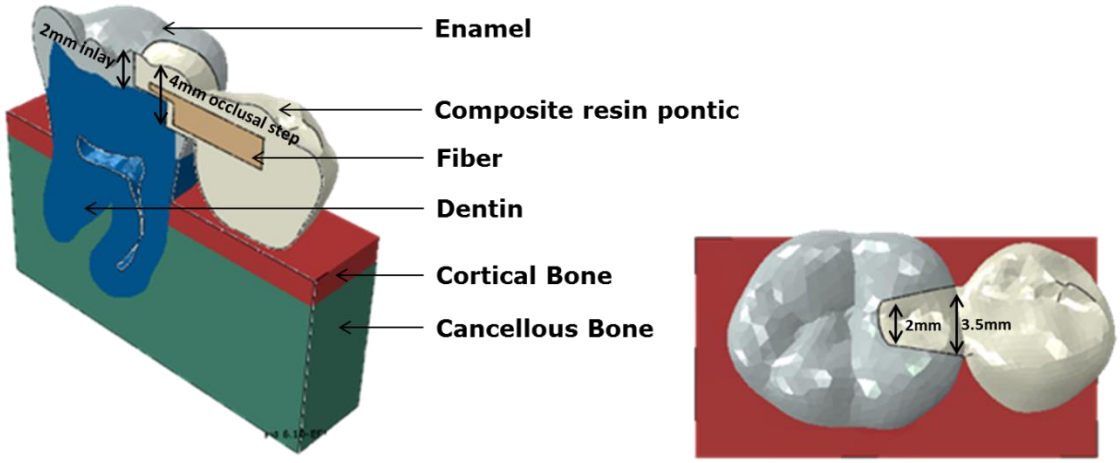

Figure 9.4 The conventional design of the 2-unit cantilevered FRC bridge.

9.3 Results

9.3.1 Shape optimization of the 2-unit cantilevered FRC bridge

The results showed that, irrespective of the failure stress (σ_{Ref}) assumed, the cavity/retainer derived from the SMT optimization was shovel-shaped (Figure 9.5). If a lower bond strength was considered a larger cavity preparation was required. For example, the cavity preparation may need to be extended to the central fossa of the molar if the bond strength is lower than 20 MPa. The results based on a failure stress of 25 MPa, which was lower than the reported bond strength [321], were used conservatively for constructing the model for the optimal design. The size of the optimized retainer was slightly smaller than the conventional step-box shaped design (26.1 mm^3 versus 26.2 mm^3); however, in terms of the area of the bonding surface, the optimal design was 17.5% smaller than the conventional one (31.3 mm^2 versus 38.0 mm^2).

According to the results from the second step of the SMT optimization, fibers should be placed at the top of the connector region where tensile stress was highest (Figure 9.6). The lower is the assumed failure strength of the resin material, the more fibers need to be used, and vice versa.

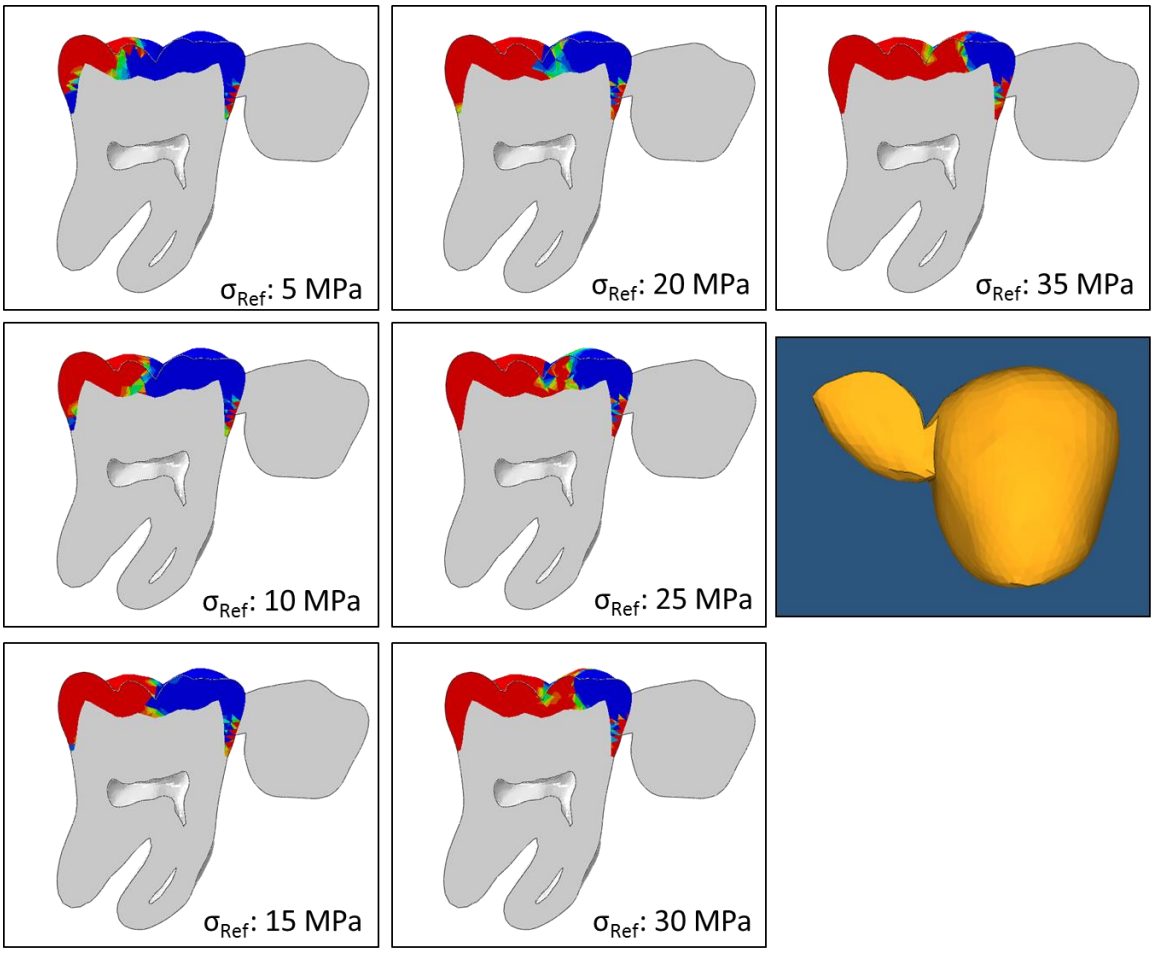

Figure 9.5 Results from the first step of SMT optimization (cavity/retainer design).

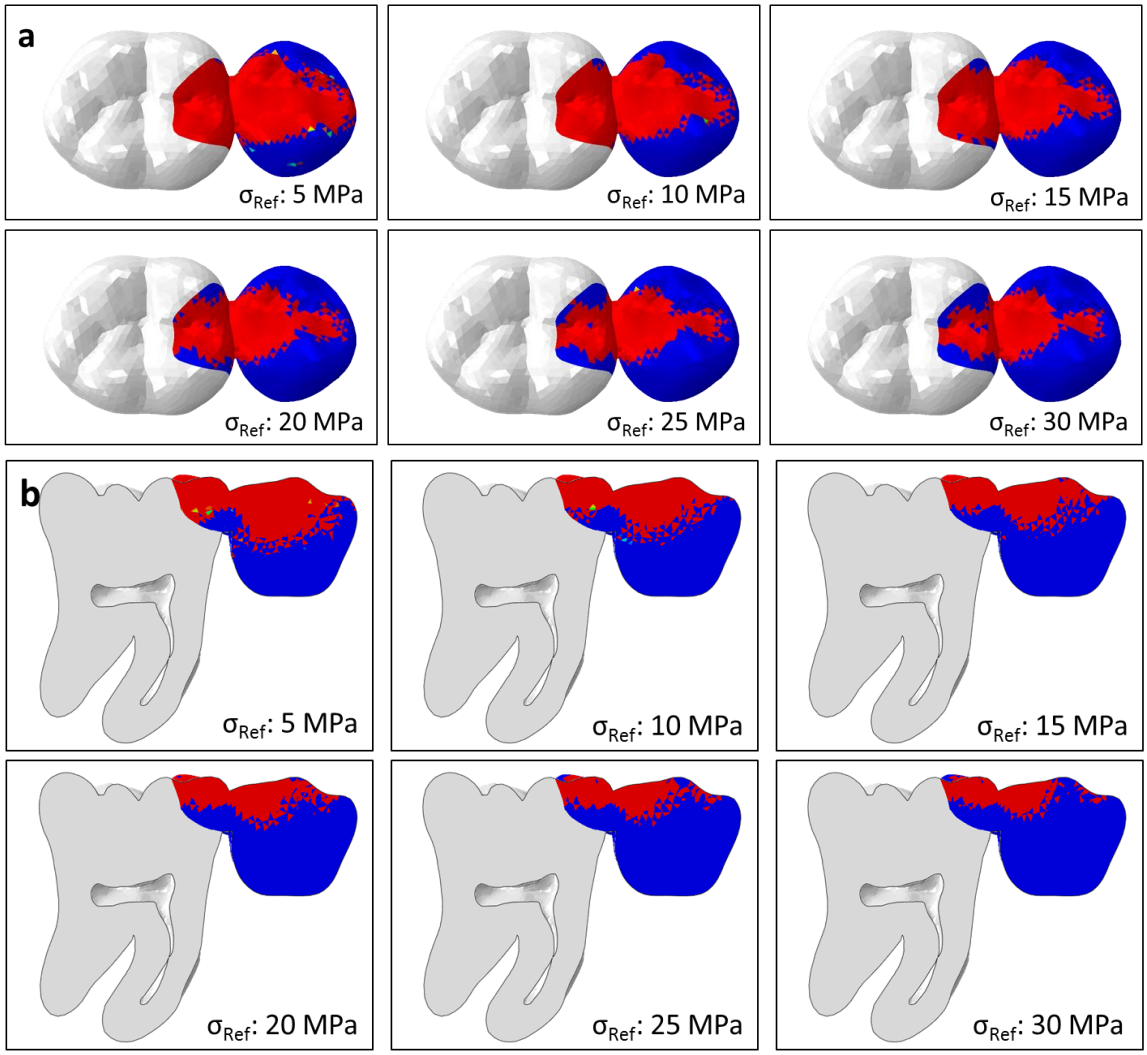

Figure 9.6 Profiles of the fiber layout suggested by the SMT optimization with different values of failure stress for the resin composite: (a) top view. (b) cross-sectional view.

9.3.2 Comparison between the conventional design and optimized design

Figure 9.7 shows the stress profiles of the two designs under a vertical load of 200N at the mesial fossa of the second-premolar pontic. High tensile stresses can be seen in the occlusal third of the connector region. In the optimized design, the fiber substructure carries most of the high tensile stresses. In contrast, the composite resin material in the conventional design is not reinforced properly. Only the top half of the fiber substructure carries tensile stresses, and high tensile stresses can be found in the weaker veneering composite. Compared with the conventional step-box design, the shovel-shaped cavity preparation has a 70% reduction (189.6 MPa versus 57.04 MPa) in the maximum interfacial tensile stress (Figure 9.8a). With the optimized design, the maximum principal stresses in the veneering composite and in the tooth structure are also reduced by 45% (638.8 MPa versus 356.5 MPa; Figure 9.8b) and 30% (372.2 MPa versus 253.1 MPa; Figure 9.9), respectively.

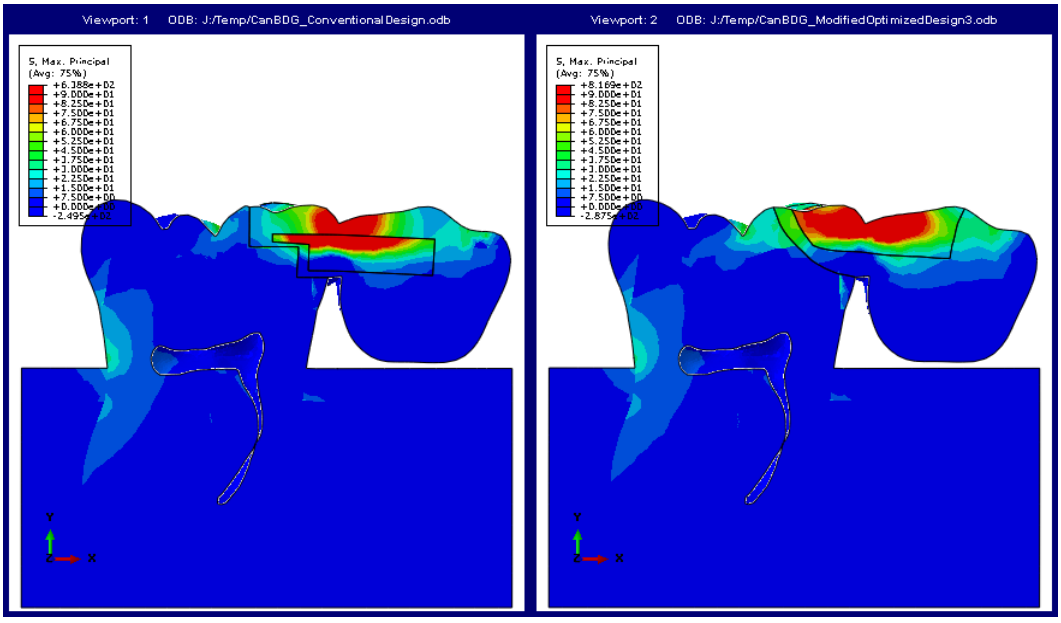

Figure 9.7 Stress profiles of the conventional (left) and optimized (right) designs.

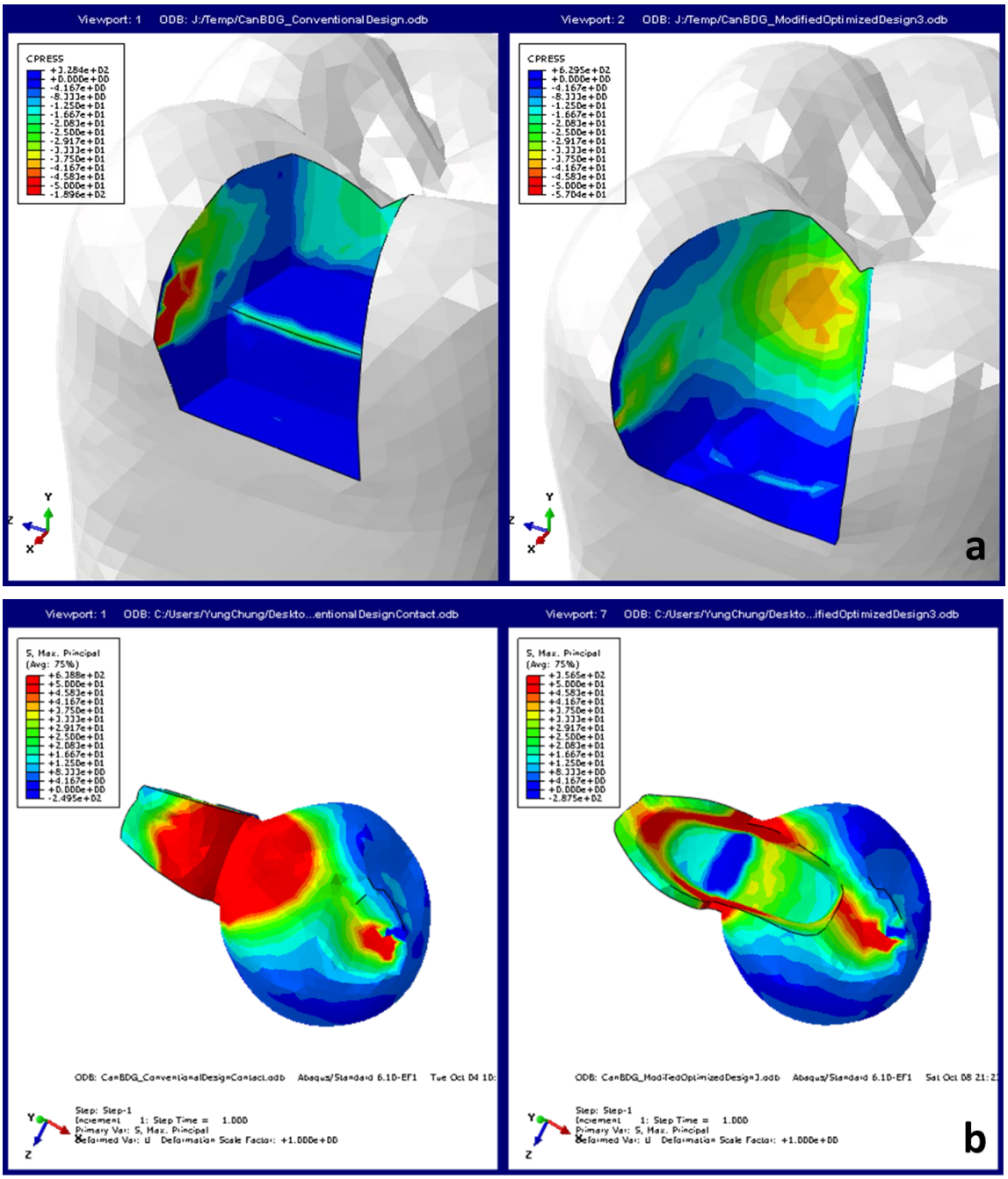

Figure 9.8 Stress plots of the conventional (left) and optimized (right) designs: (a) normal stress distribution at the tooth-restoration interface; (b) maximum principal stress distribution within the restoration.

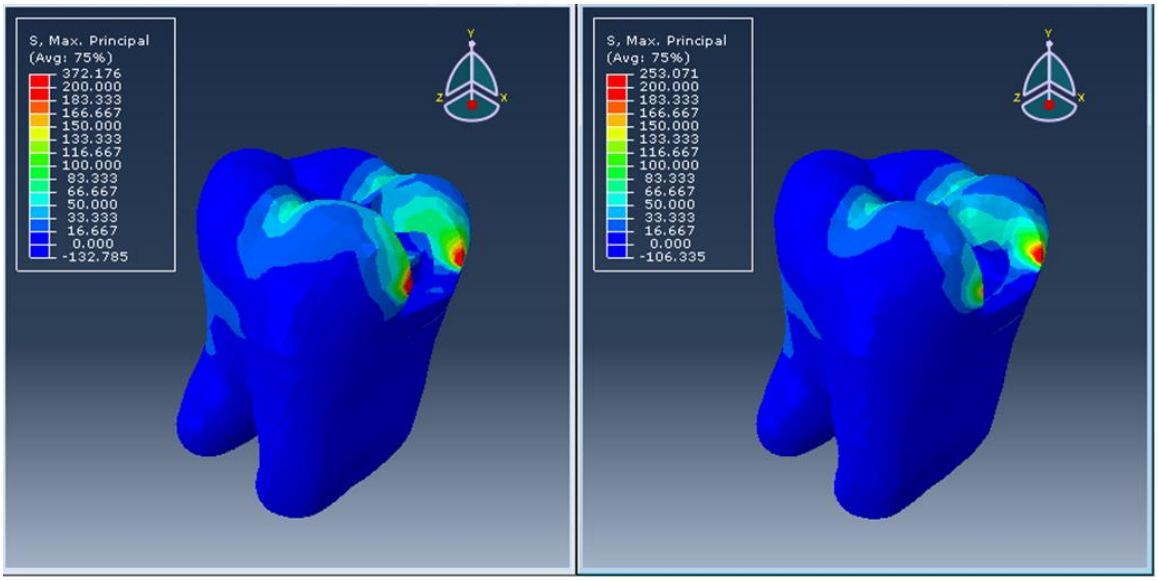

Figure 9.9 Maximum principal stress distributions within the tooth with the conventional (left) and optimized (right) designs.

9.4 Discussion

The optimized design of the 2-unit cantilevered FRC bridge uses the same amount of reinforcing fibers as the conventional design; however, its mechanical performance was far better. With roughly the same bonding surface, the optimized shovel-shaped cavity has lower interface stresses, which means that the risk of debonding can be reduced with the optimized cavity design. Comparison between the stress profiles of the two designs confirms that the fiber substructure of the optimized design is better aligned with the maximum principal stress trajectories; therefore, it minimized the normal and shear stress at the resin-fiber interface to lower the risk of delamination. The results of stress analysis also showed that the maximum principal stress within the veneering resin of the optimized design is reduced by 45%, which is expected to decrease the occurrence of cracking within the restoration.

It has been reported that inlay-retained FRC bridges often fail at lower loads than those having more extensive-coverage retainers such as wing-retained or onlay-retained [116, 156]. In an era of minimally-invasive dentistry, the conservation of tooth tissues should be the first priority when designing a dental restoration for patients. The present study aimed at seeking an optimal cavity design that can improve the retention for inlay-retained cantilever bridges.

In this study, a bond strength of 25 MPa between the tooth and restoration was selected so that the optimized design had a similar cavity/retainer size to the conventional one. This allowed the influence of changing the fiber layout to be assessed properly and independently. The actual bond strength between the tooth and composite resin is usually

higher than 25 MPa; therefore, the size of the cavity preparation can be even smaller so that more tooth tissues can be preserved. However, there should be enough room in the cavity to accommodate the fiber reinforcement. Clinically, the suggested dimensions of the inlay cavity are at least 2 mm wide by 2 mm deep. The cavity size derived from the SMT optimization using 25 MPa as the failure stress (σ_{Ref}) conformed to this clinical guideline. While the area of the bonding surface was reduced by 17.5%, it is believed that the lower interfacial stress would help to better retain the restoration.

As suggested by the SMT optimization, the fiber has to be placed at the top of the connector. With this configuration, the high tensile stresses will be suitably carried by the fiber material so that the maximum principal stress in the veneering composite can be reduced by 45%. Figure 9.10 showed a similar fiber layout that has been proposed by Keulemans et al [156]. In that design, fibers were placed near the occlusal surface where high tensile stresses are expected. They also distributed additional fiber-reinforcement in the inlay from the top to the bottom, which is not suggested by the SMT optimization. Thus, the amount of fiber used in their design may not be efficient. In fact, to more closely follow the maximum principal stress distribution, the SMT optimization suggested that the best shape of the fiber should be that of a bowtie (Figure 9.6). Given the difficulty to fabricate a bowtie-shaped fiber in practice, a simple rectangular box was used in our final design. Compared to the conventional design, this can still reduce the maximum principal stress by 45%.

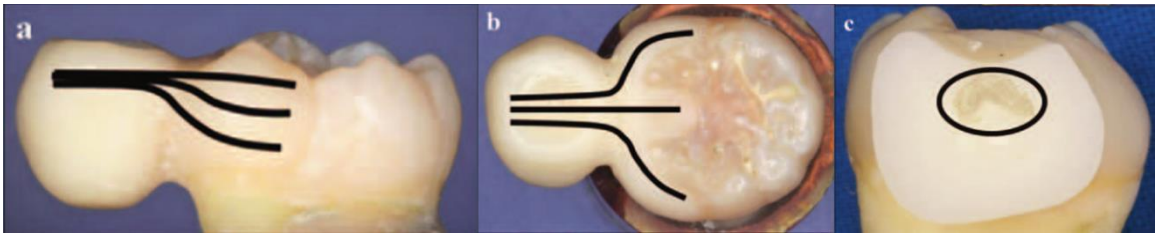

Figure 9.10 Fiber layout in a two-unit cantilevered FRC bridge [156]. (a) lateral view (b) occlusal view (c) cross-sectional view through the pontic.

As shown in Figure 9.8a, high interfacial tensile stress concentrated on the labial and lingual axial walls of the cavity, particularly in the conventional design. These are also the places where debonding of the restoration usually initiates clinically. Previous studies have reported tooth fracture as one of the failure modes of the inlay-retained restoration [322, 323]. This is because the intracoronal preparations weaken the tooth structure, especially those with the box-shaped design that has many sharp line angles resulting in an unfavorable stress distribution. With the optimized shovel-shaped cavity design, the peak maximum principal stress in the tooth is reduced by 30%, which is expected to help lower the risk of tooth fracture.

Clinically, the FRC cantilevered bridge restoration has been mainly used as an interim prosthesis. Also, most of the studies focused on the application of the cantilevered bridge in the anterior region [324, 325]. Compared to the 3-unit bridge, the cantilevered bridge involves less tooth preparation, and it allows oral hygiene to be maintained more easily. These are attractive advantages. With improved mechanical performance, the optimized FRC cantilevered bridge will be a promising design for longer-term use.

9.5 Conclusion

The results of this study proposed a 2-unit cantilevered bridge with a shovel-shaped retainer and reinforcing fiber placed at the top of the connector area. With its lower interfacial and structural stresses, the new, optimized design is expected to perform better mechanically than the conventional design. This can potentially offer a more conservative treatment option for replacing the single missing tooth.

Chapter 10 In vitro validation of shape-optimized fiber-reinforced composite dental bridges

10.1 Background

As mentioned in Chapter 9, fiber-reinforced composite (FRC) bridges have the advantages of being minimally invasive and providing a metal-free prosthetic reconstruction with excellent esthetics. FRC systems have been extensively used for fabricating adhesive fixed partial denture (AFPD). Current designs of FRC bridges, however, do not have an adequate lifespan. The main failure mode was documented as delamination between the fibers and the resin matrix [115-119]. Fractures also occurred at the loading point [117, 118, 120], the Pontic, and the connectors linking the pontic to the abutments [121-123].

In a recent study, the innovative stress-induced material transformation (SMT) shape optimization technique, was used in conjunction with the FE method to optimize the FRC substructure layout of a 3-unit FPD [314]. This was achieved by gradually reinforcing the regions with high tensile stresses with FRC material such that the fibers were aligned with the direction of the maximum principal stress. Using the SMT technique, parameters such as the volume, position and orientation of the fibers in a dental restoration can be simultaneously optimized according to the stress distribution. The optimization analysis indicated a U-shape FRC substructure for the 3-unit bridge that followed the bottom profile of the pontic. The numerical results showed that the proposed optimized design significantly reduced the highest maximum principal stress in the veneering composite at both the connector and pontic positions. The SMT technique has

also been used to design the 2-unit cantilevered bridge and the cavity design for the abutment tooth. The detailed optimization procedures and the results for this FPD have already been given in Chapter 9.

The aim of this chapter was to validate the new AFPD designs of inlay-retained 3-unit and 2-unit (cantilevered) bridges obtained by the SMT technique using simulated occlusal loading. To detect subcritical cracking more effectively, acoustic emission (AE) measurement was performed during the mechanical test. Although AE measurement has been performed in investigations of the fracture behavior of dental materials [138-141], the present study represents the first attempt at using the AE technique for monitoring the fracture behavior of FRC bridges during in-vitro mechanical testing.

10.2 Materials and Methods

10.2.1 Preparation of inlay-retained 3-unit FRC dental bridge specimens

To prepare the FRC bridge specimens, a prosthetic restoration jaw model (D18FE-500A-QF, Nissin, Japan) was modified to duplicate the edentulous condition considered in the previous structural optimization study [314]. The right mandibular first molar was removed from the model, and the remaining socket was filled with paraffin wax. Two proximal boxes were prepared, respectively, in the distal region of the second premolar (with the size of 3mm × 2mm × 3mm) and the mesial region of the second molar (with the size of 4mm × 3mm × 3mm); see Figure 10.1a. Then, a half-arch impression was taken with vinyl polysiloxane impression material (Examixfine™ (injection type), GC, Japan) and silicone putty (Vertex™ Putty 1:1, Vertex-Dental, The Netherlands). The mold was poured with a stone material (Die-Keen, Columbus Dental, St. Louis, MO) to fabricate the working cast for the FRC bridges.

In total, forty-one 3-unit posterior inlay FRC bridges were fabricated with unidirectional glass fibers (FibreKor 2k bundle, Jeneric/Pentron, Wallingford, CT, USA) as the substructure, which was surrounded by a veneering composite (Gradia, GC, Japan). Fiber strips of 3 mm wide and 0.3 mm thick were used in this study. These were cut with a pair of ceramic scissors to the appropriate inter-abutment length. Three fiber strips were condensed and bonded together with a flowable composite (Filtek™ Supreme XT Flowable, 3M, USA), with each strip being light polymerized for 40 seconds with a curing machine (GC STEPLIGHT SL I, GC, Japan) as it was laid down in the desired position to form the FRC substructure. Two different layouts of the FRC substructure

were prepared: the conventional (n=20) and the optimized layout (n=21) considered in the previous structural optimization study [314]. The conventional layout was a straight beam linking one proximal box to the other, while the optimized layout was a curved beam following the bottom profile of the pontic; see Figure 10.1b.

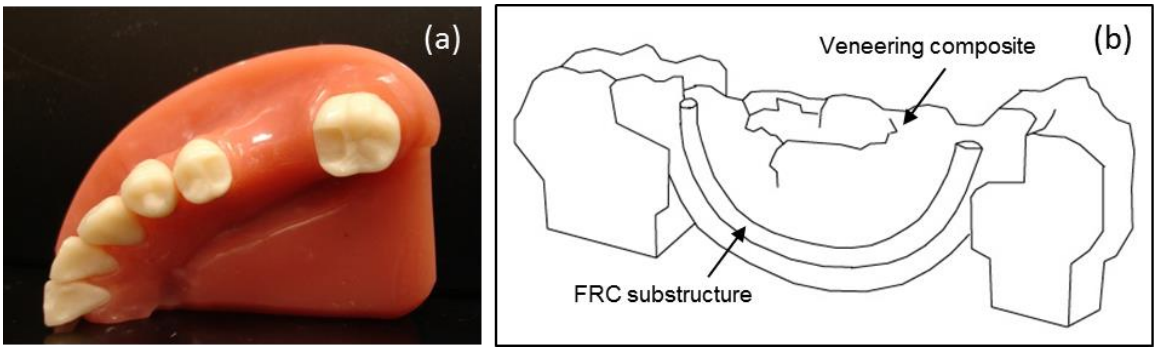

Figure 10.1 (a) Duplicated right mandibular model with prepared proximal boxes on the abutment teeth. (b) The optimized layout of the FRC substructure.

The layer of veneering composite resin was built up incrementally and polymerized with the same curing machine (GC STEPLIGHT SL I, GC, Japan) used for curing the fibers. The size and outline of the whole FRC bridge were controlled by a prefabricated silicone mold to ensure uniformity among the specimens. According to a previous study [326], using a handheld light-curing unit would not provide an adequate degree of monomer conversion and cross-linking in the resin matrix. An additional 10-minute light polymerization was performed with another curing unit (CURE-LITE Plus, Jeneric/Pentron, Wallingford, CT, USA) specifically built for preparing FRC bridges. Each sample was polished with a low-speed air brush together with a fine paste (Universal Polishing Paste, Ivoclar-Vivadent, Schaan, Lichtenstein).

10.2.2 Preparation of inlay-retained 2-unit cantilevered FRC dental bridge specimens

For the 2-unit cantilevered FRC dental bridge, a two-step optimization process was used to first obtain a cavity design for improving the retentive strength and then the fiber position for enhancing the structural strength. Accordingly, samples prepared for validating the optimized design of this prosthesis were divided into two groups: resin-based cantilevered bridges without glass fibers (n=20; ten for each cavity design: step-box and shovel-shaped) and those with glass fibers (n=20; ten for each fiber layout: conventional and optimized), to test their bond strength and structural strength. As suggested by the results from Chapter 9, the optimized design should have a shovel-shaped retainer and the fiber should be placed in the top region of the connector where the stresses are highly concentrated. The same specimen preparation protocol as described in 10.2.1 was applied for fabricating the bridges containing fibers. To ensure dimensional uniformity of the cavities and bridges without fibers, a CAD/CAM system (ARDENTA, Activity 850, Taiwan) with its bundled software exoCAD dental (build 4903, exoCAD GmbH, Germany) was used to design and fabricate the abutments and the cantilevered bridges with conventional step-box and optimized shovel-shaped retainers (Figure 10.2). A polymethyl methacrylate (PMMA) material, which can provide similar bonding capability and mechanical properties to human dentin, was used for the fabrication of the abutments. A total of 40 abutments were made and mounted individually in Delrin rings using an orthodontic resin (Caulk, DENSPLY, Milford, DE, USA).

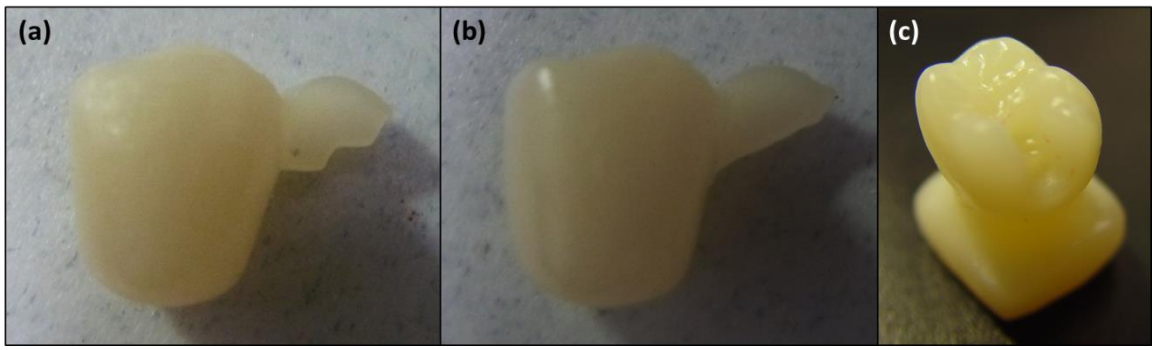

Figure 10.2 Specimens prepared for validating the cavity design for the 2-unit cantilevered bridge: (a) Conventional step-box retainer, (b) optimized shovel-shaped retainer and (c) resin-based abutment.

10.2.3 Loading

A servo-hydraulic testing machine (MTS 810, MTS, Minneapolis, MN, USA) was used to apply a compressive load to the individual specimen placed at the lower part of the testing machine. The 3-unit bridges were secured onto the duplicated stone model (working cast) using a cyanoacrylates-based adhesive (Scotch® Super Glue Gel, 3M, St. Paul, MN, USA). The 2-unit cantilevered bridges without fibers were cemented to the resin abutment using a resin-based dental cement (RelyX™ Ultimate, 3M ESPE, St. Paul, MN, USA). Those with reinforcing fibers were cemented to the resin abutment using a cyanoacrylates-based adhesive to ensure that they remained in place without debonding while they were loaded to fracture.

For the 3-unit bridges, the force, up to 400 N, was applied using a steel ball of 6 mm diameter and a loading speed of 0.2 mm per minute on the central fossa of the pontic replacing the right mandibular first molar. For the 2-unit cantilevered bridges, they were

loaded on the mesial fossa of the premolar pontic until the occurrence of debonding or fracture using the same loading apparatus and speed. Displacement of the 3-unit specimens could result in the bottom of the pontic coming into contact with the working cast, leading to unrepresentative loading conditions. Therefore, to prevent the above from happening, a thin layer (~1.5 mm) of material underneath the pontic was removed from the stone cast. During loading, both the force and displacement of the loading sphere were recorded by computer software (LJstream, LabJack, Lakewood, CO, USA) for subsequent analysis.

10.2.4 Acoustic emission measurement

A two-channel acoustic emission (AE) system, which comprises a signal sensor, a preamplifier and a recording device, was used to monitor the development of cracks in the specimens during loading. Measuring AE signals while mechanically testing the FRC bridges could provide real-time detection and monitoring of their fracture development with a higher sensitivity [141, 327]. An AE wideband sensor (S9225, Physical Acoustic Corporation (PAC), NJ, USA) was glued onto the middle third of the buccal surface of the molar, which was the pontic for the 3-unit bridge, and the abutment for the 2-unit cantilevered bridge. Signals detected by the sensor were passed through a preamplifier (Model 2/4/6, PAC, NJ, USA) with a 40 dB gain and a band pass of 100 kHz to 2MHz. Recording of the signals was performed with the AEwin software (PAC, NJ, USA) using a sampling frequency of 1 MHz. A threshold value of 35 dB was imposed on the signals to filter out the background noise.

10.2.5 Data processing

The load-displacement data and the AE results obtained from the compressive test of each specimen were processed by using the computing software Matlab (The Mathworks, USA). After filtering out the noise from the data, the accumulated number of AE events and the amplitude of individual AE event for each specimen were extracted. Further, the sum of amplitudes from all AE events was calculated to provide a measure of the total strain energy released by each specimen. The plot of AE signal amplitude versus time was superimposed upon the load-displacement curve as shown in Figure 10.3. The first cracking event was determined from both the first abrupt drop in the load-displacement curve and the first detectable AE signal (amplitude > 35 dB). The time and corresponding force level of the first detectable cracking event were noted from the two sets of data. The mean and standard deviation of all the measured values were computed. The T-test was used to evaluate the statistical significance of the differences in the measurements between the two specimen groups: conventional and optimized design. The level of statistical significance was set at $\alpha = 0.05$.

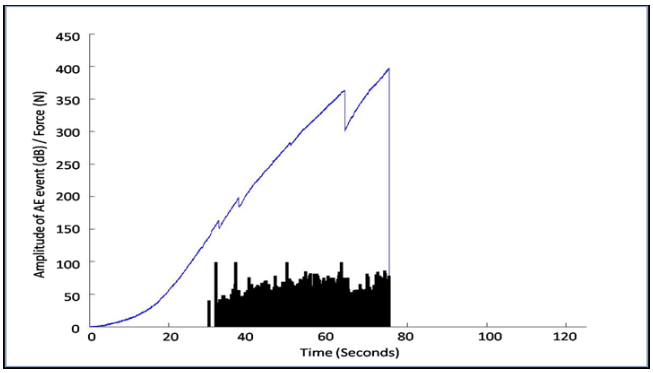

Figure 10.3 The superimposition of the load-displacement curve and amplitudes of AE events for a specimen under loading.

10.2.6 Qualitative analysis

After mechanical loading, all specimens were examined with a stereo microscope (MVX10, Olympus, Japan) at 20X magnification. To detect subsurface cracks nondestructively, all specimens were scanned with a micro-CT system (HMX XT H 255, X-tek system, Brighton, MI, USA). Micro-CT images were taken with a tube voltage of 110 kV and a tube current of 90 µA. For each specimen, 720 projections and 4 frames per projection were acquired. The images obtained were processed using the software CT Pro 3D (Metris, Hertfordshire, United Kingdom) with the following sequence of operation: beam hardening correction, noise reduction, and three-dimensional reconstruction. After reconstruction, volume rendering of each specimen was performed using the software VG Studio (Version 2.0 64bit, Volume Graphics GmbH, Germany).

10.3 Results

10.3.1 3-unit bridges: conventional straight-beam vs. optimized U-shaped fiber layout

No damage was visible on the duplicated stone model after testing with it all the specimens to 400 N. When the specimens were examined with the stereo microscope, cracks could clearly be seen on the surfaces of all the specimens from the conventional group; their directions being approximately perpendicular to the trajectories of the most tensile stresses (Figure 10.4a). Fractures could also be observed around the loading point on the specimens from this group (Figure 10.4b). As for the optimized group, only six specimens were found with small cracks in the connector areas; no cracks were seen near the loading point.

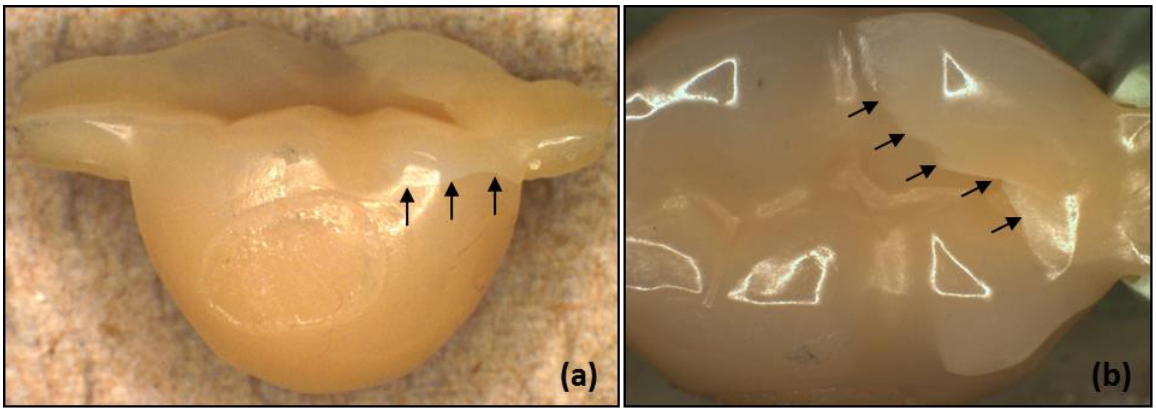

Figure 10.4 (a) A visible crack at the connecter area between the pontic and the second premolar; (b) Fracture around the loading point.

Figure 10.5 shows the micro-CT images of the FRC bridges after testing from both the conventional and optimized groups. The maximum length of the small number of cracks found in the optimized group was approximately 0.70 mm, and they only existed within the resin under the connector area. In contrast, the cracks in the

conventional group went through the fiber substructure with a maximum length of around 3.72 mm.

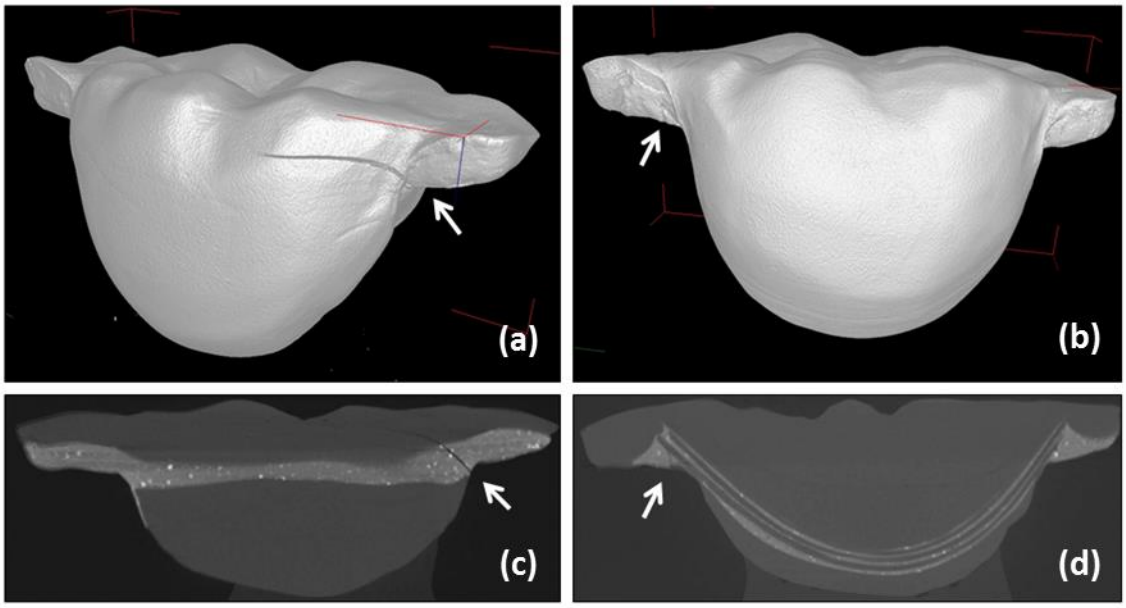

Figure 10.5 Micro-CT images of 3-unit FRC dental bridges after mechanical test: (a) 3-D reconstruction of a specimen from the conventional group, (b) 3-D reconstruction of a specimen from the optimized group, (c) CT image slice from the conventional group showing that the crack went through the fiber substructure and (d) CT image slice from the optimized group showing limited crack propagation within the connector area.

The load-displacement curves of the two groups displayed significant differences. The group of specimens with the conventional design showed larger deflections under the same load level, indicating their lower stiffness. There were several abrupt drops in the load corresponding to local damage of the structure. This phenomenon was absent in the group of specimens with the optimized design, which displayed smoother as well as steeper load-displacement curves (Figures 10.6a and 10.6b). The shape-optimized specimens were stiffer and stronger in resisting fracture. The plot of the cumulative

number of AE events for all specimens showed that cracking began at around 40 seconds after loading (Figure 10.6c). Both the rate of occurrence and the total number of AE events were substantially higher in the conventional design group.

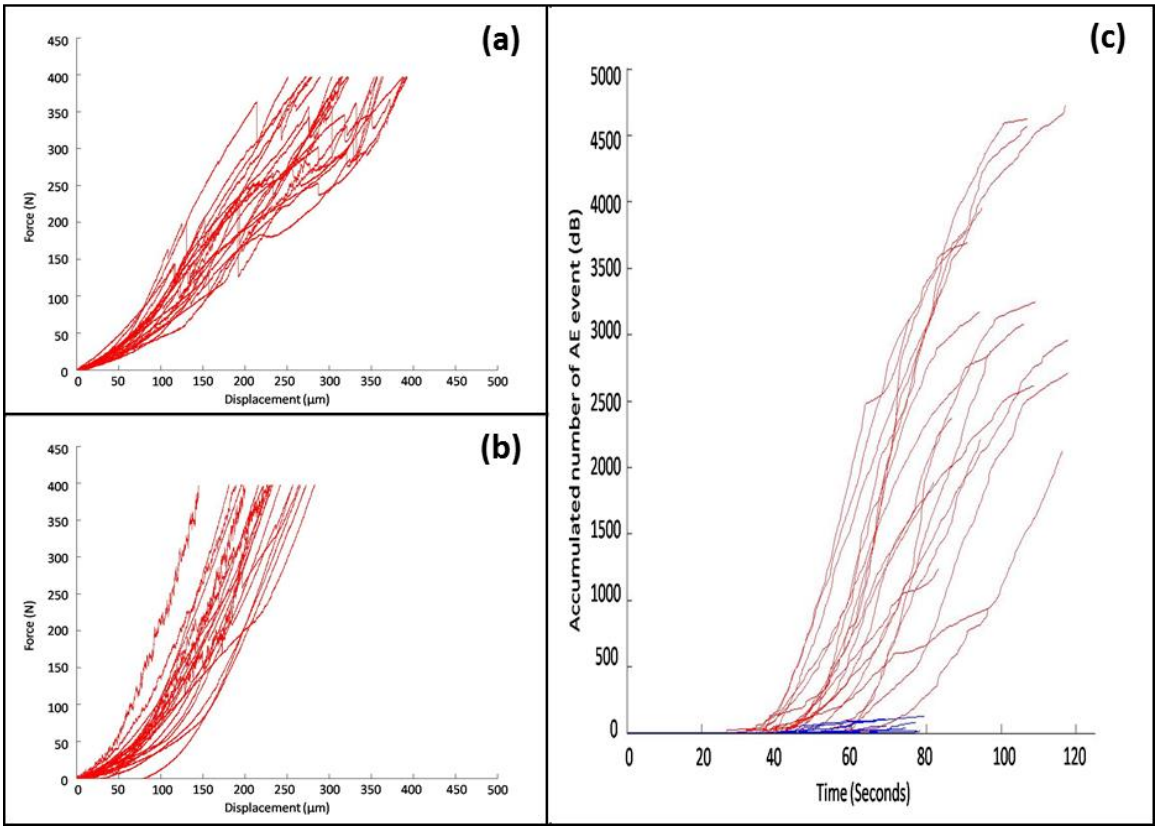

Figure 10.6 Mechanical test results: (a) load-displacement curves of specimens from the conventional group, (b) load-displacement curves of specimens from the optimized group, and (c) the cumulative number of AE events. The curves of the conventional group are plotted in red and those of the optimized group are plotted in blue.

The mean number of AE events per specimen in the group of the conventional design was significantly higher than that in the group of the optimized design (Conventional group: 2969 ± 1034; Optimized group: 38 ± 42; P-value < 0.001). One specimen in the optimized group showed no detectable AE signals at all. In terms of the

mean amplitude for each AE event, there was no statistically significant difference between the two groups (Conventional group: 45.4 ± 0.5 dB; Optimized group: 44.4 ± 10.7 dB; P-value = 0.65). The mean accumulated amplitude of all AE events per specimen, a measure of the strain energy released calculated by multiplying together the mean amplitude of the AE signal and the mean number of AE events, further demonstrated the significant difference in the mechanical performance between the two groups of specimens (Conventional group: 134914.2 ± 47302.1 dB; Optimized group: 1749.9 ± 1911.9 dB; P-Value < 0.001).

The sensitivity of the two methods, load and AE measurements, used to detect cracking in this study was assessed by comparing the time corresponding to the first drop in force level with that corresponding to the first AE event detected. Because no abrupt drops could be discerned from the load-displacement curves of the specimen group with the optimized design, the comparison was only made for the group with the conventional design. The time and force level corresponding to the first cracking event indicated by the two methods were very different. The mean time to the first detectable AE signal was significantly earlier than that to the first abrupt drop in load (Load-displacement curve: 43.7 ± 8.7 seconds; AE measurement: 35.1 ± 11.5 seconds; P-Value < 0.001) (Figure 10.7a). Correspondingly, the AE system also detected the first cracking event at a lower force level than the load-displacement curve did (Load-displacement curve: 161.9 ± 39.2 N; AE measurement: 109.0 ± 40.1 N; P-Value < 0.001) (Figure 10.7b).

When comparing the times to the first cracking event as given by the AE data between the two groups of specimens, no statistically significant difference was found

(Conventional group: 35.1 ± 11.5 seconds; Optimized group: 40.2 ± 14.0 seconds; P-value = 0.22); see Figure 10.7c; however, the corresponding force levels were modestly different between the two groups. The first cracking event in the shape-optimized group was detected at a higher force level (Conventional group: 109.0 ± 40.1 N; Optimized group: 164.7 ± 93.0 N; P-value = 0.02); see Figure 10.7d.

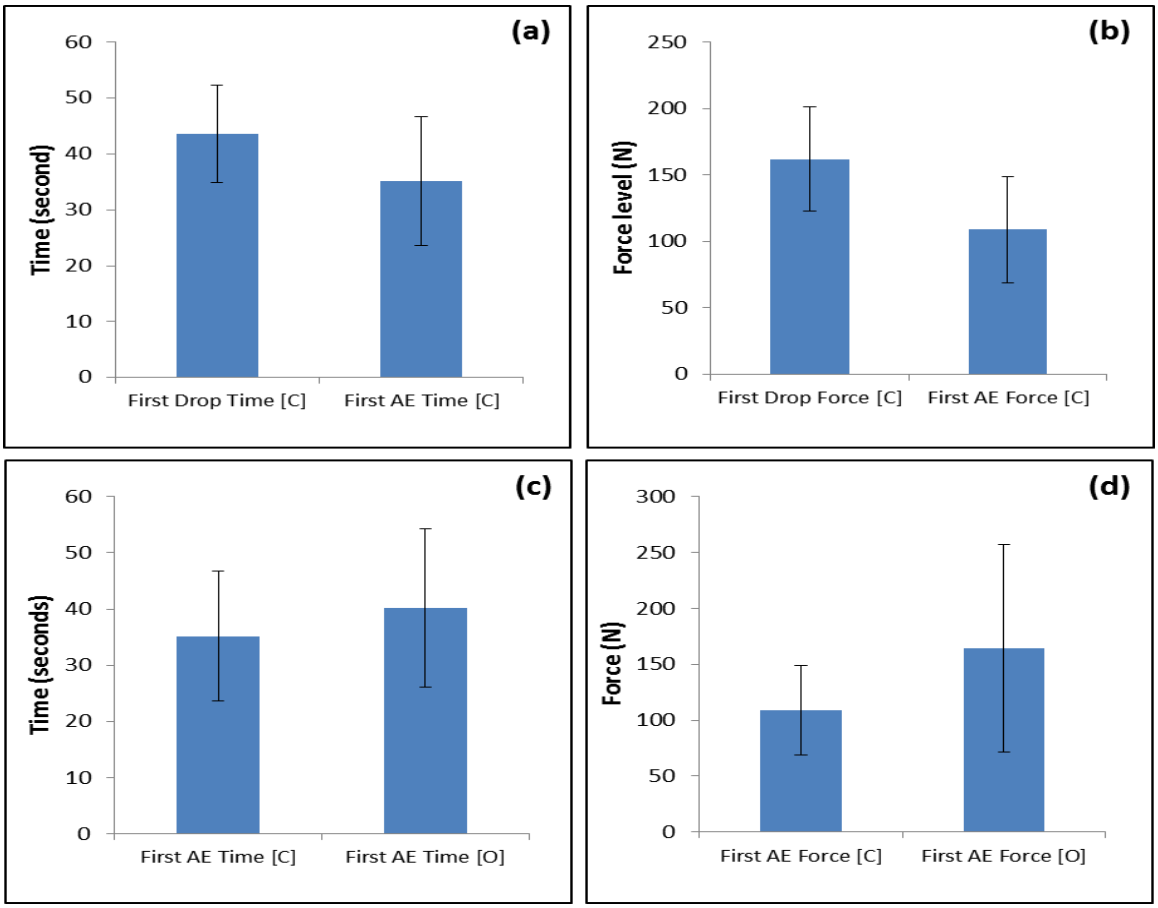

Figure 10.7 (a) Comparison of the times of the first cracking event indicated by the load-displacement curve and AE measurement. (b) Comparison of the force levels of the first cracking event indicated by the load-displacement curve and AE measurement. (c) Comparison of the times of the first cracking event between the conventional and optimized group. (d) Comparison of the force levels of the first cracking event between the conventional and optimized group.

10.3.2 Validation of cavity design for 2-unit cantilevered bridges: conventional step-box vs. optimized shovel-shaped design

The 2-unit bridge specimens were loaded until they fractured totally or were dislocated from the abutments, which is different from the in vitro validation of the 3-unit bridge. No subcritical crack length measurement was performed. All specimens without the reinforcing fibers debonded before they fractured, and no cracks were seen within them. The pontic of one specimen with the conventional step-box retainer was found to have contacted the base during loading, so it was excluded from the analysis. With the unreinforced bridges, the average failure load using the optimized shovel-shaped cavity design was 212% higher than the conventional step-box design (step-box design: 15.98 ± 6.57 N; Shovel-shaped design: 49.95 ± 17.33 N; P-value < 0.001); see Table 10.1. The mean number of AE events per specimen (step-box design: 49 ± 34; Shovel-shaped design: 63 ± 32; P-value = 0.42) and the mean amplitude for each AE event (step-box design: 58.4 ± 1.2 dB; Shovel-shaped design: 59.5 ± 2.4 dB; P-value = 0.28) were not significantly different between the two designs. In terms of the time to failure, the two groups did not show a very significant difference either (step-box design: 251.71 ± 144.28 s; Shovel-shaped design: 297.51 ± 66.73 s; P-value = 0.45); however, the optimized shovel–shaped design had a smaller standard deviation, i.e. a more consistent outcome.

10.3.3 Validation of optimized 2-unit cantilevered bridge with reinforcing fibers

In terms of the failure mode, eight specimens from the conventional FRC group fractured at the connector region and the other two specimens debonded from the abutments. In contrast, only four specimens from the optimized group fractured at the connector region, five remained intact but their abutments fractured, and only one debonded from its abutment.

The optimized design had a 108% higher mean final failure load than the conventional step-box design (conventional group: 97.32 ± 21.10 N; Optimized group: 203.35 ± 28.02 N; P-value < 0.001); see Table 10.2. Figure 10.8 demonstrates that major cracking occurred at a higher load level in the optimized design, indicating its superior load capacity. Again, the mean number of AE events per specimen (conventional group: 28 ± 19; Optimized group: 52 ± 53; P-value = 0.24) and the mean amplitude for each AE event (conventional group: 64.9 ± 4.2 dB; Optimized group: 61.7 ± 5.2 dB; P-value = 0.18) were not significantly different between the two groups. The results from the mechanical test of the 2-unit cantilevered bridges are summarized in Tables 10.1 and 10.2.

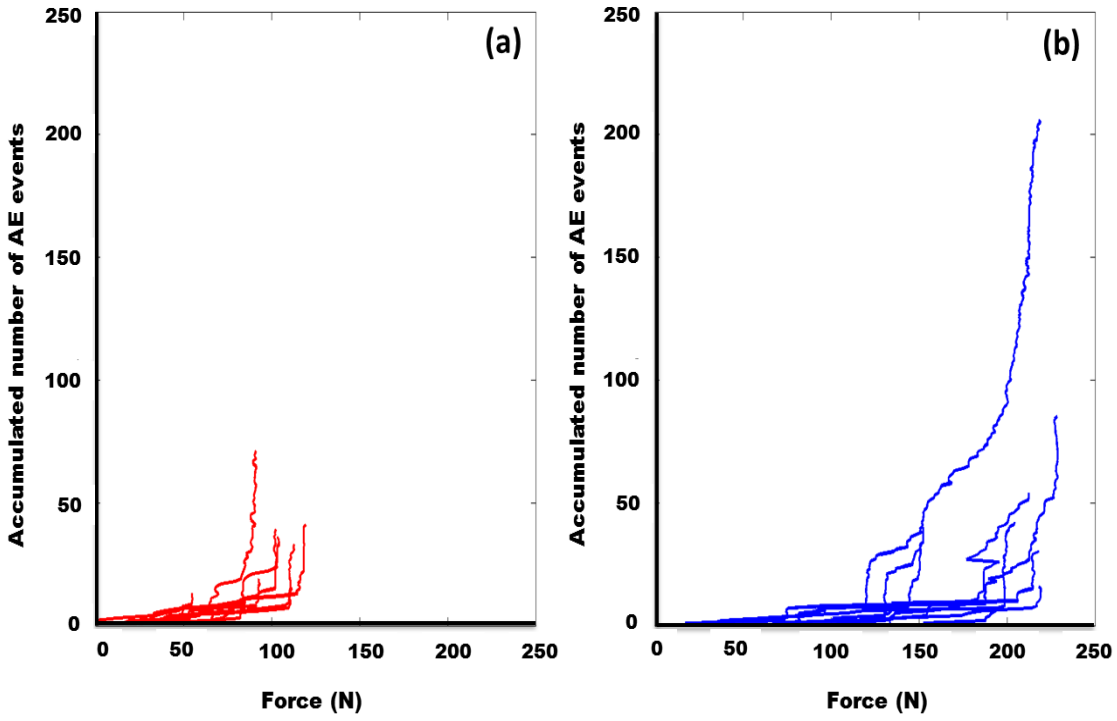

Figure 10.8 Plots of accumulated numbers of acoustic emission events against force: (a) Conventional fiber layout with the step-box retainer design and (b) Optimized fiber layout with the shovel-shaped retainer design.

Table 10.1 Results of the validation test for the cavity design using unreinforced specimens

	Shovel-Shaped Design		Step-box Design	
Sample #	**Failure Load**	**No. of AE Event**	**Failure Load**	**No. of AE Event**
1	69.824	145	12.891	79
2	68.750	38	10.742	37
3	38.672	59	8.594	1
4	33.301	70	25.781	100
5	56.934	93	236.328*	116*
6	53.711	56	10.742	28
7	42.969	71	24.707	89
8	26.855	35	15.039	12
9	30.078	43	19.336	13
10	78.418	20	25.781	83
Average (±S.D.)	49.95 ± 17.33	63 ± 32	38.99 ± 15.98	56 ± 40
Excluding outlier*			17.07 ± 6.23	49 ± 34

Table 10.2 Results of the validation test for the 2-unit FRC cantilevered bridge

	Optimized Group		Conventional Group	
Sample #	**Failure Load**	**No. of AE Event**	**Failure Load**	**No. of AE Event**
1	207.32	8	116.02	15
2	166.50	8	123.54	41
3	221.29	54	95.61	71
4	160.06	40	85.94	9
5	227.73	16	108.50	39
6	237.40	85	62.30	13
7	209.47	42	118.16	33
8	226.66	30	54.79	7
9	154.69	33	108.50	36
10	222.36	206	99.90	19
Average (±S.D.)	203.35 ± 28.02	52 ± 53	97.32 ± 21.10	28 ± 19

10.4 Discussion

10.4.1 3-unit bridges

According to the finite element analysis of the previous study [314], the 3-unit FRC bridge had high tensile stresses concentrated near the loading point and the connector regions that linked the pontic and the teeth. Fracture was predicted to occur perpendicularly to the trajectories of the most tensile stresses. In this in-vitro experiment, major crack lines could be observed only in the conventional group, the locations and patterns of fracture being in line with the previous FE results. Chipping was also seen near the loading point in this group of specimens where high tensile stresses were predicted. The lack of visible cracking in the group of shape-optimized specimens showed that the new fiber layout and the much thicker veneering composite under the loading point were effective in helping the dental bridge to resist fracture and chipping.

The posterior teeth sustain 90 percent of the occlusal force (Premolar: 12 ± 7 %; Molar: 78 ± 8%) [328]. The FRC bridge is expected to experience relatively high loads if it is used to replace these teeth. The maximum load used in the present study (400 N) was lower than the reported maximum masticatory force [329]. This was mainly limited by the mechanical strength of the working stone cast used for supporting the specimens during loading. Nevertheless, the applied load was sufficient to cause major structural damage to the conventional FRC bridges. In fact, significant damage occurred at a relatively low force level (161.9 ± 39.2 N). Failure at such a low force level represents a risk to the clinical performance of the dental bridge. The lack of major structural damage

in the optimized design confirmed that fiber reinforcement in the appropriate region could significantly increase the load capacity of this type of prosthesis.

With the more sensitive AE system, the present study was able to monitor the subcritical micro-crack and fracture development more precisely. The AE system was able to pick up micro-cracking in the materials that cannot be detected by the load-displacement curve; see Figure 10.3. It was also shown in Figures 10.7a and 10.7b that the time and force level of the first cracking event detected by the AE system were significantly earlier and lower than those from the load-displacement curves. Therefore, to monitor the development of fracture more effectively, it is essential to use the AE measurement technique.

The mean AE signal amplitude was not significantly different between the two groups of specimens (Conventional group: 45.4 ± 0.5 dB; Optimized group: 44.4 ± 10.7 dB; P-value = 0.65), indicating that the mechanisms of fracture, i.e. fiber delamination and veneer fracture, were probably similar for the two groups. Although the mean amplitude of an AE event was similar between the two groups, specimens of the conventional design had far more AE events during the course of loading (Conventional group: 2969; Optimized group: 38). This indicated that they had a much lower load capacity, releasing more strain energy irreversibly under load.

There was also no significant difference in the time to the first cracking event between the two groups (Conventional group: 35.1 ± 11.5 seconds; Optimized group: 40.2 ± 14.0 seconds; P-value = 0.22); see Figure 10.7c. There was, however, a small difference in the force level at which the first cracking occurred between the two groups,

as shown in Figure 10.7d, with the optimized group starting to crack later. The optimized group had a steeper load-displacement curve (Figure 10.6b), which was related to the enhanced structural stiffness of the new fiber layout. The increased stiffness of the FRC bridge reduced the deflection of the structure under load. Because the load was applied by a stroke-controlled mode, i.e. at a constant rate of 0.2 mm/min, the steeper load-displacement curve of the optimized sample (Figure 10.6a and 10.6b) led to a steeper load-time curve; therefore, at a particular time, the force level in the optimized sample was higher than the conventional one.

Previous studies suggested that a low-amplitude AE signal can be correlated to the internal cracking of the veneering materials and a high-amplitude AE signal can be correlated to the interfacial delamination between the fibers and the veneering materials [135, 137, 141, 330, 331]. Results from the present study showed that AE signals with a higher amplitude coincided with the abrupt drops in the load-displacement curve (Figure 10.3). The latter method, therefore, does not seem to be able to detect the early cracking in the veneering materials. Although the mean AE signal amplitude was not significantly different between the two groups, the conventional group contains much more AE events of high amplitude (>60 dB) than the optimized group (Conventional group: 6841 in total; Optimized group: 332 in total).

10.4.2 2-unit cantilevered bridges

Again, the mean AE signal amplitude was not significantly different between the two groups of specimens in both validation tests ((1) Step-box design: 58.4 ± 1.2 dB; Shovel-shaped design: 59.5 ± 2.4 dB; P-value = 0.28; (2) Conventional group: 64.9 ± 4.2 dB; Optimized group: 61.7 ± 5.2 dB; P-value = 0.18); however, the mean AE signal amplitude from the second validation test for the 2-unit FRC bridges was found to be higher than that from the first test for the cavity designs. This could be due to the fact that the second test involved fiber delamination, and/or that the veneering resin used in the 2-unit FRC bridges was different from that used in the unreinforced ones.

In the validation tests, all specimens were loaded at the mesial fossa to simulate the worst chewing scenario. The mean failure load of the optimized design was around 200 N, which is acceptable for clinical use. A meticulous occlusal adjustment, which can balance the occlusal force and reduce excessive occlusal contacts on the pontic, should further increase the clinical performance of the optimized design.

Unlike the 3-unit bridges, the mean number of AE events did not show any significant statistical difference between the conventional and optimized groups (Conventional group: 28 ± 19; Optimized group: 52 ± 53; P-value = 0.24). This was probably because all 2-unit specimens were loaded until they fractured totally or debonded from the abutments, and most of the AE events occurred towards the end of failure, irrespective of the design.

The present study was limited to using static loading as a means of in-vitro validation of the optimized designs. Failure of dental restorations was mostly caused by

cyclic mechanical loading with a lower force, resulting in more progressive crack initiation and development [332]. An increased static strength is a strong indicator of improved mechanical performance, even under cyclic loading. To more closely test the long-term durability in the oral environment, the influence of intraoral moisture, multiaxiality of the occlusal force, and the cushioning effect of the periodontal ligament can be investigated in future studies.

10.5 Conclusion

The in-vitro experiments carried out in this study validated the optimized design of the 3-unit bridge proposed by the previous study [314] and that of the 2-unit bridge derived in Chapter 9. The much lower number of AE events and a much smoother load-displacement curve for the 3-unit bridge and the much higher failure load for the 2-unit cantilever bridge indicated that the optimized FRC bridge designs had a higher load capacity. It is expected that the optimized designs will significantly improve the clinical performance of FRC bridges.

Chapter 11 Summary and Future works

11.1 Summary

This project was aimed at exploring, at multiple levels, various features of a natural tooth's inherent structural design that enable it to perform its mechanical functions effectively, and then applying design principles inspired by these investigations to the design of prostheses for replacing a single missing tooth. The findings from analyzing the natural tooth's structures, including orientations of enamel rods, spatial distributions of material properties, and inclination of a tooth within a jaw bone, support our general hypothesis that these arrangements, which range from the micro to the macro scale, are optimized for accommodating the functional demands, i.e. occlusal loading. The directional orientation of the enamel rods introduces anisotropy to the crown, which is beneficial for transferring the load directly into the tougher dentin underneath and for reducing unfavorable stress concentration along the DEJ. The graded material distribution, with which the local stiffness decreases gradually from the outer part of a tooth towards the inner part, results in a better stress distribution and mechanical performance. The natural inclination of the incisors does leads to a more pleasing appearance, less occlusal interference, and a more favorable stress distribution within the tooth and the surrounding bone structures.

Based on these findings, two optimized designs were developed for dental restorations to replace the single missing tooth: a two-unit cantilevered fiber-reinforced composite bridge, and a bi-layered all-ceramic crown. Both of these designs take advantage of the design principles found in nature. To reinforce a composite resin-based

restoration using anisotropic glass-fiber material, it is very important for the fibers to be placed in the region of high tensile stress concentration and to be oriented along the maximum principal stress plane to maximize their efficiency. For a two-unit cantilevered fiber-reinforced composite dental bridge that restores a missing molar, the design of the retainer also needs to be optimized to prevent it from debonding due to the heavy occlusal load. Shape optimization of the retainer was achieved by using an UMAT subroutine that can update material properties interactively with results from the stress analysis. Optimization of the material layout for the all-ceramic crown was achieved by using the graded material distribution found in natural enamel. The layered all-ceramic crown with the optimized material layout demonstrated final fracture strength comparable to that of the conventional zirconia-porcelain design and reduced incidences of chipping, the major of failure clinically. Moreover, manufacturing of the optimized crown can take full advantage of modern CAD/CAM techniques, which will result in greater productivity with less laboratory error. The in vitro validation tests of both prostheses indicated that the mechanical performance of the optimized designs were superior to the conventional ones.

11.2 Suggestions for future work

- The optimization algorithm can be tailored to simulate bone formation and resorption. This would replace the trial-and-error approach used in this study for seeking an optimal position and orientation for the placement of a dental implant.. The same algorithm can also be used for predicting the movement of teeth during orthodontic treatments.

- The structural optimization of the fiber-reinforced composite restoration can be applied to other types of dental prostheses such as complete dentures or removable partial dentures.
- Other laboratory protocols for fabricating the optimized bi-layered ceramic crown should be investigated; for example, using pressable ceramic materials. Furthermore, glass-infiltrated alumina-based ceramics can be considered for establishing the graded material distribution found in nature.
- Although the superior performance of the proposed optimized designs has been partly validated with mechanical tests, clinical trials should be performed in the future to more fully test their performance.

Bibliography

1. Agerholm DM, Sidi AD: **Reasons given for extraction of permanent teeth by general dental practitioners in England and Wales**. *British dental journal* 1988, **164**(11):345-348.
2. Ong G: **Periodontal disease and tooth loss**. *International dental journal* 1998, **48**(3 Suppl 1):233-238.
3. Hamasha AA, Sasa I, Al-Qudah M: **Risk indicators associated with tooth loss in Jordanian adults**. *Community dentistry and oral epidemiology* 2000, **28**(1):67-72.
4. Gilbert GH, Miller MK, Duncan RP, Ringelberg ML, Dolan TA, Foerster U: **Tooth-specific and person-level predictors of 24-month tooth loss among older adults**. *Community dentistry and oral epidemiology* 1999, **27**(5):372-385.
5. Brown LJ: **Trends in tooth loss among U.S. employed adults from 1971 to 1985**. *Journal of the American Dental Association* 1994, **125**(5):533-540.
6. Suominen-Taipale AL, Alanen P, Helenius H, Nordblad A, Uutela A: **Edentulism among Finnish adults of working age, 1978-1997**. *Community dentistry and oral epidemiology* 1999, **27**(5):353-365.
7. Dye BA, Tan S, Smith V, Lewis BG, Barker LK, Thornton-Evans G, Eke PI, Beltran-Aguilar ED, Horowitz AM, Li CH: **Trends in oral health status: United States, 1988-1994 and 1999-2004**. *Vital Health Stat 11* 2007(248):1-92.
8. Griffin SO, Barker LK, Griffin PM, Cleveland JL, Kohn W: **Oral health needs among adults in the United States with chronic diseases**. *Journal of the American Dental Association* 2009, **140**(10):1266-1274.
9. Thean HP, Wong ML, Koh GC, Wong AS: **Oral health status and treatment needs of elderly residents in a Singapore nursing home**. *Annals of the Academy of Medicine, Singapore* 2009, **38**(3):282-283.
10. Aguirre-Zero O, Greene M, Wright ER: **Oral health needs in Indiana: developing an effective and diverse workforce**. *J Indiana Dent Assoc* 2009, **88**(4):6-13.
11. **National Institute of Dental and Craniofacial Research: Dental Caries (Tooth Decay) in Adults (Age 20 to 64)** [https://www.nidcr.nih.gov/DataStatistics/FindDataByTopic/DentalCaries/DentalCariesAdults20to64.htm]
12. Leclercq MH, Barmes DE, Infirri JS: **Oral health: global trends and projections**. *World health statistics quarterly Rapport trimestriel de statistiques sanitaires mondiales* 1987, **40**(2):116-128.
13. Cortelli JR, Pallos D, Krug T, Cortelli SC, Hart TC: **Prevalence of missing teeth in adolescents and young adults**, vol. 4; 2010.
14. **Committee Opinion No. 569: oral health care during pregnancy and through the lifespan**. *Obstetrics and gynecology* 2013, **122**(2 Pt 1):417-422.
15. **Global goals for oral health in the year 2000. Federation Dentaire Internationale**. *International dental journal* 1982, **32**(1):74-77.
16. Hobdell MH, Myburgh NG, Kelman M, Hausen H: **Setting global goals for oral health for the year 2010**. *International dental journal* 2000, **50**(5):245-249.
17. Hobdell M, Petersen PE, Clarkson J, Johnson N: **Global goals for oral health 2020**. *International dental journal* 2003, **53**(5):285-288.
18. Chrisopoulos S: **Oral health and dental care in Australia: Key facts and figures 2012**. 2012.

19. **The Status of Oral Disease in Massachusetts: A Great Unmet Need 2009.** Boston, Massachusetts Massachusetts Department of Public Health, Office of Oral Health.; 2009.
20. Paul AF: **Evidence-Based Decision Making: Replacement of the Single Missing Tooth**. *Dental clinics of North America* 2009, **53**(1):97-129.
21. Fugazzotto PA: **Evidence-based decision making: replacement of the single missing tooth**. *Dent Clin North Am* 2009, **53**(1):97-129, ix.
22. **Dental Crowns and Bridges Can Restore Your Smile** [http://www.xrtc.org/?p=12]
23. Pjetursson BE, Bragger U, Lang NP, Zwahlen M: **Comparison of survival and complication rates of tooth-supported fixed dental prostheses (FDPs) and implant-supported FDPs and single crowns (SCs)**. *Clinical oral implants research* 2007, **18 Suppl 3**:97-113.
24. Rubinstein S, Nidetz A: **A multidisciplinary approach to single-tooth replacement**.
25. Seltzer S, Bender IB: **The Dental Pulp: Biologic Considerations in Dental Procedures**: Lippincott Williams & Wilkins; 1984.
26. Ericson S, Hedegard B, Wennstrom A: **Roentgenographic study of vital abutment teeth**. *J Prosthet Dent* 1966, **16**(5):981-987.
27. Selby A: **Fixed prosthodontic failure. A review and discussion of important aspects**. *Australian dental journal* 1994, **39**(3):150-156.
28. Bergenholtz G, Nyman S: **Endodontic complications following periodontal and prosthetic treatment of patients with advanced periodontal disease**. *Journal of periodontology* 1984, **55**(2):63-68.
29. Cheung GS: **A preliminary investigation into the longevity and causes of failure of single unit extracoronal restorations**. *J Dent* 1991, **19**(3):160-163.
30. Karlsson S: **A clinical evaluation of fixed bridges, 10 years following insertion**. *J Oral Rehabil* 1986, **13**(5):423-432.
31. Valderhaug J, Jokstad A, Ambjornsen E, Norheim PW: **Assessment of the periapical and clinical status of crowned teeth over 25 years**. *J Dent* 1997, **25**(2):97-105.
32. Priest GF: **Esthetic Comparisons of Alternatives for Replacement of a Single Missing Tooth**. *Journal of Esthetic and Restorative Dentistry* 1996, **8**(2):58-65.
33. Mankoo T: **Contemporary implant concepts in aesthetic dentistry--Part 1: Biologic width**. *Practical procedures & aesthetic dentistry : PPAD* 2003, **15**(8):609-616; quiz 618.
34. Dhir S: **Significance and clinical relevance of biologic width to implant dentistry**. *Journal of Interdisciplinary Dentistry* 2012, **2**(2):84.
35. Romanos GE, Traini T, Johansson CB, Piattelli A: **Biologic width and morphologic characteristics of soft tissues around immediately loaded implants: studies performed on human autopsy specimens**. *Journal of periodontology* 2010, **81**(1):70-78.
36. Tarnow D, Elian N, Fletcher P, Froum S, Magner A, Cho S-C, Salama M, Salama H, Garber DA: **Vertical distance from the crest of bone to the height of the interproximal papilla between adjacent implants**. *Journal of periodontology* 2003, **74**(12):1785-1788.
37. Misch CE: **Contemporary Implant Dentistry**: Mosby Elsevier; 2008.
38. Esposito M, Grusovin MG, Kwan S, Worthington HV, Coulthard P: **Interventions for replacing missing teeth: bone augmentation techniques for dental implant treatment**. *Australian dental journal* 2009, **54**(1):70-71.
39. Esposito M, Grusovin MG, Coulthard P, Worthington HV: **The efficacy of various bone augmentation procedures for dental implants: a Cochrane systematic review of randomized controlled clinical trials**. *The International journal of oral & maxillofacial implants* 2006, **21**(5):696.

40. Rocchietta I, Fontana F, Simion M: **Clinical outcomes of vertical bone augmentation to enable dental implant placement: a systematic review**. *Journal of clinical periodontology* 2008, **35**(s8):203-215.
41. Chiapasco M, Casentini P, Zaniboni M: **Bone augmentation procedures in implant dentistry**. *The International journal of oral & maxillofacial implants* 2009, **24**:237.
42. Mombelli A, Lang NP: **The diagnosis and treatment of peri-implantitis**. *Periodontology 2000* 1998, **17**(1):63-76.
43. Mattheos N, Schittek Janda M, Zampelis A, Chronopoulos V: **Reversible, non-plaque-induced loss of osseointegration of successfully loaded dental implants**. *Clinical oral implants research* 2012.
44. Steigenga J, Al-Shammari K, Misch C, Nociti Jr FH, Wang H-L: **Effects of implant thread geometry on percentage of osseointegration and resistance to reverse torque in the tibia of rabbits**. *Journal of periodontology* 2004, **75**(9):1233-1241.
45. Chun HJ, Cheong SY, Han JH, Heo SJ, Chung JP, Rhyu IC, Choi YC, Baik HK, Ku Y, Kim MH: **Evaluation of design parameters of osseointegrated dental implants using finite element analysis**. *Journal of oral rehabilitation* 2002, **29**(6):565-574.
46. Hansson S, Werke M: **The implant thread as a retention element in cortical bone: the effect of thread size and thread profile: a finite element study**. *Journal of biomechanics* 2003, **36**(9):1247-1258.
47. Mendonça G, Mendonca D, Aragao FJ, Cooper LF: **Advancing dental implant surface technology–from micron-to nanotopography**. *Biomaterials* 2008, **29**(28):3822-3835.
48. Schuler M, Owen GR, Hamilton DW, de Wild M, Textor M, Brunette DM, Tosatti SG: **Biomimetic modification of titanium dental implant model surfaces using the RGDSP-peptide sequence: a cell morphology study**. *Biomaterials* 2006, **27**(21):4003-4015.
49. Braem A, Chaudhari A, Vivan Cardoso M, Schrooten J, Duyck J, Vleugels J: **Peri-and intra-implant bone response to microporous Ti coatings with surface modification**. *Acta biomaterialia* 2014, **10**(2):986-995.
50. Merz BR, Hunenbart S, Belser UC: **Mechanics of the implant-abutment connection: an 8-degree taper compared to a butt joint connection**. *The International journal of oral & maxillofacial implants* 1999, **15**(4):519-526.
51. Piattelli A, Scarano A, Paolantonio M, Assenza B, Leghissa GC, Bonaventura GD, Catamo G, Piccolomini R: **Fluids and microbial penetration in the internal part of cement-retained versus screw-retained implant-abutment connections**. *Journal of periodontology* 2001, **72**(9):1146-1150.
52. Porter SS: **Platform switching: a new concept in implant dentistry for controlling postrestorative crestal bone levels**. *Dent, contemporary dentistry* 2006, **26**:9-17.
53. Canullo L, Rasperini G: **Preservation of peri-implant soft and hard tissues using platform switching of implants placed in immediate extraction sockets: a proof-of-concept study with 12-to 36-month follow-up**. *The International journal of oral & maxillofacial implants* 2006, **22**(6):995-1000.
54. Cappiello M, Luongo R, Di Iorio D, Bugea C, Cocchetto R, Celletti R: **Evaluation of peri-implant bone loss around platform-switched implants**. *The International journal of periodontics & restorative dentistry* 2008, **28**(4):347-355.
55. Sethi A, Kaus T, Sochor P: **The use of angulated abutments in implant dentistry: five-year clinical results of an ongoing prospective study**. *The International journal of oral & maxillofacial implants* 1999, **15**(6):801-810.

56. Planning OT: **Congenitally missing maxillary lateral incisors and orthodontic treatment considerations for the single-tooth implant**. *Journal* 2001, **67**:25-28.
57. Hagi D, Deporter D, Pilliar R, Arenovich T: **A targeted review of study outcomes with short (≤ 7 mm) endosseous dental implants placed in partially edentulous patients**. *Journal of periodontology* 2004, **75**(6):798-804.
58. Sun HL, Huang C, Wu YR, Shi B: **Failure rates of short (≤ 10 mm) dental implants and factors influencing their failure: a systematic review**. *The International journal of oral & maxillofacial implants* 2011, **26**(4):816.
59. Buser D, Martin W, Belser UC: **Optimizing esthetics for implant restorations in the anterior maxilla: anatomic and surgical considerations**. *The International journal of oral & maxillofacial implants* 2003, **19**:43-61.
60. Rosenstiel SF, Land MF, Fujimoto J: **Contemporary fixed prosthodontics**, 4th edn. St. Louis, Mo.: Mosby/Elsevier; 2006.
61. Castellani D, Baccetti T, Giovannoni A, Bernardini UD: **Resistance to fracture of metal ceramic and all-ceramic crowns**. *Int J Prosthodont* 1994, **7**(2):149-154.
62. Rosenstiel SF, Martin F, Fujimoto J: **Contemporary fixed prosthdontics**: Elsevier Health Sciences; 2006.
63. Shoher I, Whiteman AE: **Reinforced porcelain system: a new concept in ceramometal restorations**. *The Journal of prosthetic dentistry* 1983, **50**(4):489-496.
64. Sgrò S: **Principles of the metal framework design in metal-ceramic reconstructions**. *Quintessence Dent Technol* 2002, **21**:52.
65. Joska L, Venclikova Z, Poddana M, Benada O: **The mechanism of gingiva metallic pigmentations formation**. *Clinical Oral Investigations* 2009, **13**(1):1-7.
66. O'Boyle KH, Norling BK, Cagna DR, Phoenix RD: **An investigation of new metal framework design for metal ceramic restorations**. *The Journal of prosthetic dentistry* 1997, **78**(3):295-301.
67. Wall JG, Cipra DL: **Alternative crown systems. Is the metal-ceramic crown always the restoration of choice?** *Dent Clin North Am* 1992, **36**(3):765-782.
68. Taylor JA: **History of dentistry: a practical treatise for the use of dental students and practitioners**: Lea & Febiger; 1922.
69. White JD, McQuillen JH, Ziegler GJ, White JW, Kirk EC: **The Dental Cosmos: A Monthly Record of Dental Science. Devoted to the Interests of the Profession**: Jones & White; 1906.
70. McLean J: **The alumina reinforced porcelain jacket crown**. *The Journal of the American Dental Association* 1967, **75**(3):621-628.
71. Mackert JR, Butts MB, Morena R, Fairhurst CW: **Phase Changes in a Leucite-Containing Dental Porcelain Frit**. *Journal of the American Ceramic Society* 1986, **69**(4):C-69-C-72.
72. Mackert Jr J, Butts M, Fairhurst C: **The effect of the leucite transformation on dental porcelain expansion**. *Dental Materials* 1986, **2**(1):32-36.
73. Mackert J, Evans A: **Effect of cooling rate on leucite volume fraction in dental porcelains**. *Journal of dental research* 1991, **70**(2):137-139.
74. Garvie RC, Nicholson PS: **Structure and Thermomechanical Properties of Partially Stabilized Zirconia in the CaO-ZrO2 System**. *Journal of the American Ceramic Society* 1972, **55**(3):152-157.
75. Hannink RH, Kelly PM, Muddle BC: **Transformation Toughening in Zirconia-Containing Ceramics**. *Journal of the American Ceramic Society* 2000, **83**(3):461-487.

76. Brochu J-F, El-Mowafy O: **Longevity and clinical performance of IPS-Empress ceramic restorations-a literature review**. *Journal-Canadian Dental Association* 2002, **68**(4):233-238.
77. Denry I, Kelly JR: **State of the art of zirconia for dental applications**. *Dental Materials* 2008, **24**(3):299-307.
78. Bindl A, Mormann WH: **Fit of all-ceramic posterior fixed partial denture frameworks in vitro**. *The International journal of periodontics & restorative dentistry* 2007, **27**(6):567-575.
79. Kohorst P, Junghanns J, Dittmer MP, Borchers L, Stiesch M: **Different CAD/CAM-processing routes for zirconia restorations: influence on fitting accuracy**. *Clin Oral Investig* 2011, **15**(4):527-536.
80. Att W, Komine F, Gerds T, Strub JR: **Marginal adaptation of three different zirconium dioxide three-unit fixed dental prostheses**. *J Prosthet Dent* 2009, **101**(4):239-247.
81. Komine F, Gerds T, Witkowski S, Strub JR: **Influence of framework configuration on the marginal adaptation of zirconium dioxide ceramic anterior four-unit frameworks**. *Acta odontologica Scandinavica* 2005, **63**(6):361-366.
82. Tinschert J, Natt G, Mautsch W, Augthun M, Spiekermann H: **Fracture resistance of lithium disilicate-, alumina-, and zirconia-based three-unit fixed partial dentures: a laboratory study**. *Int J Prosthodont* 2001, **14**(3):231-238.
83. Sundh A, Molin M, Sjogren G: **Fracture resistance of yttrium oxide partially-stabilized zirconia all-ceramic bridges after veneering and mechanical fatigue testing**. *Dental materials : official publication of the Academy of Dental Materials* 2005, **21**(5):476-482.
84. Att W, Stamouli K, Gerds T, Strub JR: **Fracture resistance of different zirconium dioxide three-unit all-ceramic fixed partial dentures**. *Acta odontologica Scandinavica* 2007, **65**(1):14-21.
85. Att W, Grigoriadou M, Strub JR: **ZrO2 three-unit fixed partial dentures: comparison of failure load before and after exposure to a mastication simulator**. *J Oral Rehabil* 2007, **34**(4):282-290.
86. Wolfart S, Ludwig K, Uphaus A, Kern M: **Fracture strength of all-ceramic posterior inlay-retained fixed partial dentures**. *Dental materials : official publication of the Academy of Dental Materials* 2007, **23**(12):1513-1520.
87. Bahat Z, Mahmood DJ, Vult von Steyern P: **Fracture strength of three-unit fixed partial denture cores (Y-TZP) with different connector dimension and design**. *Swedish dental journal* 2009, **33**(3):149-159.
88. Vult von Steyern P, Kokubo Y, Nilner K: **Use of abutment-teeth vs. dental implants to support all-ceramic fixed partial dentures: an in-vitro study on fracture strength**. *Swedish dental journal* 2005, **29**(2):53-60.
89. Vult von Steyern P, Carlson P, Nilner K: **All-ceramic fixed partial dentures designed according to the DC-Zirkon technique. A 2-year clinical study**. *J Oral Rehabil* 2005, **32**(3):180-187.
90. Larsson C, Holm L, Lovgren N, Kokubo Y, Vult von Steyern P: **Fracture strength of four-unit Y-TZP FPD cores designed with varying connector diameter. An in-vitro study**. *J Oral Rehabil* 2007, **34**(9):702-709.
91. Tinschert J, Schulze KA, Natt G, Latzke P, Heussen N, Spiekermann H: **Clinical behavior of zirconia-based fixed partial dentures made of DC-Zirkon: 3-year results**. *Int J Prosthodont* 2008, **21**(3):217-222.

92. Molin MK, Karlsson SL: **Five-year clinical prospective evaluation of zirconia-based Denzir 3-unit FPDs**. *Int J Prosthodont* 2008, **21**(3):223-227.
93. Crisp RJ, Cowan AJ, Lamb J, Thompson O, Tulloch N, Burke FJ: **A clinical evaluation of all-ceramic bridges placed in UK general dental practices: first-year results**. *British dental journal* 2008, **205**(9):477-482.
94. Edelhoff D, Florian B, Florian W, Johnen C: **HIP zirconia fixed partial dentures--clinical results after 3 years of clinical service**. *Quintessence international* 2008, **39**(6):459-471.
95. Schmitter M, Mussotter K, Rammelsberg P, Stober T, Ohlmann B, Gabbert O: **Clinical performance of extended zirconia frameworks for fixed dental prostheses: two-year results**. *J Oral Rehabil* 2009, **36**(8):610-615.
96. Wolfart S, Harder S, Eschbach S, Lehmann F, Kern M: **Four-year clinical results of fixed dental prostheses with zirconia substructures (Cercon): end abutments vs. cantilever design**. *Eur J Oral Sci* 2009, **117**(6):741-749.
97. Sailer I, Gottnerb J, Kanelb S, Hammerle CH: **Randomized controlled clinical trial of zirconia-ceramic and metal-ceramic posterior fixed dental prostheses: a 3-year follow-up**. *Int J Prosthodont* 2009, **22**(6):553-560.
98. Schmitt J, Holst S, Wichmann M, Reich S, Gollner M, Hamel J: **Zirconia posterior fixed partial dentures: a prospective clinical 3-year follow-up**. *Int J Prosthodont* 2009, **22**(6):597-603.
99. Ortorp A, Kihl ML, Carlsson GE: **A 3-year retrospective and clinical follow-up study of zirconia single crowns performed in a private practice**. *J Dent* 2009, **37**(9):731-736.
100. Beuer F, Edelhoff D, Gernet W, Sorensen JA: **Three-year clinical prospective evaluation of zirconia-based posterior fixed dental prostheses (FDPs)**. *Clin Oral Investig* 2009, **13**(4):445-451.
101. Beuer F, Stimmelmayr M, Gernet W, Edelhoff D, Guh JF, Naumann M: **Prospective study of zirconia-based restorations: 3-year clinical results**. *Quintessence international* 2010, **41**(8):631-637.
102. Roediger M, Gersdorff N, Huels A, Rinke S: **Prospective evaluation of zirconia posterior fixed partial dentures: four-year clinical results**. *Int J Prosthodont* 2010, **23**(2):141-148.
103. Lin W-S, Ercoli C, Feng C, Morton D: **The Effect of Core Material, Veneering Porcelain, and Fabrication Technique on the Biaxial Flexural Strength and Weibull Analysis of Selected Dental Ceramics**. *Journal of Prosthodontics* 2012, **21**(5):353-362.
104. Beuer F, Schweiger J, Eichberger M, Kappert HF, Gernet W, Edelhoff D: **High-strength CAD/CAM-fabricated veneering material sintered to zirconia copings — A new fabrication mode for all-ceramic restorations**. *Dental Materials* 2009, **25**(1):121-128.
105. Chaar MS, Witkowski S, Strub JR, Att W: **Effect of veneering technique on the fracture resistance of zirconia fixed dental prostheses**. *Journal of Oral Rehabilitation* 2013, **40**(1):51-59.
106. Preis V, Letsch C, Handel G, Behr M, Schneider-Feyrer S, Rosentritt M: **Influence of substructure design, veneer application technique, and firing regime on the in vitro performance of molar zirconia crowns**. *Dental Materials* 2013, **29**(7):e113-e121.
107. Schmitter M, Mueller D, Rues S: **In vitro chipping behaviour of all-ceramic crowns with a zirconia framework and feldspathic veneering: comparison of CAD/CAM-produced veneer with manually layered veneer**. *Journal of Oral Rehabilitation* 2013, **40**(7):519-525.

108. Kuriyama S, Terui Y, Higuchi D, Goto D, Hotta Y, Manabe A, Miyazaki T: **Novel fabrication method for zirconia restorations: Bonding strength of machinable ceramic to zirconia with resin cements**. *Dental Materials Journal* 2011, **30**(3):419-424.
109. Preis V, Behr M, Hahnel S, Handel G, Rosentritt M: **In vitro failure and fracture resistance of veneered and full-contour zirconia restorations**. *Journal of Dentistry* 2012, **40**(11):921-928.
110. Guess PC, Bonfante EA, Silva NRFA, Coelho PG, Thompson VP: **Effect of core design and veneering technique on damage and reliability of Y-TZP-supported crowns**. *Dental Materials* 2013, **29**(3):307-316.
111. Tang X, Nakamura T, Usami H, Wakabayashi K, Yatani H: **Effects of multiple firings on the mechanical properties and microstructure of veneering ceramics for zirconia frameworks**. *Journal of Dentistry* 2012, **40**(5):372-380.
112. **Reinforcement of Polymers**. *Journal of Dental Research* 1967, **46**(6):1193.
113. MC Creight LR: **Overview of Fiber Composites**. *Journal of Dental Research* 1967, **46**(6):1191-1192.
114. Heumen CCMv, Kreulen CM, Creugers NHJ: **Clinical studies of fiber-reinforced resin-bonded fixed partial dentures: a systematic review**. *European Journal of Oral Sciences* 2009, **117**(1):1-6.
115. Behr M, Rosentritt M, Leibrock A, Schneider-Feyrer S, Handel G: **In-vitro study of fracture strength and marginal adaption of fibre-reinforced adhesive fixed partial inlay dentures**. *Journal of Dentistry* 1999, **27**(2):163-168.
116. Dyer SR, Lassila LVJ, Alander P, Vallittu PK: **Static strength of molar region direct technique glass fibre-reinforced composite fixed partial dentures**. *Journal of Oral Rehabilitation* 2005, **32**(5):351-357.
117. Dyer SR, Sorensen JA, Lassila LVJ, Vallittu PK: **Damage mechanics and load failure of fiber-reinforced composite fixed partial dentures**. *Dental Materials* 2005, **21**(12):1104-1110.
118. Ozcan M, Breuklander MH, Vallittu PK: **The effect of box preparation on the strength of glass fiber-reinforced composite inlay-retained fixed partial dentures**. *The Journal of Prosthetic Dentistry* 2005, **93**(4):337-345.
119. Xie Q, Lassila LVJ, Vallittu PK: **Comparison of load-bearing capacity of direct resin-bonded fiber-reinforced composite FPDs with four framework designs**. *Journal of Dentistry* 2007, **35**(7):578-582.
120. Song H-Y, Yi Y-J, Cho L-R, Park D-Y: **Effects of two preparation designs and pontic distance on bending and fracture strength of fiber-reinforced composite inlay fixed partial dentures**. *The Journal of Prosthetic Dentistry* 2003, **90**(4):347-353.
121. Kolbeck C, Rosentritt M, Behr M, Lang R, Handel G: **In vitro examination of the fracture strength of 3 different fiber-reinforced composite and 1 all-ceramic posterior inlay fixed partial denture systems**. *Journal of Prosthodontics* 2002, **11**(4):248-253.
122. Li W, Swain MV, Li Q, Ironside J, Steven GP: **Fibre reinforced composite dental bridge.: Part I: experimental investigation**. *Biomaterials* 2004, **25**(20):4987-4993.
123. Vallittu PK: **The effect of glass fiber reinforcement on the fracture resistance of a provisional fixed partial denture**. *The Journal of Prosthetic Dentistry* 1998, **79**(2):125-130.
124. Pospiech P, Rammelsberg P, Goldhofer G, Gernet W: **All-ceramic resin-bonded bridges A 3-dimensional finite-element analysis study**. *European Journal of Oral Sciences* 1996, **104**(4):390-395.

125. Magne P, Perakis N, Belser UC, Krejci I: **Stress distribution of inlay-anchored adhesive fixed partial dentures: A finite element analysis of the influence of restorative materials and abutment preparation design**. *The Journal of Prosthetic Dentistry* 2002, **87**(5):516-528.
126. Nakamura T, Ohyama T, Waki T, Kinuta S, Wakabayashi K, Takano N, Yatani H: **Finite element analysis of fiber-reinforced fixed partial dentures**. *Dental materials journal* 2005, **24**(2):275.
127. Ootaki M, Shin-Ya A, Gomi H, Nakasone Y: **Optimum design for fixed partial dentures made of hybrid resin with glass fiber reinforcement by finite element analysis: effect of vertical reinforced thickness on fiber frame**. *Dental materials journal* 2007, **26**(2):280-289.
128. Rappelli G, Scalise L, Procaccini M, Tomasini EP: **Stress distribution in fiber-reinforced composite inlay fixed partial dentures**. *The Journal of Prosthetic Dentistry* 2005, **93**(5):425-432.
129. Chung, Lin, Wang: **Flexural strength of a provisional resin material with fibre addition**. *Journal of Oral Rehabilitation* 1998, **25**(3):214-217.
130. Dyer SR, Lassila LVJ, Jokinen M, Vallittu PK: **Effect of fiber position and orientation on fracture load of fiber-reinforced composite**. *Dental Materials* 2004, **20**(10):947-955.
131. Dyer SR, Lassila LVJ, Jokinen M, Vallittu PK: **Effect of cross-sectional design on the modulus of elasticity and toughness of fiber-reinforced composite materials**. *The Journal of Prosthetic Dentistry* 2005, **94**(3):219-226.
132. Ellakwa AE, Shortall AC, Shehata MK, Marquis PM: **The influence of fibre placement and position on the efficiency of reinforcement of fibre reinforced composite bridgework**. *Journal of Oral Rehabilitation* 2001, **28**(8):785-791.
133. Narva KK, Lassila LVJ, Vallittu PK: **Flexural fatigue of denture base polymer with fiber-reinforced composite reinforcement**. *Composites Part A: Applied Science and Manufacturing* 2005, **36**(9):1275-1281.
134. Hamstad M: **Testing fiber composites with acoustic emission monitoring**. *Name: J Acoust Emiss* 1982.
135. Hamstad M: **Composite characterization techniques- Acoustic emission**. *ManTech Journal* 1985, **10**(3):24-32.
136. Hamstad M: **A review: Acoustic emission, a tool for composite-materials studies**. *Experimental Mechanics* 1986, **26**(1):7-13.
137. Narisawa I, Oba H: **An evaluation of acoustic emission from fibre-reinforced composites**. *J Mater Sci* 1984, **19**(6):1777-1786.
138. Duray SJ, Lee S-Y, Menis DL, Gilbert JL, Lautenschlager EP, Greener EH: **Laser acoustic emission thermal technique (LAETT): A technique for generating acoustic emission in dental composites**. *Dental Materials* 1996, **12**(1):13-18.
139. Fennis WMM, Tezvergil A, Kuijs RH, Lassila LVJ, Kreulen CM, Creugers NHJ, Vallittu PK: **In vitro fracture resistance of fiber reinforced cusp-replacing composite restorations**. *Dental Materials* 2005, **21**(6):565-572.
140. Kim K-H, Okuno O: **Microfracture behaviour of composite resins containing irregular-shaped fillers**. *Journal of Oral Rehabilitation* 2002, **29**(12):1153-1159.
141. Pasi A, Lippo VJL, Arzu T, Pekka KV: **Acoustic emission analysis of fiber-reinforced composite in flexural testing**. *Dental materials : official publication of the Academy of Dental Materials* 2004, **20**(4):305-312.

142. Shifman, LauFer BZ, Chweidan: **Posterior bite collapse – revisited**. *Journal of Oral Rehabilitation* 1998, **25**(5):376-385.
143. Kishen A, Ramamurty U, Asundi A: **Experimental studies on the nature of property gradients in the human dentine**. *Journal of Biomedical Materials Research* 2000, **51**(4):650-659.
144. Carter DR, Hayes WC: **The compressive behavior of bone as a two-phase porous structure**. *The Journal of bone and joint surgery American volume* 1977, **59**(7):954-962.
145. Jeng Y-R, Lin T-T, Hsu H-M, Chang H-J, Shieh D-B: **Human enamel rod presents anisotropic nanotribological properties**. *Journal of the Mechanical Behavior of Biomedical Materials* 2011, **4**(4):515-522.
146. Jitcharoen J, Padture NP, Giannakopoulos AE, Suresh S: **Hertzian-Crack Suppression in Ceramics with Elastic-Modulus-Graded Surfaces**. *Journal of the American Ceramic Society* 1998, **81**(9):2301-2308.
147. Williams KR, Edmundson JT, Rees JS: **Finite element stress analysis of restored teeth**. *Dental Materials* 1987, **3**(4):200-206.
148. Thresher RW, Saito GE: **The stress analysis of human teeth**. *Journal of Biomechanics* 1973, **6**(5):443-449.
149. Rubin C, Krishnamurthy N, Capilouto E, Yi H: **Clinical Science: Stress Analysis of the Human Tooth Using a Three-dimensional Finite Element Model**. *Journal of Dental Research* 1983, **62**(2):82-86.
150. Xu HHK, Smith DT, Jahanmir S, Romberg E, Kelly JR, Thompson VP, Rekow ED: **Indentation Damage and Mechanical Properties of Human Enamel and Dentin**. *Journal of Dental Research* 1998, **77**(3):472-480.
151. Zheng J, Zhou Z, Zhang J, Li H, Yu H: **On the friction and wear behaviour of human tooth enamel and dentin**. *Wear* 2003, **255**(7):967-974.
152. Li H, Zhou ZR: **Wear behaviour of human teeth in dry and artificial saliva conditions**. *Wear* 2001, **249**(10–11):980-984.
153. Poole DFG, Brooks AW: **The arrangement of crystallites in enamel prisms**. *Archives of Oral Biology* 1961, **5**(1):14-IN15.
154. Spears IR: **A Three-dimensional Finite Element Model of Prismatic Enamel: A Re-appraisal of the Data on the Young's Modulus of Enamel**. *Journal of Dental Research* 1997, **76**(10):1690-1697.
155. Spears IR, Van Noort R, Crompton RH, Cardew GE, Howard IC: **The Effects of Enamel Anisotropy on the Distribution of Stress in a Tooth**. *Journal of Dental Research* 1993, **72**(11):1526-1531.
156. Keulemans F, De Jager N, Kleverlaan C, Feilzer A: **Influence of retainer design on two-unit cantilever resin-bonded glass fiber reinforced composite fixed dental prostheses: an in vitro and finite element analysis study**. *The journal of adhesive dentistry* 2008, **10**(5):355.
157. Li W, Swain MV, Li Q, Steven GP: **Towards automated 3D finite element modeling of direct fiber reinforced composite dental bridge**. *Journal of Biomedical Materials Research Part B: Applied Biomaterials* 2005, **74B**(1):520-528.
158. Shinya A, Lassila L, Vallittu P: **Three-dimensional finite element analysis of posterior fiber reinforced composite fixed partial denture: framework design for pontic**. *The European journal of prosthodontics and restorative dentistry* 2009, **17**(2):78.

159. Shinya A, Yokoyama D, Lassila L, Vallittu P: **Three-dimensional finite element analysis of metal and FRC adhesive fixed dental prostheses**. *The journal of adhesive dentistry* 2008, **10**(5):365.
160. Rossow M, Taylor J: **A finite element method for the optimal design of variable thickness sheets**. *AIAA Journal* 1973, **11**(11):1566-1569.
161. Atrek E, Kodali R: **Optimum design of continuum structures with SHAPE**. *CAD/CAM Robotics and Factories of the Future* 1989, **2**:11-15.
162. Atrek E: **SHAPE: a structural shape optimization program**. *International series of numerical mathematics* 1992:229-229.
163. Young V, Querin O, Steven G, Xie Y: **3D and multiple load case bi-directional evolutionary structural optimization (BESO)**. *Structural optimization* 1999, **18**(2-3):183-192.
164. Mattheck C: **Design of Nature: Learning from Trees**: Springer; 1998.
165. Bendsøe MP: **Optimal shape design as a material distribution problem**. *Structural optimization* 1989, **1**(4):193-202.
166. Zhou M, Rozvany G: **On the validity of ESO type methods in topology optimization**. *Struct Multidisc Optim* 2001, **21**(1):80-83.
167. Li S: **Shape optimization of Dental Restorations using the Principle of Biological Adaptive Growth**. University of Manchester; 2007.
168. ABAQUS: **ABAQUS/CAE User's Manual: 1.1.50 UTEMP: User subroutine to specify prescribed temperatures.** In.: ABAQUS; 2012.
169. Shi L, Fok AS, Qualtrough A: **A two-stage shape optimization process for cavity preparation**. *Dental Materials* 2008, **24**(11):1444-1453.
170. Shi L, Fok AS: **Structural optimization of the fibre-reinforced composite substructure in a three-unit dental bridge**. *Dental materials* 2009, **25**(6):791-801.
171. Shi L, Li H, Fok A, Ucer C, Devlin H, Horner K: **Shape optimization of dental implants**. *The International journal of oral & maxillofacial implants* 2006, **22**(6):911-920.
172. Stern N, Revah A, Becker A: **The tilted posterior tooth. Part I: Etiology, syndrome, and prevention**. *The Journal of Prosthetic Dentistry* 1981, **46**(4):404-407.
173. Ainamo J: **Relationship between malalignment of the teeth and periodontal disease**. *European Journal of Oral Sciences* 1972, **80**(2):104-110.
174. Mihram WL, Nemetz H: **The tilted molar: a prosthetic and periodontal dilemma**. *Oral health* 1991, **81**(10):11-15.
175. Simon RL: **Rationale and practical technique for uprighting mesially inclined molars**. *The Journal of Prosthetic Dentistry* 1984, **52**(2):256-259.
176. Svanberg G, Lindhe J: **Experimental tooth hypermobility in the dog. A methodological study**. *Odontologisk revy* 1972, **24**(3):269-282.
177. Svanberg GK, King GJ, Gibbs CH: **Occlusal considerations in periodontology**. *Periodontology 2000* 1995, **9**(1):106-117.
178. Meitner S: **Co-destructive factors of marginal periodontitis and repetitive mechanical injury**. *Journal of Dental Research* 1975, **54**(3 suppl):C78-C85.
179. Ericsson I, Lindhe J: **Effect of longstanding jiggling on experimental marginal periodontitis in the beagle dog**. *Journal of clinical periodontology* 1982, **9**(6):497-503.
180. Davies S, Gray R: **Occlusion: What is occlusion?** *British dental journal* 2001, **191**(5):235-245.
181. Beall AE: **Can a new smile make you look more intelligent and successful?** *Dental Clinics of North America* 2007, **51**(2):289-297.

182. Sarver DM, Ackerman MB: **Dynamic smile visualization and quantification: Part 1. Evolution of the concept and dynamic records for smile capture**. *American journal of orthodontics and dentofacial orthopedics* 2003, **124**(1):4-12.
183. KERNS LL, SILVEIRA AM, KERNS DC, RECENNITTER FJ: **Esthetic preference of the frontal and profile views of the same smile**. *Journal of Esthetic and Restorative Dentistry* 1997, **9**(2):76-85.
184. Sarver D, Proffit W: **Special considerations in diagnosis and treatment planning**. *Grabel', Vanarsdall, Vig, editors Orthodontics Current Principles and Techniques St Louis: Mosby* 2005.
185. Ghaleb N, Bouserhal J, Bassil-Nassif N: **Aesthetic evaluation of profile incisor inclination**. *The European Journal of Orthodontics* 2011, **33**(3):228-235.
186. Devanna R: **Turning subjective into objective: Profile smile perception of I2 (incisor inclination) and its impact on treatment planning**. *Journal of Orthodontic Research* 2013, **1**(1):27.
187. Braun S, Legan HL: **Changes in occlusion related to the cant of the occlusal plane**. *American journal of orthodontics and dentofacial orthopedics* 1997, **111**(2):184-188.
188. Paquette DE: **Importance of the occlusal plane in virtual treatment planning**. *Journal of Clinical Orthodontics* 2011, **45**(4):217.
189. Spear FM, Kokich VG, Mathews DP: **Interdisciplinary management of anterior dental esthetics**. *Journal of the American Dental Association* 2006, **137**(2):160-169.
190. ABAQUS: **ABAQUS/CAE User's Manual: 28.1.3 Two-dimensional solid element library**: ABAQUS; 2012.
191. Farah J, Craig R, Meroueh K: **Finite element analysis of three-and four-unit bridges**. *Journal of Oral Rehabilitation* 1989, **16**(6):603-611.
192. Peyton F, Mahler D, Hershenov B: **Physical properties of dentin**. *Journal of Dental Research* 1952, **31**(3):366-370.
193. Carter DR, Hayes WC: **The compressive behavior of bone as a two-phase porous structure**. *The Journal of bone and joint surgery American volume* 1977, **59**(7):954-962.
194. Couegnat G, Fok SL, Cooper JE, Qualtrough AJE: **Structural optimization of dental restorations using the principle of adaptive growth**. *Dental Materials* 2006, **22**(1):3-12.
195. Yettram A, Wright K, Houston W: **Centre of rotation of a maxillary central incisor under orthodontic loading**. *British journal of orthodontics* 1977, **4**(1):23.
196. Geiger AM, Wasserman BH: **Relationship of Occlusion and Periodontal Disease: Part IX—Incisor Inclination and Periodontal Status**. *The Angle Orthodontist* 1976, **46**(2):99-110.
197. Proffit WR, Fields HW: **Contemporary orthodontics**: Mosby; 2000.
198. Yared KFG, Zenobio EG, Pacheco W: **Periodontal status of mandibular central incisors after orthodontic proclination in adults**. *American Journal of Orthodontics and Dentofacial Orthopedics* 2006, **130**(1):6.e1-6.e8.
199. Nguyen Q, Bezemer P, Habets L, Prahl-Andersen B: **A systematic review of the relationship between overjet size and traumatic dental injuries**. *The European Journal of Orthodontics* 1999, **21**(5):503-515.
200. Rupp RP, Dillehay JK, Squire CF: **Orthodontics, prosthodontics, and periodontics: a multidisciplinary approach**. *General dentistry* 1997, **45**(3):286-289.
201. **Large Labial Concavity: Best Treatment Option for Implant Placement?** [http://www.osseonews.com/large-labial-concavity-best-treatment-option-for-implant-placement/]

202. Ata-Ali J, Penarrocha-Oltra D, Candel-Marti E, Penarrocha-Diago M: **Oral rehabilitation with tilted dental implants: a metaanalysis**. *Medicina oral, patologia oral y cirugia bucal* 2012, **17**(4):e582-587.
203. Tabrizi R, Pourdanesh F, Zare S, Daneste H, Zeini N: **Do angulated implants increase the amount of bone loss around implants in the anterior maxilla?** *Journal of oral and maxillofacial surgery : official journal of the American Association of Oral and Maxillofacial Surgeons* 2013, **71**(2):272-277.
204. Tian K, Chen J, Han L, Yang J, Huang W, Wu D: **Angled abutments result in increased or decreased stress on surrounding bone of single-unit dental implants: a finite element analysis**. *Medical engineering & physics* 2012, **34**(10):1526-1531.
205. Martini AP, Barros RM, Junior AC, Rocha EP, de Almeida EO, Ferraz CC, Pellegrin MC, Anchieta RB: **Influence of platform and abutment angulation on peri-implant bone. A three-dimensional finite element stress analysis**. *The Journal of oral implantology* 2013, **39**(6):663-669.
206. Martini AP, Freitas ACJ, Rocha EP, de Almeida EO, Anchieta RB, Kina S, Fasolo GB: **Straight and Angulated Abutments in Platform Switching: Influence of Loading on Bone Stress by Three-Dimensional Finite Element Analysis**. *Journal of Craniofacial Surgery* 2012, **23**(2):415-418 410.1097/SCS.1090b1013e31824b31829c31817.
207. Saab XE, Griggs JA, Powers JM, Engelmeier RL: **Effect of abutment angulation on the strain on the bone around an implant in the anterior maxilla: a finite element study**. *J Prosthet Dent* 2007, **97**(2):85-92.
208. Dubois G, Daas M, Bonnet A, Lipinski P: **Biomechanical study of a prosthetic solution based on an angled abutment: Case of upper lateral incisor**. *Medical engineering & physics* 2007, **29**(9):989-998.
209. Hasan I, Röger B, Heinemann F, Keilig L, Bourauel C: **Influence of abutment design on the success of immediately loaded dental implants: Experimental and numerical studies**. *Medical engineering & physics* 2012, **34**(7):817-825.
210. Kao H-C, Gung Y-W, Chung T-F, Hsu M-L: **The influence of abutment angulation on micromotion level for immediately loaded dental implants: a 3-D finite element analysis**. *International Journal of Oral & Maxillofacial Implants* 2008, **23**(4).
211. Pellizzer EP, Falcón-Antenucci RM, de Carvalho PSP, Sánchez DMIK, Rinaldi GAT, de Aguirre CC, Goiato MC: **Influence of Implant Angulation With Different Crowns on Stress Distribution**. *Journal of Craniofacial Surgery* 2011, **22**(2):434-437 410.1097/SCS.1090b1013e318207477c.
212. Sadrimanesh R, Siadat H, Sadr-Eshkevari P, Monzavi A, Maurer P, Rashad A: **Alveolar Bone Stress Around Implants With Different Abutment Angulation: An FE-Analysis of Anterior Maxilla**. *Implant Dentistry* 2012, **21**(3):196-201 110.1097/ID.1090b1013e31824c31302e.
213. Lin CL, Wang JC, Ramp LC, Liu PR: **Biomechanical response of implant systems placed in the maxillary posterior region under various conditions of angulation, bone density, and loading**. *The International journal of oral & maxillofacial implants* 2008, **23**(1):57-64.
214. Katranji A, Misch K, Wang H-L: **Cortical Bone Thickness in Dentate and Edentulous Human Cadavers**. *Journal of periodontology* 2007, **78**(5):874-878.
215. **Chapter 15 - Dental and Orofacial Implants**. In: *Craig's Restorative Dental Materials (Thirteenth Edition).* edn. Edited by Sakaguchi RL, Powers JM. Saint Louis: Mosby; 2012: 355-367.
216. **IPS e.max Scientific Documentation** In.: Ivoclar Vivadent AG; 2011.

217. Jurczyk M: **Bionanomaterials for Dental Applications**: Pan Stanford; 2012.
218. Evans FG, Lissner HR: **Tensile and Compressive Strength of Human Parietal Bone**. *Journal of Applied Physiology* 1957, **10**(3):493-497.
219. Cowin SC: **Bone Mechanics Handbook, Second Edition**: Taylor & Francis; 2001.
220. Natali AN: **Dental Biomechanics**: Taylor & Francis; 2003.
221. Tanne K, Nagataki T, Matsubara S, Kato J, Terada Y, Sibaguchi T, Tanaka E, Sakuda M: **Association between mechanical stress and bone remodeling**. *The Journal of Osaka University Dental School* 1990, **30**:64-71.
222. Firoozbakhsh K, Aleyaasin M: **The effect of stress concentration on bone remodeling: theoretical predictions**. *Journal of biomechanical engineering* 1989, **111**(4):355-360.
223. Kawashima H, Ikegame M, Shimomura J, Ishibashi O, Komori T, Noda T, Ozawa H: **Tensile stress induced osteoblast differentiation and osteogenesis in mouse calvarial suture in culture: possible involvement of BMP-4 and other genes**. *Journal of gravitational physiology : a journal of the International Society for Gravitational Physiology* 2000, **7**(2):P121-122.
224. Ikegame M, Ishibashi O, Yoshizawa T, Shimomura J, Komori T, Ozawa H, Kawashima H: **Tensile stress induces bone morphogenetic protein 4 in preosteoblastic and fibroblastic cells, which later differentiate into osteoblasts leading to osteogenesis in the mouse calvariae in organ culture**. *Journal of bone and mineral research : the official journal of the American Society for Bone and Mineral Research* 2001, **16**(1):24-32.
225. Myer K: **BONE MECHANICS**. In: *Standard Handbook of Biomedical Engineering & Design.* edn.: McGraw Hill Professional, Access Engineering; 2003.
226. Zhu J, Zhang X, Wang C, Peng X, Zhang X: **Different Magnitudes of Tensile Strain Induce Human Osteoblasts Differentiation Associated with the Activation of ERK1/2 Phosphorylation**. *International Journal of Molecular Sciences* 2008, **9**(12):2322-2332.
227. Jackson AP, Vincent JFV, Turner RM: **The Mechanical Design of Nacre**. *Proceedings of the Royal Society of London Series B Biological Sciences* 1988, **234**(1277):415-440.
228. Chen PY, Lin AYM, Lin YS, Seki Y, Stokes AG, Peyras J, Olevsky EA, Meyers MA, McKittrick J: **Structure and mechanical properties of selected biological materials**. *Journal of the Mechanical Behavior of Biomedical Materials* 2008, **1**(3):208-226.
229. Marshall GW, Balooch M, Gallagher RR, Gansky SA, Marshall SJ: **Mechanical properties of the dentinoenamel junction: AFM studies of nanohardness, elastic modulus, and fracture**. *Journal of Biomedical Materials Research* 2001, **54**(1):87-95.
230. Fong H, Sarikaya M, White SN, Snead ML: **Nano-mechanical properties profiles across dentin–enamel junction of human incisor teeth**. *Materials Science and Engineering: C* 2000, **7**(2):119-128.
231. Balooch G, Marshall GW, Marshall SJ, Warren OL, Asif SAS, Balooch M: **Evaluation of a new modulus mapping technique to investigate microstructural features of human teeth**. *Journal of Biomechanics* 2004, **37**(8):1223-1232.
232. Willems G, Celis JP, Lambrechts P, Braem M, Vanherle G: **Hardness and young's modulus determined by nanoindentation technique of filler particles of dental restorative materials compared with human enamel**. *Journal of Biomedical Materials Research* 1993, **27**(6):747-755.
233. Cuy JL, Mann AB, Livi KJ, Teaford MF, Weihs TP: **Nanoindentation mapping of the mechanical properties of human molar tooth enamel**. *Archives of Oral Biology* 2002, **47**(4):281-291.

234. Zhou J, Hsiung LL: **Depth-dependent mechanical properties of enamel by nanoindentation**. *Journal of Biomedical Materials Research Part A* 2007, **81A**(1):66-74.
235. Ge J, Cui FZ, Wang XM, Feng HL: **Property variations in the prism and the organic sheath within enamel by nanoindentation**. *Biomaterials* 2005, **26**(16):3333-3339.
236. Mahoney E, Holt A, Swain M, Kilpatrick N: **The hardness and modulus of elasticity of primary molar teeth:an ultra-micro-indentation study**. *Journal of Dentistry* 2000, **28**(8):589-594.
237. Habelitz S, Marshall SJ, Marshall Jr GW, Balooch M: **Mechanical properties of human dental enamel on the nanometre scale**. *Archives of Oral Biology* 2001, **46**(2):173-183.
238. Barbour ME, Parker DM, Jandt KD: **Enamel dissolution as a function of solution degree of saturation with respect to hydroxyapatite: a nanoindentation study**. *Journal of Colloid and Interface Science* 2003, **265**(1):9-14.
239. Staines M, Robinson WH, Hood JAA: **Spherical indentation of tooth enamel**. *Journal of Materials Science* 1981, **16**(9):2551-2556.
240. Habelitz S, Marshall Jr GW, Balooch M, Marshall SJ: **Nanoindentation and storage of teeth**. *Journal of Biomechanics* 2002, **35**(7):995-998.
241. Allen MR, Burr DB: **Mineralization, microdamage, and matrix: How bisphosphonates influence material properties of bone**. *IBMS BoneKEy* 2007, **4**(2):49-60.
242. Huang TT, He LH, Darendeliler MA, Swain MV: **Correlation of mineral density and elastic modulus of natural enamel white spot lesions using X-ray microtomography and nanoindentation**. *Acta biomaterialia* 2010, **6**(12):4553-4559.
243. ABAQUS_Documentation: **User subroutine to define a material's mechanical behavior**. In., 6.10 edn. Waltham, MA, USA: Dassault Syetemes Simulia; 2010.
244. **Zirconium Oxides (Zirconia)**. In: *Bioceramics.* edn.: Springer New York; 2009: 136-161.
245. Schwass DR, Swain MV, Purton DG, Leichter JW: **A System of Calibrating Microtomography for Use in Caries Research**. *Caries Research* 2009, **43**(4):314-321.
246. Huang TTY, He L-H, Darendeliler MA, Swain MV: **Correlation of mineral density and elastic modulus of natural enamel white spot lesions using X-ray microtomography and nanoindentation**. *Acta Biomaterialia* 2010, **6**(12):4553-4559.
247. Clementino-Luedemann TNR, Kunzelmann K-H: **Mineral Concentration of Natural Human Teeth by a Commercial Micro-CT**. *Dental Materials Journal* 2006, **25**(1):113-119.
248. Dowker SE, Elliott JC, Davis GR, Wassif HS: **Longitudinal study of the three-dimensional development of subsurface enamel lesions during in vitro demineralisation**. *Caries research* 2003, **37**(4):237-245.
249. Dowker SE, Elliott JC, Davis GR, Wilson RM, Cloetens P: **Synchrotron x-ray microtomographic investigation of mineral concentrations at micrometre scale in sound and carious enamel**. *Caries research* 2004, **38**(6):514-522.
250. Wong FS, Anderson P, Fan H, Davis GR: **X-ray microtomographic study of mineral concentration distribution in deciduous enamel**. *Archives of Oral Biology* 2004, **49**(11):937-944.
251. Little MF, Posen J, Singer L: **Chemical and physical properties of altered and sound enamel. 3. Fluoride and sodium content**. *Journal of Dental Research* 1962, **41**:784-789.
252. Weidmann SM, Weatherell JA, Hamm SM: **Variations of enamel density in sections of human teeth**. *Archives of Oral Biology* 1967, **12**(1):85-97.
253. Niu X, Rahbar N, Farias S, Soboyejo W: **Bio-inspired design of dental multilayers: Experiments and model**. *Journal of the Mechanical Behavior of Biomedical Materials* 2009, **2**(6):596-602.

254. Huang M, Rahbar N, Wang R, Thompson V, Rekow D, Soboyejo WO: **Bioinspired design of dental multilayers**. *Materials Science and Engineering: A* 2007, **464**(1–2):315-320.
255. Romeed SA, Fok SL, Wilson NHF: **A comparison of 2D and 3D finite element analysis of a restored tooth**. *Journal of oral rehabilitation* 2006, **33**(3):209-215.
256. Nanci A: **Ten Cate's Oral Histology: Development, Structure, and Function**: Mosby Elsevier; 2008.
257. Meyers MA, Lin AY, Chen PY, Muyco J: **Mechanical strength of abalone nacre: role of the soft organic layer**. *J Mech Behav Biomed Mater* 2008, **1**(1):76-85.
258. Habelitz S, Marshall S, Marshall Jr G, Balooch M: **Mechanical properties of human dental enamel on the nanometre scale**. *Archives of Oral Biology* 2001, **46**(2):173-183.
259. He LH, Fujisawa N, Swain MV: **Elastic modulus and stress–strain response of human enamel by nano-indentation**. *Biomaterials* 2006, **27**(24):4388-4398.
260. Marshall Jr GW, Marshall SJ, Kinney JH, Balooch M: **The dentin substrate: structure and properties related to bonding**. *Journal of Dentistry* 1997, **25**(6):441-458.
261. Shimizu D, Macho GA, Spears IR: **Effect of prism orientation and loading direction on contact stresses in prismatic enamel of primates: implications for interpreting wear patterns**. *American journal of physical anthropology* 2005, **126**(4):427-434.
262. Jiang Y, Spears I, Macho G: **An investigation into fractured surfaces of enamel of modern human teeth: a combined SEM and computer visualisation study**. *Archives of oral biology* 2003, **48**(6):449-457.
263. Spears I, Van Noort R, Crompton R, Cardew G, Howard I: **The effects of enamel anisotropy on the distribution of stress in a tooth**. *Journal of dental research* 1993, **72**(11):1526-1531.
264. Ji B, Gao H: **Mechanical properties of nanostructure of biological materials**. *Journal of the Mechanics and Physics of Solids* 2004, **52**(9):1963-1990.
265. Nakamura T, Lu C, Korach CS: **Mechanical Properties of Tooth Enamel: Microstructural Modeling and Characterization**. In: *Mechanics of Biological Systems and Materials, Volume 2.* edn.: Springer; 2011: 171-179.
266. **American Academy of Implant Dentistry: Dental Implants Facts and Figures** [http://www.aaid.com/about/Press_Room/Dental_Implants_FAQ.html]
267. Achermann G: **How will dentistry look in 2020?** In: *STRAUMANN'S 2012 Capital Markets Day.* Amsterdam; 2012.
268. Lin WS, Ercoli C, Feng C, Morton D: **The effect of core material, veneering porcelain, and fabrication technique on the biaxial flexural strength and weibull analysis of selected dental ceramics**. *Journal of Prosthodontics* 2012, **21**(5):353-362.
269. Chaar M, Witkowski S, Strub J, Att W: **Effect of veneering technique on the fracture resistance of zirconia fixed dental prostheses**. *Journal of Oral Rehabilitation* 2013, **40**(1):51-59.
270. Beuer F, Schweiger J, Eichberger M, Kappert HF, Gernet W, Edelhoff D: **High-strength CAD/CAM-fabricated veneering material sintered to zirconia copings—a new fabrication mode for all-ceramic restorations**. *dental materials* 2009, **25**(1):121-128.
271. Preis V, Letsch C, Handel G, Behr M, Schneider-Feyrer S, Rosentritt M: **Influence of substructure design, veneer application technique, and firing regime on the in vitro performance of molar zirconia crowns**. *Dental Materials* 2013.
272. Schmitter M, Mueller D, Rues S: **In vitro chipping behaviour of all-ceramic crowns with a zirconia framework and feldspathic veneering: comparison of CAD/CAM-produced veneer with manually layered veneer**. *Journal of oral rehabilitation* 2013.

273. Kuriyama S, Terui Y, Higuchi D, Goto D, Hotta Y, Manabe A, Miyazaki T: **Novel fabrication method for zirconia restorations: Bonding strength of machinable ceramic to zirconia with resin cements**. *Dental materials journal* 2011(0):1105140147.
274. Preis V, Behr M, Hahnel S, Handel G, Rosentritt M: **In vitro failure and fracture resistance of veneered and full-contour zirconia restorations**. *Journal of Dentistry* 2012.
275. Guess PC, Zhang Y, Thompson V: **Effect of veneering techniques on damage and reliability of Y-TZP trilayers**. *The European journal of esthetic dentistry: official journal of the European Academy of Esthetic Dentistry* 2009, **4**(3):262.
276. Wagner W, Chu T: **Biaxial flexural strength and indentation fracture toughness of three new dental core ceramics**. *The journal of prosthetic dentistry* 1996, **76**(2):140-144.
277. Xu H, Smith D, Jahanmir S, Romberg E, Kelly J, Thompson V, Rekow E: **Indentation damage and mechanical properties of human enamel and dentin**. *Journal of Dental Research* 1998, **77**(3):472-480.
278. Willems G, Celis J-P, Lambrechts P, Braem M, Vanherle G: **Hardness and Young's modulus determined by nanoindentation technique of filler particles of dental restorative materials compared with human enamel**. *Journal of biomedical materials research* 1993, **27**(6):747-755.
279. Chen P-Y, Lin A, Lin Y-S, Seki Y, Stokes A, Peyras J, Olevsky E, Meyers M, McKittrick J: **Structure and mechanical properties of selected biological materials**. *Journal of the Mechanical Behavior of Biomedical Materials* 2008, **1**(3):208-226.
280. Kodaka T, Debari K, Yamada M, Kuroiwa M: **Correlation between microhardness and mineral content in sound human enamel**. *Caries research* 1992, **26**(2):139-141.
281. Staines M, Robinson W, Hood J: **Spherical indentation of tooth enamel**. *Journal of materials science* 1981, **16**(9):2551-2556.
282. Zhang Y, Chai H, Lawn BR: **Graded Structures for All-ceramic Restorations**. *Journal of Dental Research* 2010, **89**(4):417-421.
283. **VITA VM 9 for individualizing VITABLOCS**. In.: VITA Zahnfabrik; 2012.
284. **VITABLOCS Working Instruction**. In.: VITA Zahnfabrik; 2012.
285. Baker B: **Global Markets for Dental CAD/CAM Systems 2012**. In.: Millennium Research Group; 2012.
286. Aboushelib MN, Feilzer AJ, de Jager N, Kleverlaan CJ: **Prestresses in bilayered all-ceramic restorations**. *Journal of Biomedical Materials Research Part B: Applied Biomaterials* 2008, **87B**(1):139-145.
287. Rekow ED, Silva NRFA, Coelho PG, Zhang Y, Guess P, Thompson VP: **Performance of Dental Ceramics: Challenges for Improvements**. *Journal of Dental Research* 2011, **90**(8):937-952.
288. Swain MV: **Unstable cracking (chipping) of veneering porcelain on all-ceramic dental crowns and fixed partial dentures**. *Acta biomaterialia* 2009, **5**(5):1668-1677.
289. Schmitter M, Mueller D, Rues S: **Chipping behaviour of all-ceramic crowns with zirconia framework and CAD/CAM manufactured veneer**. *Journal of Dentistry* 2012, **40**(2):154-162.
290. **IPS e.max® CAD-on Scentific Documentation**. In.: Ivoclar vivadent; 2011.
291. Guess PC, Zavanelli RA, Silva NR, Bonfante EA, Coelho PG, Thompson VP: **Monolithic CAD/CAM lithium disilicate versus veneered Y-TZP crowns: comparison of failure modes and reliability after fatigue**. *International Journal of Prosthodontics* 2010, **23**(5).
292. **Chairside Preparation Guide for IPS Empress® and IPS e.max®**. In.: Ivoclar Vivadent AG; 2008.

293. Bakke M, Holm B, Jensen BL, Michler L, Moller E: **Unilateral, isometric bite force in 8-68-year-old women and men related to occlusal factors**. *Scandinavian journal of dental research* 1990, **98**(2):149-158.
294. Raigrodski AJ, Chiche GJ, Potiket N, Hochstedler JL, Mohamed SE, Billiot S, Mercante DE: **The efficacy of posterior three-unit zirconium-oxide–based ceramic fixed partial dental prostheses: A prospective clinical pilot study**. *The Journal of Prosthetic Dentistry* 2006, **96**(4):237-244.
295. Sailer I, Feher A, Filser F, Gauckler LJ, Luthy H, Hammerle CH: **Five-year clinical results of zirconia frameworks for posterior fixed partial dentures**. *Int J Prosthodont* 2007, **20**(4):383-388.
296. Tsalouchou E, Cattell MJ, Knowles JC, Pittayachawan P, McDonald A: **Fatigue and fracture properties of yttria partially stabilized zirconia crown systems**. *Dental Materials* 2008, **24**(3):308-318.
297. Ellerbrock C: **The computer-aided overpress (CAO) technique--principles and a case example**. *International journal of computerized dentistry* 2010, **13**(2):155-167.
298. Beuer F, Edelhoff D, Gernet W, Sorensen J: **Three-year clinical prospective evaluation of zirconia-based posterior fixed dental prostheses (FDPs)**. *Clinical Oral Investigations* 2009, **13**(4):445-451.
299. Raigrodski AJ, Hillstead MB, Meng GK, Chung K-H: **Survival and complications of zirconia-based fixed dental prostheses: A systematic review**. *The Journal of Prosthetic Dentistry* 2012, **107**(3):170-177.
300. Nanci A: **Ten Cate's oral histology: development, structure, and function**: Elsevier Health Sciences; 2007.
301. Kerebel B, Daculsi G, Kerebel LM: **Ultrastructural studies of enamel crystallites**. *J Dent Res* 1979, **58**(Spec Issue B):844-851.
302. Bres EF, Waddington WG, Voegel JC, Barry JC, Frank RM: **Theoretical detection of a dark contrast line in twinned apatite bicrystals and its possible correlation with the chemical properties of human dentin and enamel crystals**. *Biophysical journal* 1986, **50**(6):1185-1193.
303. Ang SF, Bortel EL, Swain MV, Klocke A, Schneider GA: **Size-dependent elastic/inelastic behavior of enamel over millimeter and nanometer length scales**. *Biomaterials* 2010, **31**(7):1955-1963.
304. Yettram A, Wright K, Pickard H: **Finite element stress analysis of the crowns of normal and restored teeth**. *Journal of Dental Research* 1976, **55**(6):1004-1011.
305. Ibsen RL: **Fixed prosthetics with a natural crown pontic using an adhesive composite. Case history**. *J South Calif Dent Assoc* 1973, **41**(2):100-102.
306. Ibsen RL: **One-appointment technic using an adhesive composite**. *Dent Surv* 1973, **49**(2):30-32.
307. Rochette AL: **Attachment of a splint to enamel of lower anterior teeth**. *The Journal of Prosthetic Dentistry* 1973, **30**(4, Part 1):418-423.
308. Murdoch-Kinch CA, McLean ME: **Minimally invasive dentistry**. *The Journal of the American Dental Association* 2003, **134**(1):87-95.
309. **What is Maryland Bridge** [http://www.choufanidental.com/maryland-bridges/]
310. Kern M, Knode H, Strubb JR: **The all-porcelain, resin-bonded bridge**. *Quintessence international* 1991, **22**(4):257-262.
311. Freilich MA: **Fiber-reinforced composites in clinical dentistry**: Quintessence Pub. Co.; 2000.

312. Behr M, Zeman F, Baitinger T, Galler J, Koller M, Handel G, Rosentritt M: **The clinical performance of porcelain-fused-to-metal precious alloy single crowns: chipping, recurrent caries, periodontitis, and loss of retention**. *Int J Prosthodont* 2014, **27**(2):153-160.
313. Chong KH, Chai J: **Probability of failure of veneered glass fiber-reinforced composites and glass-infiltrated alumina with or without zirconia reinforcement**. *Int J Prosthodont* 2003, **16**(5):487-492.
314. Shi L, Fok ASL: **Structural optimization of the fibre-reinforced composite substructure in a three-unit dental bridge**. *Dental Materials* 2009, **25**(6):791-801.
315. Wyatt CC: **Resin-bonded fixed partial dentures: what's new?** *Journal (Canadian Dental Association)* 2007, **73**(10):933-938.
316. Imbery TA, Eshelman EG: **Resin-bonded fixed partial dentures: a review of three decades of progress**. *J Am Dent Assoc* 1996, **127**(12):1751-1760.
317. Botelho MG, Nor LC, Kwong HW, Kuen BS: **Two-unit cantilevered resin-bonded fixed partial dentures--a retrospective, preliminary clinical investigation**. *Int J Prosthodont* 2000, **13**(1):25-28.
318. Shi L, Fok AS: **Structural optimization of the fibre-reinforced composite substructure in a three-unit dental bridge**. *Dent Mater* 2009, **25**(6):791-801.
319. ABAQUS: **ABAQUS/CAE User's Manual: 27.1.4 Three-dimensional solid element library**: ABAQUS; 2012.
320. Bortolotto T, Monaco C, Onisor I, Krejci I: **In Vitro Assessment of Single-Retainer Tooth-Colored Adhesively Fixed Partial Dentures for Posterior Teeth**. *International Journal of Dentistry* 2010, **2010**.
321. Vaz RR, Hipólito VD, D'Alpino PHP, Goes MFd: **Bond Strength and Interfacial Micromorphology of Etch-and-Rinse and Self-Adhesive Resin Cements to Dentin**. *Journal of Prosthodontics* 2012, **21**(2):101-111.
322. Çötert HS, Şen BH, Balkan M: **In vitro comparison of cuspal fracture resistances of posterior teeth restored with various adhesive restorations**. *International Journal of Prosthodontics* 2001, **14**(4).
323. St-Georges AJ, Sturdevant JR, Swift Jr EJ, Thompson JY: **Fracture resistance of prepared teeth restored with bonded inlay restorations**. *The Journal of prosthetic dentistry* 2003, **89**(6):551-557.
324. Culy G, Tyas MJ: **Direct resin-bonded, fibre-reinforced anterior bridges: A clinical report**. *Australian Dental Journal* 1998, **43**(1):1-4.
325. Auplish G, Darbar UR: **Immediate anterior tooth replacement using fibre-reinforced composite**. *Dent Update* 2000, **27**(6):267-270.
326. Alander P, Lassila LVJ, Tezvergil A, Vallittu PK: **Acoustic emission analysis of fiber-reinforced composite in flexural testing**. *Dental Materials* 2004, **20**(4):305-312.
327. Ereifej N, Silikas N, Watts DC: **Initial versus final fracture of metal-free crowns, analyzed via acoustic emission**. *Dent Mater* 2008, **24**(9):1289-1295.
328. Bakke M: **Bite Force and Occlusion**. *Seminars in Orthodontics* 2006, **12**(2):120-126.
329. BAKKE M, HOLM B, JENSEN BL, MICHLER L, MÖLLER E: **Unilateral, isometric bite force in 8-68-year-old women and men related to occlusal factors**. *European Journal of Oral Sciences* 1990, **98**(2):149-158.
330. Kim S-T, Lee Y-T: **Characteristics of damage and fracture process of carbon fiber reinforced plastic under loading-unloading test by using AE method**. *Materials Science and Engineering A* 1997, **234-236**:322-326.

331. Giordano M, Calabro A, Esposito C, D'Amore A, Nicolais L: **An acoustic-emission characterization of the failure modes in polymer-composite materials**. *Composites Science and Technology* 1998, **58**(12):1923-1928.
332. Drummond JL: **Degradation, Fatigue, and Failure of Resin Dental Composite Materials**. *Journal of Dental Research* 2008, **87**(8):710-719.